# CONSERVATION OF CALCIUM REGULATION ACROSS VOLTAGE-GATED CALCIUM AND SODIUM CHANNELS.

by

Manu Ben Johny

A dissertation submitted to Johns Hopkins University in conformity with the requirements for the degree of Doctor of Philosophy

Baltimore, Maryland

February, 2015

*In reverent memory of*

*Professor David T. Yue,*

*a great scientist, mentor and friend.*

> “Every so often, the veil of confusing experimental results is parted, and something deep and beautiful about how biological life works is revealed. It is as if a syllable that God spoke becomes suddenly audible. The thrill of unearthing such ‘God speak’ is one of the special rewards of my profession”
>
> David T. Yue, 2006

# ABSTRACT

The voltage-gated $Ca^{2+}$ and Na channels represent two major ion-channel superfamilies with distinct biophysical properties that support diverse and vital physiological functions. Accordingly, these superfamilies have long been studied as distinct entities. That said, the carboxyl tail of these channels exhibit remarkable homology, hinting at a purposeful module long-shared amongst these molecules. If these homologous tail domains elaborated functions of like correspondence, a common origin of such a module might be suggested. For $Ca^{2+}$ channels, the interaction of CaM with their carboxy-terminus evokes robust and recognizably similar forms of $Ca^{2+}$ regulation. By contrast, over a decade of research has revealed subtle and variable $Ca^{2+}$ effects on Na channels, calling into question the very existence of a shared module. Here, using $Ca^{2+}$ photouncaging, we find that these dissimilarities in Na channels are only apparent, and that $Ca^{2+}$ regulatory function and mechanism are fundamentally conserved. To identify the molecular states underlying channel regulation, we develop a structure-function approach relating the strength of regulation to the affinity of underlying calmodulin/channel interactions, by a Langmuir relation. By application of this theoretical framework to $Ca^{2+}$ channels, we uncovered an unprecedented switching of CaM interaction on the channel carboxy-terminus. This system of structural plasticity furnishes a unified mechanistic framework to understand $Ca^{2+}$ and Na channel regulation and offers shared principles to approach related channelopathic diseases. In all, these results help substantiate the persistence of an ancient $Ca^{2+}$ regulatory design across channel superfamilies – a relic that has been preserved for much of living history.

*Thesis committee:* David T. Yue, M.D., Ph.D. (primary advisor); Michael J. Caterina, M.D., Ph.D. (reader); Sandra B. Gabelli, Ph.D.; Gordon F. Tomaselli, M.D. (reader), Ph.D.; Eric D. Young, PhD.

# ACKNOWLEDGMENTS

Graduate school was undeniably the best years of my life so far. It was not an easy journey. Every high was followed by a low and every low by a high. The ebb and flow of science made the last seven and half years seem like the blink of an eye. But in the end, what made this journey so memorable were the nurturing environment at Johns Hopkins University and the wonderful people who traveled with me.

Hopkins Biomedical Engineering will always be a very special place in my heart. It is where I fell in love with science, and it is where I was enamored by biology. For nearly all my life, I was intrigued by mathematical principles or equations that presented an elegant framework to understand nearly everything around us. But, I always felt at odds with the life sciences – things seemed idiosyncratic with more exceptions than rules, and, thus, often posing a formidable challenge to my limited memory. At Hopkins, I learned for the first time that this was not the case. Life too, subscribed to the very same physical laws that the rest of the universe was subject to, and that thermodynamics formed the core of what makes us who we are. For a young engineer, this was a spiritual experience. But that was not all. Hopkins encouraged young students like me, who came to the Charm city with nothing but the willingness to learn and the promise to work hard, and turned us into dreamers who yearn to wonder about the universe. And nowhere was this truer than at the Calcium Signals Laboratory (CSL), a *sanctum sanctorum* for science and ion channel research. This was my home – a place where being at the white-board was comforting and the two-and-half-hour weekly journal clubs refreshing.

There were many student mentors at CSL who devoted considerable effort to teach me the art of science. Michael Tadross was a wonderful influence during my early days in the lab. He taught me that molecular biology was not about following a recipe in a cookbook but rather a series of chemical reactions each with a specific purpose. I recall having many dinners with him at the JHU hospital. These dinners inevitably turned into discussions about the mechanism of $Ca^{2+}$ channel CDI and perhaps formed much of the basis for Chapters 6 – 7. Philemon Yang was my trusted lab partner for nearly all of my graduate studies. Before I came to Hopkins, I took every effort to avoid conducting any experiments. Phil spent nearly three months patiently training me in the art of patch clamping – an experimental protocol that I still feel requires the stars to align. Since then, we have worked together on nearly everything; we ate lunch together; we attended conferences together. We tag teamed through the alanine scanning project ("Manhattan project"), patching side-by-side one cell after another. Beyond his scientific capabilities, Phil is also a person with immense prudence and infinite compassion. And so, he is often the person I turn to when I am in need of advice. So in many ways, over the past years he has become an older brother to me. And this dissertation would certainly not exist if it were not for his generous help. Paul Adams was also a greatly helpful partner in this journey. I often refer to him as the apostle of biology as he was the one who taught me the inner beauty of biology. He constantly reminded me that it was paramount to think about what all of the biophysics we worked on meant in relation to human physiology. When I thought of an idea, he was often the first person I turned to. And he did the same with me. One of my most memorable moments in the lab was when we (Paul, David Yue, and I) derived an equation that relates the strength of CDI to peak open probability of a $Ca^{2+}$ channel – the so called "Adams-Yue effect." Not fifteen minutes later when Paul collected the actual data, each point decorated this relation. Seeing this synergy in quantitative reasoning and biological function was an incredible experience. All that said, Paul was even more generous as a person; he and his wife Ronee took me into their family as a *de facto* sixth member of the Adams family. Their kids Katelynn, Jacob, and Andrew became my three favorite people in the world. We spent many Saturday mornings fishing under a bridge at the Loch Raven reservoir.

There are many more in the lab who contributed greatly to my progress in science and growth as a person. Wanjun Yang is one of the most patient people I have ever met.

She is always there willing to help no matter what it is that I need. In fact, I never learned to passage cells because cells appeared magically at the appropriate density every Monday and Friday. Hojjat Bazzazi was an indispensable part of the "Manhattan project." He single-handedly conducted the alanine scan of the IQ domain and helped establish the $Ca^{2+}$ channel CaM regulation mechanism presented in Chapters 6 – 7. I admire his passion for teaching. Po Wei (Billy) Kang is an incredibly smart Master's student who I have had the pleasure to work with closely to demonstrate apoCaM regulation of Na channels. He has an incredible enthusiasm for quantitative reasoning for understanding ion channel biology and I have learned much from him. Jacqueline Niu is probably the most uplifting person I have ever known – always happy. She is also exceptionally bright and has helped out in so many ways with several projects. In particular, she was instrumental in establishing the GLT skeletal myotube culture system. Daniel Yue is arguably the smartest person I have worked with, including his own father (possibly normalized for age). We worked together on developing a novel FRET-based assay for detecting stoichiometry of macromolecular complexes in live-cells. His enthusiasm for science and his patience to do experiments were beyond that of a teenager. I worked with the talented student Jiangyu Li on developing a fluorescence-based assay to quantify the membrane trafficking of ion channels – work still in progress. I also had the pleasure of working with two rotation students Joey Bose on light-induced dimerizing systems and Shiva Razavi on detecting fluorescence from single-molecules. Rosy Joshi-Mukhurjee provided high quality guinea pig ventricular myocytes that were invaluable in demonstrating the absence of $Ca^{2+}$ regulation of Na channels in myocytes. Rahul Banerjee helped with molecular dynamics (MD) simulations of the homology model of $Ca_V1.3$ CI region in complex with apoCaM. His results argued that this model may be a stable configuration.

There are yet other members of CSL who played a key role in my growth as a student. These are extremely talented scientists for whom I have the utmost respect for, and I wish I had more opportunities to work closely with them. Ivy Dick is a member of the lab who cares greatly about its well-being. She is a gifted scientist who has a distinct way of reasoning. We shared an office for many years and she has been helpful from the very early days in many aspects of my projects. In particular, she was the one who first described the NSCaTE motif, and results in Chapter 7 are built upon from her work. Extenuating circumstances often bring out unexpected strength in people. In David's absence, Ivy stepped up immensely and has been a source of strength for the entire lab. Lingjie Sang is an incredibly talented scientist whose diligence and persistence is unmatched. She is a friend and a source of inspiration for my own work. She is always available to help. Worawan Limpitikul is a young scientist with a lot of excitement.

John Issa is also one of the brightest people I know and I am lucky to have gotten to know him as both a colleague and, perhaps most importantly, as a friend. We share a lot of enthusiasm for science especially in relation to systems neuroscience. He is the person I turn to when I have a question about the brain, and his insights never cease to amaze me. But John is more than colleague; he has also been a great friend. He has offered great advice on many aspects of my life and it is not surprising that I look up to him as a brother. Sagar Shah is a great mutual friend of John and I who has helped me become more sociable. Ambhi Ganesan, Venkata Paruchuri, and Venkata Prava are very close friends and former roommates who got to hear about my every experiment in its full detail. We spent a lot of late nights debating many "current issues," including American politics, world history, and so much more. These discussions perhaps form the core of my understanding of the world outside of science. Kartik Trehan with great foresight suggested David Yue's Lab as a possible home for me. Hadi Fatemi and Regina Tan were also good friends who helped out in my early days in my lab.

I am also thankful for my sister and my friend Manju Johny who has been a source of strength and support for as long as I have known her. Despite being many years younger than me, she exhibits much prudence and has advised me on so much. She has commented on every figure I have made. She has read every paragraph I have written. There was no way I could get this far without her. And it makes me even prouder that she chose to follow the graduate school path despite having heard of all my hardships at great length. My parents, M. J. Johny and Elizabeth Johny, are full of love and affection. They were willing to abandon much of their lives and transplant our family half-way across the world just so that my sister and I could have a great education and the chance to learn about the wonderful things in the world. I am well aware that I have not always been the most deserving son, but I am so grateful to the sacrifices they made, so that I can have these unimaginable opportunities.

Beyond my peers and my family, I have had a wonderful thesis committee who has been incredibly supportive every step of the way. These great mentors and teachers have contributed greatly to progress in science and have shaped me into who I am. Dr. Gordon Tomaselli is a humble and generous scientist and a clinician who has offered so much advice and support throughout my journey at Hopkins. He is a luminary in Na channel research and his insights are always so invaluable. Most importantly, upon David's passing away, he shouldered much responsibility and offered every help possible to move the lab forward. I sometimes wonder though whether his days are composed of more than twenty-four hours. It is people like him that make science such a wonderful endeavor. Dr. Michael Caterina is an exceptional scientist who has shared his considerable wisdom and insightful comments at every thesis committee meeting and outside. He has been very supportive of my journey in science and has offered every help to refine my work into the best it can be. Dr. Eric Young was the first person to teach me about ion channels as part of his Models of the Neuron course. He was the first person who shared the beauty of the Hodgkin and Huxley model. His course taught me that mathematical elegance could apply to the realm of biological sciences. More than that, he has been there to help me throughout my graduate school by serving on Doctoral Board Exam committee and also became a part of my thesis committee in David's absence. I am also grateful to his generous support with the hearing sciences training grant, and an associated course where I got to learn about auditory neurophysiology. Dr. Sandra Gabelli is wonderful biophysicist and crystallographer who solved the first atomic structure of the $Na_V1.5$ channel CI region in complex with apoCaM alone in collaboration with Dr. Mario Amzel and Dr. Tomaselli. This was a herculean task that David and I felt was impossible. But somehow it happened and I remember both David and I falling out of our chairs in awe as she shared this structure with us. She has been very supportive of my scientific endeavors and has shared great insights on the possible structural implications of our functional data.

Dr. Henry Colecraft, though not a member of my committee, is a prominent $Ca^{2+}$ channel physiologist. He has encouraged me throughout my long journey as a graduate student. In particular, I am incredibly grateful for his support following an intense confrontation I had with a prominent member of the ion channels field with regards to my work. He has continued to guide me by offering advice and as a shoulder to lean on in David's absence. There are many other Professors at Hopkins who have been very encouraging especially in David's absence.

Above all, I am most indebted to Professor David T. Yue – my mentor, my teacher, my role model, and my friend. There is so much to write about him and about the wonderful laboratory he built – the Calcium Signals Lab – and yet I am unsure how to. When I arrived at Hopkins in 2007, I was sure I wanted to learn neuroengineering so that I can build cool devices that one might read in a science fiction novel. But then, I heard David Yue speak at the BME retreat in Ocean city in 2007. It was a transformative experience. He spoke with such eloquence and enthusiasm that I had to find out what sort of science he did. Even though I had never learned what an ion channel was, and even though I had sworn that I would never do any biological experiments, I rotated in his lab and fell in love with his brand of science. Over the next eight years, he became the most influential person in my life. But fate is often so cruel. On December 23, 2014 David passed away as a result of cardiac arrest, leaving us behind with sorrow and grief over our hearts.

David was a very thoughtful and insightful scientist. There so many occasions when I would run into his office with a problem or a difficulty with my experiments. After listening to me carefully and then after a two minute awkward pause, David would come up with a brilliant solution that I would not even have considered. He was very generous with his time and willing no matter what we needed. Whether it was solving a difficult homework problem for a course, or balancing the air tables on our electrophysiological rig, he was always there at the ready. He visited us as we conducted experiments, so that he could be an active part of our journey in science. In fact, a few weeks ago, I was conducting single channel recordings of native sodium channels from myocytes late in the night (~10 PM). Upon witnessing an unusual number of the rare late openings of these channels, I texted him. Not five minutes later, he arrived at the rig I worked on and spent the next hour discussing with me what this fascinating result could mean. There were so many Saturdays that we spent at the whiteboard in Ross 713, brainstorming new ideas that often seemed too crazy to work. But they did and that is why I am able to write this thesis. To him, science was the pursuit of truth. And so, he often pondered the deep mysteries of the universe that were far beyond the workings of an ion channel. He spoke to us about quantum mechanics, thermodynamics, and even taught us a short primer on relativity during a lab retreat.

David was a great teacher. Teaching was an important mission in his life. He believed in inspiring young minds so that a new generation of thinkers could rise up and change the world. He taught with same passion and enthusiasm that he had for science. And he made it clear to all his students that teaching was a noble pursuit and great responsibility not to be treaded lightly. As we presented at journal clubs, he would step up and clarify our weakly-presented arguments on the whiteboard. He would derive even the simplest equations with great care and lucidity so that the most inexperienced amongst us could understand it. In his lectures, David often spoke in parables. These analogies were filled with humor that ensured that his students would never forget the underlying concept. His lectures were animated and conveyed the genuine enthusiasm of science in his heart.

More than all, David was a generous and compassionate human being. He cared about his students' health and well-being. When we attended conferences with him, he would wake us up early in the morning so that we would go running with him. And if we refused, he would politely ask us again the next morning. David also cared about the emotional maturity of his students. He did everything he can to help us grow and become better human beings. And we could confide in him all our person struggles, and he would listen patiently and respond with foresight and compassion. He invited his students to his home for thanksgiving dinner so that we would break bread with his family. And over the years, I was blessed to become a part of the Yue family with St. Nancy, Michael, Daniel, and Jonathan. Upon hearing that I was writing my thesis in a crunch, Nancy sent home with me a generous care package with groceries and a large container filled with soup. In fact, the soup sustained me throughout much of the writing of this thesis. I will forever remember this wonderful family and their invaluable contribution to my life.

There is so much more to write about David, but his memory fills our heart. My only regret in this journey in science is that I did not defend my thesis sooner, so that David would be there with me as he had been throughout my graduate education. This journey feels somewhat incomplete without him. But I know I will carry forth his brand of science with passion, excitement, and honesty.

I am proud to have been trained by David Yue.

# TABLE OF CONTENTS

ABSTRACT ........ ii

ACKNOWLEDGMENTS ........ iv

TABLE OF CONTENTS ........ xii

LIST OF FIGURES ........ xvi

CHAPTER 1 — $Ca^{2+}$ – a precious ion ........ 1

- *A serendipitous discovery* ........ 1
- *$Ca^{2+}$ comes and goes* ........ 2
- *Decoding $Ca^{2+}$ signals* ........ 3
- *$Ca^{2+}$ regulation of ion channels* ........ 11
- *$Ca^{2+}$ regulation of $Ca^{2+}$ channels* ........ 12
- *Advent of $Ca^{2+}$ channel 'calmodulation'* ........ 14
- *Molecular basis of CaM regulation* ........ 22
- *Biological consequences and prospects for new disease therapies* ........ 25
- *$Ca^{2+}$ regulation of Na channels* ........ 27
- *Mechanistic basis of Na channel regulation* ........ 29
- *Conservation of calmodulation across $Ca^{2+}$ and Na channels* ........ 32

CHAPTER 2 — Experimental Procedures ........ 54

- *Whole-cell electrophysiological recordings* ........ 54
- *Single-channel recordings* ........ 55
- *Recipes for pipet and bath solutions* ........ 55
- *$Ca^{2+}$ uncaging and fluorescence measurements* ........ 57
- *$Ca^{2+}$ measurements* ........ 57

*FRET optical imaging* ........ 58
*Molecular Biology* ........ 59
*Construction of Na channel mutants and chimeras* ........ 59
*Construction of $Ca^{2+}$ channel mutants and chimeras* ........ 60
*Construction of FRET 2-hybrid constructs* ........ 61
*Transfection of HEK293 cells* ........ 62
*Isolation of guinea-pig ventricular myocytes* ........ 63
*GLT myoblast culture* ........ 63
*Construction of phylogenetic tree* ........ 63
*Molecular Modeling* ........ 64
*De novo prediction of the CI region structures* ........ 64
*Docking of apoCaM to CI region* ........ 65
*Docking of C-lobe of $Ca^{2+}$/CaM to CI region* ........ 66

CHAPTER 3 — A rapid $Ca^{2+}$-dependent inactivation of Na channels ........ 68
RESULTS ........ 70
*Na channels lack apparent $Ca^{2+}$ regulation* ........ 70
*Rapid uncaging of $Ca^{2+}$ unveils Na channel regulation* ........ 72
*Na channel regulation by $Ca^{2+}$ spillover from $Ca^{2+}$ channels* ........ 75
DISCUSSION ........ 77

CHAPTER 4— Biophysical properties of Na channel $Ca^{2+}$ regulation ........ 97
RESULTS ........ 98
*Effects of pulse rate on the development of Na channel CDI* ........ 98
*$Ca^{2+}$ effects on Na channel steady-state inactivation* ........ 100
*Kinetics of onset of $Na_V1.4$ CDI* ........ 101

*Na channel regulation at the single-molecule level* .......................................... 102
DISCUSSION ........................................................................................................ 104

CHAPTER 5— Structural underpinnings of Na channel $Ca^{2+}$ regulation...................... 115
RESULTS ............................................................................................................ 116
*CaM as the $Ca^{2+}$ sensor for Na channel regulation* ........................................ 116
*CaMKII activation is not necessary for Na channel regulation* ........................ 118
*Functional bipartition of CaM regulation in Na channels* ................................ 119
*Structural determinants of Na channel regulation* ........................................... 120
*Pathophysiological implications of Na channel CDI* ........................................ 122
DISCUSSION ........................................................................................................ 122

CHAPTER 6— A general framework for $Ca^{2+}$ channel calmodulation ........................ 135
THEORY ............................................................................................................. 136
*A conceptual scheme for CaM regulation* ........................................................ 136
*iTL analysis of CaM /Channel regulation* ........................................................ 138
*Specific Langmuir equation for C- and N-lobe CDI subsystems* ....................... 140
*Generalization of iTL analysis to reaction schemes of arbitrary architecture* ........................................................................................ 142
DISCUSSION ........................................................................................................ 147

CHAPTER 7— Structural underpinnings of $Ca^{2+}$ channel calmodulation .................... 154
RESULTS ............................................................................................................ 156
*NSCaTE element upheld as effector site for N-lobe of $Ca^{2+}$/CaM* .................. 156
*Identification of the C-lobe $Ca^{2+}$/CaM effector interface* ................................ 157
*C-lobe CDI also requires IQ domain interaction with PCI element* ................. 158
*Likelihood of IQ-PCI-$Ca^{2+}$/CaM tripartite complex* ......................................... 160

*ApoCaM preassociation within the PCI domain* .............................................. 163

DISCUSSION ........................................................................................ 164

CHAPTER 8— Conclusions – An ancient $Ca^{2+}$ regulatory module ............................. 187

*Towards a shared structural framework of $Ca^{2+}$ and Na channels* .................. 187

*ApoCaM itself modulates channel baseline $P_O$* ................................................ 189

*CI region as a modular element* ......................................................................... 191

*Antiquity of CaM – CI module* ........................................................................... 192

REFERENCES ........................................................................................ 200

CURRICULUM VITAE ........................................................................... 229

# LIST OF FIGURES

CHAPTER 1

1.1 The helix-loop-helix EF hand $Ca^{2+}$ binding motif ........................................... 34
1.2 CaM binding to target molecules ........................................... 36
1.3 CaM binding to IQ motifs ........................................... 38
1.4 Classic U-shaped signature of $Ca^{2+}$ dependent inactivation (CDI) ........................................... 40
1.5 Calmodulation – the ingredients and the flavors ........................................... 42
1.6 Emergent behaviors of CaM explains spatial $Ca^{2+}$ decoding ........................................... 44
1.7 Towards an atomic-level understanding of $Ca^{2+}$ channel CDI ........................................... 46
1.8 Milestones in calmodulation of $Ca^{2+}$ and Na channels ........................................... 48
1.9 Experimental scheme utilized to probe $Ca^{2+}$ effects of Na channels ........................................... 34
1.10 Divergent mechanistic schemes for $Ca^{2+}$ regulation of Na channels ........................................... 34

CHAPTER 2

2.1 De novo structural prediction of $Ca_V1.3$ CI region ........................................... 67

CHAPTER 3

3.1 A conserved carboxy-tail of $Ca^{2+}$ and Na channels ........................................... 80
3.2 Simulation of free $Ca^{2+}$ attained using various $Ca^{2+}$ buffers ........................................... 81
3.3 No $Ca^{2+}$-effect of Na channels as determined by static pipet dialysis ........................................... 82
3.4 $Ca^{2+}$ photouncaging as a method for rapid $Ca^{2+}$ delivery ........................................... 84
3.5 $Ca^{2+}$ regulation absent in cardiac $Na_V1.5$ channels ........................................... 85
3.6 $Ca^{2+}$-dependent inactivation of skeletal muscle $Na_V1.4$ channels ........................................... 87
3.7 Na channel regulation by $Ca^{2+}$ spillover from $Ca^{2+}$ channels ........................................... 89
3.8 $Na_V1.4$ channel regulation by $Ca^{2+}$ spillover from $Ca^{2+}$ channels ........................................... 91

3.9 Restriction of $Ca^{2+}$ elevations to $Ca^{2+}$ channel nanodomain prevents Na channel regulation ........................................................................ 93
3.10 $Na_V1.5$ channel regulation absent with local $Ca^{2+}$ spillover from neighboring $Ca_V2.1$ channels ........................................................................ 96

CHAPTER 4

4.1 Effects of pulse rate on $Na_V1.4$ channel CDI .................................................. 105
4.2 $Na_V1.4$ current amplitudes are a function of cytosolic $Ca^{2+}$ .............................. 107
4.3 Effect of $Ca^{2+}$ on Na channel steady-state inactivation curve ............................108
4.4 $Na_V1.4$ CDI is not reversed by extreme hyperpolarizations ...............................109
4.5 Kinetics of $Na_V1.4$ CDI ........................................................................................110
4.6 Multi-channel stochastic records of $Na_V1.4$ CDI .............................................112
4.7 Na channel $Ca^{2+}$ regulation does not alter unitary conductance or kinetics of voltage-dependent inactivation .......................................................114

CHAPTER 5

5.1 Na channel dual vestigial EF hands are not the $Ca^{2+}$ sensor for CDI .............. 124
5.2 CaM is $Ca^{2+}$ sensor for Na channel CDI .......................................................... 126
5.3 Na channel $Ca^{2+}$ regulation does not depend on CaMKII .................................128
5.4 Functional bipatition of Na channel CaM regulation .......................................129
5.5 Na channel III-IV loop is not a structural determinant for $Ca^{2+}$ regulation. ......................................................................................................130
5.6 $Ca^{2+}$ regulation depends crucially on Na channel carboxy-terminus .................132
5.7 $Na_V1.4$ IQ/AA unveils latent facilitation ..........................................................133
5.8 Pathophysiological consequences of Na channel $Ca^{2+}$ regulation .....................134

CHAPTER 6

6.1 General schema for CaM regulation of L-type $Ca_V1.3$ channels...................... 148
6.2 Probing functionally relevant CaM regulatory interactions via iTL analysis........................................................................................................ 150
6.3 Langmuir equation for reaction system assuming selective mutational perturbation of $Ca^{2+}$/CaM binding to effector site. ..........................151
6.4 Variation of baseline iTL predictions for a hypothetical system featuring two effector sites for a given lobe of CaM ........................................152
6.5 Derivation of general iTL theory. ......................................................................153

CHAPTER 7

7.1 Inconsistencies with IQ domain role as $Ca^{2+}$/CaM effector site....................... 169
7.2 iTL analysis of NSCaTE module of as N-lobe $Ca^{2+}$/CaM effector site ................................................................................................................ 171
7.3 iTL analysis shows NSCaTE module is not C-lobe $Ca^{2+}$/CaM effector site ..........................................................................................................173
7.4 iTL analysis of PCI segment as C-lobe $Ca^{2+}$/CaM effector interface. ...................................................................................................175
7.5 Extended analysis of PCI region as C-lobe $Ca^{2+}$/CaM effector site.. .................177
7.6 Role of IQ domain in C-lobe CDI......................................................................179
7.7 Extended data characterizing PCI/IQ interaction .. ............................................181
7.8 Estimating the propensity of $Ca^{2+}$/CaM to leave the IQ domain.. .....................182
7.9 Footprint of apoCaM preassociation with the PCI segment .. ............................183
7.10 Next generation view of CaM regulatory configuration of $Ca_V1.3$.. ..................185

CHAPTER 8

8.1 ApoCaM binding to the CI region of $Na_V1.5$ and $Ca_V1.3$ channels ................ 193

8.2 ApoCaM modulates baseline $P_O$ of $Ca_V1.3$ channels ........................................ 194
8.3 ApoCaM modulates baseline PO of $Na_V1.4$ channels ........................................195
8.4 CI region as a shared module across $Ca^{2+}$ and Na channels ..............................196
8.5 CI region – a primordial $Ca^{2+}$ regulatory module. ..............................................197

# CHAPTER 1

## $Ca^{2+}$ – a precious ion

As the pharaoh Khufu embraced eternal afterlife, he built for himself the great pyramid of Giza, a large tomb made almost entirely from limestone. Four millennia later, Emperor Shah Jahan built the Taj Mahal as a testament of eternal love for his queen entirely out of white marble. Incidental or not, it is fitting that at the core of these great wonders of human endeavor is the soft alkaline earth metal, calcium – an element so indispensable to life as we know it.

***A serendipitous discovery*** – An early observation of such importance for $Ca^{2+}$ dates to the late 19th century, when the British physiologist Sidney Ringer performed a series of brave but systematic experiments that examined the role of various constituents of blood to support the beating of frog ventricles (Ringer, 1882a, b; Ringer and Sainsbury, 1882; Ringer, 1883, 1885). In the first report, it was identified that a minimal mixture of sodium chloride and potassium chloride at the right proportions was sufficient to support good contractility of a detached heart (Ringer, 1882a, b). But, in just less than a year, the brilliant physiologist realized that he had made a critical mistake and was willing to admit it (Ringer, 1883). The saline solution used in his first experiments was prepared from tap water that contained ~1 mM $Ca^{2+}$ (Ringer, 1883). Nonetheless, repetition of his experiments with solutions made from distilled water, revealed that $Ca^{2+}$ is essential to maintain contractility of the heart (Ringer, 1883). Perfusion of a solution containing just sodium bicarbonate and potassium chloride resulted in a loss of ventricular contractility within a short period. But addition of $Ca^{2+}$ to this solution unambiguously restored beating of the ventricle (Ringer, 1883), revealing an important physiological function of $Ca^{2+}$ ions – to trigger muscular contraction. In the end, Ringer formulated a recipe for an artificial circulating fluid containing $Na^{+}$, $Ca^{2+}$, and $K^{+}$ ions in a proportion used to this very day (Ringer, 1883, 1885). More than a century of research since has revealed $Ca^{2+}$ to be a ubiquitous second messenger molecule that supports a plethora of biological functions including vesicle secretion, gene transcription, and so much more.

***$Ca^{2+}$ comes and goes*** – Typically during rest periods, the concentration of free $Ca^{2+}$ ($[Ca^{2+}]_{free}$) in the cytoplasm of eukaryotic cells is maintained to be low (~100 nM) with respect to the extracellular space (~2 mM). However, electrical or chemical stimulation of the cell can result in transient elevation of cytosolic $[Ca^{2+}]_{free}$. These $Ca^{2+}$ transients can vary in size and duration, and may feed into a wide array of cellular signaling pathways. For example, a single action potential may evoke a small $Ca^{2+}$ transient of ~250 nM in amplitude in the dendrites of pyramidal neurons (Helmchen et al., 1996; Helmchen et al., 1997), or a larger $Ca^{2+}$ transient of ~1 μM in the rat trabeculae (Dobrunz et al., 1995), or an even larger $Ca^{2+}$ transient of ~15 μM in amplitude in the mouse fast-twitch skeletal muscle fibers (Baylor and Hollingworth, 2012). Nonetheless, cytosolic $Ca^{2+}$ is often considered synonymous with activity and the comparative ease of measuring these $Ca^{2+}$ transients has led to elegant studies that optically infer electrical activity from live animals (Chen et al., 2013; Issa et al., 2014).

At the subcellular level, $Ca^{2+}$ signals can vary spatially defining distinct $Ca^{2+}$ signaling domains (Berridge et al., 2000). For example, $Ca^{2+}$ elevations in the nanodomain of a $Ca^{2+}$ source (<100 nm) can be enormous (Neher, 1986; Stern, 1992). In fact, recent experimental measurements showed that $[Ca^{2+}]_{free}$ in the nanodomain of the voltage-gated $Ca^{2+}$ channel was far higher than predicted on theoretical grounds, suggesting that diffusion might be restricted in this space (Tay et al., 2012; Tadross et al., 2013). Importantly, various $Ca^{2+}$ sensing molecules are often localized to such $Ca^{2+}$ signaling domains and can respond to these local $Ca^{2+}$ signals. For instance, calmodulin preassociates to the $Ca^{2+}$ channel (Erickson et al., 2001) and regulates the function of the channel in response to local or global $Ca^{2+}$ (Imredy and Yue, 1994; Peterson et al., 1999; Zuhlke et al., 1999; DeMaria et al., 2001; Dick et al., 2008; Tadross et al., 2008). This form of feedback regulation will be explored extensively in subsequent chapters. Other prominent examples of localized $Ca^{2+}$ signaling include the cardiac dyad where $Ca^{2+}$ ions permeating through the voltage-gated $Ca^{2+}$ channels can bind to nearby ryanodine receptors to trigger $Ca^{2+}$-induced $Ca^{2+}$ release (CICR) (Bers, 2002) or the neuronal presynaptic terminal where $Ca^{2+}$ influx from nearby $Ca^{2+}$ channels can trigger vesicle release (Schneggenburger and Neher, 2005). Moreover, subcellular compartments such as the dendritic spine and the primary cilia are thought to be privileged $Ca^{2+}$ signaling enclaves (Denk et al., 1996; DeCaen et al., 2013). The spatial and temporal dynamics of $Ca^{2+}$ signals are rich and complex, and prove to be enormously important to the function of many physiological systems. In all, even though $Ca^{2+}$ signals often appear ephemeral, their impact on life is limitless.

***Decoding $Ca^{2+}$ signals* –** To harness the enormous power of $Ca^{2+}$ with speed and precision, cells employ a diverse family of calcium sensing proteins. The largest and most renowned subclass of $Ca^{2+}$-sensing molecules is the EF hand family – proteins that share the EF hand structural motif. The ‘EF hand’ motif was first identified in the crystal structure of parvalbumin as a segment composed of two α-helices (‘E’ and ‘F’) linked by a loop that coordinates $Ca^{2+}$ ions (Moews and Kretsinger, 1975a, b). In 1975, based on the homologies in amino-acid sequences of known $Ca^{2+}$-binding proteins, Kretsinger hypothesized that the EF hand motif was an evolutionarily conserved domain for binding $Ca^{2+}$ ions (Kretsinger, 1975), leading to the development of a computer program that can identify EF hands in novel proteins by sequence alignment based on the ‘Tufty-Kretsinger’ criteria shown atop Figure 1.1A (Tufty and Kretsinger, 1975). In general, the $Ca^{2+}$ binding loop is sandwiched between two amphipathic helices and contains five oxygen bearing residues, often aspartates or glutamates, labeled as positions X, Y, Z, -X, and –Z (Figure 1.1A). In the ~40 years since Kretsinger’s hypothesis, the EF hand motif has been identified in more than 150 different $Ca^{2+}$ modulated proteins and has been grouped into ten subfamilies based on their amino-acid sequence (Persechini et al., 1989). Amongst these subfamilies, calmodulin (CaM) features prominently as a prototypic calcium sensing molecule (Chin and Means, 2000).

In the late 1960s, W.Y. Cheung first postulated the existence of what turned out to be CaM based on his finding that the activity of purified cyclic 3′,5′-nucleotide phosphodiesterase depended on the presence of an activator molecule (Cheung, 1969, 1970). This ~17 kilodalton activator molecule was found to be acidic, highly thermostable (it could withstand boiling at $pH \leq 7.4$) and perhaps most importantly, its function strongly depended on $Ca^{2+}$ ions – thus earning its first name, “$Ca^{2+}$-dependent modulator protein” (Cheung, 1971; Kakiuchi et al., 1973; Teo and Wang, 1973; Teo et al., 1973). Soon after, $Ca^{2+}$-dependent modulator protein, dubbed ‘calmodulin,’ emerged as a critical regulator of numerous molecules including $Ca^{2+}$-activatable adenylate cyclase, myosin light chain kinase, and $Ca^{2+}$-dependent ATPase, and other biological processes (Cheung, 1980; Klee et al., 1980).

The complete amino-acid sequence of CaM was deduced from the analysis of tryptic and cyanogen bromide fragments of CaM (Watterson et al., 1980). This sequence demonstrated the high homology of CaM with Troponin C and revealed the presence of four EF hand motifs. The mRNA for CaM was subsequently isolated from the electroplax of the eel (Munjaal et al., 1980) and the cDNAs for many orthologs of CaM were identified (Putkey et al., 1983). Remarkably, the protein sequence of CaM is highly conserved across many species (Persechini et al., 1989). In fact, plant CaM is 91% identical to mammalian orthologs (Snedden and Fromm, 1998). Figure 1.1A shows an alignment of the sequences of four EF hand motifs from the human isoform of calmodulin with like EF hand motifs observed in other eukaryotic proteins (blue) such as Parvalbumin, Troponin C, and S100A and the prokaryotic protein Calerythin (yellow). Remarkably, the $Ca^{2+}$ binding loops of these proteins are nearly identical, while the hydrophobic residues of the helices are more divergent and may confer selectivity in target recognition.

Early biochemical studies showed that CaM can bind up to four $Ca^{2+}$ ions fitting with the presence of four EF hand motifs (Wolff et al., 1977; Crouch and Klee, 1980). The four sites were shown to bind $Ca^{2+}$ ions with positive cooperativity and high affinity – the dissociation constants ($K_d$) were estimated to be in the ~ 1 μM range (Wolff et al., 1977; Crouch and Klee, 1980). In addition to $Ca^{2+}$ ions, CaM has also been shown to bind various metal cations that mimic the size and charge of $Ca^{2+}$ (Chao et al., 1984). For example, divalent ions with ionic radii ~ 1Å such as $Sr^{2+}$, $Cd^{2+}$, $Hg^{2+}$, $Mn^{2+}$, and $Pb^{2+}$ can bind CaM with high affinity, while larger ions like $Ba^{2+}$ or smaller ions like $Co^{2+}$, $Ni^{2+}$, $Mg^{2+}$, and $Be^{2+}$ display weak to no binding (Chao et al., 1984). Lanthanides such as $La^{3+}$, $Tb^{3+}$, and $Sm^{3+}$ can also bind CaM with high affinity (Chao et al., 1984). Although $Mg^{2+}$ ions bind rather weakly to CaM ($K_d$ ~ 0.37 – 1.8 mM for N-lobe and $K_d$ ~ 1.7 – 5.7 mM for C-lobe of CaM), the relatively high intracellular concentration of free $Mg^{2+}$ ions implies that CaM is often $Mg^{2+}$ bound under physiological resting conditions (Tsai et al., 1987; Martin et al., 2000). In some cases, $Mg^{2+}$ has been thought of as a direct competitor of $Ca^{2+}$ for CaM (Tsai et al., 1987; Martin et al., 2000) though this issue has been controversial (Ohki et al., 1997; Gilli et al., 1998). Structurally, $Mg^{2+}$ bound CaM mimics apoCaM based on both circular dichroism experiments (Martin et al., 2000) and NMR studies (Senguen and Grabarek, 2012).

The first atomic structure of $Ca^{2+}$-bound CaM was determined using X-ray crystallography (Babu et al., 1985; Kretsinger et al., 1986). CaM was in fact the fourth member of the EF hand $Ca^{2+}$ binding protein family to be crystallized following parvalbumin (Moews and Kretsinger, 1975b), intestinal $Ca^{2+}$-binding protein (Szebenyi et al., 1981), and troponin-C (Herzberg and James, 1985). Overall, the structure of $Ca^{2+}$/CaM resembled a dumbbell with EF hand 1 and 2 forming a lobe on one end, and EF hands 3 and 4 forming another lobe adjoined by a long-extended helix (Figure 1.1B, right). Structurally, the two pairs of EF hands, often referred to as the 'N-lobe' and 'C-lobe,' do not contact each other and functionally, these lobes often act semi-independently to active target molecules (Kink et al., 1990; Ben-Johny and Yue, 2014). The individual EF hands of CaM resembled the EF hand signatures found in others proteins, further corroborating Kretsinger's hypothesis that the EF hand motif may be a universal $Ca^{2+}$ binding motif (Kretsinger, 1975; Babu et al., 1985; Kretsinger et al., 1986). A distinctive feature of the $Ca^{2+}$/CaM structure in Figure 1.1B is the unusually long helix that extended from the F-helix of EF hand 2 to the E-helix of EF hand 3, forming the linkage between the N- and C-lobes. Subsequent studies have argued that the central 5 residues of this extended helix (residues 78-81) often adopts a non-helical conformation and can act as a flexible tether between the two lobes of CaM (Persechini and Kretsinger, 1988; Barbato et al., 1992). The flexibility of this central helix may enable $Ca^{2+}$/CaM to adopt diverse conformations when binding to target molecules.

The atomic structures of apoCaM were first solved using NMR spectroscopy (Kuboniwa et al., 1995; Zhang et al., 1995). The secondary structure of apoCaM is highly similar to $Ca^{2+}$/CaM, composed of 8 helices connected by flexible loops. However, the helices are more mobile in the $Ca^{2+}$-free state of CaM compared to the $Ca^{2+}$-bound state. Figure 1.1B (left subpanel) displays the structural model of apoCaM. The two lobes of apoCaM form globular structures connected by a highly flexible linker. Much like $Ca^{2+}$/CaM, these lobes do not interact with each other. Though highly similar, the C-lobe of apoCaM is thought to be considerably less stable in solution than the N-lobe as indicated by the fast back-bone amide hydrogen exchange rates (Kuboniwa et al., 1995). The $Ca^{2+}$-binding loops are partially unstructured and appear to be highly flexible. The coordination of $Ca^{2+}$dramatically reduces the flexibility of these loops and reorients the oxygen-bearing residues toward the ion binding site. The helices of apoCaM are tightly packed. The two helices of each EF hand (helix pairs I-II and III-IV) adopting a roughly anti-parallel conformation (Figure 1.1C left subpanel). Upon $Ca^{2+}$ binding, the helices of each EF hand are reoriented to be perpendicular with respect to each other (Figure 1.1C, right subpanel). Overall, in the $Ca^{2+}$-free state, the helices of each lobe of CaM are tightly packed with the hydrophobic residues buried deeply. $Ca^{2+}$ binding reorients the helices of each EF hand (e.g., helix pairs I-II and III-IV) to be perpendicular to each other, resulting in the "opening" of each lobe like a clam shell and the exposure of hydrophobic patches that could engage target molecules (Figure 1.1B). Importantly, the conformational rearrangements of the EF hands in a lobe of CaM appear to be concerted. For example, upon $Ca^{2+}$ binding to N-lobe of CaM, helices I-II and III-IV are reoriented to be perpendicular to each other, however, the relative orientation of helix pairs I-IV, and II-III remain roughly unperturbed. This concerted change in conformation of EF hands may explain the high cooperativity in $Ca^{2+}$ binding to a lobe of CaM (Zhang et al., 1995).

The atomic structures of $Ca^{2+}$/CaM complexed with target molecules started to emerge in the early 1990's (Ikura et al., 1992; Meador et al., 1992). $Ca^{2+}$/CaM binding to the myosin light chain kinase (MLCK) enzyme is a prominent example to understand $Ca^{2+}$/CaM interaction with an effector molecule. Both the skeletal muscle and smooth muscle MLCK are activated by $Ca^{2+}$/CaM binding, and ensuing phosphorylation of the myosin light chain results in contraction of the muscle. $Ca^{2+}$/CaM binding to MLCK has been localized to an ~20 amino acid stretch that serves as a pseudosubstrate to inhibit kinase activity in the absence of $Ca^{2+}$/CaM (Kemp et al., 1987; Pearson et al., 1988). Bioinformatic analysis of $Ca^{2+}$/CaM binding to various proteins has led to the identification of commonalities in many such binding sites, resulting in their categorization as binding motifs and the development of computational algorithms to identify novel CaM binding partners (Rhoads and Friedberg, 1997). The MLCK CaM binding peptide belongs to the 1-8-14 class of $Ca^{2+}$/CaM binding motifs (Figure 1.2A), with the numbers indicating the position of conserved bulky hydrophobic residues typically phenylalanine (F), isoleucine (I), leucine (L), valine (V), or tryptophan (W) (Rhoads and Friedberg, 1997). The motif also typically contains 3 – 6 positively charged residues such as arginine (R) and lysine (K) (Figure 1.2A). Structurally, the MLCK CaM binding peptide forms an $\alpha$-helix (Figure 1.2B) and the two lobes of $Ca^{2+}$/CaM engulfs this peptide with each lobe on one face of the helix (Ikura et al., 1992; Meador et al., 1992). The C-lobe of $Ca^{2+}$/CaM binds towards the amino-terminus of the peptide, while N-lobe is located closer to the carboxy-terminus. The conserved hydrophobic residues are deeply buried and form van der Waals contacts with hydrophobic residues in CaM. Another prominent feature of this structure is the highly flexible linker between the N- and C-lobes of CaM. In the absence of a target molecule, the two lobes of CaM were found to be linked by a helical linker (Figure 1.1B). The flexibility of this linker allows the two lobes to fully engulf the MLCK peptide, and may also allow CaM to interact in diverse configurations. Other proteins that possess this $Ca^{2+}$/CaM binding motif are calcineurin A, adenylyl cyclase, Na/$Ca^{2+}$ exchanger, $Ca^{2+}$ pump, and NO synthase.

A second $Ca^{2+}$/CaM binding motif is the 1-5-10 motif, bearing bulky hydrophobic residues at positions 1, 5, and 10 (Rhoads and Friedberg, 1997). The $Ca^{2+}$-calmodulin dependent kinase (CaMK), MARCS, and synapsin I are examples of proteins containing this motif. Figure 1.2D shows the atomic structure of CaMKII 1-5-10 motif complexed with $Ca^{2+}$/CaM (Meador et al., 1993). Like the MLCK peptide, the CaMKII $Ca^{2+}$/CaM binding segment overlaps with an autoinhibitory peptide (James et al., 1995). Thus, when $Ca^{2+}$/CaM is unbound, the catalytic domain of the enzyme is inhibited (Rosenberg et al., 2005). Binding of $Ca^{2+}$/CaM relieves this inhibition, and subsequent autophosphorylation of CaM kinase keeps the enzyme active even after CaM dissociates – a form of molecular memory. The 1-5-10 motif adopts an $\alpha$-helical secondary structure (Meador et al., 1993). $Ca^{2+}$/CaM wraps around the peptide with the C-lobe of CaM binding towards the amino-terminus of the peptide and N-lobe of CaM towards the carboxy-terminus. The conserved bulky hydrophobic residues are buried within the hydrophobic patches of each of the lobes of CaM. In terms of an ideal helix, residues 1, 5, and 8 are arranged on the same face of a helix at adjacent turns, while residues 10 and 14 are on the opposing side. In this regard, both 1-8-14 and 1-5-10 $Ca^{2+}$/CaM binding motifs present the hydrophobic anchors on the either face of the central helix allowing for both C- and N-lobe to bind. The slight angular difference in the position of residue 10 compared to residue 14 implies that $Ca^{2+}$/CaM is only partially wrapped around the 1-5-10 motif compared to the 1-8-14 motif. The flexibility of the linker between the two lobes of CaM is a key structural feature that allows the two lobes of CaM to reorient with respect to each other and bind this new pattern of residues. Indeed, this structural plasticity of CaM may explain how this small protein can interact with and regulate so many biological molecules.

The third and perhaps the most famous class of motifs that CaM recognizes is the IQ domain (Rhoads and Friedberg, 1997). This motif was first identified based on the sequence similarity in CaM binding regions of unconventional myosin, neuromodulin and neurogranin (Cheney and Mooseker, 1992). Since then this motif has been observed in numerous proteins including several voltage-gated ion channels ($Na_V$, $Ca_V$, and KCNQ), protein phosphatases (PPEF), GTPase activating proteins (IQGAP), Guanosine release factors (Ras-GRF), and calmodulin-binding transcription activators (CAMTA). In general, the IQ domain can bind to both $Ca^{2+}$-free and $Ca^{2+}$-bound CaM with high affinity. However, certain IQ motifs such as for the myosin Va are thought to prefer apoCaM over $Ca^{2+}$-CaM, thus $Ca^{2+}$ elevations can result in the unbinding of a single CaM from a myosin molecule (Trybus et al., 1999; Nguyen and Higuchi, 2005). In some molecules such as the voltage-gated $Ca^{2+}$ channels, the IQ domain allows CaM to act as a dedicated $Ca^{2+}$-sensing molecule (Erickson et al., 2001). In some cases, IQ domain have been argued to shape the kinetics of $Ca^{2+}$ binding to CaM. For example, the IQ motif containing PEP-19 protein has been been argued to accelerate both the kinetics of association and dissociation of $Ca^{2+}$ to CaM (Putkey et al., 2003; Wang et al., 2010). Structurally, the IQ domain forms an amphiphilic α-helix. Figure 1.3B shows the atomic structure of apoCaM bound to an IQ domain from the unconventional myosin Va. ApoCaM wraps around the IQ domain with the C-lobe closer to the amino-terminus of the IQ domain and N-lobe near the carboxy-terminus of the peptide. The N-lobe of apoCaM is observed to be in a closed configuration, while the C-lobe adopts a semi-open configuration. The central isoleucine residue forms a hydrophobic anchor to interact with an exposed hydrophobic patch internal to the C-lobe of CaM. Other hydrophobic residues on the same face of the helix also interacts with this hydrophobic patch. The closed N-lobe of CaM interacts with the IQ domain through interactions between hydrophilic residues. Figure 1.3C shows the atomic structure of $Ca^{2+}$/CaM interacting with IQ domain from $Ca_V1.2$ channels. In this structure, $Ca^{2+}$/CaM interacts with the IQ domain with the N-lobe near the amino-terminus of the peptide and the C-lobe near the carboxy-terminus of the peptide. That said, in other cases, $Ca^{2+}$/CaM interacts in an inverted arrangement with the N-lobe near the carboxy-terminus of the IQ domain and C-lobe near the amino-terminus (Kim et al., 2008; Mori et al., 2008). For example, $Ca^{2+}$/CaM binding to the $Ca_V2.1$ IQ domain has been shown to adopt both arrangements depending on the length of the peptide, suggesting that $Ca^{2+}$/CaM binding can be remarkably flexible (Kim et al., 2008; Mori et al., 2008). Similar to binding modes observed with 1-

5-10 and 1-8-14 motifs, $Ca^{2+}$/CaM engulfs the IQ domain. The central isoleucine residue again is seen to serve as a hydrophobic anchor for the C-lobe of $Ca^{2+}$/CaM and remains buried. That said, even though this structure provides some insight on CaM binding to target molecules, the functional significance of this structure for CaM regulation of $Ca^{2+}$ channels remains controversial (Bazzazi et al., 2013; Ben-Johny et al., 2013a; Ben-Johny and Yue, 2014).

***$Ca^{2+}$ regulation of ion channels*** – Over the past three decades, CaM has emerged as a preeminent regulator of ion channel function enabling vital $Ca^{2+}$-dependent feedback into many physiological systems (Saimi and Kung, 2002). An early example of this prominent regulatory role for CaM originated when mutations in CaM was shown to result in aberrant motile behavior of Paramecium. Organisms were either ‘under-excitable’ or ‘over-excitable’ to certain stimuli, reflecting the loss of either a $Ca^{2+}$-dependent $Na^+$ current or $K^+$ current respectively (Kink et al., 1990). Numerous ion channels have since been found to be under the charm of CaM, as reviewed previously (Budde et al., 2002; Saimi and Kung, 2002; Trudeau and Zagotta, 2003; Halling et al., 2006; Gordon-Shaag et al., 2008; Minor and Findeisen, 2010; Adelman et al., 2012; Van Petegem et al., 2012; Ben-Johny and Yue, 2014).

For the small conductance $K^+$ (SK) channels, CaM associates in a $Ca^{2+}$-independent manner (Xia et al., 1998; Schumacher et al., 2004) and activates these channels in response to submicromolar elevations in cytosolic $Ca^{2+}$ (Xia et al., 1998) to generate an afterhyperpolarizing current that shapes neuronal excitabilty (Stocker, 2004; Adelman et al., 2012). The KCNQ channels are also bestowed with a $Ca^{2+}$-free CaM (apoCaM) (Ghosh et al., 2006; Wang et al., 2012), but elevations in intracellular $Ca^{2+}$ elevations may either inhibit (Gamper and Shapiro, 2003; Gamper et al., 2005) or facilitate these $K^+$ currents in an isoform specific manner (Ghosh et al., 2006; Shamgar et al., 2006). Some cyclic nucleotide-gated (CNG) ion channels are endowed with an apoCaM (Bradley et al., 2005). The association of $Ca^{2+}$-bound CaM with many CNG channels elicits a configurational change (Trudeau and Zagotta, 2004) that inhibits channel activity (Chen and Yau, 1994; Trudeau and Zagotta, 2003; Bradley et al., 2004; Bradley et al., 2005). N-methyl-D-aspartate (NMDA) receptor activity is inhibited by the direct interaction of $Ca^{2+}$/CaM with the carboxy-terminus of the channel (Ehlers et al., 1996; Zhang et al., 1998). $Ca^{2+}$/CaM has been shown to bind a number of transient receptor potential (TRP) channels, though the functional consequence of such binding remains controversial (Numazaki et al., 2003; Rosenbaum et al., 2004; Gordon-Shaag et al., 2008; Mercado et al., 2010; Lau et al., 2012). The $Ca^{2+}$ release-activated $Ca^{2+}$ (CRAC) channels undergo $Ca^{2+}$-dependent inactivation (CDI) orchestrated by CaM binding to the STIM molecules (Mullins et al., 2009). Lastly, both the voltage-gated Na (Deschenes et al., 2002; Tan et al., 2002; Biswas et al., 2008; Sarhan et al., 2009; Van Petegem et al., 2012) and the voltage-gated $Ca^{2+}$ channels (Lee et al., 1999; Peterson et al., 1999; Zuhlke et al., 1999; DeMaria et al., 2001; Budde et al., 2002; Halling et al., 2006; Minor and Findeisen, 2010) are under tight feedback regulation by $Ca^{2+}$/CaM with profound biological implications (Alseikhan et al., 2002; Xu and Wu, 2005; Adams et al., 2010). This thesis will focus on the rapid millisecond regulation of the gating of voltage-gated $Ca^{2+}$ and Na channels, rich with mechanistic elegance, therapeutic possibilities, and profound biological impact.

***$Ca^{2+}$ regulation of $Ca^{2+}$ channels*** – The earliest signs of $Ca^{2+}$-dependent regulation of $Ca^{2+}$ channels arose from data showing that elevated cytosolic $Ca^{2+}$ could potently accelerate the inactivation of $Ca^{2+}$ currents in *Paramecium* (Brehm and Eckert, 1978), invertebrate neurons (Tillotson, 1979), and insect muscle (Ashcroft and Stanfield, 1981). These results gave birth to the concept of a $Ca^{2+}$-dependent inactivation (CDI), a form of channel inactivation that stood in contrast to traditional voltage-dependent inactivation of Na channels. This idea that entities other than the transmembrane voltage could alter the rapid gating of ion channels was a countercultural notion and was to be considered an curious idiosyncrasy of the voltage-gated $Ca^{2+}$ channels for many years (Eckert and Tillotson, 1981).

Technological advances permitting routine the isolation and recording of $Ca^{2+}$ currents within vertebrate preparations revealed the existence of CDI of cardiac L-type $Ca^{2+}$ currents (carried by $Ca_V1.2$ channels) in both multicellular preparations (Kass and Sanguinetti, 1984; Mentrard et al., 1984) and isolated myocytes (Lee et al., 1985). Classic electrophysiological data demonstrating CDI of cardiac L-type currents from frog cardiomyocytes is shown in Figures 1.4A-1.4C. Robust $Ca^{2+}$ current is evoked in response to a test voltage pulse to +80 mV – $V_{\mathrm{rev}}$ (Mentrard et al., 1984) (Figure 1.4A, Ca). $Ca^{2+}$ influx during a voltage prepulse to +80 mV – $V_{\mathrm{rev}}$ caused a sharp reduction in the amplitude of $Ca^{2+}$ current evoked in response to a subsequent test pulse (Figure 1.4B, red shading) – a functional caricature of CDI. To exclude voltage depolarization as the cause of inactivation, a prepulse to +120 mV (Figure 1.4C) was be demonstrated to produce less inactivation during a subsequent test-pulse current. Since this prepulse imposed strong voltage depolarization, but diminished $Ca^{2+}$ entry via decreased driving force, the re-emergence of test $Ca^{2+}$ current suggests that the inactivation evident in Figure 1.4B could be attributed to CDI. Data of this ilk specifies an inactivation mechanism that depends upon voltage as a U-shaped function, now considered a hallmark of CDI (Eckert and Tillotson, 1981).

Still, the precise nature of effects of $Ca^{2+}$ upon channel gating remained ambiguous. For example, it was unclear whether the $Ca^{2+}$-dependent decrement in $Ca^{2+}$ current was caused by a deficit in channel gating or alterations in channel permeation. It was further ambiguous whether $Ca^{2+}$ influx through the $Ca^{2+}$ channel itself could evoke CDI or whether cytosolic $Ca^{2+}$ elevations were necessary to trigger this modulation. To address these ambiguities, the single-molecule profile of CDI was characterized (Figures 1.4D-1.4F) (Yue et al., 1990; Imredy and Yue, 1992; Imredy and Yue, 1994). Resolving data such as these continue to be technically challenging owing to the diminutive size of unitary $Ca^{2+}$ currents (~0.3 pA), and the submillisecond gating timescale involved. Nonetheless, these data demonstrate the existence of U-shaped inactivation in the gating of a single cardiac L-type $Ca^{2+}$ channel fluxing $Ca^{2+}$, as present in an adult rat ventricular myocyte (Imredy and Yue, 1994). These results established that $Ca^{2+}$ influx of a single channel suffices to trigger CDI, and demonstrated the clear correspondence of single-channel and multicellular behavior (Figure 1.4). Thus, CDI appeared to be a legitimate molecular-level regulatory process.

***Advent of $Ca^{2+}$ channel 'calmodulation'* -** The $Ca^{2+}$ sensor mediating $Ca^{2+}$ regulation of $Ca^{2+}$ channels was long contested, with proposals of both direct binding of $Ca^{2+}$ ions to the channel complex (Standen and Stanfield, 1982; Plant et al., 1983; Eckert and Chad, 1984a), and of $Ca^{2+}$-dependent phosphorylation and/or dephosphorylation of channels (Chad and Eckert, 1986; Armstrong et al., 1988). The search for the molecular identity of the $Ca^{2+}$ channel $Ca^{2+}$ sensor was greatly abetted by the cloning and expression of $Ca^{2+}$ channels in recombinant systems – a key advance that opened up an exciting era of structure-function studies of $Ca^{2+}$ channels (Snutch and Reiner, 1992). The $Ca^{2+}$ channel is, however, a large protein complex composed of roughly 2000 amino acids in the main $\alpha$-subunit alone. Identifying a molecular segment relevant for $Ca^{2+}$ regulation on the channel complex through mutagenesis appeared to be a daunting task – a search for a needle in a haystack.

Some hope arose following the bioinformatic observation (Babitch, 1990) that identified a region on the carboxy terminus of the voltage-gated $Ca^{2+}$ and Na channels with weak homology to an EF-hand $Ca^{2+}$-binding motif (Figure 1.5A, EF1). Importantly, this channel EF hand segment appeared to be vestigial in that it lacked key acidic residues necessary to coordinate $Ca^{2+}$ ions. Following the recognition of EF1, the existence of a second EF-hand-like motif became evident (Figure 1.5A, EF2). This postulate, nonetheless, led to chimeric channel analysis (de Leon et al., 1995), wherein segments of the carboxy termini of L-type ($Ca_V1.2$) and R-type ($Ca_V2.3$) $Ca^{2+}$ channels were swapped. These two types of channels respectively display strong and weak CDI under conditions of strong intracellular $Ca^{2+}$ buffering (Liang et al., 2003), making them useful for chimeric analysis. Results from such experiments revealed that the proximal third of the $Ca^{2+}$ channel carboxy terminus (Figure 1.5A, CI region) was critical for CDI, and that EF1 segment of $Ca_V1.2$ channels was an critical determinant for the strong CDI observed in these channels (de Leon et al., 1995). Accordingly, the possibility that the channel dual vestigial EF hands may binding $Ca^{2+}$ ions to elicit CDI arose anew (Standen and Stanfield, 1982; Plant et al., 1983; Eckert and Chad, 1984a). However, mutations of key acidic residues within the $Ca^{2+}$ binding loop of EF1 failed to significantly diminish CDI (Zhou et al., 1997; Peterson et al., 2000), arguing against a possible $Ca^{2+}$ binding function for this channel segment. Thus, the search for the molecular determinants of CDI focused elsewhere on the channel carboxy-terminus.

Targets of CaM binding themselves often resemble CaM, a bi-lobed molecule with each lobe composed of two EF hands (Jarrett and Madhavan, 1991). For example, the $Ca^{2+}$/CaM-dependent phosphastase calcineurin contains an obligatory CaM-like subunit calcineurin B that augments its enzymatic activity (Rusnak and Mertz, 2000). Viewed accordingly, the channel dual vestigial EF hands (Figure 1.5A) may resemble a lobe of CaM, suggesting that CaM itself might be the $Ca^{2+}$ sensor for CDI. However, prior studies had shown that pharmacological inhibition of CaM did not eliminate CDI of L-type $Ca^{2+}$ channels in both native and recombinant systems (Imredy and Yue, 1994; Zuhlke and Reuter, 1998). Nonetheless, systematic deletions within the $Ca_V1.2$ channel CI region identified a putative IQ motif (Figure 1.5A) as a critical element in CDI (Zuhlke and Reuter, 1998). Mutagenesis of this IQ domain strikingly weakened CDI (Qin et al., 1999). As IQ motifs often bind $Ca^{2+}$-free CaM (apoCaM) (Jurado et al., 1999), the possibility that CaM acts as a CDI sensor re-emerged. However, the definitive evidence for CaM as the $Ca^{2+}$ channel $Ca^{2+}$ sensor came with studies that utilized a $Ca^{2+}$-insensitive mutant form of CaM ($CaM_{1234}$), in which high affinity $Ca^{2+}$ binding is abolished by point mutations within all four EF hands (Xia et al., 1998). If 'preassociation' of apoCaM with target molecules was prerequisite for subsequent regulation by $Ca^{2+}$ binding to this apoCaM, then $CaM_{1234}$ could act as a dominant negative to silence regulation, as has been demonstrated for SK channels (Xia et al., 1998). Remarkably, when $Ca_V1.2$ channels were coexpressed with $CaM_{1234}$ or its analogs, CDI was ablated or strongly suppressed (Peterson et al., 1999; Zuhlke et al., 1999). Moreover, apoCaM was found to interact with the $Ca_V1.2$ CI region with critical dependence on the channel IQ domain (Erickson et al., 2001; Pitt et al., 2001; Erickson et al., 2003). Importantly, preassociation of apoCaM with $Ca_V1.2$ channels would sterically protect CaM from pharmacological effects (Dasgupta et al., 1989), rationalizing the relative insensitivity of CDI to such small-molecule perturbation observed in prior experiments. In all, these data firmly established CaM as the unambiguous $Ca^{2+}$ sensor for $Ca_V1.2$ channel regulation.

Initially, it was believed that CaM mediated $Ca^{2+}$ regulation may pertain only to $Ca_V1.2$ L-type channels (Figure 1.5B) (Zamponi, 2003). However, this system of 'calmodulation' has now been identified in nearly all of the $Ca_V1$ and $Ca_V2$ (but not $Ca_V3$) branches of the $Ca_V$ channel superfamily (Lee et al., 1999; DeMaria et al., 2001; Liang et al., 2003; Singh et al., 2006; Wahl-Schott et al., 2006; Yang et al., 2006; Ben-Johny and Yue, 2014) (Figure 1.5B). The considerable variety in functional attributes and $Ca^{2+}$-sensing properties of calmodulation of $Ca^{2+}$ channels lends great insight into the structural adaptability of CaM to alter channel gating. P/Q-type ($Ca_V2.1$) channels were found to be $Ca^{2+}$ regulated with a putative $Ca^{2+}$/CaM binding site downstream of the IQ element (CBD, Figure 1.5A) argued to be the primary structural determinant (Lee et al., 1999). No role for apoCaM preassociation was identified in this initial study. The structural role of the channel IQ domain was also unrecognized. Moreover, $Ca^{2+}$ regulation of $Ca_V2.1$ channels manifests as a rapid facilitation of current (Ca$^{2+}$-dependent facilitation, CDF), followed by a slowly evolving CDI. Thus, mechanistically, $Ca^{2+}$

regulation of $Ca_V2.1$ channels appeared to diverge from that of $Ca_V1.2$ channels. However, subsequent studies recognized apoCaM preassociation with $Ca_V2.1$ channels carboxy-terminus (Erickson et al., 2001). $CaM_{1234}$ molecules were shown to abolish $Ca^{2+}$ regulation in $Ca_V2.1$ channels (DeMaria et al., 2001; Lee et al., 2003). The IQ domain was determined to be an essential structural determinant for this modulation (DeMaria et al., 2001; Lee et al., 2003; Kim et al., 2008; Mori et al., 2008). Nevertheless, the role of the CBD segment remains controversial, with some studies still arguing for this segment's primacy in CDI (Lee et al., 2003). By contrast, deletion of the entire carboxy terminus downstream of the IQ domain (including the CBD element) completely spared CDF and CDI of $Ca_V2.1$ channels (DeMaria et al., 2001; Chaudhuri et al., 2005). Overall, the $Ca^{2+}$ regulation of $Ca_V2.1$ and $Ca_V1.2$ channels appears to subscribe to a largely conserved modulatory scheme. Soon thereafter, calmodulation was established for the remaining members of the $Ca_V2$ class of channels (Figure 1.5B, $Ca_V2.2$ and $Ca_V2.3$), suggesting that this regulatory system is likely conserved throughout the $Ca_V1$-2 channel superfamily (Liang et al., 2003). Strong CaM-mediated CDI was later found in $Ca_V1.3$ channels (Xu and Lipscombe, 2001; Shen et al., 2006; Yang et al., 2006); a latent capacity for CaM-mediated CDI was also observed in $Ca_V1.4$ channels (Singh et al., 2006; Wahl-Schott et al., 2006); and potential for CaM-mediated regulation of $Ca_V1.1$ channels have been described (Stroffekova, 2008, 2011). In all, over the past three decades, calmodulation of $Ca^{2+}$ channels has emerged as a general regulatory process with important physiological implications.

A few nuances in the characterization of calmodulation merits further consideration. First, certain types of calmodulation are insensitive to strong intracellular $Ca^{2+}$ buffering (e.g., $Ca_V1.2$ CDI), while others are not ($Ca_V2.3$ CDI) (Figure 1.5B). This contrasting spatial $Ca^{2+}$ selectivity allows for the usage of chimeric channels under increased $Ca^{2+}$ buffering to identify key structural determinants (de Leon et al., 1995), despite the wide-spread existence of CaM regulation across the $Ca^{2+}$ channel superfamily.

Second, the mechanisms underlying CDF in $Ca_V1.2$ channels remain mysterious – the CDF of native channels of the heart is weak and attenuated by blockade of $Ca^{2+}$ release from neighboring ryanodine receptor channels  (RYRs) (Wu et al., 2001). In addition, CDF of $Ca_V1.2$ channels is strongly present only in recombinant channels bearing point mutations within the IQ domain, and only when these channels are expressed in frog oocytes (Zuhlke et al., 2000). Curiously, CDF is absent in recombinant $Ca_V1.2$ channels expressed in mammalian cell lines (Peterson et al., 1999). By contrast, CDI of $Ca_V1.2$ channels is strong and readily observed across experimental platforms. Third, $Ca^{2+}$/CaM-dependent dephosphorylation by calcineurin has been suggested as a mechanism for CDI of $Ca^{2+}$ channels (Chad and Eckert, 1986), however, this proposition has remained controversial (Budde et al., 2002). Recently, calcineurin was found to preassemble with the $Ca_V1.2$ channel complex through the scaffolding protein AKAP79/150 associated with the channel distal carboxy terminus (Oliveria et al., 2007). Two maneuvers that altered calcineurin function were reported to impede CDI of these channels. Overexpression of a mutant AKAP79/150 incapable of binding calcineurin was shown to perturb CDI of $Ca_V1.2$ channels in hippocampal neurons (Oliveria et al., 2012). The direct inhibition of calcineurin activity was also reported to diminish CDI of these channels (Oliveria et al., 2012). However, numerous other studies have found that direct inhibition of calcineurin has no effect on the CDI of L-type channels within multiple neuronal preparations (Branchaw et al., 1997; Victor et al., 1997; Zeilhofer et al., 2000). Additionally, deletion of the entire $Ca_V1.2$ channel distal carboxy terminus, including the proposed binding segment for AKAP79/150 preserves strong CDI (de Leon et al., 1995; Erickson et al., 2001; Crump et al., 2013). Likewise, alternatively spliced $Ca_V1.3$ channels that lacking the AKAP harboring distal carboxy terminus  (Marshall et al., 2011) also fully supports CDI (Xu and Lipscombe, 2001; Shen et al., 2006; Yang et al., 2006; Bock et al., 2011). In fact, many $Ca_V1.3$ variants that include the channel distal carboxy-terminus lack strong CDI. Altogether, it is likely that calcineurin and

AKAP79/150 are indirect and context-dependent modulators of CDI, rather than a direct effector molecule as argued for in the past (Budde et al., 2002).

***Functional bipartition of CaM and selectivity for local/global $Ca^{2+}$ sources* -** the CaM regulatory mechanism for $Ca^{2+}$ channels supports exquisite forms of $Ca^{2+}$ decoding supported by the two lobes of CaM. This feature echoes earlier findings of 'functional bipartition' of CaM in *Paramecium* (Kink et al., 1990; Saimi and Kung, 2002), where mutations in the N-lobe of CaM led to 'under-excitable' behavioral strains, whereas mutations in the C-lobe resulted in 'over-excitable' strains. Thus, one lobe of CaM can mediate signaling to one set of functions, whereas the other lobe signals to an alternative set of operations. Could this remarkable separation of CaM function through its bipartite signaling interfaces extend to mammalian $Ca^{2+}$ channel regulation? The requirement of apoCaM preassociation to $Ca^{2+}$ channels permitted the usage of 'half-mutant' CaM molecules, with $Ca^{2+}$ sensing enabled in only one lobe, to directly address this question. Coexpression of $CaM_{12}$ or $CaM_{34}$, where $Ca^{2+}$-binding is enabled only in the C- or N-terminal lobes respectively, revealed that the individual lobes of CaM can elicit distinct modes of $Ca^{2+}$ channel regulation (Figure 1.5B). In most $Ca_V1$ channels, the C-lobe evokes a kinetically rapid phase of CDI, whereas the N-lobe induces a slower component (Peterson et al., 1999; Yang et al., 2006; Dick et al., 2008). Notably, early studies of $Ca_V1.2$ channels that used high intracellular $Ca^{2+}$ buffering found only minimal N-lobe mediated CDI (Peterson et al., 1999). However, upon interrogation with low intracellular $Ca^{2+}$ buffering, a slow N-lobe mediated CDI of $Ca_V1.2$ channels is recognizable (Dick et al., 2008; Simms et al., 2013). Most strikingly, in $Ca_V2.1$ channels, the lobes of CaM produce opposing polarities of regulation with the C-lobe of CaM triggering a kinetically rapid CDF, whereas the N-lobe eliciting a slower form of CDI (DeMaria et al., 2001; Lee et al., 2003). Both $Ca_V2.2$ and $Ca_V2.3$ channels manifest CDI triggered mainly by the N-lobe of CaM (Liang et al., 2003). The CaM C-lobe triggered modulation appears to be absent for these channels. Whether this scheme of bipartition orchestrates divergent classes of overall behavior in higher-order animals remains an intriguing and open question (Wei et al., 2003).

Beyond evoking distinct modes of channel function, calmodulation of mammalian $Ca^{2+}$ channels revealed that the two lobes of CaM can selectively decode $Ca^{2+}$ signals in different ways. Hints of this capability emerged from studies that demonstrated the differential sensitivity of calmodulation in various channels to $Ca^{2+}$ buffering. Processes evoked by the C-lobe of CaM are invariably insensitive to the presence of strong intracellular $Ca^{2+}$ buffering, whereas N-lobe-mediated processes in $Ca_V2$ channels can be eliminated by the same maneuver. In particular, the introduction of strong intracellular buffering alters the spatial and temporal dynamics of cytosolic $Ca^{2+}$ signals. For example, strong buffering would spare $Ca^{2+}$ signals near the cytoplasmic aperture of channels where strong point-source $Ca^{2+}$ influx would readily overwhelm local buffers (Neher, 1986; Stern, 1992). At a distance from the channel pore, however, the elevated buffering can overwhelm the $Ca^{2+}$ influx and, thus, suppress global $Ca^{2+}$ elevations. This argues that local $Ca^{2+}$ influx through individual channels triggers C-lobe signaling; in other words, the C-lobe of CaM exhibits a 'local $Ca^{2+}$ selectivity.' By contrast, a spatially global elevation of $Ca^{2+}$ (present in the absence of strong $Ca^{2+}$ buffering) is required for N-lobe signaling of $Ca_V2$ channels (DeMaria et al., 2001; Lee et al., 2003; Liang et al., 2003); thus, the N-lobe in this context exhibits a 'global selectivity.' As CaM resides in the nanodomain of the $Ca^{2+}$ channel, the existence of global spatial $Ca^{2+}$-selectivity is remarkable, as the local $Ca^{2+}$ influx yields far larger $Ca^{2+}$ elevations near a channel than does a globally sourced $Ca^{2+}$ (Tay et al., 2012; Tadross et al., 2013). One exception to this pattern is the local $Ca^{2+}$ selectivity of the N-lobe component of CDI in $Ca_V1.2/1.3$ channels as discussed below. Corroboration of spatial $Ca^{2+}$ selectivity is provided by the ability of single $Ca_V1.2$ channels to undergo CDI (Figures 1.4D-1.4F). By definition, only a local $Ca^{2+}$ source is present in the single-channel configuration; thus, the presence of CDI in this context corroborates local $Ca^{2+}$ selectivity. In addition, single-channel records of $Ca_V2.1$ channels demonstrate C-lobe triggered CDF, but not the N-lobe driven CDI (Chaudhuri et al., 2007), consistent with the proposed differential $Ca^{2+}$ selectivities for this channel. The full spectrum of CaM regulatory effects on the channel including the spatial $Ca^{2+}$ selectivity exhibited by each lobe of CaM is elaborated in Figure 1.5B.

The contrasting spatial $Ca^{2+}$ selectivities can be explained as emergent properties of a system of chemical reactions where a lobe of apoCaM transiently dissociates from a preassociation site before binding $Ca^{2+}$ ions, and then reassociates with an effector interface upon $Ca^{2+}$ binding to elicit channel regulation (Figure 1.6A, top subpanel) (Tadross et al., 2008). When the slow $Ca^{2+}$ -unbinding kinetics of the C-lobe of CaM are imposed on this scenario, local $Ca^{2+}$ sensitivity invariably results (Figure 1.6B). It is important to note that this local spatial $Ca^{2+}$ selectivity does not preclude sensing of global $Ca^{2+}$ by the C-lobe of CaM. It is merely that the local $Ca^{2+}$ signal arising from the gating of channels is sufficient to trigger C-lobe regulation. In the case of myocytes where powerful alternative $Ca^{2+}$ sources such as the ryanodine receptor are available, C-lobe CaM regulation can be evoked by $Ca^{2+}$ emanating from these sources (Imredy and Yue, 1992; Imredy and Yue, 1994). Indeed, C-lobe CDI has been evoked experimentally through global $Ca^{2+}$ elevations elicited by $Ca^{2+}$ photouncaging (Tadross et al., 2013).

By contrast, global $Ca^{2+}$ sensitivity is far more surprising in the context of $Ca^{2+}$ channel gating. For a resident $Ca^{2+}$ sensor of the $Ca^{2+}$ channel to exhibit global $Ca^{2+}$ selectivity, it must reject the large amplitude $Ca^{2+}$ elevations that arise upon the opening of channel gates and instead sense the modest sustained $Ca^{2+}$ emanating from distant sources. Remarkably, this spatial $Ca^{2+}$ selectivity can emerge from the same overall $Ca^{2+}$/CaM architecture explained above but with subtly different kinetics of $Ca^{2+}$ binding to CaM (Figure 1.6B, bottom subpanel). More specifically, if the channel preferentially binds apoCaM versus $Ca^{2+}$/CaM, as in the case of $Ca_V2$ channels, then the rapid $Ca^{2+}$-unbinding kinetics of the N-lobe leads to global spatial $Ca^{2+}$ selectivity. By contrast, if the channel preferentially interacts with $Ca^{2+}$/CaM, local $Ca^{2+}$ selectivity for the N-lobe emerges, as in the context of $Ca_V1$ channels. The relative roles of the affinities and kinetics of $Ca^{2+}$ binding to the two lobes of CaM in mediating local and global $Ca^{2+}$ selectivities have been considered at length elsewhere (Tadross et al., 2008).

A consequence of this general scheme of $Ca^{2+}$ decoding is that a given channel could, in principle, tune the spatial $Ca^{2+}$ preference for the N-lobe of CaM by altering the relative strength of $Ca^{2+}$/CaM N-lobe binding compared to apoCaM N-lobe binding. An explicit example of this phenomenon emerged with the discovery of the N-terminal spatial $Ca^{2+}$-transforming element (NSCaTE) present only on the amino terminus of $Ca_V1.2/1.3$ channels (Figure 1.5A) (Dick et al., 2008). NSCaTE is an unconventional $Ca^{2+}$/CaM binding site whose presence enhances the overall channel affinity for $Ca^{2+}$/CaM over apoCaM (Ivanina et al., 2000; Dick et al., 2008). As a consequence, on these channels, the N-lobe of CaM elicits CDI with a largely local $Ca^{2+}$ selectivity. Elimination of the NSCaTE site in these channels, which causes the channels to favor apoCaM binding, switches their N-lobe CDI to a global profile. Conversely, insertion of the NSCaTE module to $Ca_V2$ channels, which tilts the channels to favor $Ca^{2+}$/CaM binding, then endows their N-lobe CDI with local $Ca^{2+}$ selectivity (Dick et al., 2008). In this manner, the presence of NSCaTE can tune the spatial $Ca^{2+}$ selectivity of N-lobe mediated channel regulation. This overall mechanistic scheme of CaM interactions with a target molecule may generalize to numerous other regulatory systems conferring exquisite spatial $Ca^{2+}$ selectivity.

***Molecular basis of CaM regulation*** – Though the general regulatory scheme of CaM on the channel has been identified, the actual underlying molecular interfaces that contribute to channel regulation has escaped consensus. Indeed, elucidating the molecular arrangement of apoCaM and $Ca^{2+}$/CaM on $Ca^{2+}$ channels is fundamental, given the biological influence of calmodulation, and the overall prominence of this system as an ion-channel regulatory prototype (Dunlap, 2007). This crucial task, however, remains an ongoing daunting endeavor, given the large size (>2000 amino acids) of the channel pore-forming $\alpha_1$ subunit alone, the ability of multiple peptide segments of the channel to bind CaM *in vitro*, and the formidable challenge of obtaining atomic structures for these channels and their subsegments.

At an even more fundamental level, the stoichiometry of CaM interaction with channels has been debated. Crystal structures of $Ca^{2+}$/CaM complexed with portions of the carboxy tail CI region of $Ca_V1.2$ channels (Fallon et al., 2009; Kim et al., 2010), argue that multiple $Ca^{2+}$/CaM molecules may interact to produce the full spectrum of calmodulatory functions. Moreover, CaM can interact with multiple peptide segments of the channel (Ivanina et al., 2000; Tang et al., 2003; Zhou et al., 2005; Dick et al., 2008; Ben-Johny et al., 2013b). By contrast, covalent fusion of single CaM molecules to $Ca_V1.2$ channels suggests that only one CaM per channel suffices to elicit CDI (Mori et al., 2004). In the holochannel, the various CaM binding segments may be arranged in close proximity so as to allow the two lobes of CaM to preferentially interact with the distinct channel segments during $Ca^{2+}$-regulation (Dick et al., 2008; Ben-Johny et al., 2013b). Recent biochemical studies of the NSCaTE element shows this segment preferentially interacts with a single lobe of CaM (N-lobe) at a time (Liu and Vogel, 2012). Furthermore, the NSCaTE element can interact also with $Ca^{2+}$/CaM prebound to an IQ domain peptide (Taiakina et al., 2013). Thus, it seems plausible that perhaps only CaM may bind to the holochannel to elicit channel regulatory function, however, this hypothesis remains to be demonstrated explicitly.

The IQ domain (Figure 1.7A, blue circle) is a critical structural element for CaM regulation across nearly all $Ca^{2+}$ channel families. Mutations within this CaM-biunding domain substantially alter $Ca^{2+}$ regulation of $Ca_V1.2$ channels (Zuhlke and Reuter, 1998; Qin et al., 1999; Zuhlke et al., 1999; Zuhlke et al., 2000; Erickson et al., 2003), $Ca_V1.3$ channels (Yang et al., 2006; Bazzazi et al., 2013; Ben-Johny et al., 2013b), $Ca_V2.1$ channels (DeMaria et al., 2001; Lee et al., 2003; Kim et al., 2008; Mori et al., 2008), and $Ca_V2.2$ and $Ca_V2.3$ channels (Liang et al., 2003). Furthermore, apoCaM preassociation with $Ca_V1.2/1.3$ channels requires the IQ domain (Erickson et al., 2001; Pitt et al., 2001; Erickson et al., 2003; Bazzazi et al., 2013; Ben-Johny et al., 2013b). Finally, $Ca^{2+}$/CaM binds tightly to IQ-domain peptides of many $Ca_V$ channels (Peterson et al., 1999; Zuhlke et al., 1999; DeMaria et al., 2001; Pitt et al., 2001; Liang et al., 2003; Bazzazi et al., 2013; Ben-Johny et al., 2013b). All these results gave rise to the IQ-centric hypothesis shown in Figure 1.7A. Here, the IQ domain is important for both apoCaM preassociation (left cartoon), and $Ca^{2+}$/CaM binding (effector configuration shown in right cartoon). Indeed, this IQ-centric paradigm has motivated efforts to resolve atomic structures of $Ca^{2+}$/CaM complexed with IQ-domain peptides of various $Ca_V1$-2 channels (Fallon et al., 2005; Van Petegem et al., 2005; Kim et al., 2008; Mori et al., 2008), as illustrated in Figures 1.7B-1.7C. Throughout, the IQ peptide segment appears as an alpha-helical entity with N- and C-termini as labeled.

However, three important shortcomings cast doubt on this paradigm. (1) The atomic structures of $Ca^{2+}$/CaM bound to wild-type and mutant IQ peptides of $Ca_V1.2$ (Figure 1.7B) show that a central isoleucine (side chains as sticks) in the IQ element is deeply buried within the C-lobe of $Ca^{2+}$/CaM (Van Petegem et al., 2005), and that alanine substitution at this site hardly changes structure (Fallon et al., 2005). Moreover, $Ca^{2+}$/CaM dissociation constants for corresponding wild-type and mutant IQ peptides are nearly identical (Zuhlke et al., 2000; Bazzazi et al., 2013). Why then would alanine substitution at this entombed locus influence the rest of the channel to attenuate regulation (Fallon et al., 2005)? (2) For $Ca_V1.2/1.3$ channels, the N-lobe CDI critically depends upon an NSCaTE element (Figure 1.7A, oval) in the channel amino terminus (Dick et al., 2008; Tadross et al., 2008; Liu and Vogel, 2012), distinct from the IQ domain. (3) Crystal structures of $Ca^{2+}$/CaM in complex with the IQ peptide of $Ca_V2.1$ channels show that CaM can adopt either a parallel (Mori et al., 2008) or an anti-parallel configuration (Kim et al., 2008) (Figure 1.7C left and right subpanels respectively). The apparent inversion in configuration of CaM binding to IQ domain between $Ca_V1.2$ and

$Ca_V2.1$ has been proposed as a mechanism for the opposing polarity of $Ca^{2+}$-regulation observed in the two channels (Kim et al., 2008; Minor and Findeisen, 2010). However, detailed structural analysis along with functional alanine scanning mutagenesis and chimeric channel analysis argued that the C-lobe effector site resides at a site beyond the IQ module (Mori et al., 2008). Thus, the structural determinants for $Ca^{2+}$ channel regulation still remain a major unknown with controversies yet to be settled.

***Biological consequences and prospects for new disease therapies*** – the biological implications of $Ca^{2+}$ regulation by CaM promise to be wide-ranging and immense. In heart, elimination of $Ca_V1.2$ CDI by means of a dominant-negative CaM elicits marked prolongation of ventricular action potential duration (APD), implicating CDI as a dominant feedback mechanism in specifying APD (Alseikhan et al., 2002; Mahajan et al., 2008). As APD is one of the main determinants of electrical stability and arrhythmias in the heart, pharmacological manipulations of this channel regulatory mechanism may constitute a promising future antiarrhythmic strategy (Mahajan et al., 2008; Anderson and Mohler, 2009). Most recently, genome-wide linkage analysis in humans has uncovered heritable and *de novo* CaM mutations as the probable cause of several cases of catecholaminergic polymorphic ventricular tachycardia (CPVT), with altered CaM-ryanodine receptor function implicated as a major contributing factor (Nyegaard et al., 2012). Beyond this initial identification, the catalog of CaM associated disease-causing mutations – collectively termed calmodulinopathies (Limpitikul et al., 2014) – has continued to expand and the list of disorders now include a novel form of Long-QT syndrome (LQTS14/15) (Boczek et al., 2013; Crotti et al., 2013; Makita et al., 2014; Marsman et al., 2014; Reed et al., 2014). In general, these mutations occur in the $Ca^{2+}$ binding loops of CaM, and therefore strongly disrupt $Ca^{2+}$ binding affinity for CaM (Nyegaard et al., 2012; Crotti et al., 2013; Hwang et al., 2014). An important target for mutant CaM is the L-type $Ca^{2+}$ channel, and recent studies have shown that the association of mutant CaM strongly blunts CDI of these channels (Limpitikul et al., 2014;

Yin et al., 2014). As a consequence, this reduced inactivation of $Ca^{2+}$ channels causes a dramatic prolongation of the cardiac action potential, contributing to the electrical instability of the heart (Limpitikul et al., 2014).

In brain, recent analysis of genome-wide single-nucleotide polymorphisms (SNPs) have identified $Ca_V$ channels as a major risk factor for several psychiatric disorders (Cross-Disorder Group of the Psychiatric Genomics, 2013). More specific to calmodulation, $Ca_V1.3$ channels constitute an important source of $Ca^{2+}$ entry into pacemaking and oscillatory neurons (Bean, 2007), owing to their activation at low voltages. These channels are subject to extensive alternative splicing (Hui et al., 1991; Xu and Lipscombe, 2001; Shen et al., 2006; Bock et al., 2011; Tan et al., 2011) and RNA editing (Huang et al., 2012) in the carboxy tail, in ways that strongly modulate the strength of CDI (Shen et al., 2006; Liu et al., 2010; Huang et al., 2012; Bazzazi et al., 2013). This fine tuning of CDI appears to be important for circadian rhythms (Huang et al., 2012). From the specific perspective of disease, $Ca_V1.3$ channels contribute a substantial portion of $Ca^{2+}$ entry into substantia nigral neurons (Bean, 2007; Chan et al., 2007; Puopolo et al., 2007; Guzman et al.), which exhibit high-frequency pacemaking (Chan et al., 2007) that drives dopamine release critical for movement control. Importantly, loss of these neurons is intimately associated with Parkinson's disease (PD), and $Ca^{2+}$ disturbances and overload are thought to be critical to their neurodegeneration (Bezprovanny, 2009; Surmeier and Sulzer, 2013). Accordingly, a plausible therapeutic possibility for PD involves discovery of small molecules that selectively diminish $Ca_V1.3$ activity versus other closely related $Ca^{2+}$ channels (Kang et al., 2012). Thus, understanding the mechanisms underlying the modulation of $Ca_V1.3$ CDI is crucial, particularly to identify specific molecular interfaces as targets of rational screens for small-molecule modulators.

Overall, calmodulation of $Ca^{2+}$ channels appears ripe for systematic biophysical interrogation to elucidate the structural and functional mechanisms that underlie a prototypical ion channel modulation with wide-ranging biological implications and immense therapeutic promise.

***$Ca^{2+}$ regulation of Na channels*** – The Na channels also possess a conserved carboxy-terminal region that has been long-suspected to confer $Ca^{2+}$ regulation of these channels. Indeed, the study of Na channel regulation by intracellular $Ca^{2+}$ ions closely paralleled developments in calmodulation of $Ca^{2+}$ channels, though the functional outcome and underlying modulatory principles often appeared to diverge between these channel families (Figure 1.8). Extracellular $Ca^{2+}$ had been shown to alter Na currents in early studies by either blocking ion permeation at low voltages or by binding to membrane phospholipids to alter surface membrane potentials (Hille, 1984; Armstrong and Cota, 1991). The first postulate that intracellular $Ca^{2+}$ ions might regulate Na channels came from the early bioinformatic analysis of $Ca^{2+}$ and Na channels that demonstrated the presence of a conserved vestigial EF hand segment in the carboxy-terminus of these channels (Babitch, 1990). However, this possibility was nearly forgotten for almost a decade before pioneering biochemical studies explicitly demonstrated the robust binding of both apoCaM and $Ca^{2+}$/CaM to the Na channel IQ domain peptides (Mori et al., 2000), and thus renewed the interest in studying $Ca^{2+}$ regulation of Na channels. This study also identified a second nearby $Ca^{2+}$/CaM binding site, termed 'Baa motif,' immediately downstream of the Na channel IQ domain (Mori et al., 2000). While these biochemical experiments showed CaM interaction with Na channels, no conclusive functional role for this binding was identified (Mori et al., 2000).

A distinguishing feature of voltage-gated Na channels is its fast voltage-dependent inactivation, a process crucial for the generation of action potentials and cellular excitability (Hodgkin and Huxley, 1952; Hille, 1984). Classically, the steady-state propensity for this fast-inactivation process, termed *h* gate in the Hodgkin-Huxley formalism (Hodgkin and Huxley, 1952; Hille, 1984), is characterized using the voltage-pulse protocol shown in Figure 1.9. Importantly, the voltage-dependence of this steady-state relation (steady-state inactivation or $h_\infty$ curves) is a key determinant for cellular excitability. For example, at the typical resting potential of the cell a fraction of Na channels may inactivate, resulting in a diminished number of Na channels that are available to open. A hyperpolarizing shift in the channel steady-state inactivation properties would further reduce the available current resulting in an increased threshold required action potential generation (McAllister et al., 1975). By contrast, a depolarizing shift in voltage-dependence of steady-state inactivation would increase the net available Na current resulting in a diminished threshold required for triggering an action potential. Moreover, the Na channel carboxy-terminus was identified to contribute to subtle alterations in fast-inactivation of neuronal and cardiac Na channels (Mantegazza et al., 2001).

Cognizant of the role of Na channels in cellular excitability and the potential for the channel carboxy-terminus to modulate fast-inactivation, early studies probed the functional effect of $Ca^{2+}$ on Na channel inactivation properties. (Deschenes et al., 2002; Tan et al., 2002). As Na channels do not themselves furnish $Ca^{2+}$ influx, these studies typically utilized pipet dialysis of internal solutions containing known $Ca^{2+}$ ion concentrations (Figure 1.9A). Na channel inactivation properties were then characterized using well-established voltage-pulse protocols as depicted in Figure 1.9B. $Ca^{2+}$ effects on Na channel gating is then deduced by comparing inactivation properties from two populations of cells interrogated with different internal $Ca^{2+}$ concentrations (Figure 1.9). For cardiac $Na_V1.5$ channels, intracellular $Ca^{2+}$ was shown to induce a subtle ~10 mV depolarizing or right shift in the voltage-dependence of steady-state inactivation or $h_\infty$ curves (Figure 3C) – an effect that would contribute to an enhancement in Na channel availability during periods of high activity (Tan et al., 2002; Wingo et al., 2004; Biswas et al., 2008; Sarhan et al., 2009). However, this modulatory effect was not universally accepted and other studies reported no significant effect of $Ca^{2+}$ on $Na_V1.5$ steady-state inactivation curves in both recombinant and native systems (Deschenes et al., 2002;

Casini et al., 2009; Ben-Johny et al., 2014). For skeletal muscle $Na_V1.4$ channels, an initial report suggested a subtle $Ca^{2+}$-induced hyperpolarizing or left shift in voltage-dependence of steady-state inactivation curves (Deschenes et al., 2002), although later studies contested this effect and reported no significant shift of $Na_V1.4$ steady-state inactivation curves (Herzog et al., 2003; Ben-Johny et al., 2014). The wild-type neuronal $Na_V1.2$ channel was reported to be insensitive to $Ca^{2+}$, however a channelopathic mutation within the IQ domain associated with autism (R1902C) was found to unveil a hyperpolarizing or left-shift in steady-state inactivation (Wang et al., 2014). By contrast, the wild-type neuronal $Na_V1.1$ channels were argued to possess a subtle hyperpolarizing shift in voltage-dependence of steady-state inactivation in response to $Ca^{2+}$ (Gaudioso et al., 2011). The neuronal $Na_V1.6$ channels showed no significant shift in steady-state inactivation curves, while the kinetics of fast inactivation were slowed (Herzog et al., 2003). Overall, the full-spectrum of modulatory effects of $Ca^{2+}$ on Na channels appears to be complex and idiosyncratic, and has evaded consensus for nearly a decade.

***Mechanistic basis of Na channel regulation*** – The mechanistic basis of these variegated effects of $Ca^{2+}$ on the Na channels has been debated as reviewed in the past (Van Petegem et al., 2012). Of note, the identity of the $Ca^{2+}$ sensor for Na channel regulation has been debated, reflecting similar past controversies in deducing the $Ca^{2+}$ sensor of $Ca^{2+}$ channels (Ben-Johny and Yue, 2014). Based on the alignment of the sequence of Na channel carboxy-terminus with the Tufty-Kretsinger criteria (Tufty and Kretsinger, 1975) for a canonical EF hand motif, an early study identified putative $Ca^{2+}$-coordinating residues in the Na channel carboxy terminus (Wingo et al., 2004). Interestingly, this sequence alignment differed from the prior alignment by Babitch that proposed the existence of a channel EF hand (Babitch, 1990). Alanine substitution of the proposed critical $Ca^{2+}$-binding residues (termed '4X', corresponding to E1788, D1790, D1792, and E1799 in the human $Na_V1.5$ channel) abolished $Ca^{2+}$-sensitive shifts in voltage-dependence of steady-state inactivation observed for $Na_V1.5$ channels (Wingo et al., 2004; Biswas et al., 2009). Key aspects of this model are illustrated in Figure 1.10A (left subpanel). This mechanistic scheme fit well with a similar earlier proposal that demonstrated a $Ca^{2+}$-dependent depolarizing shift in the $h_\infty$ curve of $Na_V1.5$ even in the presence of a strong $Ca^{2+}$/CaM chelator (Tan et al., 2002). Thus, it appeared that Na channels may utilize an intrinsic $Ca^{2+}$ sensor to regulate channel function.

Two important modifications to this model have been proposed to account for CaM action on the channel. First, disabling the intrinsic $Ca^{2+}$ sensor of Na channels, the vestigial EF hand segment, has been argued to unveil latent CaM regulation of $Na_V1.5$ channels (Figure 1.10A, right subpanel). In this model, overexpression of wild-type CaM elicits a subtle hyperpolarizing shift of $h_\infty$ curve in the presence of elevated physiological cytosolic $Ca^{2+}$ (0.5 μM) (Biswas et al., 2009). Overexpression of mutant $CaM_{1234}$, with $Ca^{2+}$ binding disabled to all four EF hands, resulted in a depolarizing shift in $h_\infty$ curve (Biswas et al., 2009). Thus it was argued that CaM action on the channel is unveiled only in absence of $Ca^{2+}$-binding to the channel vestigial EF hands. Importantly, disease causing mutations were proposed to similarly unveil latent CaM regulation (Biswas et al., 2009). Second, CaM binding to the channel was argued to allosterically enhance $Ca^{2+}$ affinity for the Na channel vestigial EF hand as outlined in Figure 1.10B. In this model, apoCaM binds with a very high affinity to the channel IQ domain. The C-lobe of CaM is proposed to interact with the IQ domain while the N-lobe has been argued to remain in solution without a corresponding binding partner. Upon $Ca^{2+}$-binding to CaM, the affinity of the channel IQ domain for CaM is weakened (Shah et al., 2006). As such, CaM may either transiently dissociate from the IQ domain or interact with an alternative site on the channel such as the intracellular loop between domain III and domain IV transmembrane segments of the channel (Shah et al., 2006; Potet et al., 2009). This maneuver allows the IQ domain to interact with the channel EF hand segment, and thereby enhance $Ca^{2+}$ binding affinity of the channel vestigial EF hand segments (Glaaser et al., 2006; Shah et al., 2006). Importantly, a single EF hand in isolation has been argued to have weak $Ca^{2+}$

binding affinity (Linse and Forsen, 1995; Ye et al., 2001). This interaction allosterically tunes channel $Ca^{2+}$ affinity to be within the physiological range (Shah et al., 2006).

Nonetheless, several key shortcomings limit the interpretation of channel vestigial EF hands as direct channel $Ca^{2+}$ sensing elements. First, structural studies demonstrated that the proposed critical $Ca^{2+}$-binding residues ('4X') were arranged spatially in an orientation incompatible with $Ca^{2+}$ coordination (Chagot et al., 2009; Miloushev et al., 2009; Wang et al., 2012; Gabelli et al., 2014; Wang et al., 2014). Second, even in the presence of high $Ca^{2+}$ concentrations, the atomic structures of both $Na_V1.5$ and $Na_V1.2$ failed to exhibit $Ca^{2+}$ binding to the channel dual vestigial EF hand (Wang et al., 2014), though NMR studies of the channel EF hand segment argued for low affinity $Ca^{2+}$ binding (Shah et al., 2006; Miloushev et al., 2009). This argument over the functional relevance for the channel vestigial EF hand segment has continued to evade consensus (Van Petegem et al., 2012).

The role of CaM in $Ca^{2+}$ regulation of Na channels has been controversial with some studies proposing a prominent $Ca^{2+}$ sensing role (Kim et al., 2004b; Sarhan et al., 2012; Ben-Johny et al., 2014; Wang et al., 2014), while others arguing for subtle secondary functions as discussed above (Shah et al., 2006; Biswas et al., 2009; Chagot et al., 2009). The direct role of CaM was envisioned based on biochemical studies that suggested strong interaction between the channel IQ domain and both apoCaM and $Ca^{2+}$/CaM (Mori et al., 2000). Biochemically, CaM was shown to support a configurational change of the $Na_V1.2$ carboxy terminus in the context of a channelopathic mutation (Kim et al., 2004b). A direct functional role for CaM has been proposed based on the finding that $Ca^{2+}$/CaM can interact with intracellular loop between domain III and domain IV transmembrane segments of the channel (III-IV loop). In terms of broader Na channel function, classic experiments have argued for a prominent role of the III-IV loop in eliciting the canonical fast-inactivation process (Stuhmer et al., 1989; West et al., 1992a; West et al., 1992b). In this regard, a hinged-lid mechanism for Na channel fast inactivation has been suggested, and a cluster of hydrophobic residues isoleucine-phenylalanine-methionine ('IFM') has been argued to be the pore-blocking ligand for the pore domain. Surprisingly, recent studies identified a $Ca^{2+}$/CaM binding site in a region adjoining the well-known IFM motif (Sarhan et al., 2009; Sarhan et al., 2012). As such, it is conceivable that $Ca^{2+}$/CaM interaction with the Na channel III-IV loop might modulate the propensity to elicit fast inactivation. Subsequent structural studies have shown that the C-lobe of CaM may serve as the primary $Ca^{2+}$ sensing element in this model (Sarhan et al., 2012). Critical aspects of this model are illustrated in Figure 1.10C. Briefly, apoCaM is again thought to interact primarily with the channel carboxy-terminus with critical dependence on the IQ domain. Upon $Ca^{2+}$ binding, the C-lobe of $Ca^{2+}$/CaM is thought to migrate to the III-IV loop thus impeding the hinged-lid inactivation process. Unlike for $Ca^{2+}$ channels, expression of dominant negative CaM has never been shown to conclusively abolish $Ca^{2+}$ regulation of Na channels thus casting doubt on whether CaM might play a primary $Ca^{2+}$-sensing role for these channels. Overall, these dissimilarities in the modulatory process of $Ca^{2+}$ and Na channels has led many to speculate that these channel families have diverged considerable in their CaM regulatory function and any sequence homology of the carboxy-terminus maybe a vestige (Van Petegem et al., 2012).

**Conservation of calmodulation across $Ca^{2+}$ and Na channels** – This dissertation goes far in establishing calmodulation as a shared regulatory process between voltage-gated $Ca^{2+}$ and Na channels. Accordingly, by utilizing novel methods of rapid $Ca^{2+}$ delivery, we demonstrate robust $Ca^{2+}$-dependent regulation of voltage-gated Na channels mediated by CaM (Chapter 3). This modulation of Na channels is rapid and largely independent of the canonical voltage-dependent fast inactivation (Chapter 4) and demonstrates unprecedented similarities with $Ca^{2+}$ channels in terms of their regulatory mechanism (Chapter 5). Furthermore, the structural underpinnings of this modulation is deduced through rigorous analysis functional and biochemical characterization of CaM interactions with wild-type and mutant $Ca^{2+}$ channels (Chapter 6 – 7). Finally, we conclude by highlighting the uncanny structural resemblance in the CI region of $Ca^{2+}$ and Na channels that now casts this conserved stretch of ~150 residues as an functionally-preserved primordial $Ca^{2+}$-regulatory module (Chapter 8).

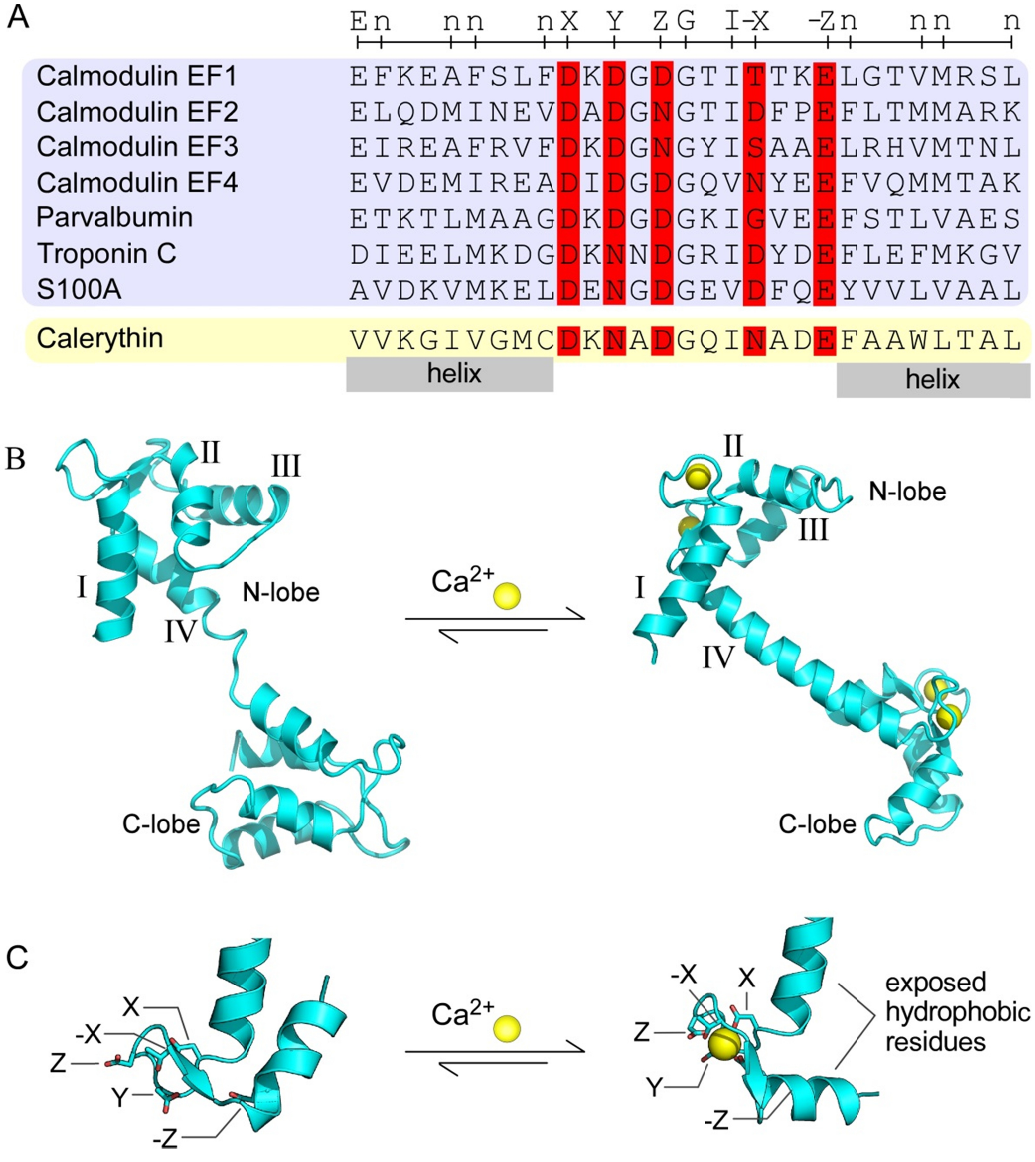
A
En nn nX Y ZG I-X -Zn nn n
Calmodulin EF1 EFKEAFSLFDKDGDGTITTKELGTVMRSL
Calmodulin EF2 ELQDMINEVDADGNGTIDFPEFLTMMARK
Calmodulin EF3 EIREAFRVFDKDGNGYISAAELRHVMTNL
Calmodulin EF4 EVDEMIREADIDGDGQVNYEEFVQMMTAK
Parvalbumin ETKTLMAAGDKDGDGKIGVEEFSTLVAES
Troponin C DIEELMKDGDKNNDGRIDYDEFLEFMKGV
S100A AVDKVMKELDENGDGEVDFQEYVVLVAAL
Calerythin VVKGIVGMCDKNADGQINADEFAAWLTAL
helix
helix
B
II
III
I
N-lobe
IV
C-lobe
$Ca^{2+}$
II
N-lobe
III
I
IV
C-lobe
C
X
-X
Z
Y
-Z
$Ca^{2+}$
-X
X
Z
Y
-Z
exposed hydrophobic residues

**Figure 1.1** The helix-loop-helix EF hand $Ca^{2+}$ binding motif.

(A) Sequence alignment of EF hand motifs found in CaM, parvalbumin, troponin C, S100A, and calerythin. The four EF hands of CaM are labeled calmodulin EF1-EF4. The 'Tufty-Kretsinger' criteria, the consensus sequence for an EF hand motif is shown on top. Oxygen-bearing residues (X, Y, Z, -X, and –Z) are highlighted in red. Blue shaded area corresponds to proteins observed in eukaryotes. Yellow shaded area corresponds to a prokaryotic $Ca^{2+}$ binding protein, calerythin.

(B) The overall structural changes associated with $Ca^{2+}$ binding to calmodulin. Left, atomic structure of apoCaM (1CFC). Right, atomic structure of $Ca^{2+}$/CaM (1CLL). In the absence of $Ca^{2+}$ ions, each lobe of CaM adopts a globular conformation. $Ca^{2+}$ binding to CaM results in the opening of the EF hand motif, thus exposing a hydrophobic crevice in each lobe that can recognize target proteins. Helices of N-lobe of CaM are labeled I-IV.

(C) Structural changes associated with $Ca^{2+}$ binding to EF hand 1 of calmodulin. Left, the atomic structure of EF hand 1 of CaM in the absence of $Ca^{2+}$ determined by NMR spectroscopy (PDB code, 1CFC). Right, the atomic structure of $Ca^{2+}$ bound EF hand 1 of CaM (PDB code, 1CLL) determined by X-ray crystallography. In the absence of $Ca^{2+}$, the oxygen-bearing residues (sticks) are flexible and adopt random orientations. Upon binding $Ca^{2+}$, the side chains of these residues reorient to coordinate the $Ca^{2+}$ ion. This $Ca^{2+}$-dependent conformational change exposes a hydrophobic crevice that can bind to target proteins. Most EF hand proteins undergo a similar conformational change following $Ca^{2+}$ binding.

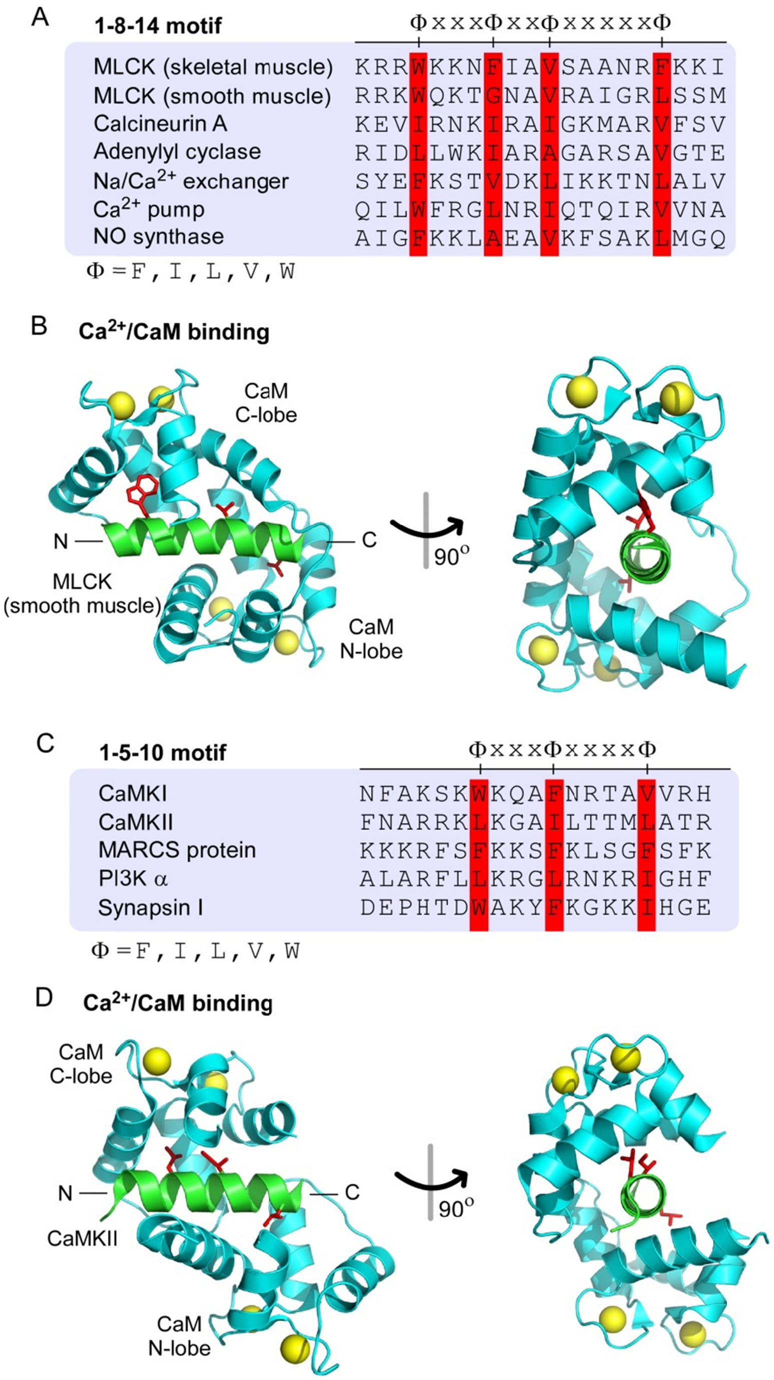
A
1-8-14 motif
ΦxxxΦxxΦxxxxxΦ
MLCK (skeletal muscle) KRRWKKNFIAVSAANRFKKI
MLCK (smooth muscle) RRKWQKTGNAVRAIGRLSSM
Calcineurin A KEVIRNKIRAIGKMARVFSV
Adenylyl cyclase RIDLLWKIARAGARSAVGTE
Na/Ca2+ exchanger SYEFKSTVDKLIKKTNLALV
Ca2+ pump QILWFRGLNRIQTQIRVVNA
NO synthase AIGFKKLAEAVKFSAKLMGQ
Φ = F, I, L, V, W
B
Ca2+/CaM binding
CaM C-lobe
N
C
MLCK (smooth muscle)
CaM N-lobe
90°
C
1-5-10 motif
ΦxxxΦxxxxΦ
CaMKI NFAKSKWKQAFNRTAVVRH
CaMKII FNARRKLKGAILTTMLATR
MARCS protein KKKRFSFKKSFKLSGFSFK
PI3K α ALARFLLKRGLRNKRIGHF
Synapsin I DEPHTDWAKYFKGKKIHGE
Φ = F, I, L, V, W
D
Ca2+/CaM binding
CaM C-lobe
N
C
CaMKII
CaM N-lobe
90°

**Figure 1.2** CaM binding to target molecules.

(A) Sequence alignment for the 1-8-14 motif. The consensus sequence for this motif is shown on top. $\phi$ corresponds to bulky hydrophobic residues (red highlight) such as phenylalanine (F), isoleucine (I), leucine (L), valine (V), or tryptophan (W). Typically, this motif also contains several positively charged residues with the net charge ranging from +3 to +6.

(B) The atomic structure of $Ca^{2+}$/CaM (cyan) bound to a 20 residue peptide from the smooth muscle myosin light chain kinase (MLCK, green) are shown from orthogonal views (PDB code, 2O5G). The conserved hydrophobic residues at positions 1, 8, and 14 are shown as red sticks. $Ca^{2+}$ ions are shown as yellow spheres. The amino and carboxy-termini of the peptide are labeled as N and C. The two lobes of CaM are labeled as N-lobe and C-lobe. $Ca^{2+}$/CaM engulfs the MLCK peptide with the key hydrophobic residues interacting with the exposed hydrophobic patch of CaM.

(C) Sequence alignment for the 1-5-10 motif. Format as in panel A. Typically, this motif contains several positively charged residues, with the net charge ranging from +3 to +6.

(D) The atomic structure of $Ca^{2+}$/CaM (cyan) bound to a short peptide from the $Ca^{2+}$/CaM-dependent protein kinase II (CaMKII, green) is shown (PDB code, 1CDM). Format as in panel B.

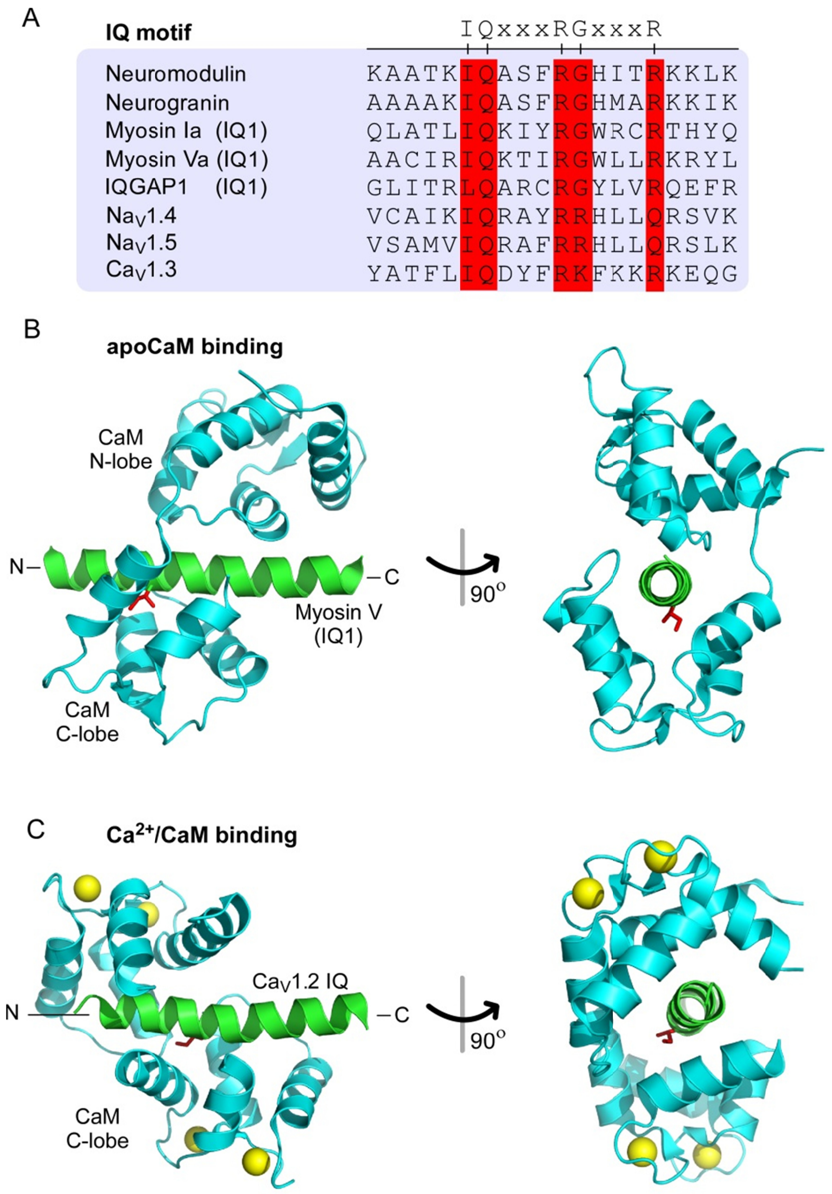
A
IQ motif
IQxxxRGxxxR
Neuromodulin KAATKIQASFRGHITRKKLK
Neurogranin AAAAKIQASFRGHMARKKIK
Myosin Ia (IQ1) QLATLIQKIYRGWRCRTHYQ
Myosin Va (IQ1) AACIRIQKTIRGWLLRKRYL
IQGAP1 (IQ1) GLITRLQARCRGYLVRQEFR
$Na_V1.4$ VCAIKIQRAYRRHLLQRSVK
$Na_V1.5$ VSAMVIQRAFRRHLLQRSLK
$Ca_V1.3$ YATFLIQDYFRKFKKRKEQG
B
apoCaM binding
CaM N-lobe
N–
–C
Myosin V (IQ1)
CaM C-lobe
90°
C
$Ca^{2+}$/CaM binding
$Ca_V1.2$ IQ
N
–C
CaM C-lobe
90°

**Figure 1.3** CaM binding to IQ motifs.

(A) Sequence alignment of various IQ motifs from diverse proteins is shown along with the corresponding consensus sequence on top. The IQ motif contains a highly conserved central isoleucine (I) or leucine (L) residue followed by a conserved pattern of basic residues. Both apoCaM and $Ca^{2+}$/CaM can bind to IQ motifs.

(B) Atomic structure of apoCaM (cyan) bound an IQ motif (green) from the unconventional myosin Va protein (PDB code, 2IX7) is shown from orthogonal perspectives. The central isoleucine residue (red sticks) form a hydrophobic anchor for the semi-open C-lobe of CaM. The N-lobe of CaM is in a closed conformation interacting with the IQ peptide through salt bridges formed between basic residues of the IQ domain and acidic residues of CaM. The N-lobe of apoCaM binds closer to the carboxy-terminus of the myosin V IQ domain while the C-lobe of apoCaM is juxtaposed to the amino-terminus.

(C) Atomic structure of $Ca^{2+}$/CaM (cyan) bound to the IQ domain of an L-type $Ca^{2+}$ channel (green). $Ca^{2+}$ ions are shown as yellow spheres. Both lobes of CaM are in the fully open state. The central isoleucine residue forms a hydrophobic anchor for the C-lobe of $Ca^{2+}$/CaM.

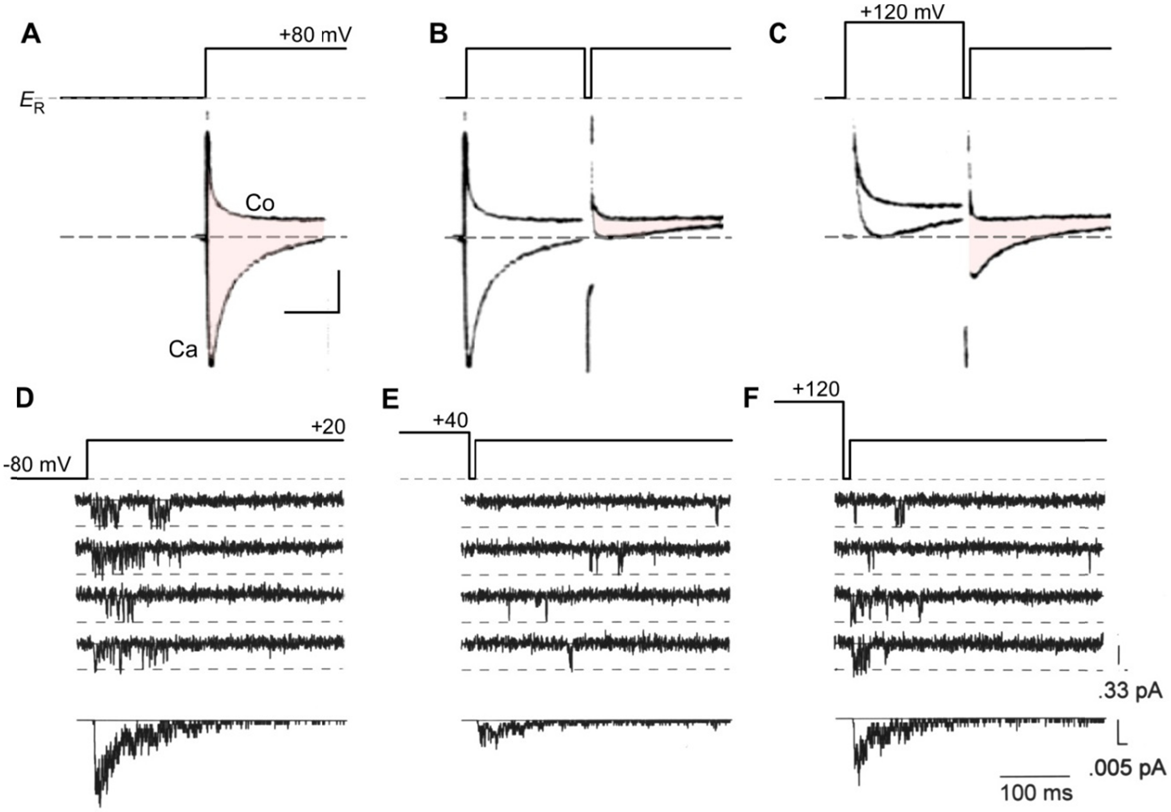
A
+80 mV
$E_R$
Co
Ca
B
C
+120 mV
D
-80 mV
+20
E
+40
F
+120
.33 pA
.005 pA
100 ms

**Figure 1.4. Classic U-shaped signature of $Ca^{2+}$ dependent inactivation (CDI).**

(A-C) Early voltage-clamp recordings from a multi-cellular preparation of frog atrial trabeculae cells demonstrates CDI of $Ca^{2+}$ currents.

(A) $Ca^{2+}$ currents (shaded pink) evoked in response to a +80mV depolarizing test pulse show robust inactivation. Fast capacitive transient was estimated by blocking these $Ca^{2+}$ currents with 3mM $Co^{2+}$ solution (Co). Vertical scale bar corresponds to 0.5 μA of current and horizontal scale bar, 100 ms.

(B) The $Ca^{2+}$ current in response to the test pulse is sharply attenuated when preceded by a +80 mV prepulse. This reduction in current amplitude reflects the inactivation of $Ca^{2+}$ channels. Format as in panel A.

(C) Further increase in the prepulse potential to +120 mV restores $Ca^{2+}$ current amplitude (compare to B). Here, the diminished $Ca^{2+}$ entry during the prepulse was insufficient to trigger CDI. Format as in panel A.

(D-F) Single channel recordings of L-type $Ca^{2+}$ channels from adult rat ventricular myocytes also exhibit U-shaped dependence of $Ca^{2+}$ channel inactivation. Adapted with permission (Imredy and Yue, 1994).

(D) Depolarizing voltage pulse to +20 mV evokes representative elementary $Ca^{2+}$ currents. Ensemble average currents are shown in bottom.

(E) When depolarizing pulse was preceded by +40 mV prepulse, the elementary $Ca^{2+}$ currents are sparser and the first opening is delayed. This reduction in open probability parallels the sharp attenuation of macroscopic $Ca^{2+}$ currents seen in panel B. Ensemble average, bottom.

(F) Further increase in prepulse voltage to +120 mV led to a reversal of this gating pattern, once again highlighting the U-shaped dependence of CDI. Ensemble average, bottom.

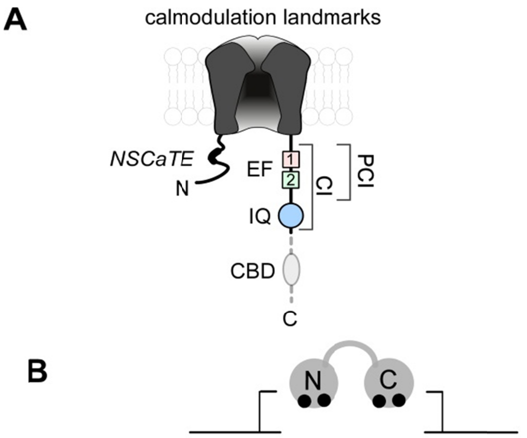

| | N-lobe triggered modulation | C-lobe triggered modulation |
|---|---|---|
| $Ca_V1.2$<br>L-type channel | CDI [1]<br>(local*) | CDI [2-3]<br>(local) |
| $Ca_V1.3$<br>L-type channel | CDI [4]<br>(local) | CDI [4]<br>(local) |
| $Ca_V1.4$*<br>L-type channel | CDI [5,6]<br>(global) | CDI [5,6]<br>(local) |
| $Ca_V2.1$<br>P/Q-type channel | CDI [7,8]<br>(global) | CDF [7,8]<br>(local) |
| $Ca_V2.2$<br>N-type channel | CDI [9]<br>(global) | (not found) [9] |
| $Ca_V2.3$<br>R-type channel | CDI [9]<br>(global) | (not found) [9] |

* intermediate local / global (Tadross *et al*, 2008)

[1] (Dick *et al*, 2007)
[2] (Peterson *et al*, 1999)
[3] (Zuhlke *et al*, 1999)
[4] (Yang *et al*, 2006)
[5] (Singh *et al*, 2006)
[6] (Wahl-Schott *et al*, 2006)
[7] (DeMaria *et al*, 2001)
[8] (Lee *et al*, 2003)
[9] (Liang *et al*, 2003)

**Figure 1.5. Calmodulation – the ingredients and the flavors.**

(**A)** Channel cartoon illustrates overall arrangement of structural landmarks critical for CDI. The C̲a$^{2+}$-i̲nactivation (CI) region, spanning ~160 residues of the channel carboxy terminus, is highly conserved across $Ca_V1/2$ channel families, is element for CDI. The proximal segment (PCI) of the CI region includes the dual vestigial EF-hand (EF) segments (shaded purple and blue-green). The IQ domain, a canonical CaM binding motif critical for CDI, is located just downstream of the PCI segment. The NSCaTE element in the amino terminus of $Ca_V1.2/1.3$ channels is an N-lobe $Ca^{2+}$/CaM effector site. The CBD element (gray) in the carboxy terminus of $Ca_V2$ channels, is a CaM binding segment thought to be critical for CDI.

(B) Table outlines functional bipartition of CaM in $Ca_V$ channels and the corresponding spatial $Ca^{2+}$ selectivities. In $Ca_V1.2$ and $Ca_V1.3$ channels, both the C-lobe and N-lobe of CaM enable fast CDI with local $Ca^{2+}$ selectivity. Latent CDI of $Ca_V1.4$ channels is revealed upon deletion of an autoinhibitory domain in the distal carboxy terminus. Throughout the $Ca_V2$ channel family, the N-lobe of CaM evokes slow CDI with global $Ca^{2+}$ spatial selectivity. In $Ca_V2.1$ channels, the C-lobe of CaM supports ultra-fast facilitation (CDF) with local $Ca^{2+}$ selectivity. No C-lobe triggered modulation has been reported for $Ca_V2.2$ and $Ca_V2.3$ channels.

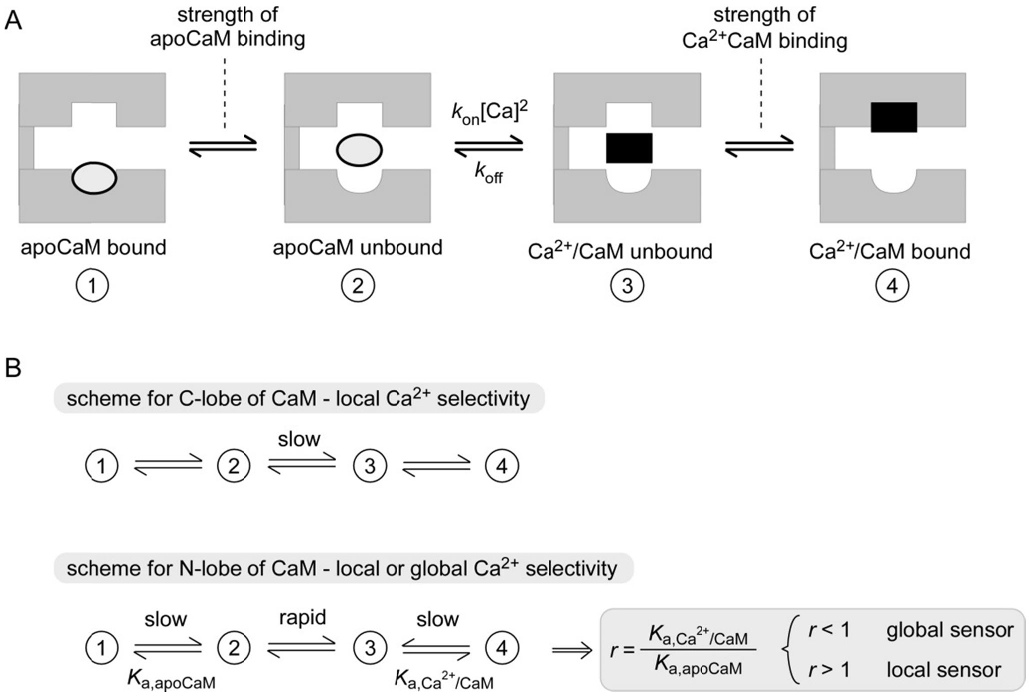
A
strength of apoCaM binding
$k_{on}[Ca]^2$
$k_{off}$
strength of $Ca^{2+}$CaM binding
apoCaM bound
①
apoCaM unbound
②
$Ca^{2+}$/CaM unbound
③
$Ca^{2+}$/CaM bound
④
B
scheme for C-lobe of CaM - local $Ca^{2+}$ selectivity
① ⇌ ② ⇌ ③ ⇌ ④
slow
scheme for N-lobe of CaM - local or global $Ca^{2+}$ selectivity
slow
rapid
slow
① ⇌ ② ⇌ ③ ⇌ ④
$K_{a,apoCaM}$
$K_{a,Ca^{2+}/CaM}$
$\Longrightarrow r = \frac{K_{a,Ca^{2+}/CaM}}{K_{a,apoCaM}}$
$r < 1$ global sensor
$r > 1$ local sensor

**Figure 1.6. Emergent behaviors of CaM explains spatial $Ca^{2+}$ decoding.**

(A) A general mechanistic scheme to understand calmodulation of $Ca^{2+}$ channels. CaM action on $Ca^{2+}$ channel is simplified into four general configurations. State 1, each lobe of apoCaM associates with a respective channel interface. State 2, apoCaM transiently unbinds but remains in the channel alcove. State 3, $Ca^{2+}$ binds to CaM. State 4, $Ca^{2+}$/CaM engages an appropriate effector site.

(B) The $Ca^{2+}$-binding kinetics of each lobe of CaM and the relative affinity of apoCaM and Ca2+/CaM binding to respective channel interfaces explain local/global spatial $Ca^{2+}$ selectivity. Top, mechanistic scheme for C-lobe of CaM. In this model, $Ca^{2+}$ binding to C-lobe is the slow limiting step. This property results in an invariably local $Ca^{2+}$ selectivity for C-lobe of CaM. By contrast, the rapid $Ca^{2+}$ binding kinetics of N-lobe of CaM enables tunable context-dependent spatial $Ca^{2+}$ selectivity for this lobe. For example, if the strength of Ca2+/CaM binding to channel effector interface is weak compared to apoCaM binding to its effector interface, then the N-lobe senses global $Ca^{2+}$ ($r < 1$). By contrast, if Ca2+/CaM engagement with its effector interface is stronger than apoCaM binding to its preassociation site, then a local spatial $Ca^{2+}$ selectivity emerges ($r > 1$). In this manner, $Ca^{2+}$ sensing by N-lobe CaM can be tuned to possess either local or global spatial selectivity.

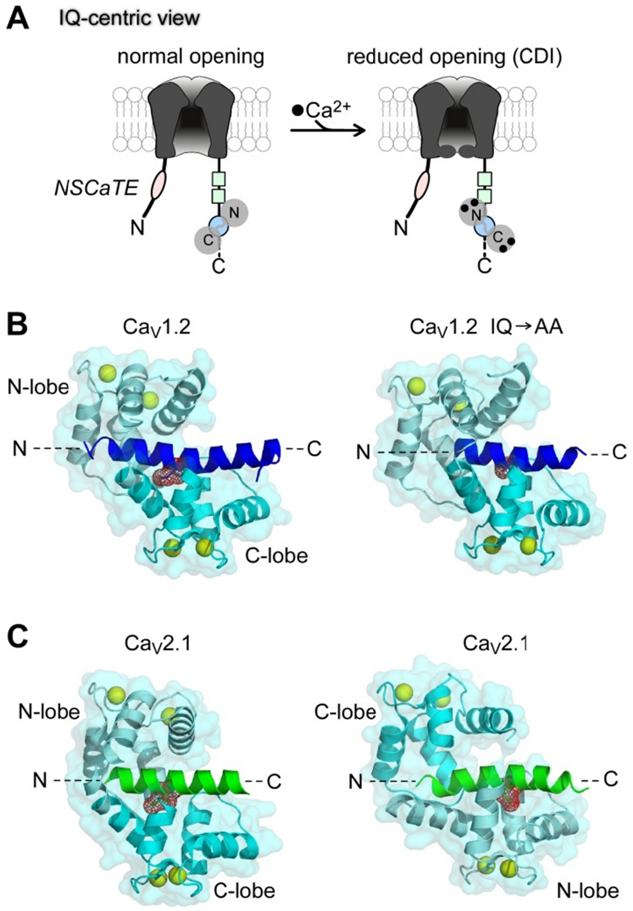
A
IQ-centric view
normal opening
reduced opening (CDI)
●Ca$^{2+}$
NSCaTE
N
C
N
C
N
N
C
C
B
Ca$_V$1.2
Ca$_V$1.2 IQ→AA
N-lobe
N
C
N
C
C-lobe
C
Ca$_V$2.1
Ca$_V$2.1
N-lobe
C-lobe
N
C
N
C
C-lobe
N-lobe

**Figure 1.7. Towards an atomic-level understanding of $Ca^{2+}$ channel CDI.**

(A) IQ-centric view of CaM regulation of $Ca_V$ channels. In this mechanistic scheme, ApoCaM is preassociated with the IQ domain (blue). Upon $Ca^{2+}$ binding, CaM rebinds the same IQ domain with a higher affinity and subtle conformational rearrangements are presumed to trigger CaM-mediated channel regulation.

(B) Left, crystal structure of $Ca_V1.2$ IQ domain peptide in complex with $Ca^{2+}$/CaM (2BE6). The IQ domain is colored blue. CaM is show in cyan (N-lobe, pale cyan; C-lobe, cyan). $Ca^{2+}$ ions are depicted as yellow spheres. The key isoleucine residue (red) serves as a hydrophobic anchor for CaM. $Ca^{2+}$/CaM adopts a parallel arrangement with the IQ domain in which the N-lobe binds closer to the amino-terminus of the IQ domain and the C-lobe binds further downstream. Right, crystal structure of $Ca^{2+}$/CaM bound to mutant $Ca_V1.2$ IQ domain with alanines substituted for the key isoleucine-glutamine residues (2F3Z). This double mutation abolishes CDI. Structurally, however, $Ca^{2+}$/CaM hugs the mutant IQ domain in a similar conformation as to its interaction with the wild-type (left).

(C) Crystal structure of $Ca^{2+}$/CaM bound to $Ca_V2.1$ IQ domain (left, 3BXK; right, 3DVM). The IQ domain is shaded green, CaM in cyan. $Ca^{2+}$/CaM was reported to bind to the $Ca_V2.1$ IQ domain in both parallel (left) and antiparallel (right) arrangements. The antiparallel arrangement in which the C-lobe of CaM binds upstream of IQ domain has led to speculation that CDF may result from this inverted polarity of $Ca^{2+}$/CaM association.

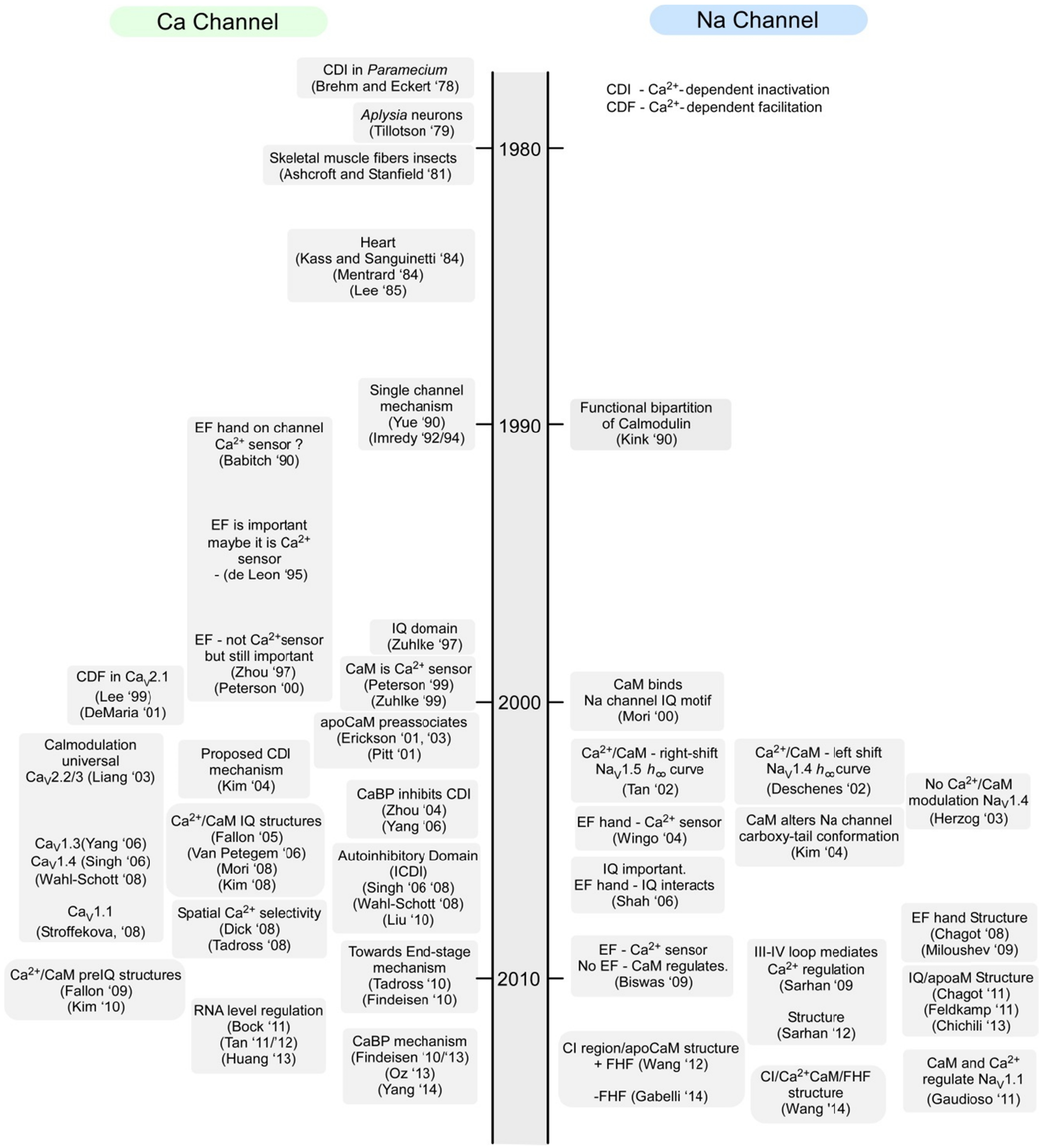
Ca Channel
Na Channel
CDI - Ca$^{2+}$- dependent inactivation
CDF - Ca$^{2+}$- dependent facilitation
1980
1990
2000
2010
CDI in *Paramecium* (Brehm and Eckert ‘78)
*Aplysia* neurons (Tillotson ‘79)
Skeletal muscle fibers insects (Ashcroft and Stanfield ‘81)
Heart (Kass and Sanguinetti ‘84) (Mentrard ‘84) (Lee ‘85)
Single channel mechanism (Yue ‘90) (Imredy ‘92/94)
EF hand on channel Ca$^{2+}$ sensor ? (Babitch ‘90)
EF is important maybe it is Ca$^{2+}$ sensor - (de Leon ‘95)
EF - not Ca$^{2+}$sensor but still important (Zhou ‘97) (Peterson ‘00)
IQ domain (Zuhlke ‘97)
CaM is Ca$^{2+}$ sensor (Peterson ‘99) (Zuhlke ‘99)
CDF in Ca$_V$2.1 (Lee ‘99) (DeMaria ‘01)
apoCaM preassociates (Erickson ‘01, ‘03) (Pitt ‘01)
Calmodulation universal Ca$_V$2.2/3 (Liang ‘03)
Ca$_V$1.3(Yang ‘06) Ca$_V$1.4 (Singh ‘06) (Wahl-Schott ‘08)
Ca$_V$1.1 (Stroffekova, ‘08)
Proposed CDI mechanism (Kim ‘04)
CaBP inhibits CDI (Zhou ‘04) (Yang ‘06)
Ca$^{2+}$/CaM IQ structures (Fallon ‘05) (Van Petegem ‘06) (Mori ‘08) (Kim ‘08)
Autoinhibitory Domain (ICDI) (Singh ‘06 ‘08) (Wahl-Schott ‘08) (Liu ‘10)
Spatial Ca$^{2+}$ selectivity (Dick ‘08) (Tadross ‘08)
Ca$^{2+}$/CaM preIQ structures (Fallon ‘09) (Kim ‘10)
Towards End-stage mechanism (Tadross ‘10) (Findeisen ‘10)
RNA level regulation (Bock ‘11) (Tan ‘11/‘12) (Huang ‘13)
CaBP mechanism (Findeisen ‘10/‘13) (Oz ‘13) (Yang ‘14)
Functional bipartition of Calmodulin (Kink ‘90)
CaM binds Na channel IQ motif (Mori ‘00)
Ca$^{2+}$/CaM - right-shift Na$_V$1.5 $h_\infty$ curve (Tan ‘02)
Ca$^{2+}$/CaM - left shift Na$_V$1.4 $h_\infty$curve (Deschenes ‘02)
No Ca$^{2+}$/CaM modulation Na$_V$1.4 (Herzog ‘03)
EF hand - Ca$^{2+}$ sensor (Wingo ‘04)
CaM alters Na channel carboxy-tail conformation (Kim ‘04)
IQ important. EF hand - IQ interacts (Shah ‘06)
EF hand Structure (Chagot ‘08) (Miloushev ‘09)
EF - Ca$^{2+}$ sensor No EF - CaM regulates. (Biswas ‘09)
III-IV loop mediates Ca$^{2+}$ regulation (Sarhan ‘09
Structure (Sarhan ‘12)
IQ/apoaM Structure (Chagot ‘11) (Feldkamp ‘11) (Chichili ‘13)
CI region/apoCaM structure + FHF (Wang ‘12)
-FHF (Gabelli ‘14)
CI/Ca$^{2+}$CaM/FHF structure (Wang ‘14)
CaM and Ca$^{2+}$ regulate Na$_V$1.1 (Gaudioso ‘11)

**Figure 1.8. Milestones in calmodulation of $Ca^{2+}$ and Na channels.**

Left, milestones in $Ca^{2+}$ regulation of voltage-gate $Ca^{2+}$ channels. $Ca^{2+}$ regulation was identified in $Ca^{2+}$ current recorded from *Paramecium* in 1978. CaM was identified as $Ca^{2+}$ sensor for this regulation in 1999. Right, milestones in $Ca^{2+}$ regulation of Na channel. CaM was shown to bind Na channels in 2000. $Ca^{2+}$ regulation of Na channels remains controversial with $Ca^{2+}$ sensor proposed to be both channel EF hands and CaM.

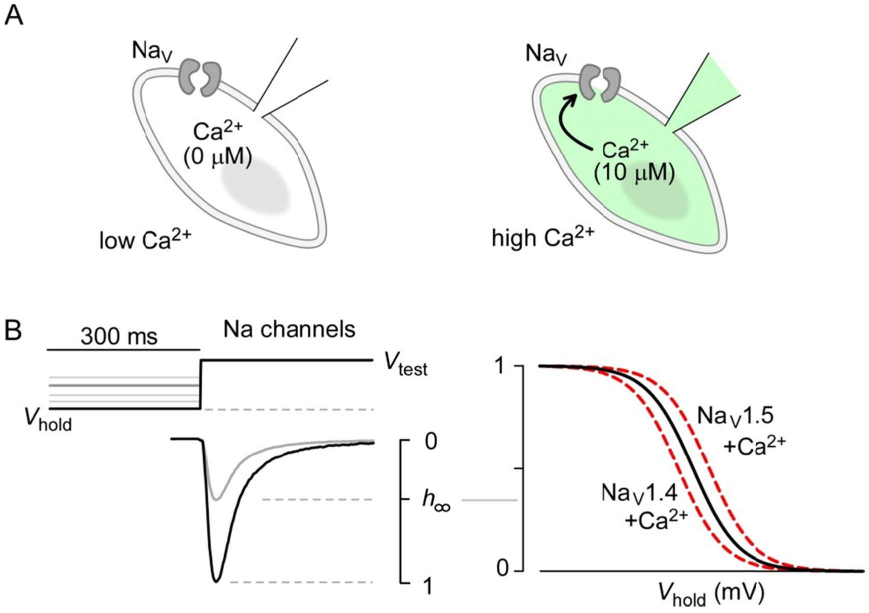
A
NaV
Ca2+
(0 μM)
low Ca2+
NaV
Ca2+
(10 μM)
high Ca2+
B
300 ms
Na channels
Vtest
Vhold
0
h∞
1
1
NaV1.5
+Ca2+
NaV1.4
+Ca2+
0
Vhold (mV)

**Figure 1.9. Experimental scheme utilized to probe $Ca^{2+}$ effects of Na channels.**

(A) Inactivation properties of Na channels from two populations of cells are compared under either low $Ca^{2+}$ (left) or high $Ca^{2+}$ (right) conditions. The control of intracellular $Ca^{2+}$ is achieved through pipet dialysis of an internal solution containing the desired concentration of free $Ca^{2+}$ ions.

(B) Classically, the effect of $Ca^{2+}$ on Na channels is proposed to be a subtle but detectable shift in their voltage-dependence of steady state inactivation ($h_\infty$). Left, the voltage-pulse protocol used to deduce steady-state inactivation properties of Na channels along with simulated currents in response to such a pulse protocol. Briefly, the cells are held at a variable pre-pulse potential for 300 ms. The Na current is subsequently evoked using a test pulse to 0 mV. After hyperpolarizing at very low $V_{\text{hold}}$ potentials, all Na channels are available to open resulting in a large Na current. By contrast, after being held at higher $V_{\text{hold}}$ potentials, only a fraction of Na channels are inactivated and thus unavailable to open. As such, the peak Na current in response to the test pulse is diminished. The ratio of peak Na current evoked after being held at a given $V_{\text{hold}}$ potential to maximal Na current obtained yields the steady state inactivation ($h_\infty$) plotted on the right. Right, purported $Ca^{2+}$ effects on $Na_V1.4$ and $Na_V1.5$ channels. For $Na_V1.5$, $Ca^{2+}$ elevation is argued to result in a depolarizing shift in channel steady-state inactivation in effect yielding a modest enhancement in Na current upon $Ca^{2+}$. By contrast, $Ca^{2+}$ has been argued to yield a modest hyperpolarizing shift in steady-state inactivation of $Na_V1.4$ channels. This effect would yield a net reduction in available Na current at typical resting potentials of cells.

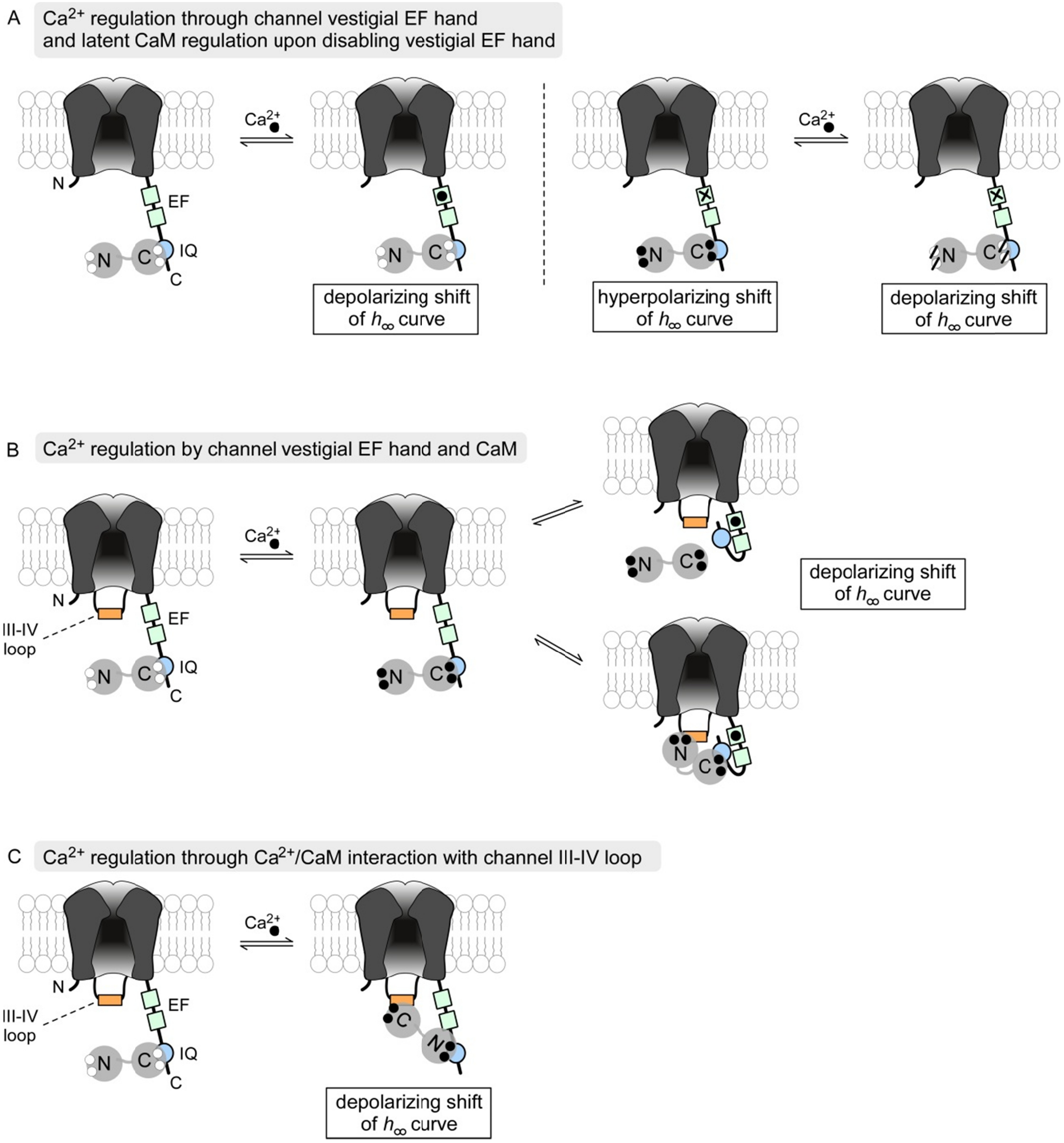
A
Ca$^{2+}$ regulation through channel vestigial EF hand and latent CaM regulation upon disabling vestigial EF hand
Ca$^{2+}$
N
EF
IQ
N
C
C
depolarizing shift of $h_\infty$ curve
hyperpolarizing shift of $h_\infty$ curve
depolarizing shift of $h_\infty$ curve
B
Ca$^{2+}$ regulation by channel vestigial EF hand and CaM
III-IV loop
depolarizing shift of $h_\infty$ curve
C
Ca$^{2+}$ regulation through Ca$^{2+}$/CaM interaction with channel III-IV loop
depolarizing shift of $h_\infty$ curve

**Figure 1.10. Divergent mechanistic schemes for $Ca^{2+}$ regulation of Na channels.**

(A) One proposed mechanism of Na channel $Ca^{2+}$ regulation is the direct binding of $Ca^{2+}$ ions to the channel vestigial EF hand segment 1 as illustrated in the left subpanel. Upon $Ca^{2+}$ binding to this channel segment, a depolarizing shift in the voltage-dependence of steady-state inactivation of the channel has been proposed. Right, upon disabling $Ca^{2+}$ binding to the channel vestigial EF hand, latent CaM regulation is proposed to emerge. Accordingly, $Ca^{2+}$/CaM is argued to elicit hyperpolarizing shift of the $h_\infty$ curve. By contrast, mutant $CaM_{1234}$ with $Ca^{2+}$ binding to all four EF hands disabled is suggested to result in a depolarizing shift of the $h_\infty$ curve.

(B) A second prominent model also argues for direct $Ca^{2+}$ binding to channel vestigial EF hand as a crucial step in regulation of Na channels. By this model, apoCaM binds tightly to the channel complex with critical dependence on the channel IQ domain. However, $Ca^{2+}$ binding to CaM, weakens this binding affinity and CaM transiently departs from the channel IQ domain. This maneuver allows for the IQ domain to interact with the channel vestigial EF hand lowering the $Ca^{2+}$ requirement for the vestigial EF segment. The direct $Ca^{2+}$ binding to the channel vestigial EF hand then evokes a depolarizing shift in voltage-dependence of $h_\infty$ curve. An alternative model suggests that $Ca^{2+}$/CaM may depart to the channel III-IV loop. Nonetheless, the departure of CaM from the IQ domain is the critical step that enables for $Ca^{2+}$ coordination within the vestigial EF hand segment.

(C) A third model discounts any role for the channel vestigial EF hand segment and instead proposes CaM as the primary $Ca^{2+}$ sensor for the channel complex. In this model, apoCaM preassociates to the channel carboxy-terminus with C-lobe interacting with the IQ domain. Upon $Ca^{2+}$ elevation, the C-lobe of CaM departs to the channel III-IV loop while the N-lobe associates with the channel IQ domain thus bridging the channel interfaces.

# CHAPTER 2

## Experimental Procedures

In this chapter, we describe at length detailed experimental procedures utilized to interrogate $Ca^{2+}$ regulation of Na and $Ca^{2+}$ channels.

***Whole-cell electrophysiological recordings*** **-** Whole-cell recordings were obtained at room-temperature (~298 K) using an Axopatch 200A amplifier (Axon Instruments). Electrodes were made from borosilicate glass capillaries (World Precision Instruments, MTW 150-F4), yielding 1–2 MΩ resistances which were in turn compensated for series resistance by >70%. These glass pipets pipettes were fabricated using a horizontal micropipette puller (model P-97, Sutter Instruments) and fire polished using a microforge (Narishige). Data acquisition utilized an ITC-18 (InstruTECH) data acquisition unit controlled by custom MATLAB software (Mathworks). For Na currents, electrical recordings were low-pass filtered at 5 kHz prior to digital acquisition at several times that frequency. For $Ca^{2+}$ channels, currents were low-pass filtered at 2 kHz prior to digital acquisition at several times that frequency. P/8 leak subtraction was used.

For $Ca^{2+}$ uncaging experiments, $Na_V1.4$ channels were repetitively pulsed to 0 mV for 15 msec during a 20-Hz train, with 30-sec rest intervals between trains. The holding potential was -90 mV unless otherwise specified. For experiments in skeletal myotubes, the same parameters were used, except that the pulses to 0 mV lasted 10 msec. For like experiments with $Na_V1.5$ channels (including ventricular myocytes), pulses to 0 mV for 15 msec were presented as 10-Hz trains punctuated by 30-sec rest intervals. The holding potential was also -90 mV unless specified in the corresponding figure legends.

***Single-channel recordings* -** All multichannel records were obtained via on-cell recordings from HEK293 cells, acquired at room temperature using the integrating mode of an Axopatch 200A amplifier (Axon Instruments). Patch pipettes (4–15 MΩ) were pulled from ultra-thick-walled borosilicate glass (BF200-116-10; Sutter Instruments) using horizontal puller (P-97, Sutter Instruments), fire polished using a microforge (Narishige), and coated with Sylgard (Dow Corning). Data acquisition again utilized ITC-18 (Instrutech) driven by a custom MATLAB software (Mathworks). Current records were filtered at 5 kHz with a four-pole Bessel filter, and sampled at 200 kHz. Leak subtraction and analysis methods were closely similar to those used previously in our laboratory (Imredy and Yue, 1992).

***Recipes for pipet and bath solutions* -** For recordings of wild-type and mutant $Ca_V1.3$ channels we used an internal solution, '0 [$Ca^{2+}$]', which contained (in mM): $CsMeSO_3$, 114; CsCl, 5; $MgCl_2$, 1; MgATP, 4; HEPES (pH 7.4), 10; and BAPTA, 10; at 290 mOsm adjusted with glucose. The bath solution contained (in mM): TEA-$MeSO_3$, 102; HEPES (pH 7.4), 10; $CaCl_2$ or $BaCl_2$, 40; at 300 mOsm adjusted by TEA-$MeSO_3$. For recordings of $Ca_V1.3$-$Na_V1.4$CT chimeric channel, we used the same bath solution and a modified internal solution containing (in mM): $CsMeSO_3$, 124; CsCl, 5; $MgCl_2$, 1; MgATP, 4; HEPES (pH 7.4), 10; and EGTA, 0.5; at 290 mOsm adjusted with glucose.

For experiments probing $Na_V$ steady-state inactivation under static $Ca^{2+}$, we used either '0 [$Ca^{2+}$]' solution described above, or a '10 [$Ca^{2+}$]' solution containing (in mM):

$CsMeSO_3$, 109; CsCl, 5; $MgCl_2$, 1; MgATP, 4; HEPES (pH 7.4), 10; HEDTA, 10; and $CaCl_2$, 5, at 290 mOsm adjusted with glucose. The bath solution contained (in mM): TEA-$MeSO_3$, 45; HEPES (pH 7.4), 10; NaCl, 100; at 300 mOsm adjusted with TEA-$MeSO_3$. The electrophysiological measurements were obtained only after ~10 minutes of pipet dialysis to permit stabilization of Na channel properties.

For all $Ca^{2+}$-uncaging experiments, internal solution contained (in mM): $CsMeSO_3$, 120; CsCl, 5; HEPES (pH 7.4 with CsOH), 10; Fluo-4FF pentapotassium salt (Invitrogen), 0.01; Alexa 568 succinimidyl ester (Invitrogen), 0.0025; Citrate, 1; DM-Nitrophen EDTA (DMN) and $CaCl_2$ were adjusted to obtain desired $Ca^{2+}$ flash. Typically, for flashes in range 0.5 – 2μM, DMN, 1 mM; and $CaCl_2$, 0.7 mM. For the 2 – 8 μM range, DMN, 2 mM; and $CaCl_2$, 1.4 mM. For larger $Ca^{2+}$ steps, DMN, 4 mM; and $CaCl_2$, 3.2 mM. Since DMN can bind $Mg^{2+}$, all experiments were conducted with 0 mM $Mg^{2+}$ internally. For recombinant Na channel experiments, the bath solution contained (in mM): TEA-$MeSO_3$, 45; HEPES (pH 7.4), 10; NaCl, 100; at 300 mOsm, adjusted with TEA-$MeSO_3$. For $Ca^{2+}$ uncaging experiments in guinea pig ventricular myocytes, we used a modified bath solution containing (in mM): NaCl, 2; Choline-Cl, 125; $CaCl_2$, 5; KCl, 4; HEPES, 10; glucose, 10; adjusted to pH 7.4 with NaOH and 300 mOsm with Choline-Cl. For $Ca^{2+}$-uncaging experiments in GLT cells, the bath solution contained (in mM): NaCl, 100; HEPES (pH 7.4), 10; Choline-Cl, 35; $MgCl_2$, 1; KCl, 4; at 290 mOsm adjusted with Choline-Cl.

For experiments coexpressing both $Na_V$ and $Ca_V$ channels, the bath solution contained (in mM): NaCl, 130; $CaCl_2$, 15; $MgCl_2$, 1; KCl, 4; $NaH_2PO_4$, 0.33; HEPES, 10; with pH 7.4 adjusted with NaOH and at 290 mOsm adjusted with NaCl. For corresponding control experiments that used $Ba^{2+}$ as charge carrier through $Ca^{2+}$ channels, we substituted 15 mM $BaCl_2$ in place of $CaCl_2$. The pipet solution, '0.5 EGTA' contained (in mM): $CsMeSO_3$, 124; CsCl, 5; $MgCl_2$, 1; MgATP, 4; HEPES (pH 7.4), 10;

and EGTA, 0.5; at 290 mOsm adjusted with glucose. For high internal buffering, we used '0 [$Ca^{2+}$]' solution described above.

For multi-channel on-cell recordings of Na channels cotransfected with $Ca^{2+}$ channels, the bath solution contained (in mM): K-glutamate, 132; KCl, 5; NaCl, 5; $MgCl_2$, 3; EGTA, 2; Glucose, 6; and HEPES, 10 (pH adjusted to 7.4). The pipet solution contained (in mM): TeA-$MeSO_3$, 30; NaCl, 100; $CaCl_2$, 10; HEPES, 10 (pH 7.4).

***$Ca^{2+}$ uncaging and fluorescence measurements* -** All $Ca^{2+}$-uncaging experiments were conducted on a Nikon TE2000 inverted microscope with a Plan Fluor Apo 40× oil objective. $Ca^{2+}$-uncaging was performed using a classic Cairn UV flash photolysis system. UV pulses of ~1.5 ms in duration were powered by a capacitor bank of 4000 μF charged to 200-300 V. PMTs were protected during UV pulse to prevent photo-damage. For simultaneous $Ca^{2+}$ imaging, Fluo4FF and Alexa568 dyes (in fixed, predetermined ratios) were dialyzed into the cell and then imaged with Argon laser excitation (514 nm). Autofluorescence for each cell was obtained prior to pipet dialysis of these dyes. The fluorescence emission from a single cell was isolated using a field-stop aperture. Dual color fluorescence emission was attained using a 545DCLP dichroic mirror, paired with a 545/40BP filter for detecting Fluo4FF, and a 580LP filter for detecting Alexa568. Uncaging experiments were conducted after ~ 2 minutes of dialysis of internal solution. Steady-state [$Ca^{2+}$] was measured 150 ms after the instant of uncaging.

***$Ca^{2+}$ measurements* -** $Ca^{2+}$ measurements were determined from ratio of Fluo4FF/Alexa fluorescence intensities ($R$), according to the relation $[Ca^{2+}] = K_d \cdot (R - R_{min}) / (R_{max} - R)$. All three parameters $K_d$, $R_{min}$, $R_{max}$ were experimentally determined in HEK293 cells dialyzed with reference $Ca^{2+}$ solutions (Yang et al., 2014) and were assumed to be same for ventricular myocytes and skeletal myotubes. Briefly, $R_{min}$ was determined with internal solution containing 40 mM EGTA, and $R_{max}$ using 4 mM $Ca^{2+}$/1 mM EGTA (~3 mM free $Ca^{2+}$) solution. An $R_{20\mu M}$ measurement was obtained with internal solution containing [$Ca^{2+}$] = 20 μM (buffered using NTA). $K_d$ was experimentally determined by solving the equation above. Calibration measurements were repeated at 1 or 4 mM DMN to account for minor differences in $R_{\mathrm{max}}$.

***FRET optical imaging* -** we conducted FRET 2-hybrid experiments in HEK293 cells cultured on glass-bottom dishes, using an inverted fluorescence microscope as extensively described by our laboratory (Erickson et al., 2003). Experiments utilized a bath Tyrode's solution containing either 2 mM $Ca^{2+}$ for experiments probing apoCaM binding or 10 mM $Ca^{2+}$ with 4 μM ionomycin (Sigma-Aldrich, MO) for elevated $Ca^{2+}$ experiments. $3^3$-FRET efficiencies ($E_A$) were computed as elaborated in our prior publications (Erickson et al., 2003). E-FRET efficiencies ($E_D$), whose measurement methodology was developed and refined in other laboratories (Chen et al., 2006), could be determined from the same single-cell $3^3$-FRET measurements using the following relationship, which expresses $E_D$ in terms of our own calibration metrics and standard measurements:

$$E_D = E_{D,\max} \cdot D_b = \frac{S_{FRET} - R_{D1} \cdot S_{CFP} - R_A \cdot S_{YFP}}{S_{FRET} - R_{D1} \cdot S_{CFP} - R_A \cdot S_{YFP} + G \cdot S_{CFP}}$$

where $G$ is a constant, defined as

$$G = R_{D1} \frac{\varepsilon_{CFP}(440\text{ nm})}{\varepsilon_{YFP}(440\text{ nm})} \frac{M_A}{M_D} \approx 1.864$$

$S_{\mathrm{FRET}}$, $S_{\mathrm{YFP}}$, and $S_{\mathrm{CFP}}$ correspond to fluorescent measurements from the same cell using FRET, YFP, and CFP cubes whose spectral properties have been detailed previously (Erickson et al., 2003). $R_{\mathrm{D1}}$ and $R_{\mathrm{A}}$ are constants relating to the respective spectral properties of ECFP and EYFP; $\varepsilon_{\mathrm{CFP}}(440\text{ nm}) / \varepsilon_{\mathrm{YFP}}(440\text{ nm})$ approximates the ratio of molar extinction coefficients of ECFP and EYFP at 440 nm, respectively; and $M_{\mathrm{A}} / M_{\mathrm{D}}$ is the ratio of optical gain factors and quantum yields pertaining to EYFP and ECFP, respectively. Detailed descriptions of these parameters and their determination appear in our prior publications (Erickson et al., 2003). For all FRET efficiencies, spurious FRET relating to unbound ECFP and EYFP moities has been subtracted (Dick et al., 2008). For

$3^3$-FRET, spurious FRET is linearly proportional to the concentration of CFP molecules, and the experimentally determined slope $A_{3^3\text{-FRET}}$ was obtained from cells coexpressing ECFP and EYFP fluorophores. Similarly, for E-FRET, the spurious FRET is linearly proportional to the concentration of EYFP molecules. The slope for this relationship $A_{\text{E-FRET}}$ can be obtained from:

$$A_{\text{E-FRET}} = A_{3^3\text{-FRET}} \cdot (R_{\text{A}} / R_{\text{D1}}) \,/\, (M_{\text{A}} / M_{\text{D}})$$

The methods for FRET 2-hybrid binding curves have been extensively described in previous publications (Erickson et al., 2001; Erickson et al., 2003; Chen et al., 2006). Briefly, binding curves were determined by least-squared-error minimization of data from multiple cells, utilizing a 1:1 binding model with adjustment of parameters $K_{\text{d,EFF}}$ and maximal FRET efficiency at saturating donor concentrations. For a small number of interactions involving mutations that strongly disrupted binding, the maximal FRET efficiency was set equal to that of the corresponding wild-type interaction and $K_{\text{d,EFF}}$ varied to minimize errors. Standard-deviation error bounds on $K_{\text{d,EFF}}$ estimates were determined by Jacobian error matrix analysis.

***Molecular biology*** - The rat skeletal muscle Na channel (Trimmer et al., 1990) ($\text{Na}_\text{V}$1.4) in pBluescript vector was cloned into pcDNA3 (Invitrogen) via flanking EcoRI sites. The channel carboxy-terminus agrees with clone Y17153.1 (GenBank). The human $\text{Na}_\text{V}$1.5 channel corresponds to clone M77235.1 (GenBank). The $\text{Ca}_\text{V}$1.3 construct, $\alpha_{1\text{D}}\Delta1626$, was derived and engineered from the native rat brain variant AF370009 (GenBank). In general, all segments subjected to PCR amplification and Quikchange mutagenesis were verified by sequencing.

***Construction of Na channel mutants and chimeras -*** To facilitate mutagenesis of $\text{Na}_\text{V}$1.4 carboxy terminus, we first PCR amplified and subcloned an ~900 bp segment containing the CI region (bounded by KpnI and XbaI restriction sites) into zero blunt TOPO II (Invitrogen) vector, yielding a convenient TOPO-$\text{Na}_\text{V}$1.4CT construct. Quikchange (Agilent) was then used to introduce channel EF-hand mutations (D[1621]A

& D[1623]A mutations; and 4× mutations), alanine substitutions of isoleucine and glutamine residues of IQ domain and channelopathic mutations (Q[1628]E; and F[1698]I) into the TOPO-$Na_V$1.4CT construct. These mutant segments were then transferred to $Na_V$1.4 pcDNA3 construct following restriction digest and ligation utilizing KpnI/XbaI sites.

To generate the $Na_V$1.4-$Na_V$1.5CT chimeric channel, we first introduced a silent XhoI site immediately downstream of the channel domain IV S6 segment (5212-ctGgag-5217 to 5212-ctCgag-5217) using Quikchange (Agilent) on TOPO-$Na_V$1.4CT construct followed by ligation into the full length $Na_V$1.4 clone. Subsequently, the entire $Na_V$1.5 carboxy-terminus starting at 1772-LENFSV-1778 was PCR amplified and cloned into $Na_V$1.4 utilizing restriction sites XhoI and XbaI. To construct $Na_V$1.5-$Na_V$1.4CT chimera, we introduced a silent NruI site into $Na_V$1.5 channel by mutagenesis of location 5329–gtggccacg–5337 into 5329–gtCgcGacg–5337. Subsequently, the entire $Na_V$1.4CT was PCR amplified starting at residue location 1596-VAT-1599 and ligated into full length $Na_V$1.5 exploiting the NruI/XbaI sites.

A similar strategy was followed for mutagenesis of the III-IV loop mutation (Y[1311]A). An ~3300 bp segment bounded by unique restriction sites BsiWI and KpnI including the III-IV loop was subcloned into zero blunt Topo II (Invitrogen) vector following PCR amplification. The Y[1311]A mutation was then introduced into this segment using Quikchange (Agilent), and subsequently transferred to the full length channel.

***Construction of $Ca^{2+}$ channel mutants and chimeras*** – To simplify mutagenesis, the wildtype construct in this study was an engineered $Ca_V$1.3 construct $\alpha_{1D\Delta1626}$, nearly identical to and derived from the native rat brain variant ($\alpha_{1D}$, AF3070009). Briefly, the $\alpha_{1D\Delta1626}$ construct, as contained with mammalian expression plasmid pCDNA6 (Invitrogen), features introduction of a silent and unique *Kpn* I site at a position corresponding to ~50 amino acid residues upstream of the carboxy terminal IQ domain

($G_{1538}T_{1539}$). As well, a unique *Bgl* II restriction site is present at a locus corresponding to ~450 amino acid residues upstream of the IQ domain. Finally, a unique *Xba* I and stop codon have been engineered to occur immediately after the IQ domain. These attributes accelerated construction of cDNAs encoding triple alanine mutations of $\alpha_{1D\Delta1626}$. Point mutations of channel segments were made via QuikChange® mutagenesis (Agilent), prior to PCR amplification and insertion into the full-length $\alpha_{1D\Delta1626}$ channel construct via restriction sites *Bgl* II/*Kpn* I, *Kpn* I/*Xba* I, or *Bgl* II/*Xba* I. Some triple alanine mutation constructs included a seven-aa extension (SRGPAVRR) after residue 1626.

To construct the $Ca_V1.3$-$Na_V1.4CT$ chimera, we first truncated the $Ca_V1.3$ channel immediately upstream of the EF hand region (terminating with residues 1471–ILGPHHLD–1479) and concurrently introduced a silent XbaI site at residue HLD by mutating base pairs, 4426–caccacttggac–4437 into 4426–caccaTCTAgac–4437 using PCR amplification and ligation utilizing BglII/XbaI restriction sites. Subsequently, the $Na_V1.4CT$ was PCR amplified using primers: (fwd) 5'-caccaTCTAgacatgttctatgagac-ctgggag-3' and (rev) 5'-gatagagtttaaacttagacaagagactctttgacccc-3' and ligated into the truncated $Ca_V1.3$ construct using XbaI/PmeI restriction sites. This maneuver created the $Ca_V1.3$-$Na_V1.4CT$ chimera with the protein sequence 1471-ILGPHHLDMFYEIW-1485 at the amino-terminal segment of the EF hand region.

***Construction of FRET 2-hybrid constructs*** **-** For FRET 2-hybrid constructs, fluorophore-tagged (all based on ECFP and EYFP) CaM constructs were made as described (Erickson et al., 2003). Other FRET constructs were constructed by replacing CaM with appropriate PCR amplified segments, via unique *Not* I and *Xba* I sites flanking CaM (Erickson et al., 2003). YFP-$CaM_C$, as used in Supplementary Fig. S4.1 was comprised of YFP fused to the C-lobe (residues 78-149) of CaM. To facilitate cloning, the YFP-tagged CI region was constructed with a twelve amino-acid extension (SRGPYSIVSPKC) by *Not* I / *Xba* I sites as mentioned above. We verified that this extension did not alter the binding affinity of apoCaM compared to a wild-type

YFP-tagged CI region (not shown). Throughout, all segments subject to PCR or QuikChange® mutagenesis were verified in their entirety by sequencing.

***Transfection of HEK293 cells* -** For whole-cell patch clamp experiments, HEK293 cells were cultured on 10-cm plates, and channels transiently transfected by calcium phosphate method (Peterson et al., 1999). For experiments involving static $Ca^{2+}$, we cotransfected 6 μg of rat $Na_V1.4$ or 6 μg of human $Na_V1.5$ with 8 μg of eYFP. For $Ca^{2+}$ uncaging experiments, we applied 6-8 μg of cDNA encoding the desired Na channel, 6 μg of eCFP, and 8 μg of rat $CaM_{WT}$. For experiments involving mutant CaM, we substituted 8 μg of $CaM_{12}$, $CaM_{34}$, or $CaM_{1234}$ instead of $CaM_{WT}$. For experiments that involved both $Ca_V2.1$ and Na channels at the whole-cell level, 6 μg rat $Na_V1.4$ or $Na_V1.5$, 8 μg of $\alpha_1$ subunit of $Ca_V2.1$ EFb $43^+/44^-/47^+$ isoform (Chaudhuri et al., 2004), 8 μg of rat brain $\beta_{2a}$ (M80545) auxiliary subunit, 5 μg of $\alpha_2\delta$ (NM012919.2), and 8 μg of rat $CaM_{WT}$ or 8 μg of $CaM_{1234}$ were cotransfected. For like coexpression experiments at the single-channel level, 1-2 μg rat $Na_V1.4$, 8-10 μg of $\alpha_1$ subunit of $Ca_V2.1$ EFb $43^+/44^-/47^+$ isoform (Chaudhuri et al., 2004), 8 μg of rat brain $\beta_{2a}$ (M80545) auxiliary subunit, 5 μg of $\alpha_2\delta$ (NM012919.2), and 8 μg of rat $CaM_{WT}$ were cotransfected. For experiments probing $Ca^{2+}$ channel CDI, we cotransfected 8 μg of $Ca_V1.3$ or $Ca_V1.3$-$Na_V1.4$CT, 8 μg of rat brain $\beta_{2a}$ auxiliary subunit, 5 μg of $\alpha_2\delta$, and 8 μg of rat $CaM_{WT}$ or 8 μg of mutant $CaM_{1234}$ All of the above cDNA constructs were included within mammalian expression plasmids driven by a cytomegalovirus promoter. To boost expression, cDNA for simian virus 40 T antigen (1-2 μg) was cotransfected. Currents were probed ~1-3 days following transfection.

For $Ca_V1.3$ alanine scanning mutagenesis experiments, we applied 8 μg of cDNA encoding the desired channel $\alpha_1$ subunit, along with 8 μg of rat brain $\beta_{2a}$ (M80545) and 8 μg of rat brain $\alpha_2\delta$ (NM012919.2) subunits. We utilized the $\beta_{2a}$ auxiliary subunit to minimize voltage-dependent inactivation. For experiments involving CaM overexpression, we coexpressed 8 μg of rat $CaM_{WT}$, $CaM_{12}$, or $CaM_{34}$, as described

(Peterson et al., 1999). All of the above cDNA constructs were included within mammalian expression plasmids with a cytomegalovirus promoter. To boost expression, cDNA for simian virus 40 T antigen (1-2 μg) was co-transfected. For fluorescence resonance energy transfer (FRET) 2-hybrid experiments, HEK293 cells were cultured on glass-bottom dishes and transfected with FuGENE$^R$ 6 (Roche), before epifluorescence microscope imaging (Erickson et al., 2003). Electrophysiology/FRET experiments were performed at room temperature 1-3 days after transfection.

***Isolation of guinea-pig ventricular myocytes*** **-** Ventricular myocytes were isolated from adult guinea pigs in accordance with guidelines established by Johns Hopkins University Animal Care and Use Committee as described in previous publication (Alseikhan et al., 2002). Briefly, hearts were excised and ventricular myocytes were isolated by enzymatic digestion using a Langendorff perfusion apparatus. Whole-cell Na currents were interrogated using patch clamp ~2 hrs after isolation.

***GLT myoblast culture*** **-** Homozygous mouse dysgenic (mdg/mdg) GLT cell lines were originally generated by stable transfection of mdg myoblasts with plasmid-encoding large-T antigen (Powell et al., 1996). The myoblasts were expanded in growth media based of F-10 Ham's media containing 20% FBS; HEPES, 25 mM; L-glutamine, 4 mM; Penicillin-Streptomycin, 100 U/ml; and βFGF, 1 ng/ml. After reaching more than 90% confluence (~3 days), the growth media was exchanged for a DMEM based differentiation media that contains 2% horse serum, Penicillin-streptomycin, 100 U/ml; and L-glutamine, 4 mM. Following differentiation (~3 days), the cells were split onto glass cover slips and patch clamp experiments were conducted the following day.

***Construction of phylogenetic tree*** **-** Protein sequences of all human $\mathrm{Ca_V1}$, $\mathrm{Ca_V2}$, $\mathrm{Ca_V3}$ and $\mathrm{Na_V1}$ channels were obtained from GenBank (Benson et al., 2005). For Figures 8.4 and 8.5, protein sequences were acquired from GenBank (Benson et al., 2005), UniProt (Consortium, 2013), JGI (Grigoriev et al., 2012), or ParameciumDB (Arnaiz and Sperling, 2011) databases. Multiple sequence alignments were made using MUSCLE algorithm (Edgar, 2004) and phylogenetic trees were constructed using MEGA5.2 software (Tamura et al., 2011).

***Molecular Modeling*** **-** *De novo* structural prediction was performed using the *Robetta* online server (Kim et al., 2004a) (http://robetta.bakerlab.org). We used web-based molecular docking programs, PatchDock (Schneidman-Duhovny et al., 2005) (http://bioinfo3d.cs.tau.ac.il/PatchDock/) and FireDock (Mashiach et al., 2008) (http://bioinfo3d.cs.tau.ac.il/FireDock/) to obtain preliminary models for molecular docking. Such preliminary models were subsequently used as starting models for further structural modeling and refinement using a customized docking protocol of PyRosetta (Chaudhury et al., 2010). All molecular models and atomic structures were visualized and rendered using PyMOL v1.2r1. (DeLano Scientific, LLC).

***De novo prediction of the CI region structures*** **-** The structural correlates for the molecular states we have identified here have yet to be determined. Nonetheless, to evaluate the structural plausibility of these states, we turn to *de novo* structural prediction using *Rosetta* (Kim et al., 2004a). We used the *Robetta* online server (http://robetta.bakerlab.org), to obtain plausible molecular models of the CI region spanning $GPH_{1474}$ (in the PCI region) through residue $K_{1620}$ in the IQ domain. Figure 2.1 displays the top 5 predicted models furnished by the server. Coarsely, the IQ domain (blue) is linked to the PCI segment (green) through a flexible linker, and thus adopts variable orientations. The PreIQ region forms a distinctive uninterrupted helix, similar to that observed in crystal structures of the homologous region in $Ca_V1.2$ channels (PDB code: 3OXQ and 3G43). The EF-hand region in model I is structurally similar to homologous segments of $Na_V$ channels, namely EF-hand-like domains (PDB code: 2KBI or 2KAV). In general, the EF-hand region adopted either a closed conformation reminiscent of N-lobe of apoCaM (models I & IV), or an open conformation like the N-lobe of $Ca^{2+}$/CaM (models II, III, or V). For subsequent docking simulations, we focused on models I and III, representing the two best respective closed and open conformations identified by *Rosetta*.

***Docking of apoCaM to CI region*** – To build a molecular model of apoCaM bound to the CI region of $Ca_V1.3$ channels, we drew upon insight from recent structural studies of the homologous $Na_V$ channel CI region. Firstly, a crystallographic structure of the $Na_V1.5$ CI region, complexed with apoCaM and FGF, shows that the EF-hand-like domain of these channels adopts a closed conformation with high structural similarity to model I of our predictions (Wang et al., 2012). Secondly, multiple structures have demonstrated that the IQ domain of these channels bind to the C-lobe of apoCaM (Chagot and Chazin, 2011; Feldkamp et al., 2011; Wang et al., 2012). Thirdly, the N-lobe of apoCaM in these latter $Na_V$ structures seem to adopt variable conformations. At the same time, our own functional studies of $Ca_V1.3$ channels point to the N-lobe of apoCaM binding to the downstream EF-hand segment of the PCI region ($EF_2$).

That said, we incorporated these trends into the development of a custom multi-step docking algorithm to model apoCaM interaction with the $Ca_V1.3$ carboxy terminus. To do so, we first used MODELLER (Sali and Blundell, 1993)to build a homology model of the $Ca_V1.3$ IQ domain interaction with the C-lobe of apoCaM, based on the NMR structures of $Na_V1.5$ (Chagot and Chazin, 2011) and $Na_V1.2$ (Feldkamp et al., 2011) IQ domains complexed with the C-lobe of apoCaM. Reassuringly, this model of the $Ca_V1.3$ IQ domain emphasizes contacts at the functionally relevant hotspots A[-4], I[0], and F[4] in the IQ domain. Next, we utilized a shape complementarity docking algorithm, PatchDock (Schneidman-Duhovny et al., 2005), to coarsely dock the N-lobe of apoCaM (1CFD) to the PCI region, as suggested from our iTL analysis. The top ten resulting docking models were then refined by FireDock (Mashiach et al., 2008). We then turned to RosettaDock and Loop refinement protocols of the PyRosetta package (Chaudhury et al., 2010) to perform high-resolution docking of the N-lobe to the PCI segment. Out of 8000 decoys generated using PyRosetta, we identified the lowest energy complex as our top model. To combine these distinct structural models (PCI region bound to the N-lobe of apoCaM, and IQ domain bound to the C-lobe of apoCaM), we used PyRosetta to develop a custom minimization and refinement protocol, as follows. We optimized the position of the IQ domain/C-lobe apoCaM complex with respect to the PCI region by altering the conformation of the linker between N- and C-lobes of apoCaM, and simultaneously minimizing both the energetics and distance between the IQ domain and $QVV_{1590}$ in the PreIQ region. Finally, the flexible linker between the PreIQ segment and the IQ domain was built and optimized via multiple rounds of energy minimization.

***Docking of C-lobe of $Ca^{2+}$/CaM to CI region* -** To build a structural model of the tripartite C-lobe CDI effector complex (IQ/PCI/C-lobe $Ca^{2+}$/CaM in Figure 7.10, right), we employed a custom, multi-step docking algorithm similar to the one above. As the starting point for the PCI segment, we chose model III (Figure 2.1) because its open EF-hand conformation permitted simultaneous interactions with the IQ segment and the C-lobe of $Ca^{2+}$/CaM (3BXL). First, we used PatchDock (Schneidman-Duhovny et al., 2005), to obtain a coarse model of the IQ domain bound to the EF-hand segments of $Ca_V1.3$ channels. Subsequently, we refined this model initially with FireDock, and then with the RosettaDock protocol of PyRosetta for a systematic second stage of refinement. Next, we coarsely docked the structure of the C-lobe of $Ca^{2+}$/CaM to the above complex using PatchDock, followed by structural refinement with FireDock (Mashiach et al., 2008) and RosettaDock (Lyskov and Gray, 2008). Finally, we optimized the conformation of the flexible PreIQ-IQ linker using PyRosetta (Chaudhury et al., 2010). These molecular models highlight the structural plausibility of the functionally relevant molecular states that we have identified.

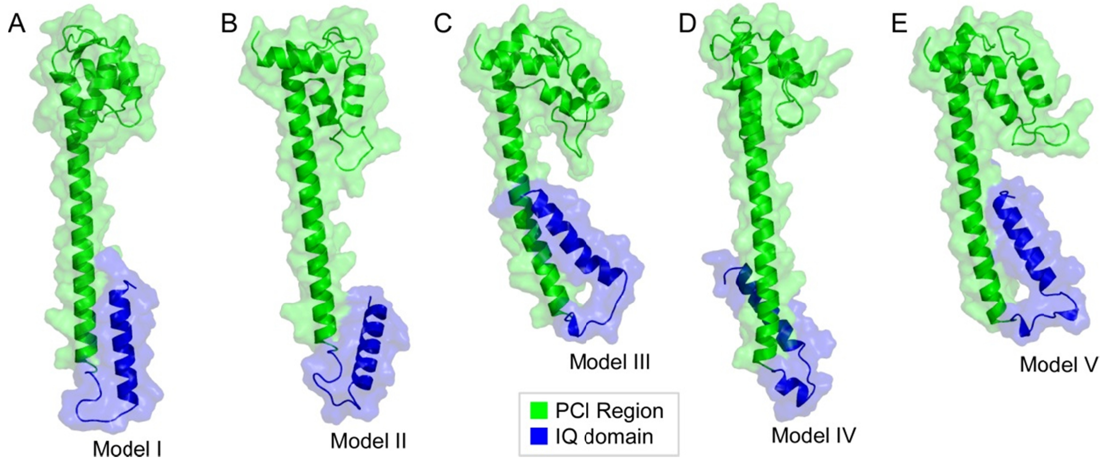
A
B
C
D
E
Model I
Model II
Model III
Model IV
Model V
🟩 PCI Region
🟦 IQ domain

**Figure 2.1.** ***De novo* structural prediction of $\text{Ca}_\text{V}$1.3 CI region.**

(A-E) Models I-V are highest scoring models output from the *Robetta* online server. The PCI segment was shaded in green. The IQ domain is shaded in blue.

# CHAPTER 3

## A rapid $Ca^{2+}$-dependent inactivation of Na channels

Voltage-gated Na and $Ca^{2+}$ channels comprise two prominent ion channel superfamilies (Jan and Jan, 1989) with distinct biophysical properties that enable customized biological functions. The Na channels are renowned for ultra-rapid activation and inactivation, while $Ca^{2+}$ channels are known for longer-lasting influx of the second messenger $Ca^{2+}$. As such, these two channel classes serve distinct and vital functions: Na channels sustain brisk spatial propagation of action potentials, while $Ca^{2+}$ channels link excitation to other biological functions including contraction, secretion and transcription (Jan and Jan, 1989; Hille, 2001; Adams and Snutch, 2007). Historically, then, these two superfamilies have often been studied as disparate entities (Hille, 2001).

A point of convergence, however, is their homologous carboxy tail region (Figure 3.1A, CI region) that demonstrates high sequence similarity, hinting at a tangible ancestral blueprint. This CI region contains two vestigial EF-hand motifs (Babitch, 1990;

de Leon et al., 1995; Chagot et al., 2009; Miloushev et al., 2009) (rose, green), and a calmodulin (CaM) binding IQ domain (Zuhlke and Reuter, 1998; Mori et al., 2000) (lavender). If this homology were to support functions of like correspondence, deep mechanistic insights and related channelopathic disease perspectives could be gleaned from combined investigation of Na and $Ca^{2+}$ channels.

For nearly all $Ca^{2+}$ channels, the CI region elaborates a robust and recognizably similar $Ca^{2+}$/CaM-dependent regulation as described at length in the introductory chapter. A typical manifestation of this $Ca^{2+}$ channel modulation is $Ca^{2+}$-dependent inactivation (CDI). For this regulation, a single apoCaM preassociates with channel and $Ca^{2+}$ binding to CaM elicits a conformational change of the channel carboxy-terminus that dramatically reduce channel open probability. A typical electrophysiological profile of CDI as observed for $Ca_V1.3$ channels is shown in Figure 3.1B-C. A convenient feature of $Ca^{2+}$ channels is that they themselves convey $Ca^{2+}$ influx that could trigger $Ca^{2+}$ regulation (Figure 3.1B). By contrast, as $Ba^{2+}$ ions bind poorly to CaM (Chao et al., 1984), this regulation is entirely absent upon $Ba^{2+}$ influx through the channel, thus serving as a straightforward negative control to robustly characterize CDI (Figure 3.1B). Accordingly, exemplar $Ca^{2+}$ currents are observed to decline rapidly as a result of CDI (Figure 3.1C, left, red trace), while $Ba^{2+}$ currents undergo minimal inactivation (Figure 3.1, left, black trace). The steady-state extent of CDI is typically characterized as fraction of peak current remaining after 300-ms depolarization ($r_{300}$). *CDI* plotted as a function of voltage demonstrates a U-shaped dependence – a hallmark of this modulation.

The effect of $Ca^{2+}$ on Na channels has been purported to subtle and static isoform-specific alterations in the voltage-dependence of steady-state inactivation properties as reviewed in the introductory chapter.  That said, the existence, functional nature, and proposed mechanisms underlying $Ca^{2+}$ regulation of Na channels has remained controversial for over a decade as discussed in the introductory chapter. This apparent discordance in the regulatory function of the two channel families has led many to suspect a divergence, weakening, or even a loss of CI region function compared to that in $Ca^{2+}$ channels, thus thwarting the long-sought unification of the two channel families (Van Petegem et al., 2012).

In this chapter, we reconsider this notion of divergence in the $Ca^{2+}$ regulatory function between the two channel families. Through methods that enable rapid delivery of $Ca^{2+}$ to Na channels, namely $Ca^{2+}$ photouncaging or $Ca^{2+}$ influx through neighboring $Ca^{2+}$ channels, we propose core revisions to the Na channel $Ca^{2+}$ regulatory landscape. The bulk of current mechanistic inferences have been drawn from extensive studies of cardiac Na channels ($Na_V1.5$). Yet, under the arguably superior $Ca^{2+}$ delivery methods used here, there is no indication of $Ca^{2+}$ modulation in our experiments, either for recombinant $Na_V1.5$ channels or native Na currents in cardiac myocytes. By contrast, for prevalent skeletal-muscle Na channels ($Na_V1.4$), also reputed to host comparatively subtle $Ca^{2+}$ effects, we demonstrate fast and robust $Ca^{2+}$ regulation that bears an uncanny resemblance to the regulation of $Ca^{2+}$ channels.

## RESULTS

***Na channels lack apparent $Ca^{2+}$ regulation*** – Using current experimental approaches we first re-examined $Ca^{2+}$ regulation of the two best studied Na channels, the cardiac $Na_V1.5$ and the skeletal muscle $Na_V1.4$. For these channels, $Ca^{2+}$ is proposed to elicit a modest shift in the steady-state inactivation characteristics of the canonical fast-inactivation process (Deschenes et al., 2002; Wingo et al., 2004; Biswas et al., 2008; Potet et al., 2009; Sarhan et al., 2012; Van Petegem et al., 2012). The experimental paradigm used to quantify this effect was reviewed in Figure 1.9. Briefly, $h_\infty$ corresponds to the fraction of current remaining at a fixed test voltage ($V_{\text{test}}$) following long depolarization to a family of prepulse voltages ($V_{\text{hold}}$; Figure 1.9B, left subpanel). Plotting $h_\infty$ versus $V_{\text{hold}}$ then yields the steady-state inactivation relation ($h_\infty$ curve), as schematically diagrammed by the black curve in Figure 1.9B (right subpanel). Because Na channels do not flux $Ca^{2+}$, testing for $Ca^{2+}$ regulation requires comparison of normalized $h_\infty$ curves measured in cells statically dialyzed with a pipet solution containing ~0 μM $[Ca^{2+}]_{free}$, with those measured in other cells set to ~10 μM (Figure 1.9A). $Ca^{2+}$ elevation is thought to shift the voltage-dependence of $h_\infty$ curves by up to ~10 mV: rightward in the case of $Na_V1.5$ (Wingo et al., 2004; Shah et al., 2006; Biswas et al., 2009; Potet et al., 2009; Sarhan et al., 2012), and leftward for $Na_V1.4$ (Deschenes et al., 2002; Biswas et al., 2008) as schematized in Figure 1.9B.

A few important technical caveats merit attention. Nearly all prior studies of Na channel $Ca^{2+}$ regulation utilized either EGTA or BAPTA as $Ca^{2+}$ buffers to nominally set intracellular $[Ca^{2+}]$ between 1-10 μM (Tan et al., 2002; Wingo et al., 2004; Shah et al., 2006; Biswas et al., 2009; Potet et al., 2009; Sarhan et al., 2012). However, the dissociation constants of $Ca^{2+}$ binding for these buffers are an order of magnitude lower with $K_d$ = 67 nM for EGTA, and $K_d$ = 192 nM for BAPTA (Bers et al., 2010). In general, $Ca^{2+}$ buffering is most effective near the dissociation constant of the buffers as a substantial reserve of free buffer molecules could effectively chelate any stray $Ca^{2+}$ ions. An explicit simulation of $Ca^{2+}$ buffering is shown in Figure 3.2 for the three commonly used $Ca^{2+}$ buffers. To attain a 10 μM $[Ca^{2+}]_{free}$ internal solution, a nearly 1:1 mixture of $Ca^{2+}$ and EGTA or BAPTA is necessary. In this regime, nearly all buffer molecules are already bound to a $Ca^{2+}$ ion, and thus small pipetting errors or stray $Ca^{2+}$ ions from the experimental setting could amount to large fluctuations in $[Ca^{2+}]_{free}$. By contrast, HEDTA, with $K_d$ = 4 μM (Bers et al., 2010), is a more appropriate $Ca^{2+}$ buffer to maintain $Ca^{2+}$ in the 1- 10 μM range (Figure 3.2, red curve).

We therefore revisited the classical experiments of $Ca^{2+}$ regulation of Na channels probed using pipet dialysis of internal solution containing either 0 μM $[Ca^{2+}]_{free}$ buffered using BAPTA or 10 μM $[Ca^{2+}]_{free}$ buffered using HEDTA (Figure 3.3A). Figure 3.3B shows exemplar currents for $Na_V1.5$ channels expressed heterologously in HEK293 cells obtained using the two $Ca^{2+}$ buffering conditions. Surprisingly, population data in Figure 3.3C shows no significant difference in the $h_\infty$ curve measured with $[Ca^{2+}]$ ~0 μM ($V_{1/2}$ =

-72.3 ± 3 mV) versus that with [$Ca^{2+}$] ~10 μM ($V_{1/2}$ = -75.5 ± 1.2 mV). Similar experiments demonstrated no significant $Ca^{2+}$ effect for $Na_V1.4$ channels ($V_{1/2}$ = -62 ± 1.8 mV at [$Ca^{2+}$] ~0 μM; $V_{1/2}$ = -60.8 ± 0.8 mV at [$Ca^{2+}$] ~10 μM). Exemplar currents are shown in Figure 3.3D and population average for $h_\infty$ curve is shown in Figure 3.3E.

This unexpected lack of $Ca^{2+}$ regulation intensified the seeming deviation of $Ca^{2+}$ regulatory function in Na versus $Ca^{2+}$ channels. Curiously, closer inspection did reveal that $Ca^{2+}$ elevation in $Na_V1.4$ channels appeared to diminish test-pulse current density relating to the plateau of $h_\infty$ curves at very negative voltages, from -318 ± 98 pA/pF ($n$ = 11) to -189 ± 33 pA/pF ($n$ = 11). Thus, $Ca^{2+}$ might scale down a true, unnormalized $h_\infty$ curve (Figure 3.3E, red-dashed curve). By contrast, no corresponding trend was observed for $Na_V1.5$ channels (-474 ± 98 pA/pF at [$Ca^{2+}$] ~0 ($n$ = 6) versus -424 ± 60 pA/pF at [$Ca^{2+}$] ~10 μM ($n$ = 11)).

***Rapid uncaging of $Ca^{2+}$ unveils Na channel regulation*** – A core limitation of delivering $Ca^{2+}$ via pipet dialysis regards the uncertainty of detecting $Ca^{2+}$-induced changes in the Na current amplitude without corresponding voltage-dependent shifts. Current size may differ in one group of cells versus another for many reasons unrelated to $Ca^{2+}$. To obviate this limitation, we utilized rapid photouncaging of $Ca^{2+}$ to produce step-like increases in intracellular [$Ca^{2+}$], whose magnitude was simultaneously measured via $Ca^{2+}$ fluorescent indicators (Tadross et al., 2010). Figure 3.4 outlines this experimental scheme. Briefly, cells are dialyzed with a pipet solution containing caged-$Ca^{2+}$ molecules ($Ca^{2+}$-bound DM-Nitrophen). Na currents are recorded from cells under a whole-cell voltage-clamp protocol. $Ca^{2+}$ concentrations are simulataneously obtained based on fluorescent measurements of a known ratio of $Ca^{2+}$-sensitive dye Fluo-4FF and Alexa 568, a red dye. A brief but intense UV pulse is used to rapidly elevate cytosolic $Ca^{2+}$ concentrations (Figure 3.4B).

Figure 3.5A summarizes the outcome for $Na_V1.5$ channels. Na currents ($I_{Na}$) were evoked every 100 ms by the voltage-pulse train to 0 mV. Without $Ca^{2+}$ uncaging, peak currents remained steady (gray dots), confirming stability of the preparation. The ambient cytosolic $Ca^{2+}$ concentration is below 100 nM prior to $Ca^{2+}$-uncaging. Upon presentation of a UV flash (vertical cyan line), cytosolic $Ca^{2+}$ readily increases to ~10 μM in a step-like fashion. However, the peak Na currents remained unperturbed in the subsequent course of the black $I_{\mathrm{Na}}$ trace. Population data plotting steady-state current inhibition (*CDI*) versus $Ca^{2+}$ step amplitude yielded a relation at the zero level (bottom subpanel). This outcome corroborates a total lack of $Ca^{2+}$ regulation of recombinant $Na_V1.5$ in our experiments.

Even though recombinant $Na_V1.5$ channels failed to exhibit $Ca^{2+}$ regulation probed using $Ca^{2+}$-uncaging, it is still possible that native cardiac myocytes might furnish critical auxiliary factors. Indeed, other prominent ion channel regulatory mechanisms, such as beta-adrenergic response of $Ca^{2+}$ currents in the heart have been difficult to reconstitute in reduced preparations and often require a native system to observe robust functional effects (Miriyala et al., 2008). Thus, we performed $Ca^{2+}$ uncaging experiments in freshly isolated ventricular myocytes of adult guinea pigs, where $Na_V1.5$ channels convey the bulk of native Na current. Figure 3.5B shows exemplar currents obtained from ventricular myocytes. Fitting with our results from recombinant $Na_V1.5$ channels, a $Ca^{2+}$-step of ~ 8 mM in amplitude failed to evoke any alterations in peak Na current. Population data further substantiates a complete absence of $Ca^{2+}$-dependent effects on endogenous Na currents in ventricular myocytes.

To exclude subtle $Ca^{2+}$ dependent alterations in the kinetics of Na channel activation or inactivation, we further scrutinized the Na current waveforms obtained from recombinant $Na_V1.5$ channels heterologously expressed in HEK293 cells during $Ca^{2+}$ uncaging experiments. Figure 3.5C left subpanel (black trace) shows typical rapidly activating and inactivating Na currents in response to a step depolarization to 0 mV prior to $Ca^{2+}$ uncaging. Reassuringly, the kinetics of both channel activation and inactivation are unperturbed following $Ca^{2+}$ uncaging (Figure 3.5C, right subpanel). Importantly, the resting potential during the train of step depolarizations were held at -90 mV, a voltage just beyond the saturating phase of their $h_\infty$ curve. Accordingly, a small fraction of channels are pre-inactivated, and thus the peak Na current should be sensitive to subtle shifts in the voltage-dependence of $h_\infty$ curves. Together, these results stand in contrast to prior proposals of $Ca^{2+}$ regulation of $Na_V1.5$ channels, and argue for a complete lack of $Ca^{2+}$ regulation of $Na_V1.5$ channels in both recombinant and native settings.

On the other hand, $Ca^{2+}$ uncaging experiments on $Na_V1.4$ channels afforded a very different outcome (Figure 3.6). Here, Na currents were evoked every 50 ms by a voltage-pulse train to 0 mV. The accelerated recovery from inactivation observed for these channels permitted the usage of a faster pacing rate, and further allows for the characterization of any $Ca^{2+}$-dependent effect with a higher temporal resolution. As with $Na_V1.5$ channels, the peak currents prior to $Ca^{2+}$ uncaging remained steady (Figure 3.6A, gray dots and fit). Here, however, $Ca^{2+}$ uncaging to ~2 μM was sufficient to elicit a rapid inhibition of peak Na currents during the pulse train (black $I_{Na}$ trace). The timecourse of development for this effect follows the red envelope relation and spanned ~100 ms (rose curve). Population data showed a robust maximal *CDI* reaching ~0.35, with a half-maximal effect achieved at a $K_{1/2}$ ~1.5 μM. The overall *CDI* –$[Ca^{2+}]$ relation defines a Hill function with steepness coefficient ~1.8 (black curve, bottom subpanel). This steepness coefficient suggests that two $Ca^{2+}$ ions cooperatively induces this channel regulation. The $Ca^{2+}$ responsiveness of $Na_V1.4$ CDI is similar in magnitude to that observed with $Ca^{2+}$ regulation of $Ca_V1.2$ and $Ca_V1.3$ channels (Dick et al., 2012; Tadross et al., 2013). Indeed, this decrement of current upon $Ca^{2+}$ uncaging defines a novel $Ca^{2+}$-dependent inactivation (CDI) of Na channels, with timecourse similar to that observed in $Ca^{2+}$ channels (compare rose curve in Figure 3.6A with Figure 3.1C).

We next turned to skeletal myotubes to test for $Ca^{2+}$ regulation of native $Na_V1.4$ channels. Accordingly, we undertook whole-cell voltage-clamp of GLT cells derived from dysgenic mouse skeletal myotubes, a well-established system to study cellular correlates of skeletal muscle biology (Powell et al., 1996). Figure 3.6B illustrates exemplar Na currents from these cells. In the absence of $Ca^{2+}$ uncaging, the peak Na current remains steady (gray dots) and the cytosolic $Ca^{2+}$ is below 100 nM. In response to a $Ca^{2+}$ step of ~ 10 μM in amplitude, the peak Na current declines robustly (Figure 3.6B). Population data substantiates the presence of Ca2+-regulation of native Na currents in skeletal muscle. Importantly, the native Na currents appear to require larger amplitude $Ca^{2+}$ steps to achieve half-maximal CDI. Nonetheless, this $Ca^{2+}$ sensitivity is easily spanned by physiological $Ca^{2+}$ transients (Hollingworth et al., 2012). This result perhaps represents the first direct demonstration of $Ca^{2+}$ regulation of endogenous Na currents.

Finally, to explore any potential $Ca^{2+}$ dependent effects on the kinetics of Na channel activation and inactivation, we carefully analyzed the Na current waveforms (Figure 3.6A) obtained before $Ca^{2+}$-uncaging and after reaching steady-state $Ca^{2+}$ effect. Figure 3.6C shows Na current waveforms on an expanded time base to facilitate comparison of channel activation and inactivation. Upon $Ca^{2+}$ uncaging, the peak Na current declines ~ 30%. However, normalized current after $Ca^{2+}$ uncaging shows that the kinetics of channel activation and inactivation are unperturbed by $Ca^{2+}$. Thus, the effect of $Ca^{2+}$ on the Na channel appears to be a simple reduction in the peak amplitude without any overt changes in the voltage-dependent activation and inactivation processes. These results substantiate the presence of a rapid and robust $Ca^{2+}$ regulation of Na channels that bears some likeness to the well-established $Ca^{2+}$ regulation of $Ca^{2+}$ channels. The biophysical properties of this novel CDI of Na channels will be considered at length in Chapter 4.

***Na channel regulation by $Ca^{2+}$ spillover from $Ca^{2+}$ channels*** – We next sought to induce $Ca^{2+}$ regulation of Na channels by a more physiological $Ca^{2+}$ delivery method. This maneuver would allow us to exclude unsuspected photouncaging effects that might artifactually produce the results in Figure 3.5-3.6, and also sets the stage to permit the observation of $Ca^{2+}$ regulation at the level of single Na channel molecules, impractical in the electrical environment of photouncaging equipment.

In many physiological systems, the voltage-gated $Ca^{2+}$ channels convey $Ca^{2+}$ influx that triggers ensuing $Ca^{2+}$ signaling in cells. Accordingly, $Na_V1.4$ and $Ca_V2.1$ $Ca^{2+}$ channels were coexpressed within the same cells, to test whether $Ca^{2+}$ spillover from a $Ca^{2+}$ channel source could inhibit nearby Na channels (Figure 3.7A). In this experimental scheme, a low intracellular $Ca^{2+}$ buffering that mimics physiological buffering is utilized to enable robust $Ca^{2+}$ spillover near the Na channels. Moreover, owing to the higher threshold of voltage activation for $Ca_V2.1$ versus $Na_V1.4$ channels, Na current alone could be evoked by modest depolarizations to 0 mV (Figure 3.7B-C), which bookend the voltage pulse protocol shown in Figure 3.8B. Indeed, only minimal $Ca_V2.1$ current is activated at this voltage, permitting the robust resolution of Na current (Figure 3.7C). Na currents ($I_{Na}$) evoked in this manner have the same magnitude (Figure 3.8B). By contrast, insertion of an intervening 30-mV pulse activates $Ca^{2+}$ currents, as shown by the red shading in Figure 3.8C. Importantly, the second Na current response was then substantially diminished, as if $Ca^{2+}$ influx through adjacent $Ca^{2+}$ channels triggered Na channel CDI (Figure 3.8C). To exclude voltage-dependent inhibition as the cause of a diminished second response, the intervening voltage pulse was further increased to the $Ca^{2+}$ channel reversal potential (~90 mV), where negligible $Ca^{2+}$ entry would occur. Reassuringly, the second Na response appeared identical to the first (Figure 3.8D), arguing that the reduction of Na current above (Figure 3.8C) was due to $Ca^{2+}$ influx, and not voltage itself. Analyzing population data for the fraction of current remaining in the second versus first Na responses ($r_{Na}$ in Figure 3.8C) confirmed a U-shaped dependence of CDI on intervening pulse potential (Figure 3G, red). Additionally, we examined the effects of substituting $Ba^{2+}$ for $Ca^{2+}$ as a charge carrier through $Ca^{2+}$ channels. Since $Ba^{2+}$ binds poorly to CaM (Chao et al., 1984), we expected Na channel CDI to disappear (Figure 3.8A, right subpanel), as confirmed experimentally in Figures 3.8E-G (black).

These experiments further corroborate the existence of rapid CDI of Na channels that could be evoked in a matter of milliseconds.

Moreover, in this mode of rapid $Ca^{2+}$ delivery, restricting $Ca^{2+}$ elevations to the Na channel nanodomain should abolish any residual $Ca^{2+}$ spillover and thereby prevent regulation of $Na_V1.4$ current. Accordingly, we repeated the experimental protocol utilized in Figure 3.8 with the exception of now adding 10 mM BAPTA to the dialysate to prevent any $Ca^{2+}$ spillover from $Ca^{2+}$ channels. Remarkably, this maneuver abolished the robust decrement in peak Na current observed following $Ca^{2+}$ influx through $Ca^{2+}$ channels (compare Figure 3.9B to Figure 3.8B). Not surprisingly, $Ba^{2+}$ influx through the $Ca_V2.1$ channel does not alter peak Na currents. Population data confirms the absence of $Na_V1.4$ CDI upon eliminating $Ca^{2+}$ spillover from $Ca^{2+}$ channels. These results highlight the dependence of Na channel CDI on $Ca^{2+}$, and illustrate how physiological $Ca^{2+}$ sources could potently regulate Na channel activity.

Lastly, to confirm the absence of rapid $Ca^{2+}$-regulation of $Na_V1.5$ channels observed using $Ca^{2+}$ photouncaging, we explored whether local $Ca^{2+}$ spillover from $Ca^{2+}$ channels could alter $Na_V1.5$ current. Reassuringly, the $Na_V1.5$ peak current amplitudes were unperturbed despite robust $Ca^{2+}$ influx through $Ca^{2+}$ channels (Figure 3.10). Thus, the $Na_V1.5$ currents appear to be not regulated by $Ca^{2+}$ ions even with the physiologically-inspired mode of $Ca^{2+}$ delivery by spillover from $Ca^{2+}$ channels.

Nevertheless, it is notable that the whole-cell functional profile for Na channel CDI, as manifest in $Na_V1.4$ (Figure 3.8G, both $Ca^{2+}$ and $Ba^{2+}$ relations) resembles that for $Ca^{2+}$ channels (Figure 3.1C) and recapitulates the classic engram of native $Ca^{2+}$ regulation of $Ca^{2+}$ channels historically established by Eckert and colleagues (Eckert and Chad, 1984b).

## DISCUSSION

Through novel approaches that enable rapid and quantitative $Ca^{2+}$ delivery to Na channels (photouncaging of $Ca^{2+}$, and $Ca^{2+}$ spillover from neighboring $Ca^{2+}$ channels), this work goes far in resetting the current understanding of $Ca^{2+}$ regulation of Na channels. First, most mechanistic deductions in the field have been derived from observations on recombinant cardiac Na channels ($Na_V1.5$), and these deductions have argued that $Ca^{2+}$ regulation of Na channels differs fundamentally from that in $Ca^{2+}$ channels (Van Petegem et al., 2012). However, by using arguably enhanced modes of $Ca^{2+}$-delivery to Na channels, our experiments argue for the absence of $Ca^{2+}$ modulation of either recombinant $Na_V1.5$ channels, or their native counterparts in cardiac ventricular myocytes. This surprising finding poses important questions about prior structure-function relations (Tan et al., 2002; Wingo et al., 2004; Shah et al., 2006; Biswas et al., 2009; Potet et al., 2009; Sarhan et al., 2012), and may require core revisions to the current understanding of $Ca^{2+}$ regulation in Na channels. For the skeletal-muscle $Na_V1.4$ channels, the very existence and the underlying mechanism of $Ca^{2+}$ regulation has been debated in the past. Here, our experiments that utilize rapid $Ca^{2+}$ delivery instead unveils a fast and unambiguous $Ca^{2+}$ regulation of $Na_V1.4$ channels, characterized with quantitative precision. This regulation could be readily evoked using physiological $Ca^{2+}$ concentrations, suggesting that this regulatory mechanism may be biological critical as an activity dependent control of cellular excitability. To our knowledge, the direct demonstration of $Ca^{2+}$ regulation of endogenous $Na_V1.4$ current in skeletal myotubes may be the first quantitative characterization of its kind in any native system. The biophysical properties and structural underpinnings of this novel form of ion channel regulation will be elaborated in Chapters 4 and 5.

Importantly, our present study failed to substantiate $Ca^{2+}$-dependent effects on the voltage-dependence of Na channel steady-state inactivation curves (i.e., $h_\infty$ curves) upon which prior postulates of Na channel regulation have been based. It is important to consider potential differences in that experimental conditions that could explain these differences. One important difference as explained earlier is the usage of internal solutions containing EGTA and BAPTA to nominally buffer free $Ca^{2+}$ concentrations at levels substantially higher than the dissociation constants for these compounds. If the actual $Ca^{2+}$ concentrations in these solutions were to exceed 10 μM, it would be difficult to undertake whole-cell patch clamp, so it is understandable that many of these studies have resorted to intracellular solutions containing CsF. Fluoride anions, though facilitates electrical recording, indiscriminately activates G-protein signaling (Helmchen et al., 1996), among numerous other effects (Van Petegem et al., 2012). Moreover, before measurements are taken, time-dependent voltage shifts in $h_\infty$ curves are typically allowed to equilibrate following the onset of whole-cell pipet dialysis (Biswas et al., 2009), and it is conceivable that ambiguities as to actual equilibration may contribute to conflicts among prior reports. To overcome these ambiguities, we will reconsider the issue of $Ca^{2+}$-induced shifts in steady-state inactivation of $Na_V1.4$ channels in Chapter 4 using rapid photouncaging of $Ca^{2+}$ with simultaneous readouts of $Ca^{2+}$. Nonetheless, these results about voltage shifts in $h_\infty$ relations merits continued attention, and will require further scrutiny by other laboratories in the field.

More excitingly, the methods are now at hand to undertake a new era of discovery regarding potential $Ca^{2+}$ regulation of the many other Na channel isoforms ($Na_V1.1$-$Na_V1.9$). These channels are critical for the generation and propagation of action potentials in the central and peripheral nervous system, and many other excitable cells. Moreover, numerous channelopathic mutations have been identified on the conserved carboxy-terminus of these channels that result in a wide-range of disorders including autism and epileptic disorders (Lossin, 2009; Catterall et al., 2010). Accordingly, it is likely that the carboxy-terminus of these channels may elaborate powerful CaM regulatory effects yet to be fully substantiated, and presents an exciting avenue for future research.

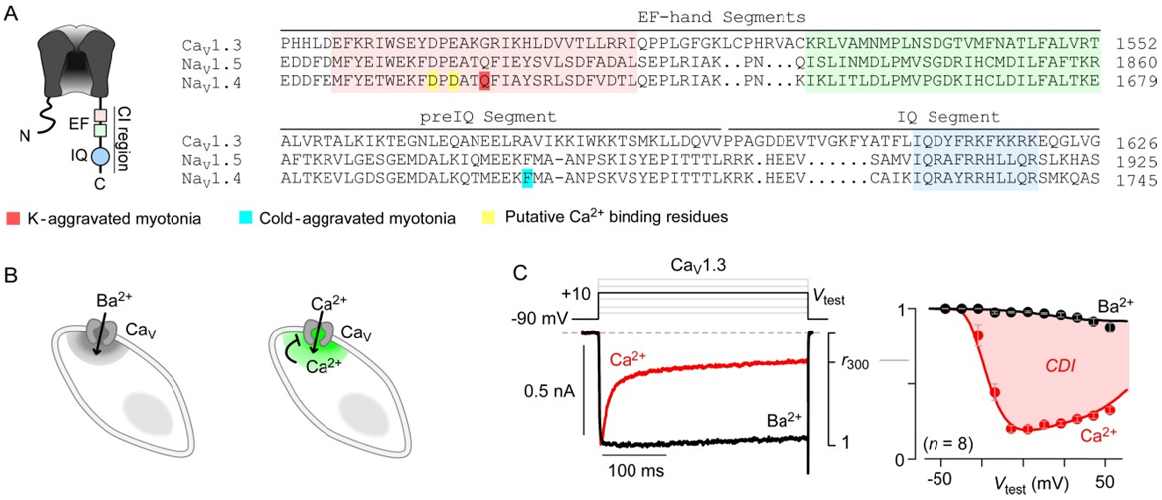

## Figure 3.1. A conserved carboxy-tail of $Ca^{2+}$ and Na channels.

(A) Left, channel cartoon depicting overall arrangement of $Ca^{2+}$ and Na channel segments critical for $Ca^{2+}$ regulation. The CI region ($Ca^{2+}$-inactivating region) on the carboxy-terminus of both channel families contain two vestigial EF hand segments (rose and green) and an IQ domain (blue). Right, sequence alignment of $Ca^{2+}$ and Na channel CI segment.

(B) $Ca^{2+}$ regulation of $Ca^{2+}$ channels is conveniently triggered by $Ca^{2+}$ influx through the channel. Substitution of $Ba^{2+}$ as permeant ion through the channel serves as a powerful negative control.

(C) Functional signature of $Ca^{2+}$ regulation of $Ca_V1.3$ channels. Left, exemplar $Ca_V1.3$ currents shows inhibition of $Ca^{2+}$ versus $Ba^{2+}$ traces termed $Ca^{2+}$-dependent inactivation (CDI). Right, population average for $r_{300}$, fraction of peak current remaining after 300-ms depolarization in $Ba^{2+}$ (black) and $Ca^{2+}$ (red). Each symbol represents mean ± SEM from 8 cells. Red shaded area corresponds to CDI. The U-shaped dependence of CDI on voltage is a signature of $Ca^{2+}$-dependent regulation.

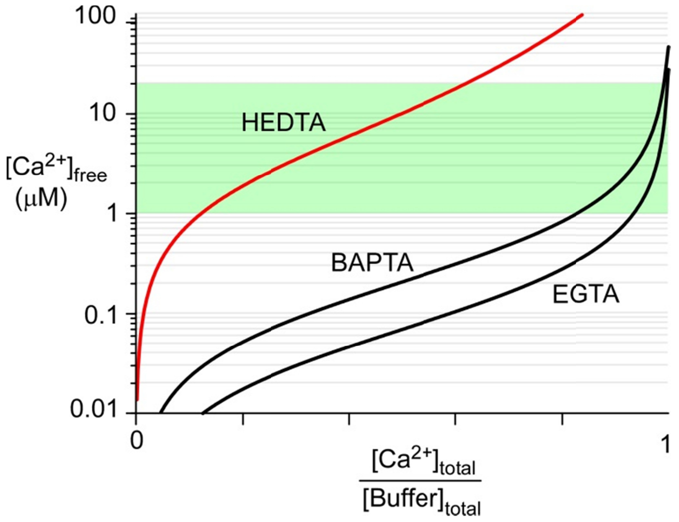

**Figure 3.2. Simulation of free Ca$^{2+}$ attained using various Ca$^{2+}$ buffers.**

Computational simulation of Ca$^{2+}$ buffering using EGTA, BAPTA, and HEDTA as buffers. The free [Ca$^{2+}$] concentration is plotted against the ratio of total Ca$^{2+}$ to total buffer ($[Ca^{2+}]_{total}$ / $[Buffer]_{total}$), with $[Buffer]_{total}$ = 10 mM. In general, a buffer is most effective at maintaining free Ca$^{2+}$ concentrations near its Ca$^{2+}$ dissociation constant. Thus, EGTA and BAPTA (black lines) having $K_d$ = 67 nM and 192 nM respectively, are effective at buffering Ca$^{2+}$ in the 30–600 nM concentration range, but become ineffective at higher Ca$^{2+}$ concentrations. For instance, to attain $[Ca^{2+}]_{free}$ ~10 μM with these buffers, $[Ca^{2+}]_{total}$ must approximately equal $[Buffer]_{total}$. In this regime, most buffer molecules are bound to a Ca$^{2+}$ ion and, therefore, any excess contaminant ions will be unbuffered. Thus, small pipeting errors and stray Ca$^{2+}$ ions from the experimental setting could amount to large fluctuations of $[Ca^{2+}]_{free}$ in the solution. By contrast, HEDTA (red line) with $K_d$ = 4 μM is an ideal buffer to clamp $[Ca^{2+}]_{free}$ in the 1–20 μM range. This simulation accounts for the precise experimental conditions used (10 mM HEDTA, 4 mM ATP, 5 mM Mg$^{2+}$). So with HEDTA as buffer, $[Ca^{2+}]_{free}$ can be effectively maintained near ~10 μM.

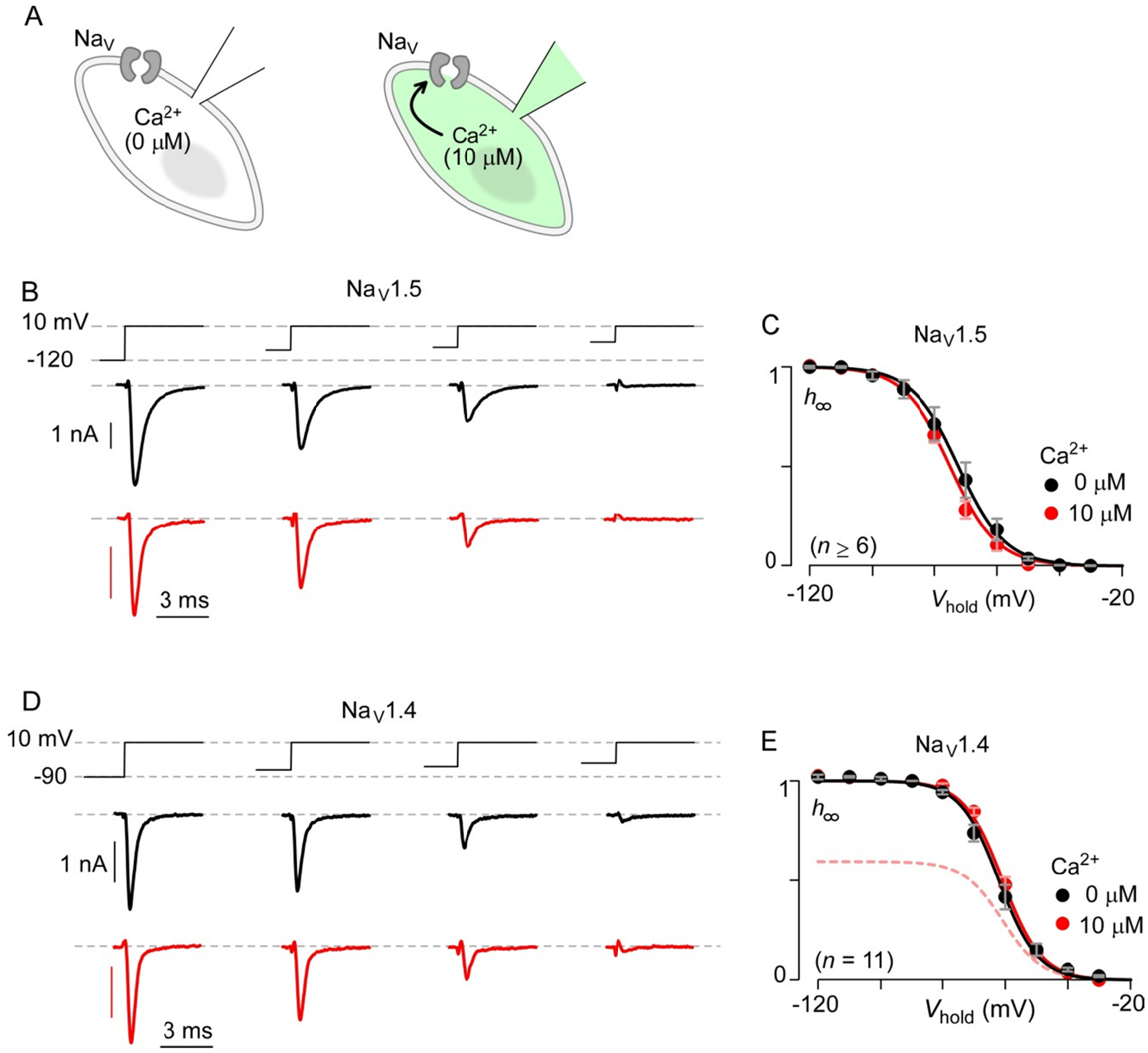
A
Na$_V$
Ca$^{2+}$
(0 μM)
Na$_V$
Ca$^{2+}$
(10 μM)
B
Na$_V$1.5
10 mV
-120
1 nA
3 ms
C
Na$_V$1.5
1
$h_\infty$
Ca$^{2+}$
0 μM
10 μM
($n \geq 6$)
0
-120
$V_{hold}$ (mV)
-20
D
Na$_V$1.4
10 mV
-90
1 nA
3 ms
E
Na$_V$1.4
1
$h_\infty$
Ca$^{2+}$
0 μM
10 μM
($n$ = 11)
0
-120
$V_{hold}$ (mV)
-20

**Figure 3.3. No $Ca^{2+}$-effect of Na channels as determined by static pipet dialysis.**

(A) $Ca^{2+}$ regulation of Na channels probed using pipet dialysis of internal solution containing either 0 μM $Ca^{2+}$ or 10 μM $Ca^{2+}$ appropriately buffered.

(B) Exemplar $Na_V1.5$ currents evoked using steady-state inactivation protocol (Figure 1.9B) with 0 μM (black) or 10 μM internal [$Ca^{2+}$] (red). The 0 μM internal [$Ca^{2+}$] solution was buffered using BAPTA, while the 10 μM internal [$Ca^{2+}$] solution was buffered using HEDTA as shown in Figure 3.2. The fractional current remaining appears similar in both conditions.

(C) Population data shows no significant shift in the voltage-dependence of $h_\infty$ curve for $Na_V1.5$ between 0 μM (black) or 10 μM (red) internal [$Ca^{2+}$] conditions.

(D) Exemplar $Na_V1.4$ currents evoked using steady-state inactivation protocol with 0 μM (black) or 10 μM internal [$Ca^{2+}$] (red). The fractional peak currents remain the same under both conditions.

(E) No significant $Ca^{2+}$-induced shift in $h_\infty$ curve for $Na_V1.4$ as evident from population data. That said, the peak Na currents appeared to ~40% smaller on average with 10 μM [$Ca^{2+}$] than with 0 μM [$Ca^{2+}$]. This reduction in overall current amplitude is depicted as a scaling down of steady-state inactivation curve (red dashed line).

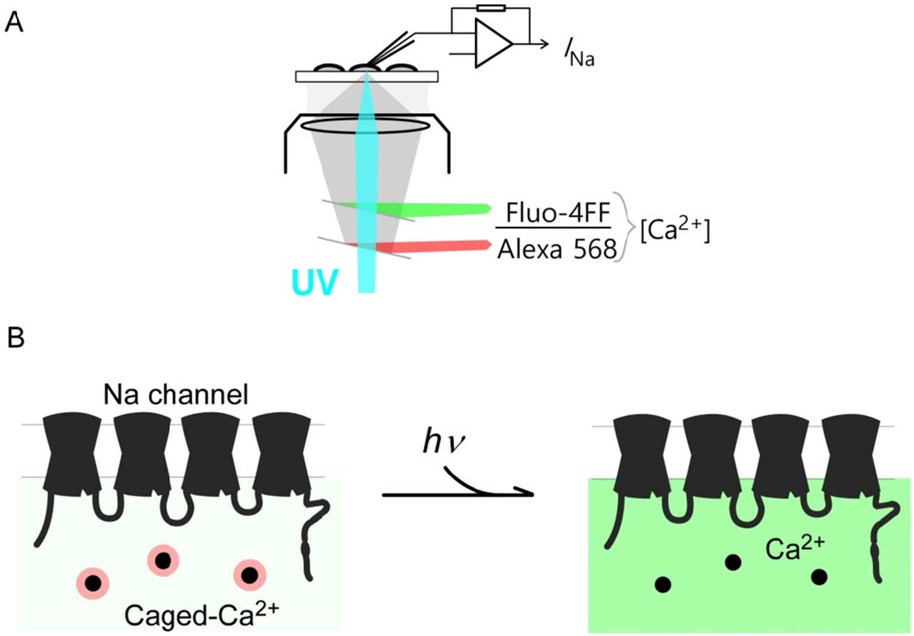

**Figure 3.4. Ca$^{2+}$ photouncaging as a method for rapid Ca$^{2+}$ delivery.**

(A) Schematic depicts experimental setup for quantitative patch fluorimetry and Ca$^{2+}$-photouncaging. Na currents are recorded from cells under voltage-clamp. Intracellular [Ca$^{2+}$] concentrations are determined from ratiometric fluorescence measurements of Ca$^{2+}$-sensitive Fluo-4FF and a known concentration of the red dye Alexa 568.

(B) Caged-Ca$^{2+}$ molecules are delivered into the cell through pipet dialysis. A brief but strong UV pulse is used to rapidly uncage Ca$^{2+}$ at will. Effects on Na current are probed simultaneously.

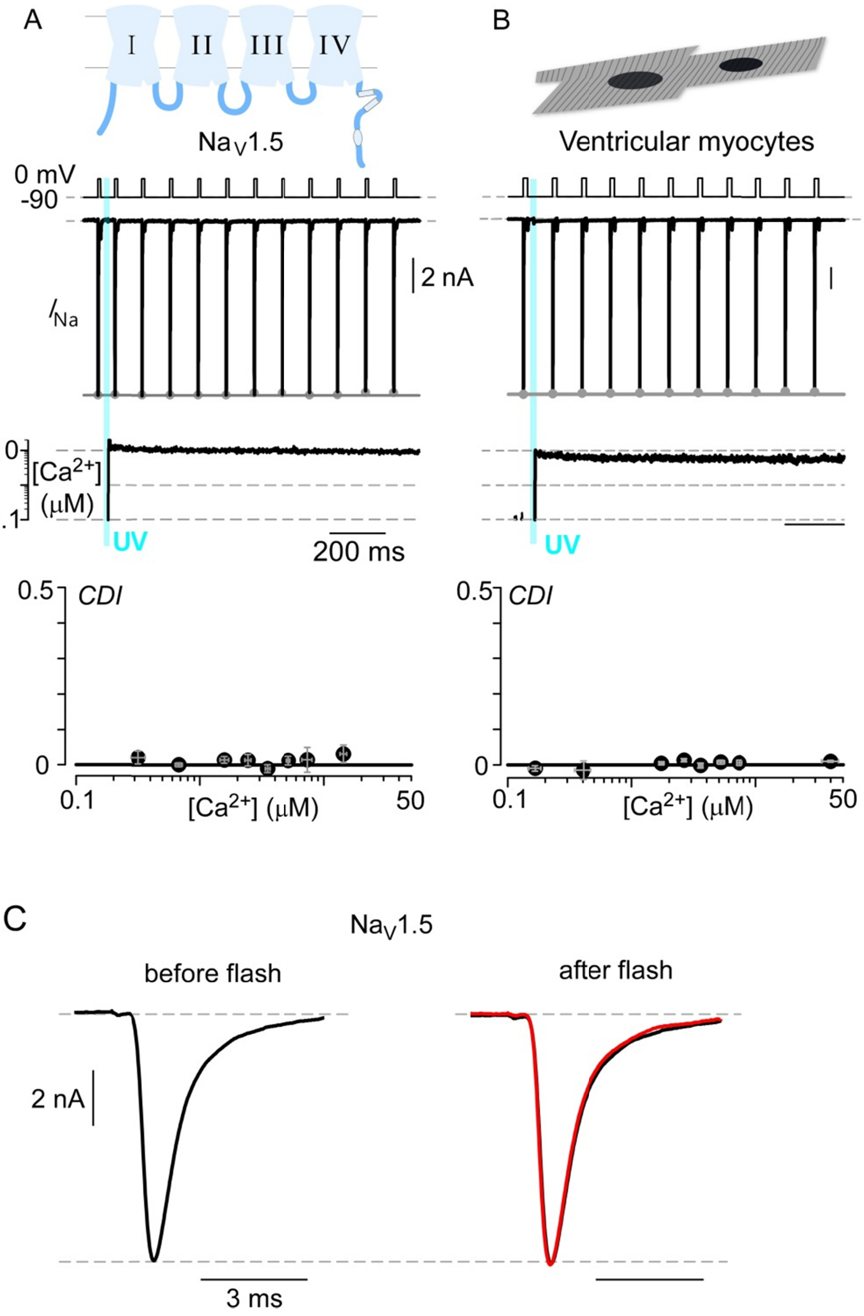
A
I
II
III
IV
NaV1.5
B
Ventricular myocytes
0 mV
-90
2 nA
INa
10
[Ca2+]
(μM)
0.1
UV
200 ms
UV
0.5
CDI
0
0.1
[Ca2+] (μM)
50
0.5
CDI
0
0.1
[Ca2+] (μM)
50
C
NaV1.5
before flash
after flash
2 nA
3 ms

**Figure 3.5. $Ca^{2+}$ regulation absent in cardiac $Na_V1.5$ channels.**

(A) $Ca^{2+}$ regulation is absent in recombinant $Na_V1.5$ channels expressed in HEK293 cells. Top, channel cartoon depicts $Na_V1.5$ channel overall structure. Middle, exemplar $Na_V1.5$ currents unperturbed by ~10 μM $Ca^{2+}$ step. A train of step depolarizations was used to evoke Na current. $Ca^{2+}$ measurements were obtained simultaneously. Gray dots, peak currents before uncaging. Bottom, population data for *CDI* versus $Ca^{2+}$-step amplitude. *CDI* = 1 – average peak $I_{Na}$ of last 3-4 responses after $Ca^{2+}$ uncaging / peak $I_{Na}$ before uncaging. Each symbol represents mean ± SEM of approximately 5 uncaging events compiled from 35 cells.

(B) $Ca^{2+}$ regulation is absent for native $Na_V1.5$ that predominates in adult guinea pig ventricular myocytes. Format as in Panel A. Each symbol, mean ± SEM from 5-6 uncaging events compiled from 13 cells.

(C) To probe whether $Ca^{2+}$ alters the kinetics of Na channel activation and inactivation, we scrutinized the current waveform from recombinant $Na_V1.5$ channels expressed in HEK293 cells obtained from protocols analogous to those in panel A. Left, Na current obtained prior to $Ca^{2+}$ uncaging. Right, current evoked 900 ms after the onset of $Ca^{2+}$ elevation (red trace) overlaid on the waveform before uncaging (black trace underneath, copied from left subpanel). Remarkably, the traces overlay suggesting that $Ca^{2+}$ has no effect on the $Na_V1.5$ current waveform morphology. The current traces are plotted on an expanded time-base to facilitate comparison of both kinetics of activation and inactivation.

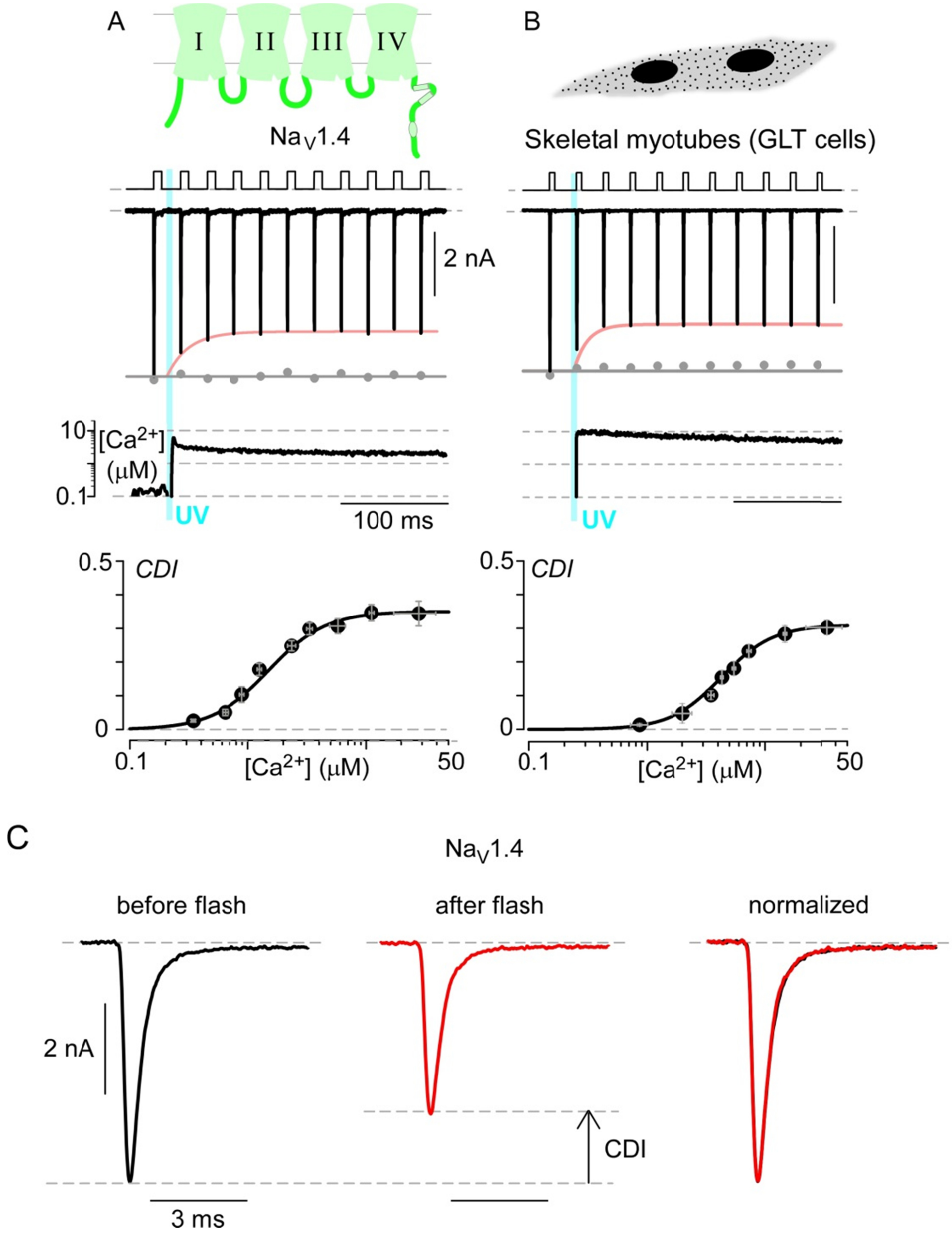
A
I
II
III
IV
NaV1.4
2 nA
10
[Ca2+]
(μM)
0.1
UV
100 ms
0.5
CDI
0
0.1
[Ca2+] (μM)
50
B
Skeletal myotubes (GLT cells)
UV
0.5
CDI
0
0.1
[Ca2+] (μM)
50
C
NaV1.4
before flash
after flash
normalized
2 nA
CDI
3 ms

**Figure 3.6. $Ca^{2+}$-dependent inactivation of skeletal muscle $Na_V1.4$ channels.**

(A) A novel $Ca^{2+}$-dependent inactivation of recombinant $Na_V1.4$ expressed in HEK293 cells unveiled by $Ca^{2+}$-photouncaging. Top, channel cartoon shows overall arrangement of $Na_V1.4$ channels. Middle, exemplar $Na_V1.4$ currents show robust decrement in peak current amplitude in response to a ~2 μM $Ca^{2+}$ step. A train of step depolarizations was used to evoke Na current. $Ca^{2+}$ measurements were obtained simultaneously. By contrast, peak Na currents before uncaging remain steady confirming the stability of the preparation (gray dots). Population data shows average *CDI* as a function of the amplitude of $Ca^{2+}$ step that triggered it. This relation follows a hill function with steepness coefficient of ~1.8 and half response observed with a $Ca^{2+}$ step of ~ 1.5 μM. Each symbol represents mean ± SEM of approximately 5 uncaging events compiled from 23 cells.

(B) Robust $Ca^{2+}$ regulation was also observed for native $Na_V1.4$ currents recorded from mouse skeletal myotubes (GLT cells). Format as in Panel A. Note that a small contaminant $Ca^{2+}$-activated Cl current (<5% of $I_{Na}$) was subtracted. The population data shows average *CDI* as a function of $Ca^{2+}$. Each symbol, mean ± SEM from 5-6 uncaging events compiled from 13 cells. Note that the $Ca^{2+}$-responsiveness is subtly weaker in the native system compared to recombinant channels. This difference may be advantageous as $Ca^{2+}$ transients in the mouse skeletal myotubes may exceed 10 μM in amplitude (Hollingworth et al., 2012).

(C) Left, $Na_V1.4$ current before $Ca^{2+}$ uncaging (Pulse #1 Panel A). Middle, Na current amplitude after $Ca^{2+}$ uncaging (pulse #11 obtain after ~450 ms after $Ca^{2+}$ uncaging) is reduced by ~30%. Right, normalized current after uncaging shows unperturbed activation and inactivation kinetics in presence of $Ca^{2+}$ (red trace after uncaging plotted on top of black trace before uncaging).

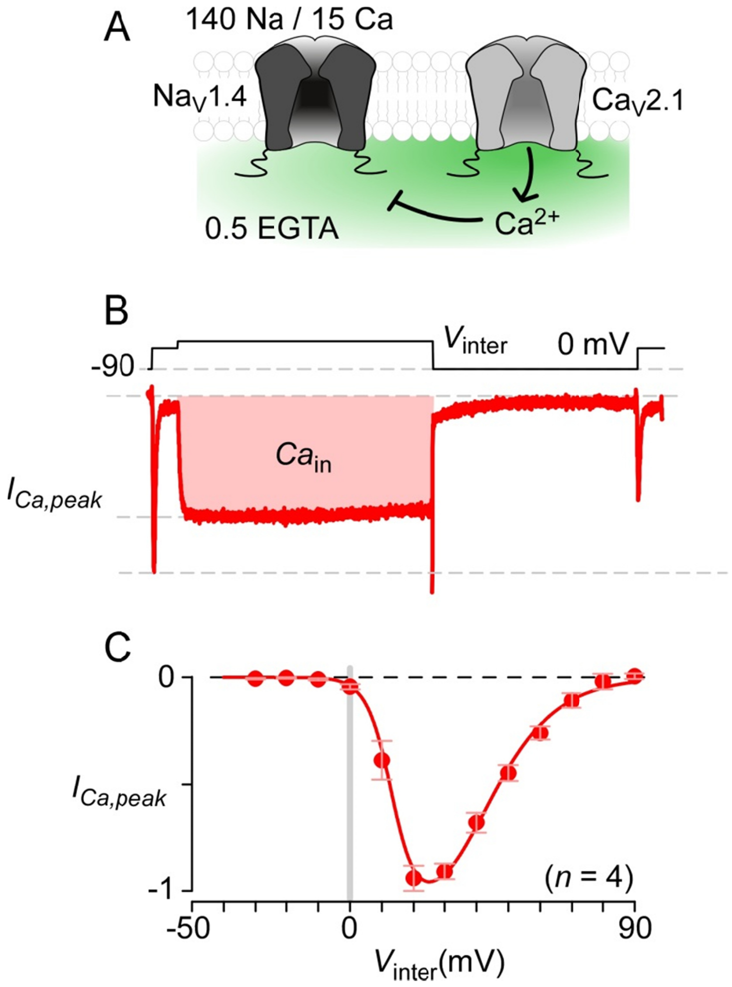
A
140 Na / 15 Ca
$Na_V1.4$
$Ca_V2.1$
0.5 EGTA
$Ca^{2+}$
B
-90
$V_{inter}$
0 mV
$Ca_{in}$
$I_{Ca,peak}$
C
0
$I_{Ca,peak}$
-1
(n = 4)
-50
0
90
$V_{inter}$(mV)

**Figure 3.7. Na channel regulation by $Ca^{2+}$ spillover from $Ca^{2+}$ channels.**

(A) In native systems, $Ca^{2+}$ channels constitute a primary source for $Ca^{2+}$ influx. Could $Ca^{2+}$ entry through such sources trigger Na channel regulation? As such, we coexpress $Na_V1.4$ channels with $Ca_V2.1$ channels, chosen deliberately for their higher threshold for voltage activation that enables selective measurement of Na currents at lower voltages. The schematic illustrates this experimental paradigm where $Ca^{2+}$ spillover from $Ca^{2+}$ channels is used to drive $Na_V1.4$ CDI.

(B) Top, stimulus protocol used to probe $Na_V1.4$ CDI. An initial depolarizing pulse to 0 mV was used to evoke Na current. Immediately following, a family of voltage pulses ($V_{\text{inter}}$) was applied to activate $Ca^{2+}$ currents. As Na channels undergo fast inactivation, the peak current measured during the intervening pulse ($V_{\text{inter}}$) represents the peak $Ca^{2+}$ current at a given voltage ($I_{\text{Ca,peak}}$).

(C) Peak $Ca^{2+}$ current measured during the intervening pulse is plotted against corresponding $V_{\text{inter}}$ to obtain the $Ca_V2.1$ current–voltage relations. At 0 mV, $Ca^{2+}$ channels are minimally activated (<5%), thus permitting activation of Na current alone. Each symbol, mean ± SEM from 4 cells.

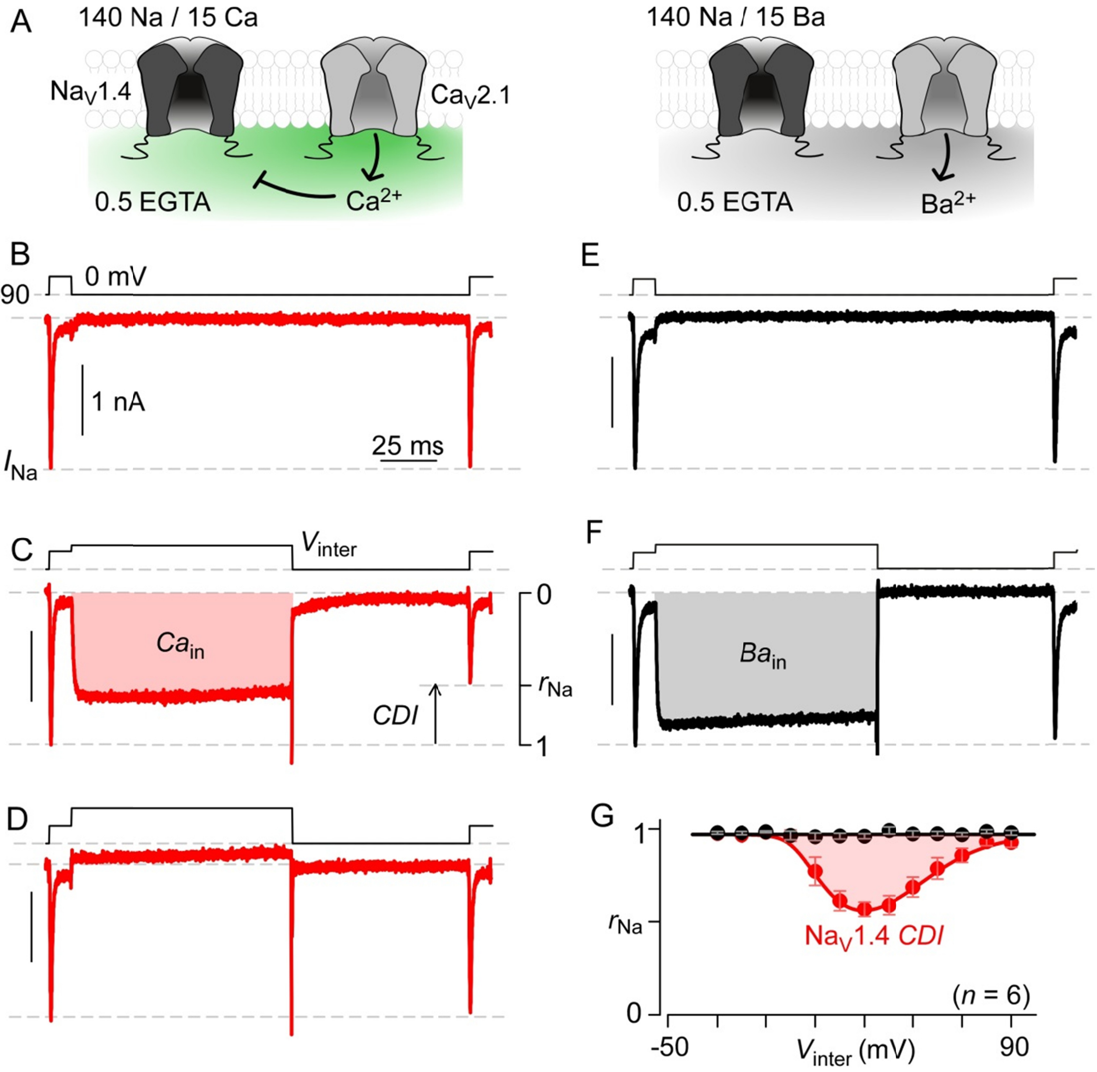
A
140 Na / 15 Ca
Na$_V$1.4
Ca$_V$2.1
0.5 EGTA
Ca$^{2+}$
140 Na / 15 Ba
0.5 EGTA
Ba$^{2+}$
B
0 mV
-90
1 nA
25 ms
$I_{Na}$
E
C
$V_{inter}$
$Ca_{in}$
0
$r_{Na}$
CDI
1
F
$Ba_{in}$
D
G
1
$r_{Na}$
Na$_V$1.4 CDI
(n = 6)
0
-50
$V_{inter}$ (mV)
90

**Figure 3.8. Na$_V$1.4 channel regulation by Ca$^{2+}$ spillover from Ca$^{2+}$ channels.**

(A) Schematic shows local Ca$^{2+}$ spillover from Ca$_V$2.1 inhibiting nearby Na channels. Low intracellular Ca$^{2+}$ buffering that mimics physiological conditions is used for these experiments. Na current is selectively evoked using a low-voltage step depolarization while Ca$^{2+}$ current is elicited using a higher voltage pulse. Substitution of Ba$^{2+}$ as the permeant ion through the Ca$^{2+}$ channel will abolish this regulation.

(B) Dual voltage-pulses to 0 mV selectively evoke identical Na$_V$1.4 currents.

(C) Intervening +30 mV pulse ($V_{\text{inter}}$) activates Ca$_V$2.1 channels conferring Ca$^{2+}$ influx. This cytosolic elevation in Ca$^{2+}$ diminishes subsequent Na current. $r_{\text{Na}}$ measures the fraction of Na current remaining following Ca$^{2+}$ influx through Ca$_V$2.1 channels.

(D) Increasing $V_{\text{inter}}$ to +90 mV, near the reversal potential of Ca$^{2+}$ current, abolishes Ca$^{2+}$ influx despite Ca$^{2+}$ channel opening. The second Na$_V$1.4 current is, however, rescued.

(E and F) Ba$^{2+}$ through Ca$_V$2.1 does not trigger *CDI*. Na current amplitude is unperturbed by Ba$^{2+}$ influx through Ca$_V$2.1 channels, irrespective of $V_{\text{inter}}$.

(G) Population average demonstrates U-shaped dependence of Na$_V$1.4 *CDI* on $V_{\text{inter}}$ (red symbols and fit with Ca$^{2+}$ as permeant ion through Ca$_V$2.1), reflecting parallel results for Ca$^{2+}$ channels in Figure 3.1C. Each symbol, Mean ± SEM from 6 cells. Black, Ba$^{2+}$ as charge carrier for Ca$_V$2.1 channels.

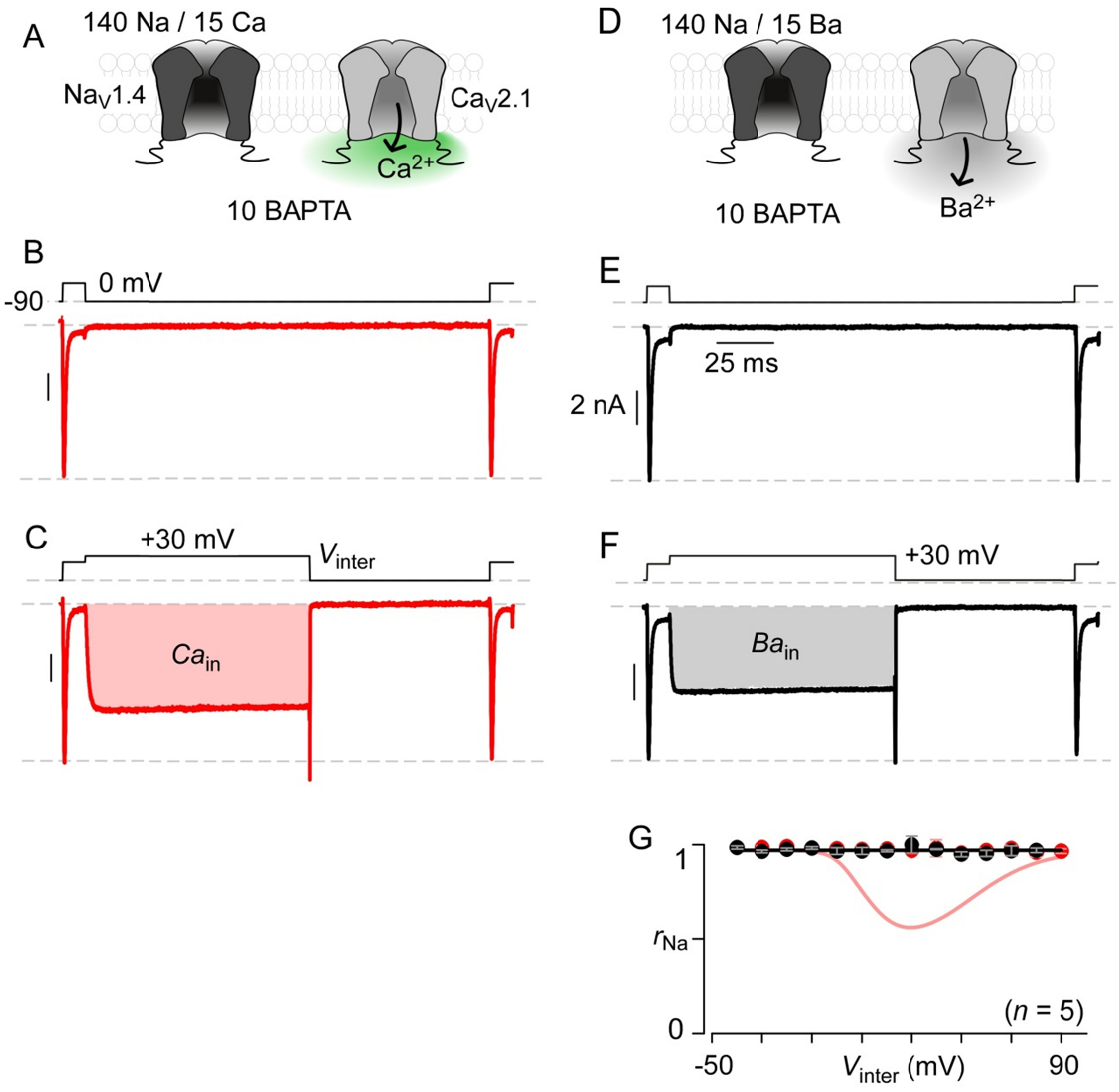
A
140 Na / 15 Ca
Na$_V$1.4
Ca$_V$2.1
Ca$^{2+}$
10 BAPTA
D
140 Na / 15 Ba
10 BAPTA
Ba$^{2+}$
B
-90
0 mV
E
25 ms
2 nA
C
+30 mV
$V_{inter}$
$Ca_{in}$
F
+30 mV
$Ba_{in}$
G
1
$r_{Na}$
0
(n = 5)
-50
$V_{inter}$ (mV)
90

**Figure 3.9. Restriction of $Ca^{2+}$ elevations to $Ca^{2+}$ channel nanodomain prevents Na channel regulation.**

(A) In experiments that utilize $Ca^{2+}$ influx through $Ca^{2+}$ channels to trigger Na channel regulation, abolishing the $Ca^{2+}$ spillover using high intracellular $Ca^{2+}$ buffering prevents Na channel regulation. Here, the high intracellular $Ca^{2+}$ restricts $Ca^{2+}$ elevations to the nanodomain of the $Ca^{2+}$ channels thus precludes the Na channels from sensing these local $Ca^{2+}$ signals.

(B) Dual voltage-pulses to 0 mV selectively elicit identical $Na_V1.4$ currents. Format as in Figure 3.7B.

(C) An intervening pulse to $V_{inter}$ = +30 mV activates robust $Ca^{2+}$ influx through $Ca_V2.1$ channels. By contrast to Figure 3.7C, the second Na current amplitude is identical to the peak Na current evoked in response to the first pulse. Even though, Ca2+ channel support robust $Ca^{2+}$ influx, the $Ca^{2+}$ elevations are restricted to Ca2+ channel nanodomain preventing $Ca^{2+}$ regulation of Na channels.

(D-F) $Ba^{2+}$ influx through $Ca_V2.1$ does not elicit Na channel regulation.

(D) Cartoon illustrates the experimental paradigm.

(E-F) Dual pulse protocols evoke identical Na currents irrespective of intervening activation of $Ba^{2+}$ currents through $Ca_V2.1$.

(G) Population average from 5 cells, demonstrating the absence of $Na_V1.4$ CDI when local $Ca^{2+}$ spillover from $Ca_V2.1$ is abolished. Format as in Figure 3.7G.

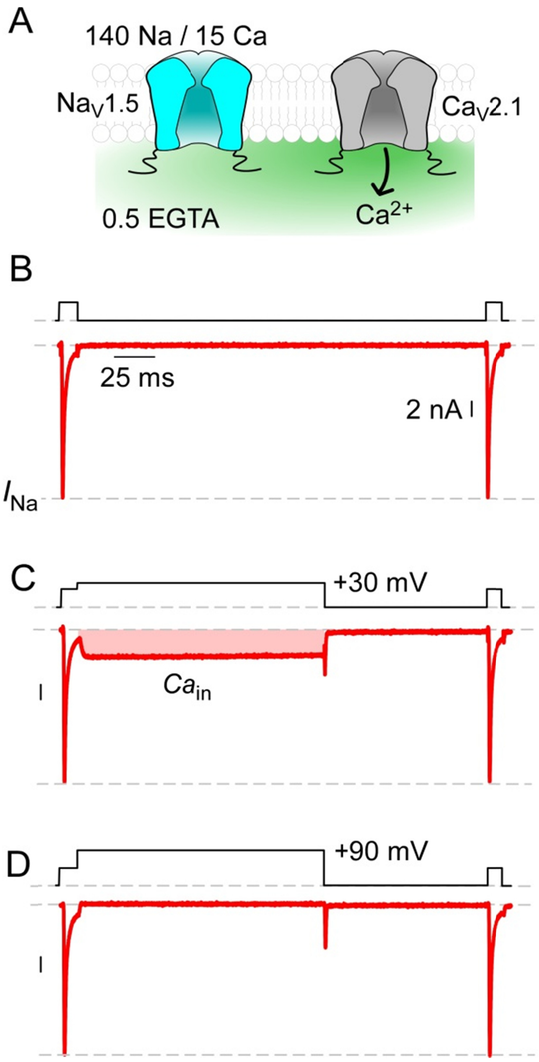
A
140 Na / 15 Ca
Na$_V$1.5
Ca$_V$2.1
0.5 EGTA
Ca$^{2+}$
B
25 ms
2 nA
$I_{Na}$
C
+30 mV
$Ca_{in}$
D
+90 mV

**Figure 3.10. $Na_V1.5$ channel regulation absent with local $Ca^{2+}$ spillover from neighboring $Ca_V2.1$ channels**

(A) Cartoon illustrates schematic of Na channel regulation using $Ca^{2+}$ spillover from $Ca^{2+}$ channels as in Figure 3.7A. Here, $Ca^{2+}$ regulation of $Na_V1.5$ channels is probed using this method of rapid $Ca^{2+}$ delivery. In this experimental paradigm, the Na Channel CDI is evoked independent of UV uncaging of $Ca^{2+}$ complexed with DM nitrophen, allowing us to control for potential artifacts that may result from release of photolytic products. Importantly, 0.5 mM EGTA is utilized as the internal $Ca^{2+}$ buffer, so as to permit robust $Ca^{2+}$ spillover from $Ca^{2+}$ channels.

(B) Dual voltage pulses evoke identical $Na_V1.5$ currents. Format as in Figure 3.8B.

(C) An intervening pulse to $V_{\text{inter}}$ = +30 mV activates robust $Ca^{2+}$ influx through $Ca_V2.1$ channels. However, the Na currents evoked using the bookend dual voltage pulse protocols are identical arguing for an absence of $Ca^{2+}$ regulation of $Na_V1.5$ channels.

(D) Increasing $V_{\text{inter}}$ to +90 mV, near the reversal potential of $Ca^{2+}$ current, also results in identical Na currents evoked by the bookend dual voltage pulses.

# CHAPTER 4

## Biophysical properties of Na channel $Ca^{2+}$-regulation

In Chapter 3, the existence of $Ca^{2+}$ regulation of Na channels was established using two methods of rapid $Ca^{2+}$ delivery. For the skeletal muscle $Na_V1.4$ channel, this modulation manifested as a robust and rapid $Ca^{2+}$-dependent decrement in peak current amplitude. The time course and the overall properties of this modulation appeared to correspond well with $Ca^{2+}$ regulation of $Ca^{2+}$ channels (Figure 3.1B). However, key uncertainties still remain as to the actual nature of this modulation, and its interrelation with the canonical voltage-dependent inactivation of these channels (as specified by the '*h* gate'). In particular, as nearly all prior studies have utilized pipet dialysis of internal solution containing various $Ca^{2+}$ concentrations, the kinetics and the reversibility of $Ca^{2+}$ regulation of Na channels has been crucially absent. Rapid millisecond control of cellar $Ca^{2+}$ through $Ca^{2+}$ photouncaging allows us to characterize these properties with quantitative precision. Moreover, the role of voltage in determining $Ca^{2+}$ regulation of Na channels still remains obscure. On the one hand, for $Na_V1.5$ channels where shifts in voltage-dependence of $h_\infty$ curve have been proposed, we identified no such regulation. Yet, the $Na_V1.4$ current amplitude was readily diminished upon $Ca^{2+}$ elevation, however, the relation of this effect to the voltage-dependence of $h_\infty$ curve remains to be fully established. Lastly, owing to technical challenges, $Ca^{2+}$ regulation of Na channels has yet to be established at the molecular level as an effect on channel gating. Prior single-molecule experiments on $Na_V1.5$ channels argued that intracellular $Ca^{2+}$ may simply alter ion permeation properties without affecting channel gating (Casini et al., 2009). In fact, extracellular $Ca^{2+}$ has been shown to reduce Na channel conductance at very low voltages presumably by binding to the channel pore and blocking ion permeation (Armstrong and Cota, 1991). Determining such biophysical properties of Na channel regulation is critical to elucidate possible biological relevance of this $Ca^{2+}$-dependent feedback regulation in skeletal muscle, and to further deduce the structural and functional determinants of this modulation. In this chapter, we establish $Ca^{2+}$ regulation of Na channels as a legitimate molecular level process that appears to be largely independent of voltage.

## RESULTS

***Effect of pulse rate on the development of Na channel CDI*** – Na channel fast inactivation is a rapid gating process that occurs within a few millseconds, while $Ca^{2+}$ regulation is a kinetically slower process that evolves over tens of milliseconds (Figure 3.6A). As such, the timecourse and magnitude of this slower process is deduced from the ‘envelope’ of peak Na currents pulsed at regular intervals following a step increase in $Ca^{2+}$ concentration. As a consequence, the channels cycles through closed, open, and inactive states regularly. The cycling rate determines the fraction of time a channel spends in each of these states. Could the variable cycling of the channels through these states alter the kinetics or steady-state $Ca^{2+}$ responsiveness of the Na channel? To clarify this scenario we undertook $Ca^{2+}$ uncaging experiments in a single cell where Na currents were elicited at multiple pulse rates (Figure 4.1A – D). Typically, we evoked $Na_V1.4$ currents using a 20 Hz pulse rate to optimally resolve the kinetics of $Ca^{2+}$-regulation

(Figure 3.6A, Figure 4.1A), as denoted by the exponential fit to the peak Na current amplitudes (rose curve in Figure 4.1A). The first peak Na current evoked ~ 5ms following $Ca^{2+}$-uncaging is only marginally altered, suggesting that $Ca^{2+}$-regulation of these channels has not fully developed. Indeed, steady-state $Ca^{2+}$ regulation is only attained after >50 ms following $Ca^{2+}$-uncaging. Remarkably, altering the pulse rate used to evoke Na currents in these experiments does not change the rate of development or the steady-state extent of CDI (rose curve in Figure 4.1B-D is identical to Figure 4.1A). In fact, at slower pulse rates, the first peak Na current evoked following $Ca^{2+}$-uncaging (now probed only after >50 ms) has already achieved steady-state current decrement given the $Ca^{2+}$ input. Importantly, for these experiments, the $Ca^{2+}$-steps used to probe modulation was similar in amplitude (~5 μM). Figure 4.1E summarizes these results to show that Na channel $Ca^{2+}$-regulation is invariant of pulse rate used to evoke the modulation. Importantly, these results argue that $Ca^{2+}$-effect of Na channels can proceed from the closed-state of the channel. Increasing the pulse rate would invariably enhance the time spent by the channel in the open and inactive state. Thus, as the kinetics and steady-state extent of $Ca^{2+}$ regulation is invariant to pulse rate, it seems plausible that the $Ca^{2+}$-effect on Na channels could proceed with similar propensity from the open and inactive states as well. For $Ca^{2+}$ channels, recent studies have argued that $Ca^{2+}$-dependent inactivation of these channels proceeds equally from both open and closed states (Tadross et al., 2010; Tadross and Yue, 2010).

Another related concern is the reversibility of $Ca^{2+}$ regulation of Na channels. Unlike with pipet dialysis where $Ca^{2+}$ elevations are permanent, $Ca^{2+}$-photouncaging allows for transient $Ca^{2+}$ elevations that may wane in the course of a minute, allowing one to probe for the reversal of $Ca^{2+}$ effects. Figure 4.2 shows results that demonstrate the potent dependence of peak Na current amplitude on cytosolic $Ca^{2+}$. Prior to $Ca^{2+}$ uncaging, the peak Na currents evoked at 20 Hz remains stable. Upon $Ca^{2+}$-uncaging to ~ 2 μM, the peak Na current amplitudes decline precipitously and achieve a new steady-state value. Approximately 20 seconds later, the cytosolic $Ca^{2+}$ concentration returns to lower levels (~ 200 nM), as excess $Ca^{2+}$ ions bind free cage molecules (DM-Nitrophen). Reassuringly, the peak Na currents return to the original levels prior to $Ca^{2+}$ uncaging, demonstrating that $Ca^{2+}$ effects on Na channels are fully reversible in a matter of seconds (Figure 4.2A). Interestingly, in cells where $Ca^{2+}$ failed to return to basal levels (as the concentration of free cage molecules was limited in these cells) the peak Na currents remained at the diminished $Ca^{2+}$-inhibited level (Figure 4.2B). It is worth noting that even though the peak currents are lower, they remain steady in response to the voltage-pulse train protocol. Together, results highlight the unique dependence of Na current amplitude on cytosolic $Ca^{2+}$ concentration and $Ca^{2+}$-dependent inhibition appears to be independent of the voltage-pulse protocol used to quantify it.

***$Ca^{2+}$ effects on Na channel steady-state inactivation*** – Under static $Ca^{2+}$ buffering (Figures 3.3B-E), we observed no shift in the $h_\infty$ curves of $Na_V1.4$ channels, yet $Ca^{2+}$ uncaging produces marked decrement in peak Na current. To resolve ambiguity in the relationship between rapid $Ca^{2+}$-dependent inhibition of $Na_V1.4$ and the well-established fast inactivation process, we evoked Na currents under a modified voltage-pulse protocol that measures $h_\infty$ curves just before and after $Ca^{2+}$ uncaging (Figure 4.3). Prior to $Ca^{2+}$ uncaging, peak currents evoked after various holding potentials demonstrated the usual changes affiliated with steady-state inactivation (Figure 4.3A, black $I_{Na}$ trace). Normalizing these currents by that of the first pulse yielded a baseline $h_\infty$ curve (Figure 4.3A, bottom subpanel), here averaged over multiple cells. Figure 4.3B shows the effect of $Ca^{2+}$ uncaging in same cell. The initial current, obtained just prior to $Ca^{2+}$ uncaging, exhibits the identical amplitude as its analog in Figure 4.3A, confirming minimal rundown. By contrast, after $Ca^{2+}$ uncaging, the resulting currents (Figure 4.3B, black $I_{Na}$ trace after UV flash) seemed to be uniformly suppressed compared to their analogs in Figure 4.3A. Normalizing these responses (after $Ca^{2+}$ uncaging) by that of the first pulse (before uncaging) yielded the $Ca^{2+}$-regulated $h_\infty$ curve shown below (Figure 4.3B, bottom subpanel, red data and fit), as averaged over multiple cells. For reference, the fit to the $h_\infty$ curve obtained before $Ca^{2+}$ uncaging is reproduced in black (Figure 4.3B). Comparison of these curves confirms that $Ca^{2+}$ elevation simply scales down the $h_\infty$ curve, without an overt shift along the voltage axis. This outcome is corroborated by scaling up the fit to the $h_\infty$ curve following $Ca^{2+}$ uncaging, to superimpose (rose curve) on the control in black. It is not then surprising that no $Ca^{2+}$ effect of $Na_V1.4$ channels was observed upon interrogation with static pipet dialysis.

Fitting with this data, we also found that CDI of Na channels is not reversed by extreme hyperpolarization of the cell (Figure 4.4). In this experiment, $Na_V1.4$ CDI was first elicited using a 10 μM $Ca^{2+}$-step while the cell is held at -90 mV. Subsequently, the holding potential was lowered to -160 mV, resulting in only a minor enhancement of peak current amplitude from the $Ca^{2+}$ inhibited level. In fact, this minor restoration of Na current was also observed prior to $Ca^{2+}$-photouncaging and thus may relate to the recovery of a very small fraction of channels that were voltage-inactivated at -90 mV. It now appears that $Ca^{2+}$ does not alter the steady-state propensity ($h_\infty$) and the kinetics ($\tau_h$) of fast inactivation. Together, these results argue that CDI of Na channel is distinct from canonical fast-inactivation of Na channels.

***Kinetics of onset of $Na_V1.4$ CDI*** – The steady-state $Ca^{2+}$-responsiveness of Na channels was obtained in Chapter 3 (Figure 3.6A) using $Ca^{2+}$-photouncaging. The ability to deliver step-like $Ca^{2+}$ inputs to the Na channels also enables us to quantitatively deduce the onset kinetics of CDI and its dependence upon both $Ca^{2+}$ and voltage. As expected for a genuine $Ca^{2+}$-dependent process, the CDI of Na channels is exquisitely sensitive to the $Ca^{2+}$ concentration eliciting this modulation. Figure 4.5 illustrates this $Ca^{2+}$-sensitivity. In response to a 1 μM $Ca^{2+}$ step, the Na channel $Ca^{2+}$ dependent inhibition is slowly evolving and reaches a lower steady-state value. By contrast, a larger $Ca^{2+}$ step to ~ 3 μM evokes a faster and deeper inhibition of Na current. To quantitatively characterize this phenomenon, peak Na currents following the UV pulse is fit using a single exponential function. Figure 4.5B plots the time constants ($\tau$) for these fits against $Ca^{2+}$-step amplitude. Remarkably, this relation is well approximated (Figure 4.5B, black fit) by a system where channels transition from a normal mode of gating to a reduced-probability mode of gating via a rate constant given by $k_{on} \times [Ca^{2+}]^n$, with return rate constant $k_{off}$. According to this model, the $\tau = k_{on} \times [Ca^{2+}]^n + k_{off}$. $k_{on}$ was determined to be $3.2 \times 10^{12}$ $M^{-2}s^{-1}$ while $k_{off}$ was found to be 4.7 $s^{-1}$ with hill coefficient $n = 2$. Importantly, by this model, the steady-state $Ca^{2+}$-sensitivity would be predicted to be $(k_{off}/k_{on})^{1/2} \sim 1.3$ μM consistent with the measured half-sensitivity estimated based on steady-state measurements. At very high $Ca^{2+}$ concentrations, the $\tau – [Ca^{2+}]$ relationship appeared to saturate around 10 ms suggesting the existence of a limiting gating step in the Na channel CDI process. Importantly, the $Na_V1.4$ CDI time-constant measurements obtained in voltage-pulse protocols with holding potential $V_{hold}$ = -120 mV also followed the same relation obtained with $V_{hold}$ = -90 mV (Figure 4.5B, red dots). This maneuver of changing $V_{hold}$ = -120 mV also resulted in a highly similar *CDI –*$[Ca^{2+}]$ steady-state measurements (Figure 4.5C) arguing that onset of CDI is independent of voltage. Indeed, similar observations have been reported for $Ca_V1.3$ $Ca^{2+}$ channels (Tadross et al., 2013). Overall, Na channel CDI is a rapid process that dynamically tunes Na currents in response to cytosolic $Ca^{2+}$ elevations.

**Na channel regulation at a single-molecule level** – At the macroscopic level, $Ca^{2+}$-regulation manifests as a decrement of the overall Na current amplitude. Nonetheless, the mechanism of $Ca^{2+}$ regulation of Na channels is yet to be established at the single-molecule level. To this end, our strategy of coexpressing Na and $Ca^{2+}$ channels could be extended from cells (Figures 3.7-3.10) to isolated patches of membrane, thus permitting observations of regulation at the level of individual Na channels. Figure 4.6A shows the activity of a patch containing several $Na_V1.4$ channels coexpressed with hundreds of $Ca_V2.1$ $Ca^{2+}$ channels. A multi-channel stochastic record is shown at the top (multi-channel record), along with the voltage-pulse protocol. Only Na channels were activated during test-pulse depolarizations to -30 mV at the left (labeled i) and right (labeled ii) ends of the record, while $Ca^{2+}$ channels were activated only during the interpulse to a more positive voltage of 30 mV (shaded in red). The ensemble average of many such records is shown below. Thus oriented, it is clear that Na channel activity evoked after intense interpulse $Ca^{2+}$ entry was substantially decreased (pulse ii), compared to the activity before the interpulse (pulse i). As a control, data from a separate patch containing only $Na_V1.4$ channels without $Ca_V2.1$ channels demonstrated no such difference between first and second test pulses (Figure 4.6B). Thus, $Ca^{2+}$ entry caused the marked reduction of second pulse activity in Figure 4.6A, an effect confirmed in multiple patches, with a 45.4 ± 8.8 % (mean ± SEM, $n = 6$) mean decrement of current. These results are strikingly similar to macroscopic observations presented in Figure 2.6A.

To deduce the elementary mechanism of inhibition, we analyzed the unitary current $i$ approximated by the horizontal dashed line on the multi-channel record (Figure 4A, labeled $i \sim -1$ pA). This unitary current was not visibly changed in the second test pulse compared to the first, suggesting that single-channel conductance was unaffected by CDI. This outcome is explicitly confirmed in Figure 4.7A-B by amplitude histogram analysis, where the smooth curve fit to data (in black) is generated by stochastic simulation of multi-channel activity added to gaussian noise, followed by lowpass filtering present in our system (Prod'hom et al., 1987). Using this method, essentially the same underlying value of $i$ was estimated before and after $Ca^{2+}$ influx (vertical dashed lines). Accordingly, since ensemble average current $I = N P_O i$, and the number of channels $N$ must have been the same in the first and second test pulses (separated by only hundreds of milliseconds), it could be concluded that Na channel CDI occurred by decreased open probability $P_O$, just as in $Ca^{2+}$ channel CDI (Imredy and Yue, 1994). To exclude appreciable interaction of this CDI-mediated decrease in open probability with the fast inactivation process, we confirmed that the time constant of inactivation was not detectably changed by CDI (Figure 4.7C-D), recapitulating whole-cell results already shown in Figure 3.6C.

Admittedly, this current decay may also include a small component of channel deactivation. Thus, CDI and fast inactivation appear to be largely parallel processes.

## DISCUSSION

Overall, $Ca^{2+}$-regulation of Na channels now emerges as a highly dynamic process that potently controls the peak Na current. Much like $Ca^{2+}$ regulation of $Ca^{2+}$ channels, this Na channel modulation possesses exquisite $Ca^{2+}$-sensitivity and appears to be largely independent of voltage effects. In particular, CDI of Na currents cannot be reversed by hyperpolarizing the membrane potentials. As $Ca^{2+}$ signals in cells could be evoked independent of voltage, this feature would allow the Na current to be inhibited even during rest periods through activation of other cellular signaling pathways independent of voltage. In fact, phospholipase C, classically known to activate $Ca^{2+}$ release from internal stores through IP3 receptors, was shown to diminish propensity for action potential generation in the skeletal muscle without altering the resting membrane potential (Albuquerque and Thesleff, 1967; Powell et al., 2001). At the single-molecule level, our results establish $Ca^{2+}$-regulation to be a genuine effect of channel gating without any change in permeation properties of the Na channels as previously suspected (Casini et al., 2009).

In terms of skeletal muscle physiology, a single twitch could trigger a $Ca^{2+}$ transient that persists for 10-20 milliseconds, insufficient to develop significant CDI. However, during periods of high activity (action potential could be triggered at greater than 50 Hz), significant residual $Ca^{2+}$ build up along with the slow off-kinetics of CDI would imply a dramatic reduction in Na current, thus increasing the voltage-threshold necessary to trigger an action potential. In this manner, Na channel CDI may serve as an important feedback mechanism that allows the muscle to relax following tetanic contractions. Dysregulation of this modulation may then contribute to persistent muscle tone or possibly cramps as might occur in some myotonias or periodic paralyses.

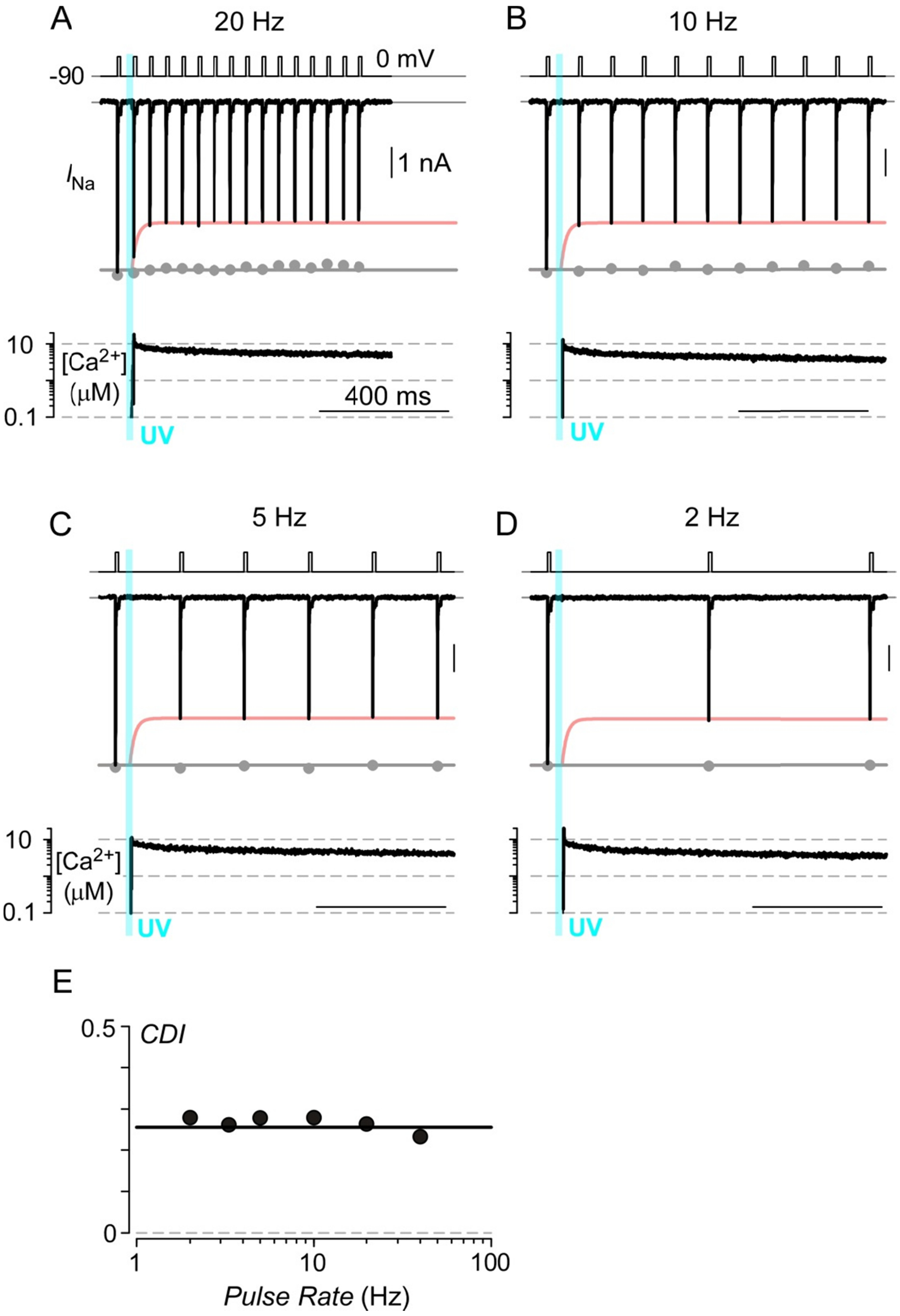
A
20 Hz
-90
0 mV
$I_{Na}$
1 nA
10
[Ca2+]
(μM)
0.1
400 ms
UV
B
10 Hz
UV
C
5 Hz
10
[Ca2+]
(μM)
0.1
UV
D
2 Hz
UV
E
0.5
CDI
0
1
10
100
Pulse Rate (Hz)

‘

**Figure 4.1. Effects of pulse rate on Na$_V$1.4 channel CDI.**

(A – D) Since Na channels undergo fast inactivation within the first few milliseconds following depolarization, the timecourse and magnitude of the slower Ca$^{2+}$-dependent regulation of Na channels was deduced from the ‘envelope’ of peak Na currents pulsed at regular intervals after Ca$^{2+}$ uncaging. To ensure that Na$_V$1.4 Ca$^{2+}$ regulation is independent of this pulse rate, CDI was characterized for Na currents evoked at multiple pulse rates (20 Hz, panel A; 10 Hz, panel B; 5 Hz, panel C; 2 Hz, panel D) in a single cell. Gray dots and fit correspond to peak currents prior to Ca$^{2+}$ uncaging. Following Ca$^{2+}$ uncaging (cyan line), current amplitudes declined rapidly, revealing CDI in response to ~5 μM Ca$^{2+}$ steps. Red envelope curves are identical for various pulse rates, confirming that the onset of CDI is independent of pulse rate.

(E) Summary relationship further confirms that CDI magnitude (obtained from records in panel A) is independent of the pulse rate used to evoke Na$_V$1.4 current.

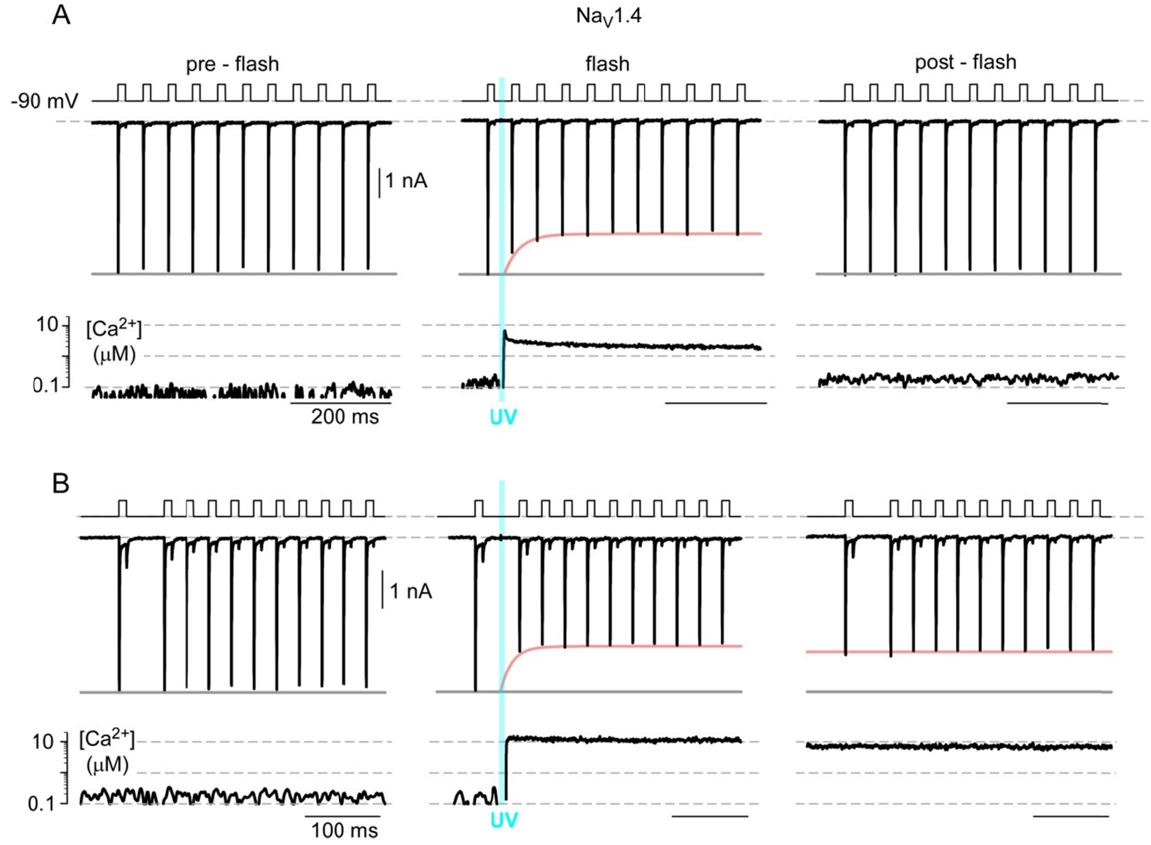

**Figure 4.2. Na$_V$1.4 current amplitudes are a function of cytosolic Ca$^{2+}$.**

(A) Exemplar Na$_V$1.4 currents show CDI and recovery from CDI following return of Ca$^{2+}$ to resting levels. Left, Na current evoked by pulse train prior to Ca$^{2+}$ uncaging. Middle, onset of CDI as evident from decrement of Na current following Ca$^{2+}$ step to ~2 μM. Right, once intracellular Ca$^{2+}$ returned to basal levels (~150 nM), the Na current amplitude also recovered.

(B) In a different cell, when the cytosolic Ca$^{2+}$ remained high after uncaging to ~10 μM Ca$^{2+}$, the Na current amplitude also remained at the inactivated level, confirming the exquisite Ca$^{2+}$ dependence of this novel type of modulation.

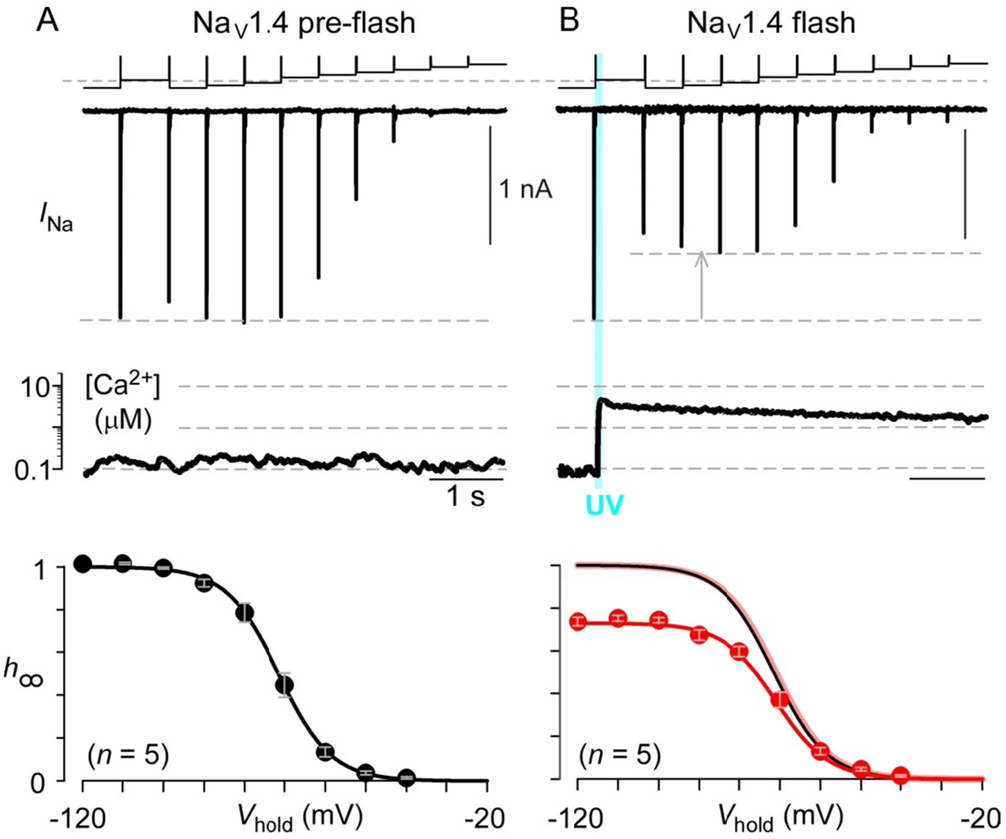

**Figure 4.3. Effect of $Ca^{2+}$ on Na channel steady-state inactivation curve.**

(A) A concatenated voltage-pulse protocol is used to deduce Na channel steady-state inactivation curve ($h_\infty$ curve). Top, Na current is evoked in response to an initial test pulse to 0 mV after being held at $V_{hold}$ = -120 mV for 500 ms. Subsequently, a series of test pulses to 0 mV are elicited after being held at a family of holding potentials ($V_{hold}$) for 500 ms. Normalizing the peak Na current in response to each of these test pulses to the initial peak Na current yields the $h_\infty$ curve. Simultaneously, cytosolic $Ca^{2+}$ concentrations are obtained from ratiometric fluorescence measurements. Bottom, population average for $h_\infty$ curve. Each symbol, mean ± SEM from 5 cells.

(B) A $Ca^{2+}$ step to ~3 μM uniformly suppressed peak Na currents. Bottom, population average, red symbols and fit. Upwardly normalized $h_\infty$ curve (rose relation) is identical to before uncaging arguing against a shift in voltage-dependence of $h_\infty$ curve (curve in black). Each symbol, mean ± SEM from 5 cells.

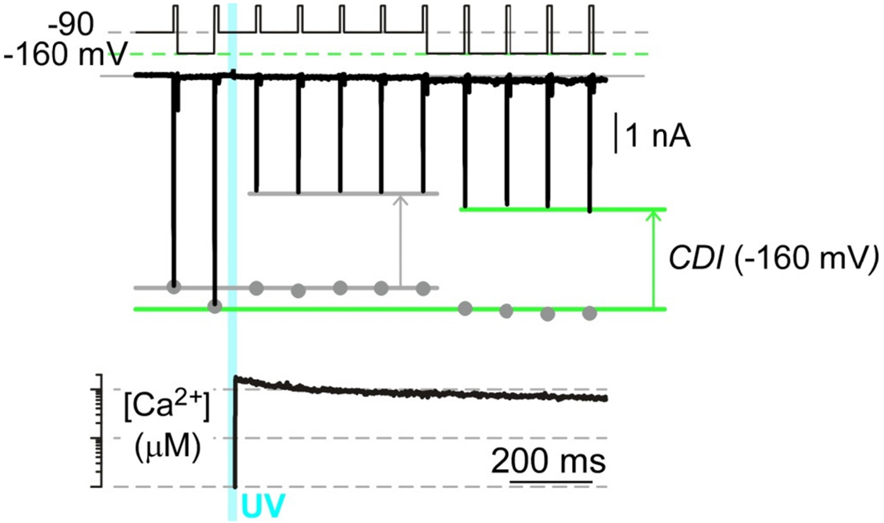

**Figure 4.4. Na$_V$1.4 CDI is not reversed by extreme hyperpolarizations.**

CDI is not reversed by setting holding potential to -160 mV. After evoking CDI at -90 mV (horizontal gray lines), changing to -160 mV does not change the extent of inhibition (horizontal green lines). These results agree with a scaling down of steady-state inactivation (Figure 4.2B).

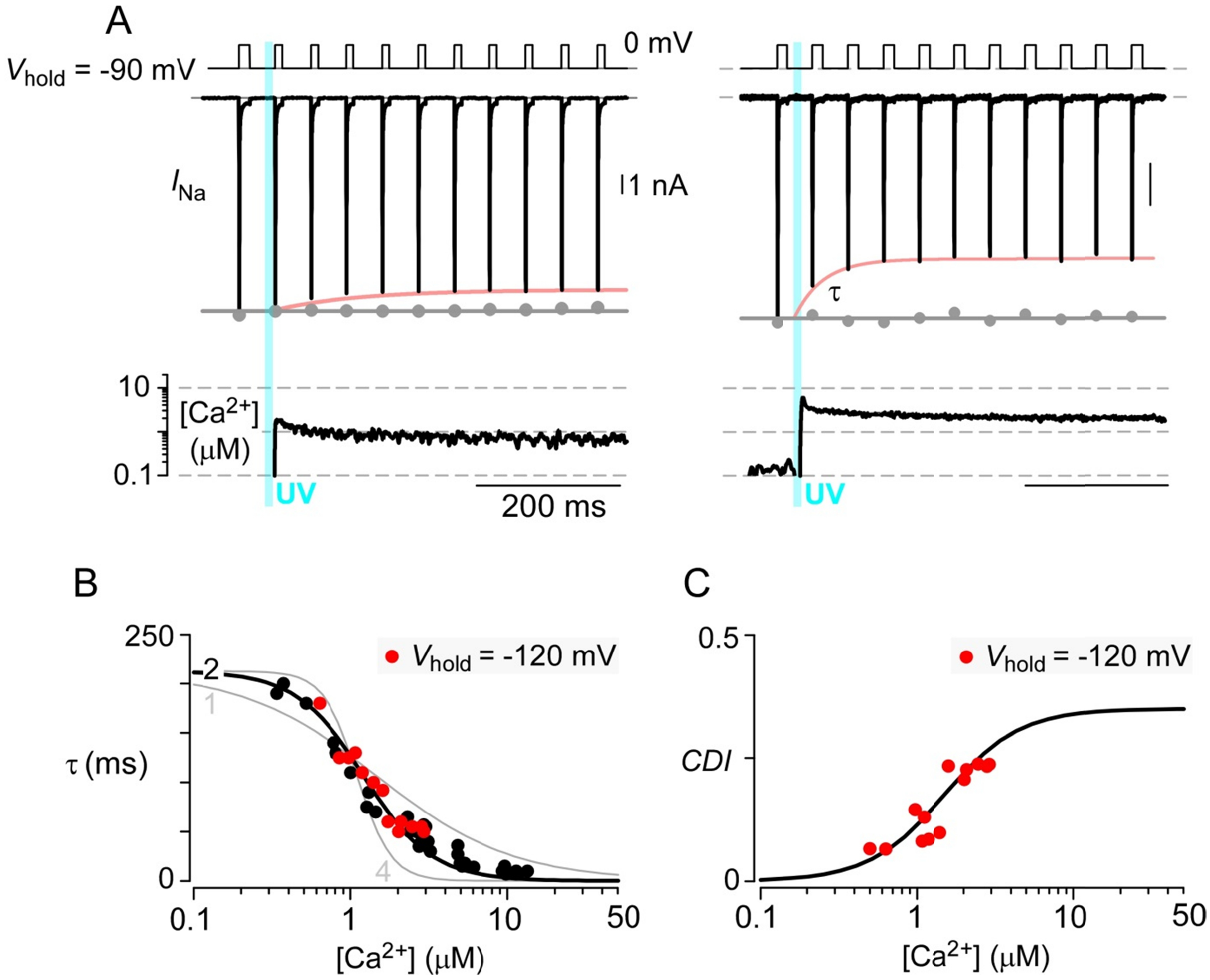
A
0 mV
$V_{\text{hold}}$ = -90 mV
$I_{\text{Na}}$
1 nA
τ
10
$[\text{Ca}^{2+}]$
(μM)
0.1
UV
200 ms
UV
B
250
2
1
4
τ (ms)
0
0.1
1
10
50
$[\text{Ca}^{2+}]$ (μM)
● $V_{\text{hold}}$ = -120 mV
C
0.5
CDI
0
0.1
1
10
50
$[\text{Ca}^{2+}]$ (μM)
● $V_{\text{hold}}$ = -120 mV

**Figure 4.5. Kinetics of $Na_V$1.4 CDI**

(A) CDI elicited by $Ca^{2+}$ steps of different amplitudes. The time constant (τ) for the onset of CDI was estimated by single exponential fits to peak current amplitudes following $Ca^{2+}$ uncaging ('red envelope'). Left, CDI onset is slower in response to a smaller $Ca^{2+}$ step. Right, CDI onset is much faster with a larger $Ca^{2+}$ step. Format as in Figure 3.5A.

(B) The time constant of CDI onset (τ) plotted versus the magnitude of $Ca^{2+}$ step with holding potential ($V_{\text{hold}}$) near -90 mV ($n$ = 21 cells). This relation is well approximated (black fit) by system where channels transition from a normal mode of gating to a reduced-probability mode of gating via a rate constant given by $k_{\text{on}} \times [Ca^{2+}]^n$, with return rate constant $k_{\text{off}}$. Specifically, $k_{\text{on}} = 3.2 \times 10^{12}$ $M^{-2}s^{-1}$, $k_{\text{off}} = 4.7$ $s^{-1}$, and hill coefficient $n = 2$. Indeed, it is reassuring that $(k_{\text{off}} / k_{\text{on}})^{1/2}$ ~1.3 μM is consistent with the measured $K_d$ of steady-state *CDI*–[$Ca^{2+}$] relations (Figure 3.6B). Gray fit, predicted relations for hill coefficient $n$ = 1 or $n$ = 4 diverge from the experimental data. Overall, these results conform well with the dominance of a single lobe (N-lobe) of CaM in triggering CDI (Chapter 4). Red symbols, τ – [$Ca^{2+}$] relation obtained with holding potential set to -120 mV also overlay same relation, again consistent with CDI being a largely $Ca^{2+}$-dependent process.

(C) Steady-state relation for CDI versus $Ca^{2+}$ concentration, obtained with $V_{\text{hold}}$ = -120 mV, overlays standard black relation reproduced from Figure 3.6B. Thus, the steady-state extent of $Na_V$1.4 CDI also appears independent of the holding potential.

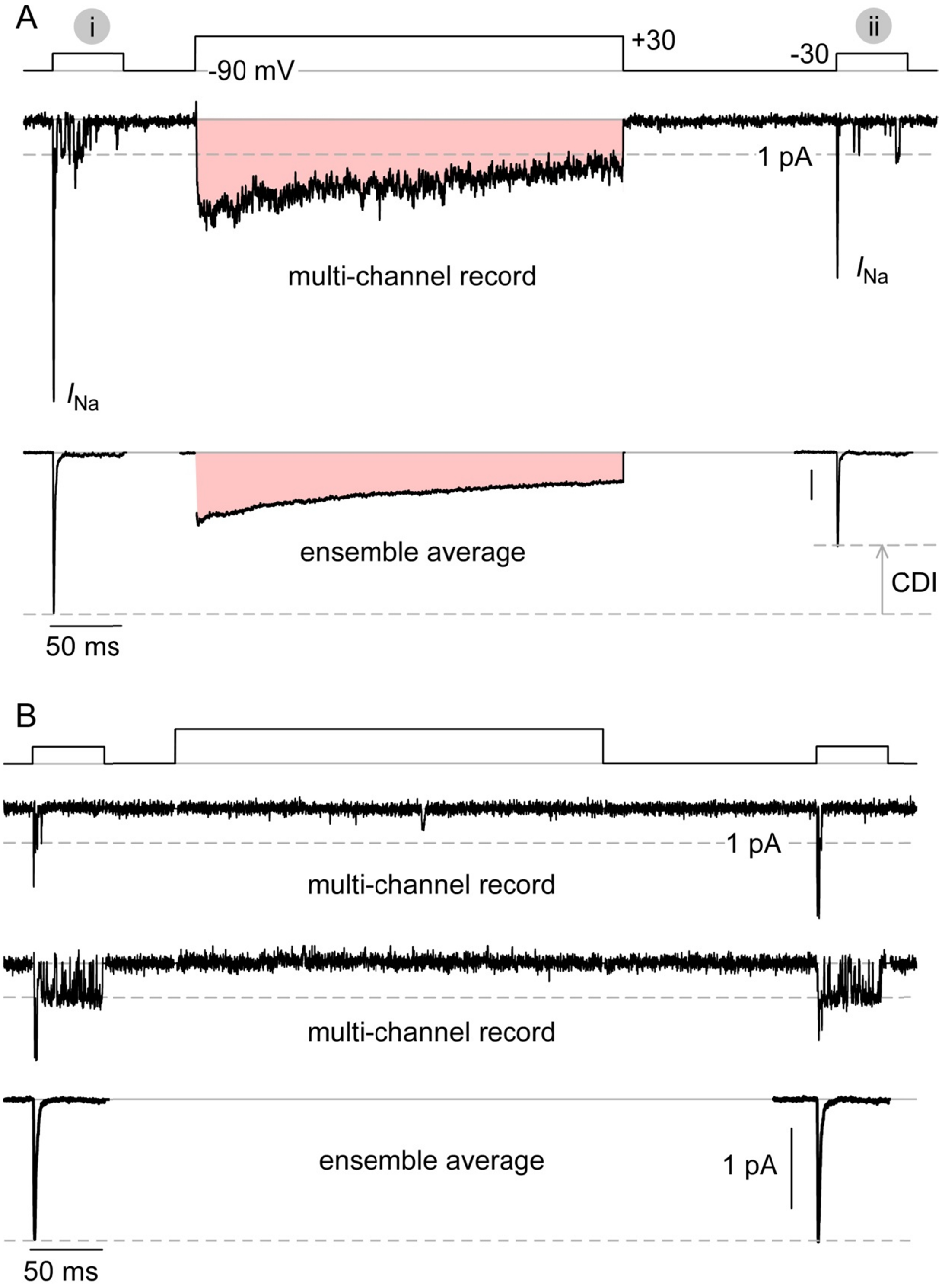
A
i
ii
+30
-90 mV
-30
1 pA
multi-channel record
$I_{Na}$
$I_{Na}$
ensemble average
CDI
50 ms
B
1 pA
multi-channel record
multi-channel record
ensemble average
1 pA
50 ms

**Figure 4.6. Multi-channel stochastic records of $Na_V1.4$ CDI.**

(A) Multi-channel records of on-cell patch from HEK293 cells coexpressing $Na_V1.4$ and $Ca_V2.1$. Voltage-pulse protocol (top), exemplar multi-channel record (middle), and ensemble average current (bottom). Red shading denotes periods of $Ca^{2+}$ entry. Ensemble average record demonstrates marked reduction of Na channel activity evoked after intense interpulse $Ca^{2+}$ entry (pulse ii), compared to before activating $Ca_V2.1$ (pulse i). Dashed horizontal line, current amplitude of a single opening. Scale bar in lower subpanel corresponds to 1 pA.

(B) Multi-channel stochastic records of a separate patch containing only $Na_V1.4$ channels show no significant difference in channel activity before and after the intervening pulse (mean decrement ~ 0.2 ± 3%, *n* = 5 patches). The second multi-channel record is chosen for the rare occurrence of a persistent gating mode that clearly resolves the unitary current level. Format as in panel A.

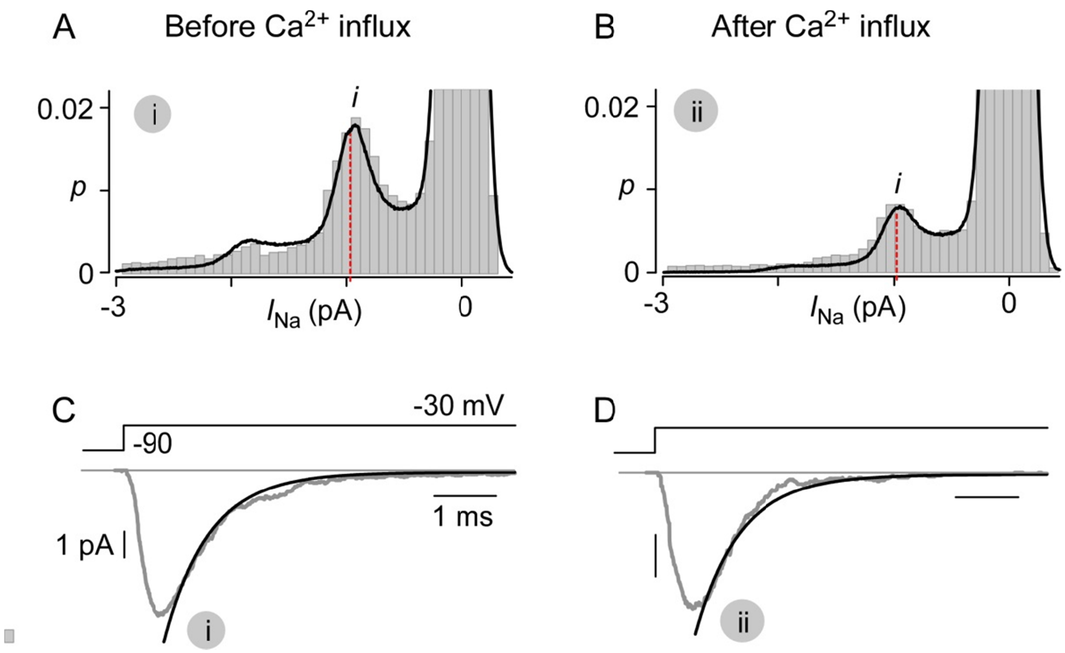

**Figure 4.7. Na channel Ca$^{2+}$ regulation does not alter unitary conductance or kinetics of voltage-dependent inactivation.**

(A – B) Amplitude histogram analysis of patch from panel A shows no change in unitary current following Ca$^{2+}$ entry (panel A, before interpulse; panel B, after interpulse). Fits (black) to data (gray bars) were deduced by undertaking stochastic simulation of channel activity, addition of gaussian noise, and then lowpass filtering. This data was then used to calculate an amplitude histogram. Vertical dashed-red lines indicate value of unitary current *i* used in generating black curve fits.

(C – D) Ensemble average currents before (panel C) and after (panel D) prepulse Ca$^{2+}$ entry during the intervening pulse. The timecourse of fast inactivation is essentially identical, as shown be superposition of identical monoexponential fits (black curves) onto ensemble average currents derived from the patch described in panel A.

# CHAPTER 5

## Structural underpinnings of Na channel $Ca^{2+}$-regulation

With the existence and the molecular nature of $Ca^{2+}$ regulation of Na channels firmly established, we next turned to elucidate the structural underpinning of this modulatory mechanism. Of note, the prevailing theories of Na channel regulation based on studies of $Na_V1.5$ channels argue for two possible $Ca^{2+}$ sensing mechanisms. First, $Ca^{2+}$ binding to the channel dual vestigial EF hand has been argued to be the primary determinant of Na channel $Ca^{2+}$ regulation. However, this view is highly contested as reviewed in Chapter 1. Second, the role of CaM in channel regulation has been debated. Based on structural data of $Ca^{2+}$/CaM interaction with channel III-IV loop, some studies argue for CaM as the primary $Ca^{2+}$ sensor (Sarhan et al., 2012), while others propose CaM as an auxiliary factor (Shah et al., 2006) whose function may be unveiled upon disabling channel EF hand $Ca^{2+}$ binding (Biswas et al., 2008). Another point of controversy has been the underlying channel structural elements critical for Na channel $Ca^{2+}$-regulation (Figure

1.10). Some studies have argued that the channel III-IV loop is the functionally critical $Ca^{2+}$/CaM binding interface on the Na channel (Sarhan et al., 2012), while others have argued for the channel carboxy-terminus (Kim et al., 2004b; Shah et al., 2006; Biswas et al., 2008; Biswas et al., 2009). These scenarios are reviewed at length in Chapter 1 (Figure 1.10). By contrast, for $Ca^{2+}$ channels, $Ca^{2+}$ regulation has been shown to result from a configurational rearrangement of CaM on various channel interfaces with the channel carboxy-terminus being a key structural determinant. In all, this inconsistent Na channel landscape (Tan et al., 2002; Wingo et al., 2004; Biswas et al., 2008; Biswas et al., 2009; Potet et al., 2009; Sarhan et al., 2012; Van Petegem et al., 2012) suggests divergence, weakening, or even loss of CI regulatory function, compared to that in $Ca^{2+}$ channels. Altogether, a recent review surmises that 'substantial discrepancies ... mediate the different functional effects' in $Ca^{2+}$ versus Na channels (Van Petegem et al., 2012). Thus, hopes for a unified perspective on CI region function across superfamilies has waned over the past decade.

In this chapter, we reconsider these issues using methods of rapid $Ca^{2+}$ delivery to identify the underlying structure-function determinants of Na channel regulation. Our findings in this chapter illustrates the uncanny similarity between $Ca^{2+}$ and Na channels in terms of their CaM regulatory function, and sets the stage to consider the carboxy-tail of the two channel families as a shared structural module.

## RESULTS

**CaM as the $Ca^{2+}$ sensor for Na channel regulation** – To identify the $Ca^{2+}$ sensor for Na channel regulation, we first considered the potential direct interaction of $Ca^{2+}$ ions with the channel itself through its carboxy-terminal vestigial EF hand segments. Prior structural studies have identified two acidic residues that could potentially coordinate $Ca^{2+}$ ions to trigger channel regulation (Chagot et al., 2009). We therefore introduced alanines at these potential $Ca^{2+}$-coordinating residues in the first EF hand of $Na_V1.4$ channels (Figure 5.1A, D[1621] and D[1623]). These residues are represented as yellow sticks in the structure of $Na_V1.5$ (Figure 5.1A, right subpanel). If this EF hand were to coordinate $Ca^{2+}$ ions, then introducing these alanines would be predicted to reduce $Ca^{2+}$ affinity by 10-1000 fold (Linse and Forsen, 1995). Nonetheless, this mutant channel still exhibited rapid and strong CDI, indistinguishable from wild type (Figure 5.1B), as shown by overlaying the wild-type profile (gray) on the *CDI* – [$Ca^{2+}$] relation. Historically, an alternative set of residues (termed '4×') were originally proposed to coordinate $Ca^{2+}$ ions based on molecular modeling (Wingo et al., 2004). However, later structural studies have shown that these residues are in a spatial arrangement incompatible with potential $Ca^{2+}$ coordination (Van Petegem et al., 2012) (Figure 5.1A, cyan residues). Nonetheless, functional experiments demonstrate that alanine substitutions of $Na_V1.4$ '4×' residues spared CDI (Figure 5.1C). However, it is worth noting that this mutation subtly altered $Ca^{2+}$-sensitivity of Na channel $Ca^{2+}$ regulation, as evident from comparison of black fit in Figure 5.1C (bottom subpanel) to gray control relations. These results suggest that while the channel dual vestigial EF hands may be structurally relevant for Na channel $Ca^{2+}$ regulation, this locus is unlikely to act as direct $Ca^{2+}$ sensor, paralleling outcomes in $Ca^{2+}$ channels (Zhou et al., 1997; Peterson et al., 2000).

$Ca^{2+}$ binding to a resident CaM serves as the primary $Ca^{2+}$-sensing event in the regulation of $Ca^{2+}$ channels (Peterson et al., 1999; Zuhlke et al., 1999). Likewise, some studies of Na channels have argued that CaM may be at least one of the pertinent $Ca^{2+}$ sensors, based on biochemical and structural inferences (Kim et al., 2004b; Sarhan et al., 2012). Crucially lacking, however, has been a key result seen with $Ca^{2+}$ channels coexpressed with a dominant-negative mutant CaM ($CaM_{1234}$), where $Ca^{2+}$ binding has been severely attenuated by alanine substitutions into all its EF hands. Importantly, coexpressing $CaM_{1234}$ with $Ca^{2+}$ channels fully abolishes their $Ca^{2+}$ regulation, arguing clearly for CaM as the $Ca^{2+}$ sensor (Peterson et al., 1999; Zuhlke et al., 1999). By contrast, no prior Na channel study has demonstrated elimination of $Ca^{2+}$ regulation by

$CaM_{1234}$. Rather, the effects have been variable and inconsistent (Van Petegem et al., 2012). By contrast, in $Ca^{2+}$-photouncaging experiments, we find that coexpression of $CaM_{1234}$ with $Na_V1.4$ channels completely eliminates $Ca^{2+}$-dependent inactivation as evident from exemplar current traces in Figure 5.2A. Population data further demonstrates a total suppression of Na channel CDI, a result that strongly advocates CaM as a resident $Ca^{2+}$-sensor for Na channels. Reassuringly, a similar suppression of Na channel CDI upon coexpression of $CaM_{1234}$ is observed when probed using $Ca^{2+}$ influx through neighboring $Ca^{2+}$ channels (Figure 5.2B).

Together these results establish CaM as the $Ca^{2+}$ sensor for Na channel regulation, reflecting similar findings for $Ca^{2+}$ channel regulation. Importantly, even though direct $Ca^{2+}$ binding to the channel dual vestigial EF hands was excluded, our functional experiments indicate that this channel segment may, nonetheless, play some role in eliciting $Ca^{2+}$ regulation. Indeed, for $Ca_V1.3$ channels, the dual vestigial EF hand segments in conjunction with a lobe of $Ca^{2+}$/CaM is thought to engage the channel IQ domain resulting in CDI of these channels (Ben-Johny et al., 2013a). It remains to be seen whether a similar scheme of channel regulation may pertain to Na channels.

**CaMKII activation is not necessary for Na channel regulation –** Given the critical role of CaM in Na channel modulation, one remaining concern is that CaM action on the channel may result from indirect mechanisms that utilize a $Ca^{2+}$/CaM sensitive enzyme, such as CaMKII. Importantly, prior studies of $Na_V1.5$ have argued that activation of CaMKII may phosphorylate certain Na channels and, thereby, alter various channel gating properties (Aiba et al., 2009; Ashpole et al., 2012). It is unknown whether such phosphorylation sites are preserved in $Na_V1.4$ channels. Nonetheless, here we explicitly demonstrate that Na channel CDI is unaltered by inhibition of CaMKII activity using a specific inhibitor KN-93 (Figure 5.3A). In the exemplar trace, robust $Na_V1.4$ CDI is evoked in response to ~ 10 μM $Ca^{2+}$-step. Remarkably, both the steady-state extent and the kinetics of CDI is unperturbed by application of KN-93. Population data further corroborates this outcome by showing that the *CDI* – [$\mathrm{Ca}^{2+}$] relation upon CaMKII inhibition overlays the wildtype relation (Figure 5.3B). Thus, Na1.4 CDI does not require activation of CaMKII, and CaM action on the channel likely results from a direct interaction with the channel complex. Indeed, prior studies have also shown that CaMKII activation is not necessary for this $\mathrm{Ca}^{2+}$ channel CDI (Budde et al., 2002).

**Functional bipartion of CaM regulation in Na channels** – Additionally, the strong actions of $\mathrm{CaM}_{1234}$ permitted higher-order testing to determine whether one lobe of CaM or the other suffices to trigger Na channel regulation. Such single-lobe signaling would add to the ranks of a functional bipartition paradigm (Preston et al., 1991), richly observed throughout the $\mathrm{Ca}^{2+}$ channel superfamily (Peterson et al., 1999; DeMaria et al., 2001; Liang et al., 2003; Yang et al., 2006). In this regard, we utilized a mutant $\mathrm{CaM}_{12}$ construct, featuring selective inhibition of $\mathrm{Ca}^{2+}$ binding to the N-lobe, but not C-lobe. Coexpressing $\mathrm{Na_V}1.4$ channels with $\mathrm{CaM}_{12}$ also fully abolished $\mathrm{Ca}^{2+}$ regulation (Figure 5.4A), arguing that $\mathrm{Ca}^{2+}$ binding to the N-lobe is essential for CDI. Alternatively, coexpressing $\mathrm{Na_V}1.4$ channels with $\mathrm{CaM}_{34}$ (selective inhibition of $\mathrm{Ca}^{2+}$ binding to C-lobe) entirely preserved CDI (Figure 5.4D), with a profile nearly indistinguishable from control (reproduced as gray). Thus, $\mathrm{Ca}^{2+}$ binding to the N-lobe of CaM is both necessary and sufficient to trigger Na channel CDI. Indeed, the two $\mathrm{Ca}^{2+}$ binding sites within the critical N-lobe fits well with the Hill steepness coefficient of 1.8 observed in *CDI* –[$\mathrm{Ca}^{2+}$] relations (Linse and Forsen, 1995). We note that our result stands in stark contrast to a prior proposal that $\mathrm{Ca}^{2+}$ binding to C-lobe triggers regulation of Na channels (Sarhan et al., 2012; Van Petegem et al., 2012). These results further extend the scheme of functional bipartition well-established in $\mathrm{Ca}^{2+}$ channels to the Na channels. Notably, as Na channels do not convey $\mathrm{Ca}^{2+}$ influx, Na channel regulation is by definition evoked by $\mathrm{Ca}^{2+}$ entry from distant sources. Thus, the N-lobe dependence of Na channel regulation corresponds well with the spatial global $\mathrm{Ca}^{2+}$ decoding scheme established for $\mathrm{Ca_V}2.2$ and $\mathrm{Ca_V}2.3$ channels (Figure 1.5).

**Structural determinants of Na channel regulation -** The CI region of $Ca^{2+}$ channels (Figure 1.5A) suffices to confer $Ca^{2+}$ regulation (de Leon et al., 1995). Yet, prior work in Na channels emphasizes the necessary role of the III-IV loop, a critical determinant for fast inactivation of these channels (Stuhmer et al., 1989; West et al., 1992a). A recent crystal structure of $Ca^{2+}$/CaM complexed with the III-IV loop of $Na_V1.5$ channels further suggests that a conserved tyrosine anchor is necessary for $Ca^{2+}$/CaM binding, and that this binding is required for $Ca^{2+}$ modulation (Figure 5.5A) (Sarhan et al., 2012; Van Petegem et al., 2012). Figure 5.5A contextualizes the location of this anchor in relation to other Na channel landmarks and further demonstrates the conservation of this putative site on the $Na_V1.4$ channels.

Accordingly, we substituted alanine for the homologous tyrosine in $Na_V1.4$ channels (Y[1311]A), and tested for $Ca^{2+}$ regulation. In contrast to prior work, we observed that $Ca^{2+}$ regulation was fully present (Figure 5.5B), with a functional profile indistinguishable from that of wild-type channels. Importantly, a similar $Ca^{2+}$/CaM binding site has been identified in the III-IV loop of $Ca_V1.3$ channels. FRET 2-hybrid data substantiates this binding interaction between YFP-tagged $Ca_V1.3$ III-IV loop with CFP-tagged $Ca^{2+}$/CaM (Figure 5.5C). Deletion of the distal 13 residues from the carboxy-terminus of the III-IV loop peptide strongly diminishes this binding interaction (Figure 5.5C). Functionally, alanine substitution of this entire 13 residue segment failed to alter CDI (Figure 5.5D). Thus, both Na and $Ca^{2+}$ channels do not require $Ca^{2+}$/CaM binding to the III-IV loop for $Ca^{2+}$ regulation.

For $Ca^{2+}$ channels, $Ca^{2+}$ regulation depends strongly upon a CI module in the carboxy-terminus of these channels (de Leon et al., 1995; Ben-Johny et al., 2013a). To explore the role of the Na channel CI region in supporting $Ca^{2+}$ regulation, we undertook a convenient chimeric-channel approach, exploiting the lack of $Ca^{2+}$ regulation in $Na_V1.5$ versus $Na_V1.4$. When the carboxy terminus of $Na_V1.4$ was substituted with its Nav1.5 counterpart, $Ca^{2+}$ regulation was completely eliminated (Figure 5.6A), suggesting that the

$Na_V1.4$ carboxy-terminus contains key structural determinants for Na channel CDI. Yet more telling are results from the 'inverse' chimera that transferred the $Na_V1.4$ carboxy-tail onto the $Na_V1.5$ backbone (Figure 5.6B). Remarkably, this maneuver confers latent $Ca^{2+}$ regulation onto the $Na_V1.5$ channels, with $Ca^{2+}$ responsiveness nearly identical to that of $Na_V1.4$ (Figure 5.6B, gray trace). These results strongly suggest that the Na channel carboxy-terminus contains essential structural components necessary for $Ca^{2+}$ regulation. Moreover, it could be suggested that ancestral $Na_V1.5$ channels overtly exhibited CDI, but that modern-day variants possess a latent capability for CDI owing to sequence drift at a limited number of carboxy tail positions. Furthermore, it is interesting that similar chimeric studies that swapped the carboxy-tail domains of $Ca^{2+}$ channels have successfully demonstrated the transference of CaM regulatory properties (Mori et al., 2008). Thus, the overall regulatory scheme of both Na and $Ca^{2+}$ channels appears to depend crucially on their conserved carboxy-tail segments.

Encouraged by these findings, we further considered the effects of limited mutations within the IQ element (Figure 3.1A, blue shaded zone), which potently alter $Ca^{2+}$ regulation of $Ca^{2+}$ channels (Peterson et al., 1999; Zuhlke et al., 1999; Zuhlke et al., 2000; Bazzazi et al., 2013; Ben-Johny et al., 2013a). When dual alanines were substituted for contiguous isoleucine and glutamine residues in the center of the $Na_V1.4$ IQ element, the $Ca^{2+}$-dependent inhibition of these channels was not merely eliminated, but converted into outright facilitation (CDF, Figure 5.7A). Coexpression of mutant $CaM_{1234}$ abolished this latent CDF of $Na_V1.4$ IQ/AA channels, suggesting that this switch in Na channel regulatory function still depended upon CaM as a $Ca^{2+}$-sensor. More importantly, similar effect has been reported for L-type $Ca^{2+}$ channels where CDI is converted into an outright facilitation upon mutagenesis of analogous loci (Zuhlke et al., 1999; Zuhlke et al., 2000; Pitt et al., 2001). The mechanistic basis of this switch in polarity of CaM regulatory function is an important question that remains to be resolved. In all, like $Ca^{2+}$ channels, the carboxy tail of Na channels contains the needed structural determinants for CDI, even regarding inversion of regulatory polarity by like mutations therein.

**Pathophysiological implications of Na channel CDI** – Of further biological concern, several channelopathic mutations have been identified in the carboxy terminus of Na channels, but the alterations in channel function that underlie pathogenesis have not been fully resolved. Given the prominent role of the Na channel carboxy-terminus in eliciting $Ca^{2+}$/CaM regulation, could these channelopathic mutations result in diminished regulatory function? Figure 5.8 explicitly investigates this possibility for $Na_V1.4$ channelopathic mutations associated with potassium-aggravated myotonia (Kubota et al., 2009) and cold-aggravated myotonia (Wu et al., 2005). In both instances, $Ca^{2+}$ regulation is substantially reduced (Figure 5.8 A-B). Thus, altered $Ca^{2+}$/CaM regulation of Na channels may contribute to the various pathophysiological mechanisms underlying heritable forms of myotonia and other skeletal muscle disorders. More generally, numerous channelopathic mutations have also been identified in the carboxy-terminus of other Na channels resulting in a wide-range of diseases (Bezzina et al., 1999; Zimmer and Surber, 2008; Lossin, 2009; Catterall et al., 2010; Dolz-Gaiton et al., 2013). As such, the potential role for alterations in $Ca^{2+}$/CaM regulation of Na channels in relation to human disease represents an important frontier with far-reaching consequences.

## DISCUSSION

In all, our functional results demonstrate that $Ca^{2+}$ regulation of both $Ca^{2+}$ and Na channels are eerily similar. Both channel families outsource $Ca^{2+}$ sensing functions to the ubiquitous $Ca^{2+}$ sensing molecule, CaM. The ‘functional-bipartition’ scheme of CaM function well-established in $Ca^{2+}$ channels now extends in a highly similar manner to Na channels. Both channels utilize a conserved carboxy-terminal channel segment to support both apoCaM and $Ca^{2+}$/CaM interactions. That said, the precise nature of these interactions and downstream conformational changes associated with CaM regulation of both channel families is yet to be determined. The commonalities identified in $Ca^{2+}$ and

Na channel $Ca^{2+}$ regulation raise hope towards a general regulatory scheme that pervades across both channel families. Thus, the CI region of both channels may correspond to an ancient $Ca^{2+}$ regulatory design that has been long-shared between these channel families – a possibility further considered in Chapter 8.

Of biological relevance, the demonstration of $Ca^{2+}$ regulation in skeletal myotubes (Figure 3.6B) along with finding that channelopathic mutations dramatically alter $Ca^{2+}$ regulation of Na channels raise the attractive hypothesis that Na channel CDI may play a physiological role in activity-dependent feedback control of skeletal-muscle excitability. This CDI might normally raise the threshold for muscle excitation during repetitive activity, thereby protecting against overexcitability caused by rapidly elevating levels of extracellular K seen during sustained contraction (Cannon, 1997). Weakening of CDI by channelopathic mutations might predispose for these debilitating myotonias (Hayward et al., 1997). In this regard, the results in this chapter furnish the essential foundations for testing these and other related hypotheses.

Lastly, the identification of latent $Ca^{2+}$/CaM regulation of $Na_V1.5$ channels raises the possibility that perhaps only a few amino-acid dissimilarities in the carboxy-terminal region may underlie the switching of $Ca^{2+}$ regulation. Could post-transcriptional or post-translational modifications of the $Na_V1.5$ channel then re-enable $Ca^{2+}$ regulation? In fact, recent studies of $Ca^{2+}$ channels have demonstrated that alternative splicing of their carboxy-termini could enable $Ca^{2+}$/CaM regulation isoforms (Tan et al., 2011). Moreover, given the high degree of sequence homology between carboxy-termini of various Na channel isoforms, it now seems likely that many of these channels may also elaborate functional $Ca^{2+}$/CaM regulation. These possibilities represent an exciting new frontier of research.

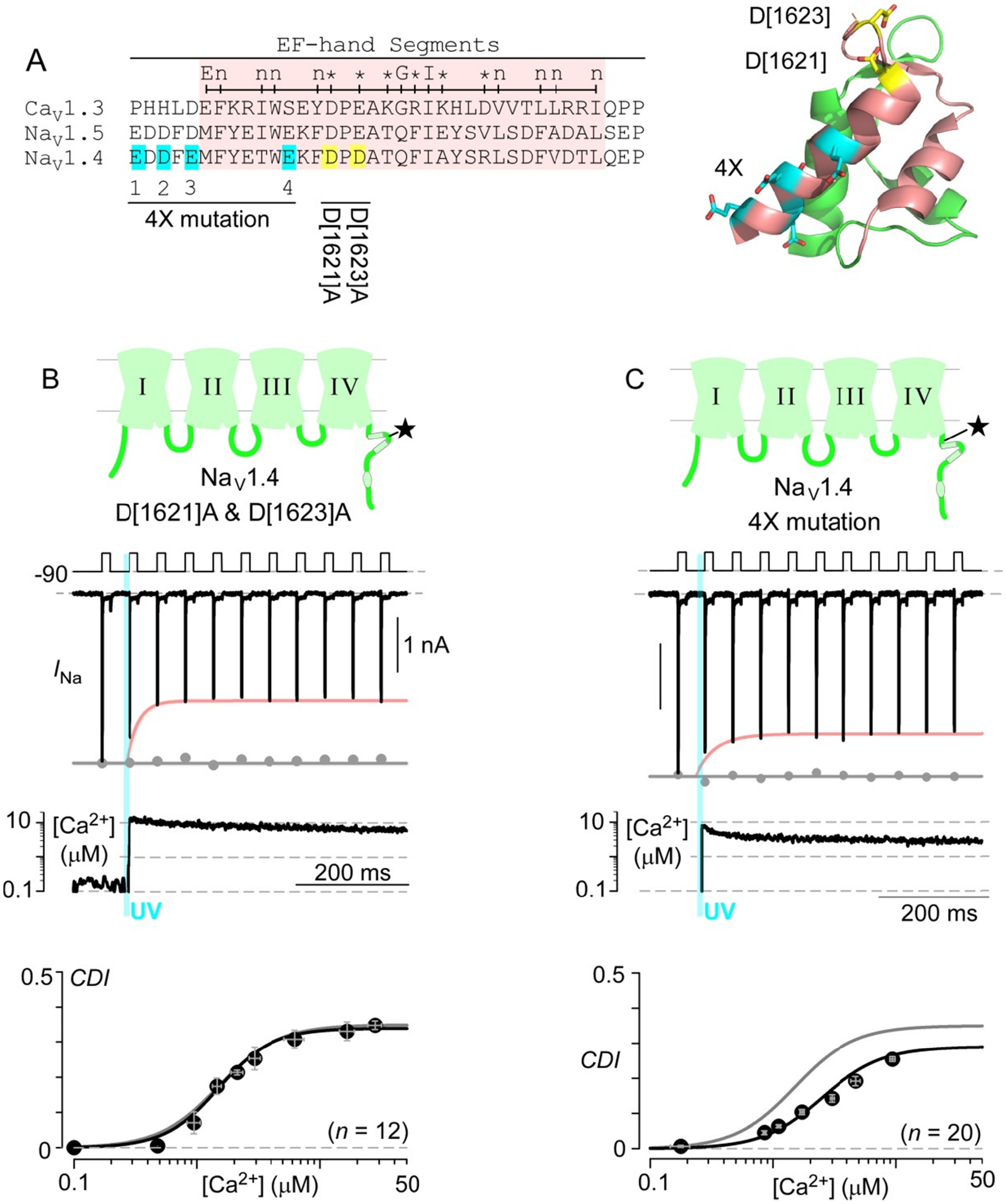
A
EF-hand Segments
En nn n* * *G*I* *n nn n
CaV1.3 PHHLDEFKRIWSEYDPEAKGRIKHLDVVTLLRRIQPP
NaV1.5 EDDFDMFYEIWEKFDPEATQFIEYSVLSDFADALSEP
NaV1.4 EDDFEMFYETWEKFDPDATQFIAYSRLSDFVDTLQEP
1 2 3 4
4X mutation
D[1621]A
D[1623]A
D[1623]
D[1621]
4X
B
I
II
III
IV
NaV1.4
D[1621]A & D[1623]A
-90
1 nA
INa
10
[Ca2+]
(μM)
0.1
200 ms
UV
0.5
CDI
0
(n = 12)
0.1
[Ca2+] (μM)
50
C
I
II
III
IV
NaV1.4
4X mutation
10
[Ca2+]
(μM)
0.1
UV
200 ms
0.5
CDI
0
(n = 20)
0.1
[Ca2+] (μM)
50

**Figure 5.1. Na channel dual vestigial EF hands are not the $Ca^{2+}$ sensor for CDI**

(A) Left, sequence alignment of the first vestigial EF hand segment of Na and $Ca^{2+}$ channels along with Tufty-Kretsinger consensus criteria for EF hand motif. Historically, four oxygen-bearing residues (cyan highlight) of the $Na_V1.5$ vestigial EF hand region were proposed to support direct binding of $Ca^{2+}$ to Na channel ('4×') (Wingo et al., 2004; Biswas et al., 2009). However, these residues reside outside of the putative $Ca^{2+}$-binding loop of the vestigial EF hand and thus are unlikely to coordinate $Ca^{2+}$ ions. Alternative oxygen bearing residues within the Na channel vestigial EF hand is highlighted in yellow. Right, atomic structures (Miloushev et al., 2009; Wang et al., 2012) of Na channel EF-hand segment shows the location of '4×' residues (E[1621], D[1623], E[1625], E[1632]) and two oxygen-bearing residues of Na channel EF hand within the actual $Ca^{2+}$ binding loop that may bind $Ca^{2+}$ ions (D[1621] and D[1623]).

(B) Alanine substitution of D[1621] and D[1623] residues (yellow in panel A) within the $Ca^{2+}$-binding loop of Na channel vestigial EF hand 1 spares $Ca^{2+}$-dependent inactivation suggesting that any potential $Ca^{2+}$ binding to these residue may be functionally irrelevant for Na channel regulation. Each symbol, mean ± SEM of 3 uncaging events compiled from 12 cells. Format as in Figure 3.6A.

(C) $Ca^{2+}$ uncaging experiments show that $Na_V1.4$ channels with alanine substitution of the 4× residues (panel A, cyan) can undergo robust CDI, much like the alternative EF hand mutations described in panel B. Middle, exemplar Na current shows CDI in response to ~3 μM $Ca^{2+}$ step. Format as in Figure 3.6A. Bottom, population average shows average *CDI* as a function of $[Ca^{2+}]$ (black symbols and trace). The minor reduction in maximal *CDI*, and the slightly weakened $Ca^{2+}$ affinity may hint at a potential role for this region as a CDI transduction element. Each symbol, mean ± SEM from 9-10 uncaging events compiled from 20 cells.

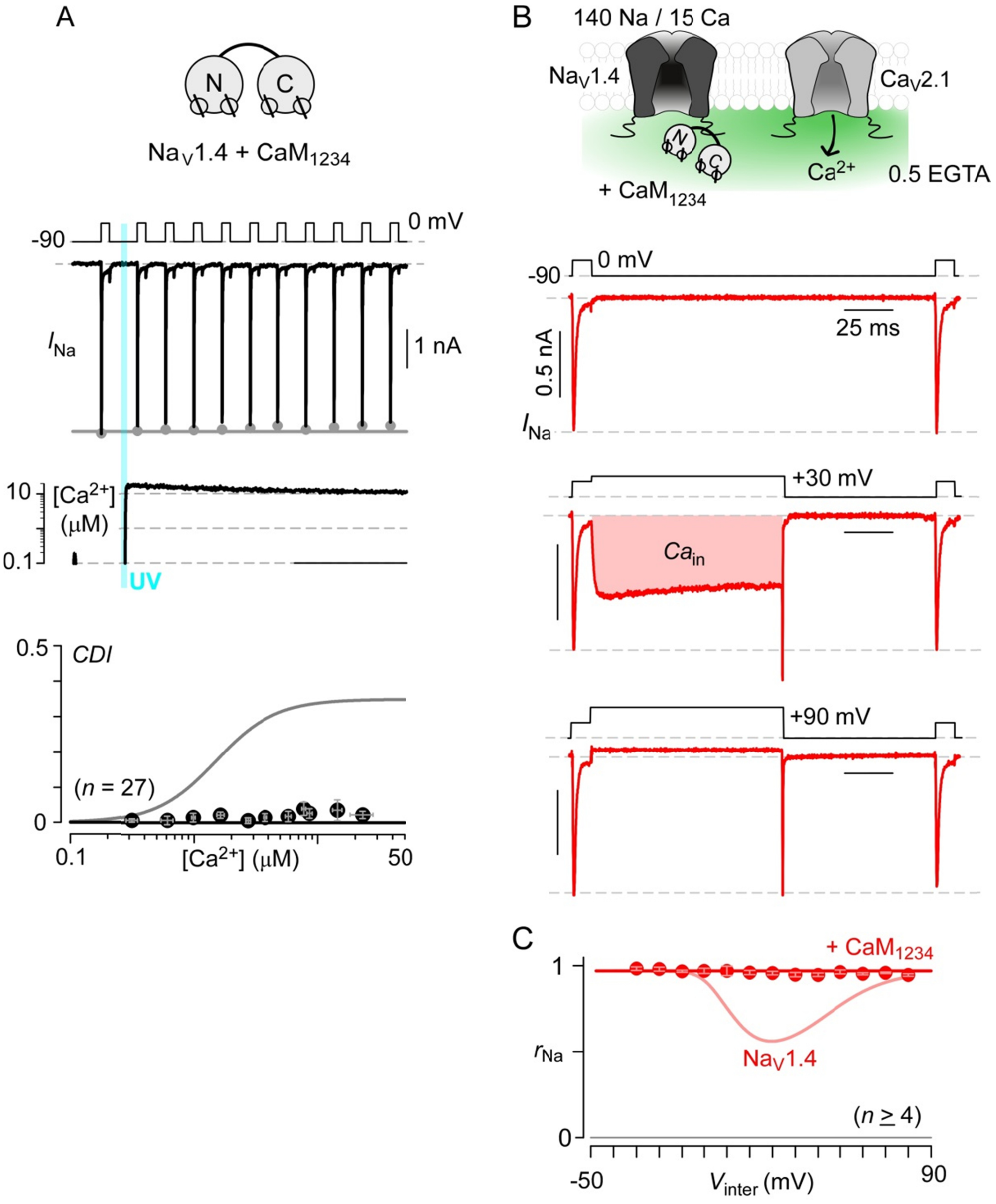
A
N
C
Na$_V$1.4 + CaM$_{1234}$
0 mV
-90
$I_{Na}$
1 nA
10
[Ca$^{2+}$]
(μM)
0.1
UV
0.5
CDI
(n = 27)
0
0.1
[Ca$^{2+}$] (μM)
50
B
140 Na / 15 Ca
Na$_V$1.4
Ca$_V$2.1
N
C
Ca$^{2+}$
+ CaM$_{1234}$
0.5 EGTA
-90
0 mV
25 ms
0.5 nA
$I_{Na}$
+30 mV
Ca$_{in}$
+90 mV
C
+ CaM$_{1234}$
1
$r_{Na}$
Na$_V$1.4
(n ≥ 4)
0
-50
$V_{inter}$ (mV)
90

**Figure 5.2. CaM is $Ca^{2+}$ sensor for Na channel CDI**

(A) Since Na channels undergo fast inactivation within the first few milliseconds following depolarization, the timecourse and magnitude of the slower $Ca^{2+}$-dependent regulation of Na channels was deduced from the 'envelope' of peak Na currents pulsed at regular intervals after $Ca^{2+}$ uncaging. To ensure that $Na_V1.4$ $Ca^{2+}$ regulation is independent of this pulse rate, CDI was characterized for Na currents evoked at multiple pulse rates (20 Hz, panel A; 10 Hz, panel B; 5 Hz, panel C; 2 Hz, panel D) in a single cell. Gray dots and fit correspond to peak currents prior to $Ca^{2+}$ uncaging. Following $Ca^{2+}$ uncaging (cyan line), current amplitudes declined rapidly, revealing CDI in response to ~5 μM $Ca^{2+}$ steps. Red envelope curves are identical for various pulse rates, confirming that the onset of CDI is independent of pulse rate.

(B) $Ca^{2+}$ regulation of Na channels can be triggered by $Ca^{2+}$ influx through nearby $Ca_V2.1$ channels (Figures 3A-3D). Here, exemplar current records show that coexpression of mutant $CaM_{1234}$ abolishes this modulation, confirming that CaM is the $Ca^{2+}$ sensor for regulation of $Na_V1.4$ channels. Format as in Figures 3.8B-3.8D.

(C) Population data plots $Ca^{2+}$ regulation metric $r_{Na}$ (Figure 3.8C) as a function of interpulse voltage $V_{inter}$. Format as in Figure 3.8G. Indeed, coexpression of $CaM_{1234}$ abolishes CDI of $Na_V1.4$ channels, with rose fit reproduced from Figure 3.8G as reference. These results argue that $Ca^{2+}$ regulation of $Na_V1.4$ observed with $Ca^{2+}$ uncaging or $Ca^{2+}$-spillover from nearby $Ca_V2.1$ channels, both depend on the same process as mediated by CaM. Each symbol represents mean ± SEM from 4 or more cells.

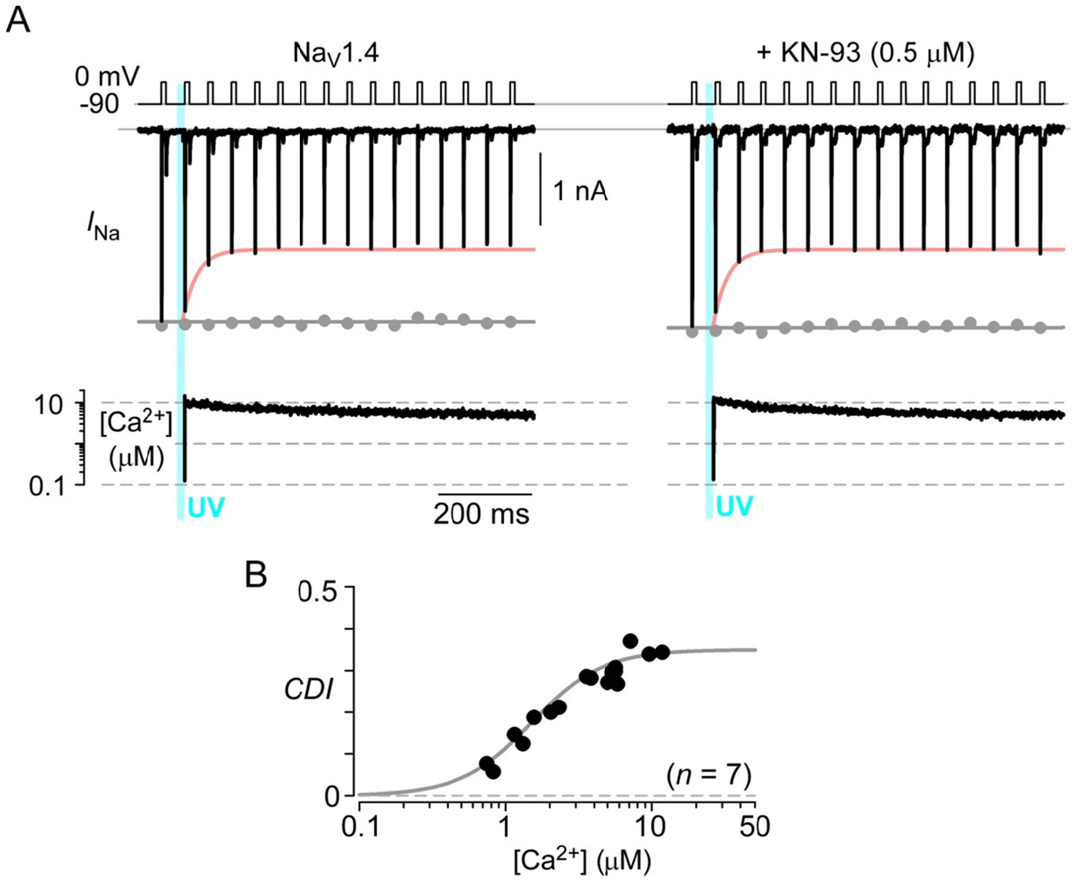

**Figure 5.3. Na channel $\text{Ca}^{2+}$ regulation does not depend on CaMKII.**

(A) Left, exemplar $\text{Na}_\text{V}$1.4 currents exhibit robust CDI. Right, this robust CDI is preserved following the application of 0.5 μM KN-93, a potent inhibitor of CaMKII, for 3-30 minutes. Indeed, the kinetics and steady-state extent of CDI appear unaltered by inhibition of CaMKII. Format as in Figure 3.6A.

(B) Population data (black symbols) confirm that application of KN-93 does not alter the steady-state CDI versus $\text{Ca}^{2+}$ relationship. Gray fit, control CDI versus $\text{Ca}^{2+}$ relationship for $\text{Na}_\text{V}$1.4 channels (from main text Figure 3.6A). Overall, these results demonstrate that CDI of Na channels does not require CaMKII activation, further strengthening the case for CaM as a direct modulator of Na channels.

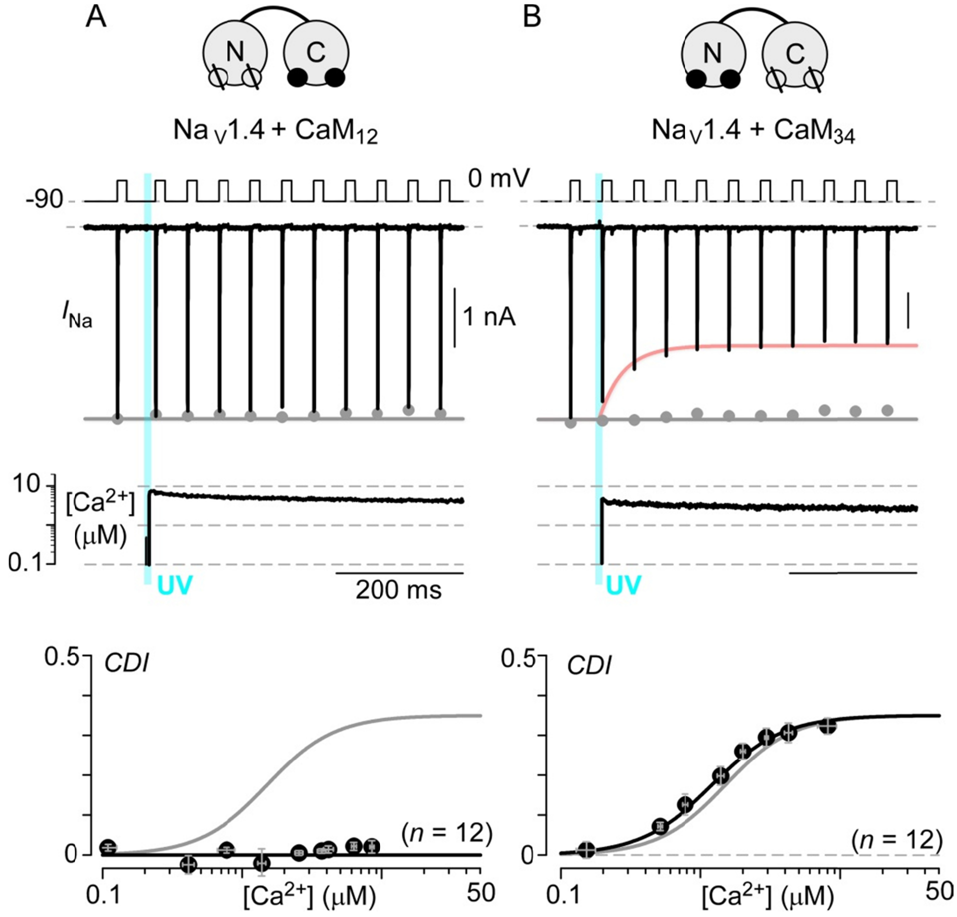

**Figure 5.4. Functional bipartition of Na channel CaM regulation.**

(A) For $Ca^{2+}$ channels, CaM regulation is 'functionally bipartitioned' whereby individual lobes of CaM can elicit distinct modes of channel regulation (Figure 1.5). For some $Ca_V2$ channels, CDI is restricted to just the N-lobe of CaM. Here, coexpression of mutant $CaM_{12}$, with $Ca^{2+}$ binding enabled only to the N-lobe, abolishes Na channel CDI suggesting that N-lobe of CaM is essential for channel regulation. Each symbol, mean ± SEM of 4-5 uncaging events compiled from 12 cells.

(B) By contrast, overexpression of $CaM_{34}$, with $Ca^{2+}$-binding to C-lobe disabled, sustains full-strength Na channel CDI arguing that $Ca^{2+}$ binding to this lobe is functionally irrelevant to CDI. Each symbol, mean ± SEM of approximately 5 uncaging events compiled from 12 cells.

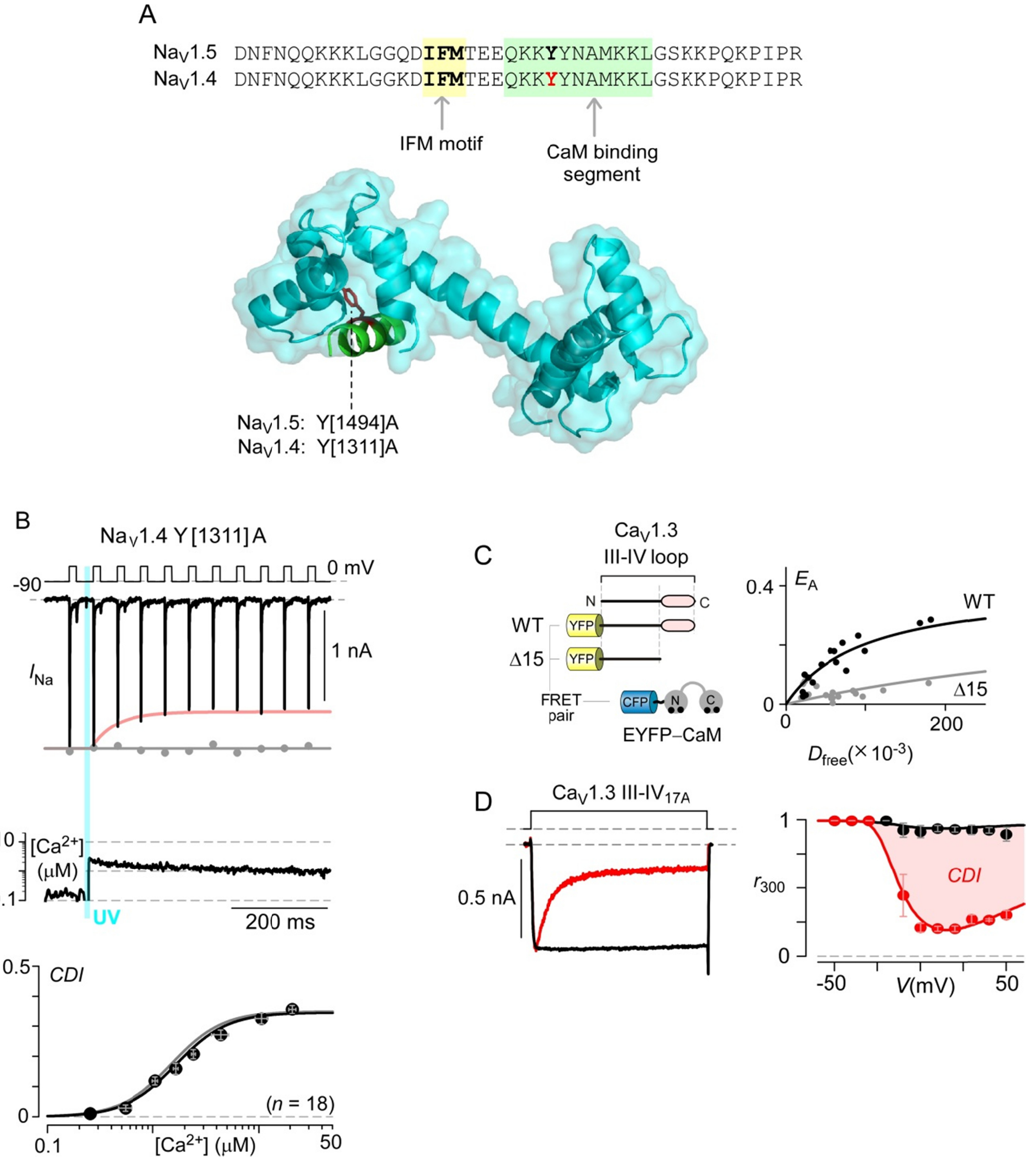
A
NaV1.5 DNFNQQKKKLGGQDIFMTEEQKKYYNAMKKLGSKKPQKPIPR
NaV1.4 DNFNQQKKKLGGKDIFMTEEQKKYYNAMKKLGSKKPQKPIPR
IFM motif
CaM binding segment
NaV1.5: Y[1494]A
NaV1.4: Y[1311]A
B
NaV1.4 Y[1311]A
0 mV
-90
1 nA
INa
10
[Ca2+]
(μM)
0.1
UV
200 ms
0.5
CDI
0
(n = 18)
0.1
[Ca2+] (μM)
50
C
CaV1.3
III-IV loop
N
C
WT
YFP
Δ15
YFP
FRET pair
CFP
N
C
EYFP–CaM
0.4
EA
WT
0
Δ15
0
200
Dfree(× 10-3)
D
CaV1.3 III-IV17A
0.5 nA
1
r300
CDI
0
-50
V(mV)
50

**Figure 5.5. Na channel III-IV loop is not a structural determinant for $Ca^{2+}$ regulation.**

(A) Top, sequence alignment of $Na_V1.4$ and $Na_V1.5$ III-IV loop. The proximity of this binding site to a primary structural determinant of fast inactivation localized to the tri-residue 'IFM' motif (West et al., 1992a) (yellow shading) is also diagrammed. $Ca^{2+}$/CaM binding site within the Na channel III-IV loop is highlighted in green. Bottom, the crystal structure of $Na_V1.5$ III-IV loop bound to $Ca^{2+}$/CaM (PDB code: 4DJC (Sarhan et al., 2012)). Engagement of the critical tyrosine residue ($Na_V1.5$, Y[1494]; $Na_V1.4$, Y[1311]) is colored in red.

(B) Mutating Na channel III-IV loop $Ca^{2+}$/CaM anchor spares CDI. Based on a crystal structure of $Na_V1.5$ III-IV loop complexed with $Ca^{2+}$/CaM (Sarhan et al., 2012; Van Petegem et al., 2012), the Y[1311] residue of $Na_V1.4$ corresponds to a highly conserved hydrophobic anchor for $Ca^{2+}$/CaM (panel A). Format as in Figure 3.6A. Each symbol, mean ± SEM of 4-5 uncaging events compiled from 18 cells.

(C) Similar to Na channels, the $Ca^{2+}$ channel ($Ca_V1.3$) III-IV loop also contains a $Ca^{2+}$/CaM binding site. Left, cartoon depicts FRET 2-hybrid experiments of $Ca^{2+}$/CaM binding to both the full-length III-IV loop segment and a variant with a 15-residue deletion from the carboxy-terminal end of this segment (Δ15). Right, plotting FRET efficiency ($E_A$) as a function of $D_{free}$ (relative free concentration of ECFP-CaM) reveals a binding relation for full-length III-IV loop (black symbols and fit). The Δ15 mutant of the III-IV loop diminishes $Ca^{2+}$/CaM binding significantly (gray symbols and fit).

(D) The functional relevance of this novel $Ca^{2+}$/CaM binding site on $Ca_V1.3$ III-IV loop was probed by substitution of the last 17 residues with alanines, since the deletion of this segment was detrimental to channel expression. CDI of $Ca^{2+}$ channels is spared by this manipulation. Left, exemplar currents for this mutant channel. Right, population average of $r_{300}$ CDI metric defined in Figure 3.1C. Each symbol corresponds to mean ± SEM.

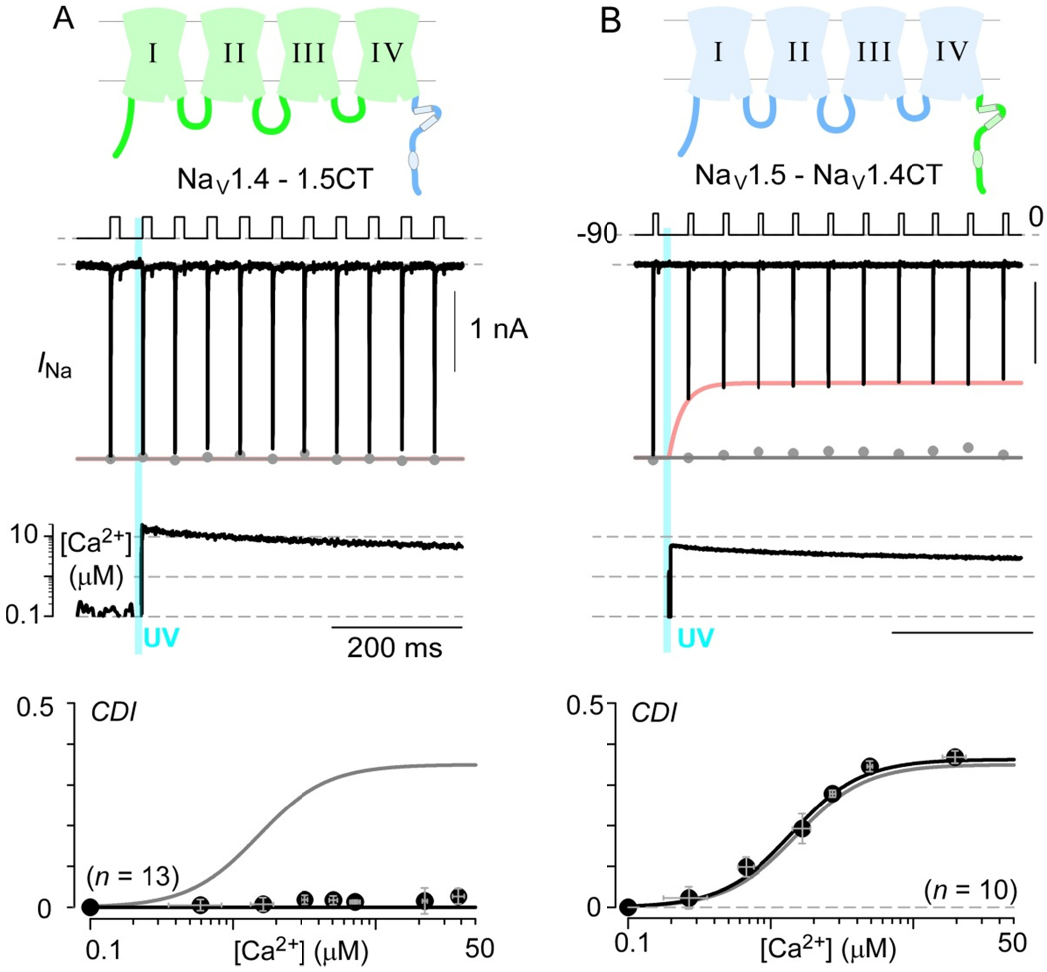

**Figure 5.6. Ca$^{2+}$ regulation depends crucially on the Na channel carboxy-terminus.**

(A) Here, we exploit the absence of Na$_V$1.5 Ca$^{2+}$ regulation to probe for functional relevance of the Na channel carboxy-terminus (CT). We constructed a chimeric Na$_V$1.4 channel with Na$_V$1.5 CT substituted. Na$_V$1.4 CDI is eliminated by this maneuver, suggesting that the = carboxy-terminus contains key structural elements for CDI. Each symbol, mean ± SEM of 4-5 uncaging events from 13 cells. Format as in Figure 3.6A.

(B) Transferring the carboxy terminus of Na$_V$1.4 to the Na$_V$1.5 backbone, yielding Na$_V$1.5-1.4CT chimeric channels, transfers latent Ca$^{2+}$-regulation with Ca$^{2+}$ sensitivity and maximal CDI similar to wild-type Na$_V$1.4 (gray fit in bottom subpanel). Format as in Figure 3.6A. Each symbol, mean ± SEM from 4-5 uncaging events from 10 cells.

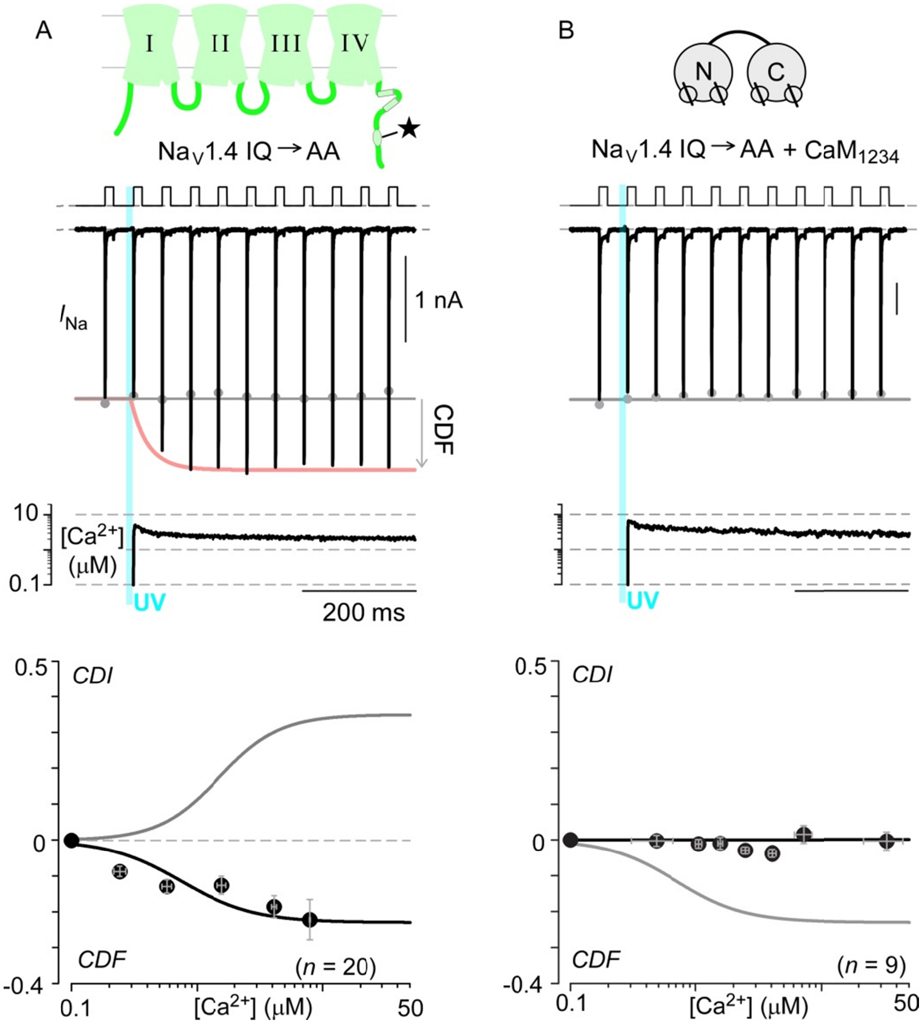

**Figure 5.7. Na$_V$1.4 IQ/AA unveils latent facilitation.**

(A) Given the importance of both CaM and Na$_V$1.4 CT in Na channel Ca$^{2+}$ regulation, we substituted dual alanines for the key isoleucine-glutamine ('IQ') residues in Na$_V$1.4 IQ domain. This mutation unveiled latent facilitation (CDF) of the Na currents. Similar effect has been observed for Ca$_V$1.2 channels. Top, exemplar currents and corresponding Ca$^{2+}$ traces. Bottom, population average depicts facilitation as negative *CDI*. Each symbol, mean ± SEM of approximately 13 uncaging events compiled from 20 cells.

(B) Coexpression of CaM$_{1234}$ abolishes latent CDF of Na$_V$1.4 IQ/AA suggesting that this process is also mediated by CaM action on the channel. The structural correlate for Na$_V$1.4 CDF remains to be identified.

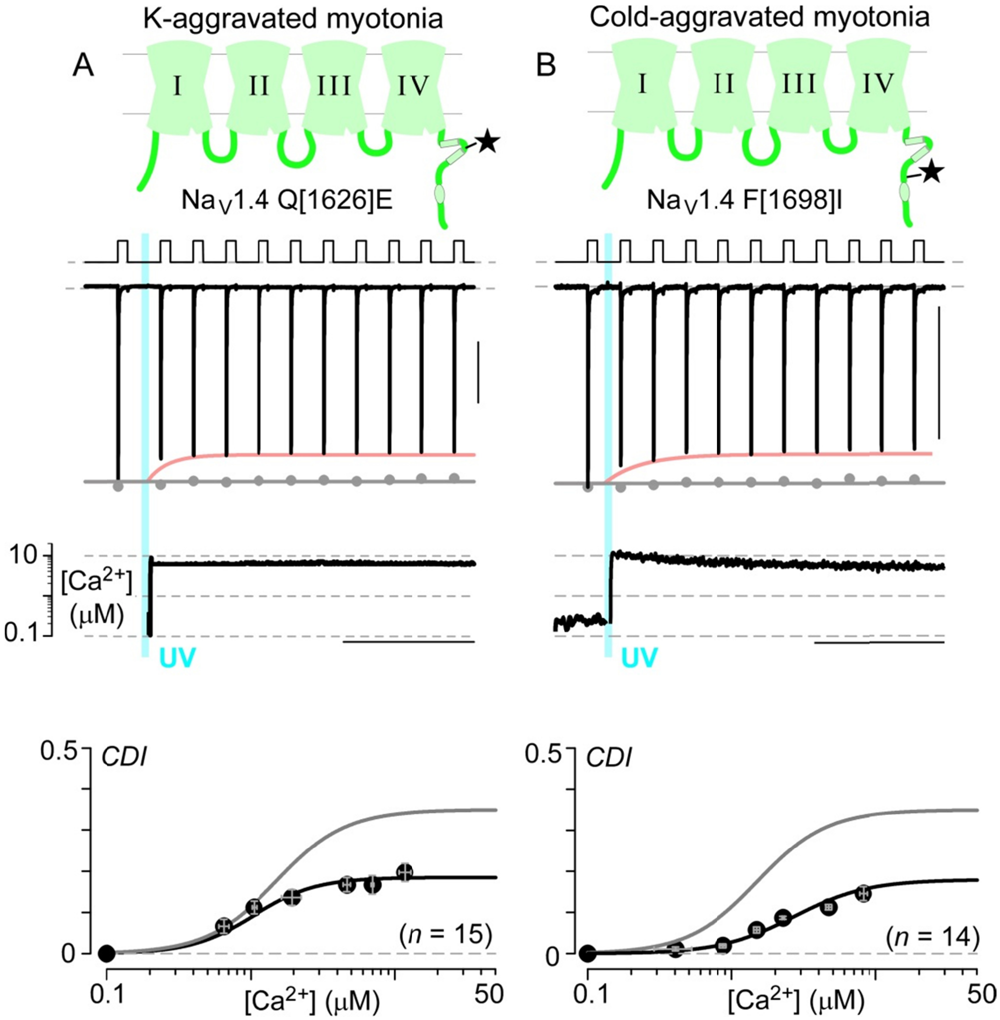

**Figure 5.8. Pathophysiological consequences of Na channel $Ca^{2+}$ regulation.**

(A) Two channelopathic mutations of Na$_V$1.4 that result in heritable forms of myotonia have been identified on the channel carboxy-terminus. The mutation Q[1626]E has been associated with K-aggravated myotonia. Recombinant Na$_V$1.4 channels bearing this mutation shows dramatically diminished CDI. Each symbol, mean ± SEM from approximately 9 uncaging events compiled from 15 cells.

(B) The mutation F[1698]I has been associated with cold-aggravated myotonia. CDI is sharply attenuated for recombinant Na$_V$1.4 channels bearing this mutation Each symbol, mean ± SEM from approximately 9 uncaging events compiled from 14 cells.

## CHAPTER 6

# A general framework for Ca$^{2+}$ channel calmodulation

Our results in Chapters 3 - 5 illustrate the unparalleled similarity in Ca$^{2+}$ regulation of Na and Ca$^{2+}$ channels. Past structural studies of the Ca$^{2+}$ channel Ca$^{2+}$ regulation has argued for an IQ centric hypothesis for channel regulation (Figure 1.7), where apoCaM starts preassociated to the channel IQ domain and then upon Ca$^{2+}$ binding, reassociates with the same segment in a subtly altered conformation. However, as discussed in the Chapter 1, this model of channel regulation has key shortcomings. Here, to elucidate the molecular underpinnings of this conserved regulatory process, we turned to the L-type Ca$^{2+}$ channel Ca$_V$1.3 with prototypic modulation for systematic structure-function analysis utilizing extensive mutagenesis. In particular, two features of these channels make them well-suited for such in-depth examination. First, Ca$^{2+}$ regulation of these channels manifests as a rapid and strong CDI readily quantifiable by comparison of steady-state current decay with Ca$^{2+}$ versus Ba$^{2+}$ ion influx (Figure 3.1B).

Second, these channels elaborate robust N- and C-lobe components of CDI even in the presence of high intracellular $Ca^{2+}$ buffering, where only local $Ca^{2+}$ signals are present. This feature ensures that $Ca^{2+}$ regulation is largely independent of current density, and thus facilitates the comparison of CDI observed from mutant channels with variable membrane expression. In this chapter, we formulate a general theoretical framework that rigorously evaluates the functional relevance of putative molecular interactions in $Ca^{2+}$ regulation of $Ca^{2+}$ channels with potential implications for Na channels.

## THEORY

***A conceptual scheme for CaM regulation*** – Critical for understanding and manipulating CaM regulatory system is identification of the conformations that underlie $Ca^{2+}$ modulation. Figure 6.1A illustrates the currently accepted scheme in conceptual form, with specific reference to $Ca_V1.3$ channels for concreteness. Configuration $E$ ('empty' of CaM) corresponds to channels that lack preassociated $Ca^{2+}$-free CaM (apoCaM). Such channels lack $Ca^{2+}$/CaM-dependent inactivation (CDI) over the typical duration of channel-activity measurements (Liu et al., 2010) (~300 msec). Over this brief period, $Ca^{2+}$/CaM from the cytosol cannot appreciably access a channel in configuration $E$ to elicit CDI (Mori et al., 2004; Yang et al., 2007; Liu et al., 2010; Findeisen et al., 2011). ApoCaM preassociation with configuration $E$ results in channels in configuration $A$, where channel openings proceed normally and CDI could be triggered. $A$ thereby denotes channels that are both 'active' and capable of CDI. The switching of channels between configurations $E$ and $A$ occurs slowly (>10s of secs (Chaudhuri et al., 2005; Adams et al., 2014)), and almost exclusively involves apoCaM, as high intracellular $Ca^{2+}$ buffering prevents global $Ca^{2+}$ elevations. Thus, there is negligible exchange with configuration $E$ in the course of a typical recording. Regarding CDI, $Ca^{2+}$ binding to the two lobes of CaM elicits configuration $I_{CN}$ (both C and N lobes of CaM engaging effector interfaces), corresponding to a $Ca^{2+}$-inactivated channel with sharply attenuated opening (Kim et al., 2004c; Halling et al., 2006). As for intermediate configurations (Peterson et al., 1999; DeMaria et al., 2001; Lee et al., 2003; Yang et al., 2006; Tadross et al., 2008), $Ca^{2+}$ binding the C-lobe of CaM alone induces configuration $I_C$, representing a C-lobe inactivated channel with diminished opening . $Ca^{2+}$ binding only to the N-lobe yields configuration $I_N$, signifying an N-lobe inactivated channel, also with reduced opening. Subsequent entry into configuration $I_{CN}$ likely involves cooperative interactions denoted by a λ symbol. Overall, CDI reflects redistribution of channels from configuration *A* into configurations $I_C$, $I_N$, and $I_{CN}$. Importantly, cases where only a single $Ca^{2+}$ binds a lobe of CaM are excluded as $Ca^{2+}$ binding within individual lobes is highly cooperative (Linse et al., 1991). Moreover, only a single CaM is included in this layout based on prior experimental evidence (Mori et al., 2004; Yang et al., 2007).

A major ambiguity with prior structure-function analyses of the channel effector interfaces such as the IQ domain is that that functional characterization was mostly performed with only endogenous CaM present (Zuhlke et al., 1999; Zuhlke et al., 2000; Pitt et al., 2001; Kim et al., 2004c; Mori et al., 2008). In this regime, observed changes in CaM regulation by IQ mutations could correspond to perturbations of multiple transitions within the conceptual layout in Figure 6.1A, whereas interpretations mainly associate the effects of mutations to altered $Ca^{2+}$/CaM binding to an IQ effector site. For example, while the high apoCaM affinity of most wild-type channels (Erickson et al., 2003; Liu et al., 2010) renders configuration *E* unlikely (Figure 6.1A), this may not be true for certain mutant channels. Mutations weakening apoCaM binding could reduce CDI by favoring configuration *E* (Figure 6.1A), without any apparent effects on $Ca^{2+}$/CaM binding. Moreover, the functional effects of channel mutations that weaken interaction with one lobe of $Ca^{2+}$/CaM could be masked by cooperative steps (λ in Figure 6.1A).

Experimentally, these challenges can be overcome by simple manipulations of the CaM regulatory system that exploits exogenous expression of wildtype and mutant CaM molecules. Figure 6.1B depicts the CDI of $Ca_V1.3$ channels recombinantly expressed in HEK293 cells, with only endogenous CaM present. Strong CDI is apparent from the rapid decay of whole-cell $Ca^{2+}$ current (black trace), compared with minimal decline of $Ba^{2+}$ current (gray trace). Because $Ba^{2+}$ binds negligibly to CaM (Chao et al., 1984), the fractional decline of $Ca^{2+}$ versus $Ba^{2+}$ current after 300-ms depolarization quantifies the steady-state extent of CDI (Figure 6.1B, right, *CDI* parameter). The CDI observed here reflects the operation of the entire Figure 6.1A system, as schematized at the bottom of Figure 6.1B. The diamond-shaped subsystem lacking configuration *E* (Figure 6.1C, bottom) can be formally isolated by utilizing mass action and several-fold overexpression of wild-type CaM ($CaM_{WT}$). CDI probed thus (Figure 6.1C) is identical to that with only endogenous CaM present (Figure 6.1B), owing to the high affinity of wild-type $Ca_V1.3$ for apoCaM. Full deconstruction of CDI can be attained with the coexpression of channels with a mutant CaM that only permits $Ca^{2+}$ binding to its C-terminal lobe (Peterson et al., 1999) (Figure 6.1D, $CaM_{12}$). This maneuver depopulates configuration *E* by mass action, and forbids access into configurations $I_N$ and $I_{CN}$ (Figure 6.1A). Thus, the isolated C-lobe component of CDI (Yang et al., 2006; Tadross et al., 2008) is resolved (Figure 6.1D), with its distinctive rapid kinetics of current decay. Importantly, this regime avoids interplay with cooperative $\lambda$ steps in Figure 6.1A. Similarly, coexpressing mutant CaM exhibiting $Ca^{2+}$ binding to its N-lobe alone (Peterson et al., 1999) ($CaM_{34}$) isolates the kinetically slower N-lobe form of CDI (Yang et al., 2006; Tadross et al., 2008) (Figure 6.1E), with attendant simplifications. Such manipulations combined with extensive alanine scanning mutagenesis of the $Ca_V1.3$ channel segments, can be utilized to identify relevant molecular interfaces underlying calmodulation, as described in Chapter 7.

**iTL analysis of CaM/channel regulation** – Deducing the actual channel effector interface for $Ca^{2+}$/CaM is a formidable challenge. The main $\alpha_1$ subunit of $Ca^{2+}$ channels alone is composed of two-thousand amino acids or more; and peptide assays suggest that $Ca^{2+}$/CaM can bind to multiple regions with uncertain functional consequences (Ivanina et al., 2000; Pate et al., 2000; Kim et al., 2004c; Fallon et al., 2009; Asmara et al.; Kim et al., 2010). Even if mutating these segments alters CaM regulation, the observed functional effects need not involve $Ca^{2+}$/CaM binding, but could reflect perturbations of transduction or preassociation. To address these ambiguities, we first consider an expanded conceptual framework believed valid for either isolated N- or C-lobe CDI (Tadross et al., 2008) (Figure 6.2A), then deduce from this scheme a simple quantitative analysis to identify actual effector sites. An apoCaM lobe begins prebound to a channel preassociation interface (state 1). $Ca^{2+}$ binding to CaM in this state is thought unlikely. However, after apoCaM detaches from the preassociation site (state 2), it may bind $Ca^{2+}$ ions to yield $Ca^{2+}$/CaM (state 3), or it may rebind the preassociation site (state 1). This transiently dislodged lobe of CaM (state 2 or 3) remains within the channel complex over the timescale of CaM regulation (≤ seconds). Finally, $Ca^{2+}$/CaM binds a channel effector site (state 4, square pocket), ultimately eliciting regulation via a transduction step to state 5. This final step may include the un/binding of alternate channel segments from/to each other.

Despite the presence of multiple transitions in this reduced subsystem for single-lobe CDI, a simple relationship that will aid detection of $Ca^{2+}$/CaM interfaces on the channel can be deduced as follows. Suppose we can introduce point alanine mutations into the channel that selectively perturb the $Ca^{2+}$/CaM binding association constant $\gamma_1$ (Figure 6.2A). Also suppose we can measure $Ca^{2+}$/CaM binding to a corresponding channel peptide, and the affiliated association constant $K_{\mathrm{a,EFF}}$ is proportional to $\gamma_1$ in the channel. It then turns out that our metric of inactivation (*CDI* in Figure 6.1B) will always follow the Langmuir function

$$CDI = CDI_{\max} \cdot K_{\mathrm{a,EFF}} / (K_{\mathrm{a,EFF}} + \Lambda) \tag{6.1}$$

where $CDI_{\max}$ is the value of *CDI* if $K_{\mathrm{a,EFF}}$ becomes exceedingly large, and $\Lambda$ is a constant comprised of other association constants in the layout. The explicit terms that contribute to $\Lambda$ for C- and N-lobe of CaM will be derived in a subsequent section. Figure 6.2B plots this function, where the green symbol marks a hypothetical wild-type-channel position, and mutations should create data symbols that follow the remainder of the curve. Importantly, this outcome will only occur if the two aforementioned conditions are satisfied.

Alternatively, several other scenarios are possible as diagrammed in Figure 6.2C-E. First, if mutations change the peptide interaction with $Ca^{2+}$/CaM ($K_{\mathrm{a,EFF}}$), but not any of the underlying association constants within the holochannel (including $\gamma_1$), the outcome in Figure 6.2C will emerge. In this case, the channel peptide can bind $Ca^{2+}$/CaM in isolation, but this reaction is unrelated to transitions within the intact holochannel. By contrast, Figure 6.2D illustrates a scenario where mutations perturb transition(s) within the holochannel that govern CDI, but does not alter $Ca^{2+}$/CaM binding to a peptide segment of the channel. In truth, a combination of these two scenarios may also be observed resulting a poor correlation between functional strength of CDI and mutational perturbations of $Ca^{2+}$/CaM binding to a peptide segment of the channel (Figure 6.2E). Yet other deviations from the Langmuir form are possible. Importantly, this set of outcomes will hold true regardless the size and complexity of the scheme in Figure 6.2A, as proven explicitly in subsequent sections. Because of this generality, we term the analysis individually Transformed Langmuir (iTL) analysis.

**Specific Langmuir equations for C- and N-lobe CDI subsystems** – For the five-state scheme in Figure 6.2A, we derive the explicit Langmuir form appropriate for mutations selectively affecting $\gamma_1$, as follows.

For N-lobe CDI, the rapid (un)binding of $Ca^{2+}$ relating to this lobe of CaM permits the rapid CaM approximation (Tadross et al., 2008), which allows the equivalent reaction scheme in Figure 6.3A. Here, states 2 and 3 of Figure 6.3A merge into a single compound 2-3 state, with corresponding adjustments to adjacent association constants. Accordingly, the following specific Langmuir equation arises:

$$CDI/CDI_{\max} = \frac{CDI}{\underbrace{CDI_{\mathrm{m}} \cdot \gamma_2 / (1+\gamma_2)}_{CDI_{\max}}} = \frac{K_{\mathrm{a,EFF}}}{K_{\mathrm{a,EFF}} + \underbrace{(1+\varepsilon \cdot (1-P_{\mathrm{O}}))/(s \cdot P_{\mathrm{O}} \cdot (1+\gamma_2))}_{\Lambda}} \qquad (2)$$

where $P_O$ is the channel open probability, $CDI_m$ is the CDI strength that would be observed if all channels ended up in state 5 at steady state, and other terms are given in Figure 6.2 and Equation 6.1 (where $\gamma_1 = s \cdot K_{a,EFF}$, and $s$ is a constant of proportionality).

For C-lobe CDI, the slow unbinding of $Ca^{2+}$ from the C-terminal lobe of CaM permits the slow-CaM approximation as derived in prior studies (Tadross et al., 2008). This allows the time-varying rate constants between states 2 and 3 of Figure 6.2A to assume their time-invariant analogs as diagrammed in Figure 6.3B. Accordingly, the following specific Langmuir equation arises

$$\begin{aligned} CDI / CDI_{\max} &= \frac{CDI}{\underbrace{CDI_m \cdot \gamma_2 / (1+\gamma_2)}_{CDI_{\max}}} \\ &= \frac{K_{a,EFF}}{K_{a,EFF} + \underbrace{[1+(1+\varepsilon)\cdot k_{off} / (P_O \cdot C_{spike}^2 \cdot k_{on})] / [s\cdot(1+\gamma_2)]}_{\Lambda}} \end{aligned} \tag{3}$$

where $C_{spike}$ is the free $Ca^{2+}$ concentration in the channel nanodomain, as sensed by the C-terminal lobe of CaM. Experimental estimates of $C_{spike}$ far exceed 50 μM (Tay et al., 2012). Once again, the explicit lamgmuir form holds true.

**Uniqueness of the Langmuir equation outcome** – The derivations above indicate that a Langmuir equation will result if two conditions are met. (1) Point mutations only affect one transition within the system, assumed to be $\gamma_1$ in these derivations. (2) $K_{a,EFF}$, the association constant measured from channel-peptide experiments, is proportional to the corresponding association constant within the holochannel ($\gamma_1 = s \cdot K_{a,EFF}$, and $s$ is a constant). Is this outcome (of data following a Langmuir equation) unique to these two conditions? By carefully considering Equations 6.2 and 6.3, we can argue for such uniqueness. For example, if mutations were to affect more than one transition ($\gamma_1$ in Figure 6.3), then Λ would not be a constant with respect to $K_{a,EFF}$, and a Langmuir equation (defined with Λ being a constant) would not result. As another example, suppose that $K_{a,EFF}$ (measured from peptide experiments) does not maintain a strict constant of proportionality with $\gamma_1$ (pertaining to holochannels), so that $s$

is no longer a constant in the relationship $\gamma_1 = s \cdot K_{a,EFF}$. Inspection of Equations 6.2 and 6.3 again reveals that $\Lambda$ will no longer be a constant with respect to $K_{a,EFF}$, and a Langmuir equation will no longer result.

Another potentially important scenario concerns the possible existence of an additional effector site for a lobe of CaM, which is not addressed experimentally in our alanine scan (Chapter 7). For example, consider a configuration with two effector sites for the $Ca^{2+}$-bound N-lobe of CaM ($N_1$ and $N_2$ in Figure 6.4A below). For simplicity, assume CDI to be proportional to the steady-state occupancy of states $N_1$ and $N_2$. Under overexpression of $CaM_{34}$ to restrict channels to configurations $A$, $N_1$, and $N_2$, CDI would then be proportional to $(K_1 + K_2) / (1 + K_1 + K_2)$, with equilibrium constants as shown. Suppose our alanine scan only touches on site $N_1$, such that our peptide binding assays with $Ca^{2+}$/CaM only pick up mutation effects on $K_1$. Plotting this in Figure 6.4B would still reveal a Langmuir function, but with a non-zero $y$ intercept.

Thus, the observation of a Langmuir relationship for $CDI - K_{a,EFF}$ is strong evidence that the proposed molecular interaction underlies a functionally relevant transition involved in channel regulation.

**Generalization of iTL analysis to reaction schemes of arbitrary architecture –** In this section, we generalize the iTL postulates to calmodulatory regulation systems of any architecture as schematized in Figure 6.5B, not just those in Figure 6.3. States are denoted as nodes, and transitions between them as interconnecting segments. For purposes of argument, occupancy of state *m* corresponds to a channel that has undergone CDI. We assume that the system satisfies the constraints of thermodynamic equilibrium, a presumption that will be defended later on. According to thermodynamics, we can represent the behavior of this general system as a branched network without any cycles, as shown in Figure 6.5B. Completing the cycles would not change the steady-state solution to the systems, because of thermodynamic cycle constraints (Hill, 1977). Will perturbation of a single transition within this general scheme also yield a Langmuir equation?

Consider first the simplest scenario, a linear scheme that connects states 1 to *m* (Figure 6.5A), which we call the 'forward path.' It is simple to show that the equilibrium probability of occupying state *m* (assumed tantamount to the CDI state) is given by the general form:

$$P_m = \frac{K_{12} \cdot K_{23} \cdot \ldots \cdot K_{m-2\,m-1} \cdot K_{m-1\,m}}{1 + K_{12} + K_{12} \cdot K_{23} + \ldots + K_{12} \cdot K_{23} \cdot \ldots \cdot K_{m-2\,m-1} \cdot K_{m-1\,m}} = \frac{F_{1m}}{F_{11} + F_{12} + \ldots + F_{1m}} \tag{6.4}$$

Suppose we are interested in the effects of alterations in the transition from state *i* to state *i*+1 in the forward path. This would alter the equilibrium constant $K_{i\ i+1}$. Algebraic manipulation of Equation 6.4 demonstrates that $P_\mathrm{m}$ can always be transformed into a Langmuir-like form, regardless the value of *i*. This algebraic process is shown below.

$$P_m = \frac{\left[F_{1m} / K_{i\,i+1}\right]}{\left[(1/K_{i\,i+1}) \sum_{n=i+1}^{m} F_{1n}\right]} \cdot \frac{K_{i\,i+1}}{\left[\sum_{n=1}^{i} F_{1n}\right] \cdot \left[K_{i\,i+1} / \sum_{n=i+1}^{m} F_{1n}\right] + K_{i\,i+1}} \tag{6.5}$$

Noting that none of the terms in square brackets contain the $K_{i\,i+1}$ term, we can rewrite Equation 6.5 as a genuine Langmuir function

$$P_m = A \cdot \frac{K_{i\ i+1}}{\Lambda + K_{i\,i+1}} \tag{6.6}$$

where the definitions of *A* and Λ can be obtained by comparison of Equations 6.5 and 6.6.

What happens if the system also contains states connected by branching paths (shown as black segments in Figure 6.5B) that emanate from various states in the forward path? The added complexity turns out to be easily accommodated, because it is straightforward to show that Equation 6.4 becomes the closely similar form below.

$$P_m = \frac{F_{1m}}{F_{11}(1+\Omega_1) + F_{12}(1+\Omega_2) + \ldots + F_{1m}(1+\Omega_m)} \tag{7}$$

where $\Omega_n$ is comprised of various products of equilibrium constants relating to branches emanating from state *n*. Importantly, none of the equilibrium constants in the forward path are contained within $\Omega_n$. Algebraic manipulation analogous to that in Equation 6.5 then demonstrates that Equation 6.7 can be transformed into a Langmuir function in terms of $K_{i\,i+1}$ as follows.

$$P_m = \frac{\left[F_{1m} / K_{i\,i+1}\right]}{\left[(1/K_{i\,i+1}) \sum_{n=i+1}^{m} F_{1n}(1+\Omega_n)\right]} \cdot \frac{K_{i\,i+1}}{\left[\sum_{n=1}^{i} F_{1n}(1+\Omega_n)\right] \cdot \left[K_{i\,i+1} / \sum_{n=i+1}^{m} F_{1n}(1+\Omega_n)\right] + K_{i\,i+1}} \tag{8}$$

$$P_m = A \cdot \frac{K_{i\,i+1}}{\Lambda + K_{i\,i+1}} \tag{9}$$

Now suppose we are concerned about changes in an equilibrium constant within one of the branches, not in the given forward path. The insight here is that there is nothing special about the particular forward path used thus far, as portrayed in Figure 6.5A. We might as well redefine the forward path to include the new transition of interest, as portrayed in Figure 6.5C. Then, the proof would proceed identically for the new forward path, and an appropriate Langmuir function could be formulated for $P_\mathrm{m}$.

One may worry that for the actual CDI process, the system is not in true thermodynamic equilibrium (Hill, 1977), as assumed for the deductions above. Instead, the system achieves a steady state (Hill, 1977) that arises in response to millisecond-long pulses reaching $Ca^{2+}$ concentration $C_\mathrm{spike}$. These pulses are synchronized with individual stochastic openings of the channel (Tadross et al., 2008). No sustained, global $Ca^{2+}$ inputs need be considered because all experiments are performed with 10 mM BAPTA as $Ca^{2+}$ chelator in the whole-cell dialyzate. This concern may be dealt with in two phases.

First, consider the situation when we need only account for $Ca^{2+}$ binding to the C-lobe of CaM, as in our experiments characterizing C-lobe CDI in isolation. In general, the forward binding reaction of $Ca^{2+}$ to CaM is given by a stochastically varying rate constant: when $Ca^{2+}$ is zero during channel closures, this rate constant is also zero; when $Ca^{2+}$ is equal to $C_\mathrm{spike}$ during channel openings, this rate constant is approximately equal to $k_\mathrm{on} \cdot C_\mathrm{spike}{}^2$. The unbinding rate constant is always approximately equal to $k_\mathrm{off}$. We use the term ‘approximate’ as the binding and unbinding of two $Ca^{2+}$ ions to a lobe of CaM is highly cooperative (Martin et al., 1985; Linse et al., 1991), but not infinitely so. With specific reference to the C-lobe of CaM, the unbinding of $Ca^{2+}$ is slow compared to surrounding transitions, so a ‘slow-CaM approximation’ may be invoked, as proved in the past (Tadross et al., 2008). In this slow-CaM regime, the time-varying on rate constant may be replaced by the time-invariant entity $k_{on} \cdot C_{spike}^2 \cdot P_O$, where $P_O$ is the steady-state open probability of non-inactivated channels. Hence, we have an equivalent slow-CaM system, where the $Ca^{2+}$ binding transition in question is characterized by the time-invariant equilibrium constant $k_{on} \cdot C_{spike}^2 \cdot P_O / k_{off}$. Will this equivalent system satisfy all thermodynamic cycle constraints? It turns out that the answer is yes, as follows. The actual system, being physically realizable without external energy consumption, certainly satisfies all thermodynamic cycle constraints at any steady value of $C_{spike}$ (say $C_{spike/original}$), where the equilibrium constant for $Ca^{2+}$ binding and unbinding equals $k_{on} \cdot C_{spike/original}^2 / k_{off}$. Now suppose we change the level of $C_{spike}$ to $C_{spike/new} = C_{spike/original} \cdot (P_O)^{1/2}$. The original system will of course also satisfy all thermodynamic cycle constraints, with the equilibrium constant in question now equal to $k_{on} \cdot C_{spike/original}^2 \cdot P_O / k_{off}$. But this equilibrium constant is now the same as for the equivalent system obtained with the slow-CaM approximation. Thus, the equivalent system with the slow-CaM approximation will always satisfy all thermodynamic cycle constraints.

Second, consider the situation where only $Ca^{2+}$ binding to the N-lobe of CaM need be considered, as in our experiments characterizing N-lobe CDI in isolation. The full spectrum of concerns in regard to potential violations of thermodynamics is embodied by the generic layout shown in Figure 6.5D. The four main states (1, 2, 3, and 4) correspond to those shown in Figure 6.3B, and the equilibrium constants $L$, $M$, $N$, and $R$ may represent the product of equilibrium constants for multiple interconnected transitions. For example, if states 1 and 1’ in Figure 6.5D were connected by an intermediate state $x$, where $K_{1x}$ would be the equilibrium constant from state 1 to state $x$, and $K_{x1'}$ the constant from state $x$ to state 1', then $L$ would equal $K_{1x} \cdot K_{x1'}$. In this sense, transitions affiliated with $L$, $M$, $N$, and $R$ allow representation of all classes of potential thermodynamic cycles containing the $Ca^{2+}$ binding and unbinding steps between states 2 and 3 (lobe of CaM in channel alcove undergoing $Ca^{2+}$ binding and unbinding). The 'primed' states represent the original calmodulatory states under a different configuration of the channel (e.g., hypothetically something akin to an alternate configuration of auxiliary subunit modulation of the apoCaM preassociation surface). In this N-lobe scenario, the binding and unbinding of $Ca^{2+}$ to the N-lobe is rapid enough to track the millisecond stochastic gating of channels. Accordingly, a 'rapid-CaM approximation' may be invoked, as argued in the past (Tadross et al., 2008). Under this approximation, the system morphs into the equivalent time-invariant system shown in Figure 6.5E, where certain equilibrium constants now incorporate $P_O$, the steady-state open probability of a non-inactivated channel. Does this equivalent system also satisfy thermodynamic cycle mandates? Certain constraints on this question may be deduced from the original system in Figure 6.5D, specifically by considering the green-shaded cycle. From consideration of this loop, we have the thermodynamic constraint(Hill, 1977) that

$$1 = \frac{K_{12} \cdot K_{23} \cdot C_{\text{spike}}^2 \cdot K_{34} \cdot R}{K_{12}^{/} \cdot K_{23}^{/} \cdot C_{\text{spike}}^2 \cdot K_{34}^{/} \cdot L} = \frac{K_{12} \cdot K_{23} \cdot K_{34} \cdot R}{K_{12}^{/} \cdot K_{23}^{/} \cdot K_{34}^{/} \cdot L} \tag{10}$$

Evaluating the corresponding green-shaded loop in the equivalent system of Figure 6.5E, we can check whether the thermodynamic cycle constraint will also be satisfied, as follows.

$$\text{cycle constraint parameter} = \frac{(K_{12}/(1-P_O)) \cdot K_{34} \cdot P_O \cdot R}{(K_{12}^{/}/(1-P_O)) \cdot K_{34}^{/} \cdot P_O \cdot L} = \frac{K_{12} \cdot K_{34} \cdot R}{K_{12}^{/} \cdot K_{34}^{/} \cdot L} \tag{11}$$

If we make the reasonable assumption that channel configuration does not influence $Ca^{2+}$ binding and unbinding to a lobe of CaM that is *free* in the channel alcove, then $1 = K_{23}$ /

$K_{23}^{/}$ in Equation 6.10, and the cycle constraint parameter in Equation 6.11 for the equivalent system becomes unity. Thus the equivalent calmodulin regulatory system in Figure 6.5E will satisfy thermodynamic cycle constraints in regard to the green-shaded loop. If we assume that $1 = K_{23} / K_{23}^{/}$ in Figure 6.5D, then thermodynamic constraints mandate that $M = N$. Accordingly, the middle vertical transition from compound state 2-3 in Figure 6.5E is specified by $M$. The yellow loops in Figure 6.5E will then also satisfy thermodynamic constraints. Hence, all classes of loops in the rapid-CaM approximation for N-lobe CDI satisfy thermodynamic cycling constraints, if we make the reasonable assumption that $1 = K_{23} / K_{23}^{/}$. In conclusion, iTL analysis may be applied to CDI, even as driven by pulsatile $Ca^{2+}$ driving either C- or N-lobe of CaM.

## DISCUSSION

The theoretical analysis presented in this chapter, iTL analysis, is a general method to rigorously evaluate functionally relevant molecular interactions and structural interfaces for any given macromolecule irrespective of the size or architecture of the state-transition scheme that governs its function. In particular, systematic alanine scanning mutagenesis can be utilized to perturb a molecular interface of interest, and a wide-range of binding assays may be used to quantify alterations in the relative association coefficients. Given the recent proliferation of atomic structures available for many biological macromolecules, this method of evaluating structure-function relations may prove invaluable to probe their biological relevance.

With regards to calmodulation of $Ca^{2+}$ channels, Chapter 7 presents experiments that assess the functional importance of various channel interfaces and plausible molecular interactions.

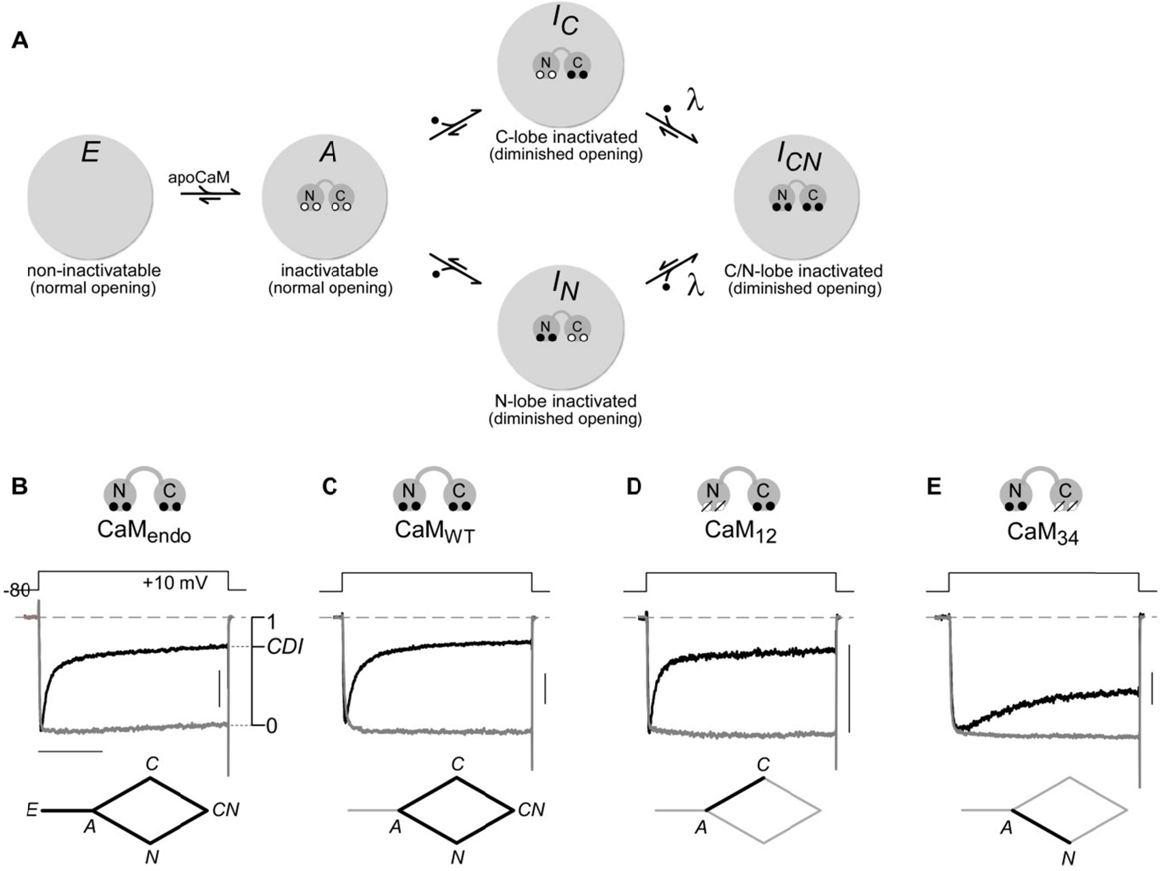
A
E
non-inactivatable
(normal opening)
apoCaM
A
inactivatable
(normal opening)
$I_C$
C-lobe inactivated
(diminished opening)
$I_N$
N-lobe inactivated
(diminished opening)
λ
λ
$I_{CN}$
C/N-lobe inactivated
(diminished opening)
B
$CaM_{endo}$
-80
+10 mV
1
CDI
0
C
$CaM_{WT}$
D
$CaM_{12}$
E
$CaM_{34}$
C
E
A
CN
N

**Figure 6.1. General schema for CaM regulation of L-type $Ca_V1.3$ channels.**

(A) Primary configurations of CaM/channel complex with respect to CaM-regulatory phenomena ($E$, $A$, $I_C$, $I_N$, and $I_{CN}$), as pertinent for $Ca_V1.3$ channels. Configuration $E$ corresponds to channel state that lacks apoCaM and therefore cannot undergo $Ca^{2+}$ regulation (CDI). Configuration $A$ corresponds to channels charged with an apoCaM and willing to undergo regulation. Configuration $I_{CN}$ corresponds to a fully $Ca^{2+}$-inactivated state with both lobes of CaM engaging respective effector interfaces. $I_C$ and $I_N$ correspond to $Ca^{2+}$-inactivated configurations where either the C- or N-lobe of CaM respectively are bound to their effector interfaces.

(B) Whole-cell $Ca_V1.3$ currents expressed in HEK293 cell, demonstrating CDI in the presence of endogenous CaM only. CDI observed here can reflect properties of the entire system diagrammed in panel A, as schematized by the stick-figure diagram at the bottom of panel B. Here and throughout, the current scale bar pertains to the $Ca^{2+}$ current (black); and the $Ba^{2+}$ current (gray) has been scaled ~3-fold downward to aid comparison of decay kinetics.

(C) Currents during overexpression of $CaM_{WT}$, isolating the behavior of the diamond-shaped subsystem at bottom.

(D) Currents during overexpression of $CaM_{12}$, isolating C-lobe form of CDI.

(E) Currents during overexpression of $CaM_{34}$, isolating N-lobe form of CDI.

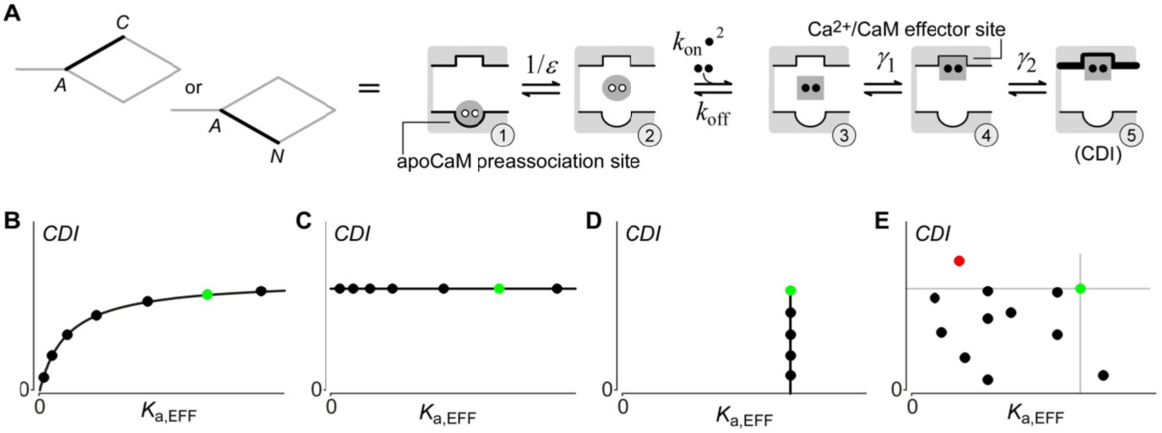
A
C
A
or
A
N
=
$1/\varepsilon$
$k_{on}\bullet^2$
$k_{off}$
Ca2+/CaM effector site
$\gamma_1$
$\gamma_2$
①
②
③
④
⑤
apoCaM preassociation site
(CDI)
B
CDI
0
0
$K_{a,EFF}$
C
CDI
0
0
$K_{a,EFF}$
D
CDI
0
0
$K_{a,EFF}$
E
CDI
0
0
$K_{a,EFF}$

**Figure 6.2. Probing functionally relevant CaM regulatory interactions via iTL analysis.**

(A) Isolated C- or N-lobe regulatory system (denoted by stick-figure diagrams on left) can be coarsely represented by a five-state scheme on right. A single lobe of apoCaM begins preassociated to channel (state 1). Following disassociation (state 2), CaM may bind two $Ca^{2+}$ ions (state 3, black dots). $Ca^{2+}$/CaM may subsequently bind to channel effector site (state 4). From here, transduction step leads to state 5, equivalent to CDI.

(B) Unique Langmuir relation (Eq. 1) that will emerge upon plotting channel *CDI* (defined Fig. 1b, right) as a function of $K_{\mathrm{a,EFF}}$ (association constant measured for isolated channel peptide), if $K_{\mathrm{a,EFF}}$ is proportional to one of the actual association constants in the scheme as in panel A. Black symbols, hypothetical results for various channel/peptide mutations; green symbol, hypothetical wild type.

(C) Predicted outcome if peptide association constant $K_{\mathrm{a,EFF}}$ has no bearing on association constants within holochannels.

(D) Outcome if mutations affect holochannel association constants, but not peptide association constants.

(E) Outcome if mutations affect holochannel association constant(s) and peptide association constant, but in ways that are poorly correlated.

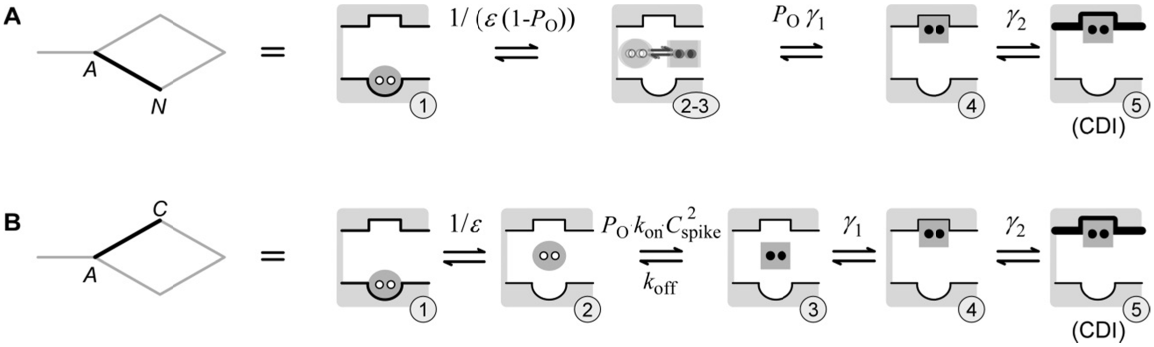
A
A
N
=
$1/(\varepsilon(1-P_O))$
$P_O \gamma_1$
$\gamma_2$
1
2-3
4
5
(CDI)
B
C
A
=
$1/\varepsilon$
$P_O \cdot k_{on} \cdot C_{spike}^2$
$k_{off}$
$\gamma_1$
$\gamma_2$
1
2
3
4
5
(CDI)

**Figure 6.3. Langmuir equation for reaction system assuming selective mutational perturbation of $Ca^{2+}$/CaM binding to effector site.**

(A) N-lobe CDI case, pertaining to subsystem as diagrammed on left (cf., Figure 6.2). Rapid $Ca^{2+}$ binding and unbinding to the N-terminal lobe of CaM enables rapid-equilibrium approximation, where states 2 and 3 merge into a single compound 2-3 state. As well, approximation makes adjustments to association constants on the left and right of state 2-3, where adjustments involve functions of open probability $P_O$.

(B) C-lobe CDI case, pertaining to subsystem as diagrammed on left (cf., Figure 6.2). Slow $Ca^{2+}$ unbinding from the C-terminal lobe of CaM permits 'slow CaM approximation,' where the rate constant for transitions from states 2 to 3 can be approximated by $P_O \cdot k_{on} \cdot C_{spike}^2$. Here, $C_{spike}$ is the free concentration of $Ca^{2+}$ at C-terminal lobe of CaM.

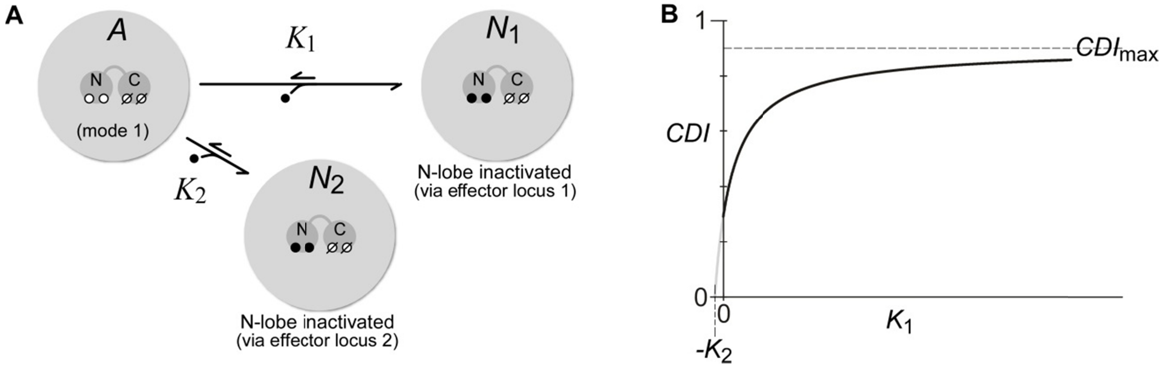
A
A
N
C
(mode 1)
K1
N1
N
C
N-lobe inactivated
(via effector locus 1)
K2
N2
N
C
N-lobe inactivated
(via effector locus 2)
B
1
CDImax
CDI
0
0
K1
-K2

**Figure 6.4. Variation of baseline iTL predictions for a hypothetical system featuring two effector sites for a given lobe of CaM.**

(A) Hypothetical example of iTL predictions for N-lobe of CaM with two effector sites. CaM regulatory subsystem as isolated by strong overexpression of $CaM_{34}$.

(B) Modified Langmuir function produced by this variant system. $CDI_{\max}$ is the maximum CDI seen when all channels are in $N_1$ or $N_2$.

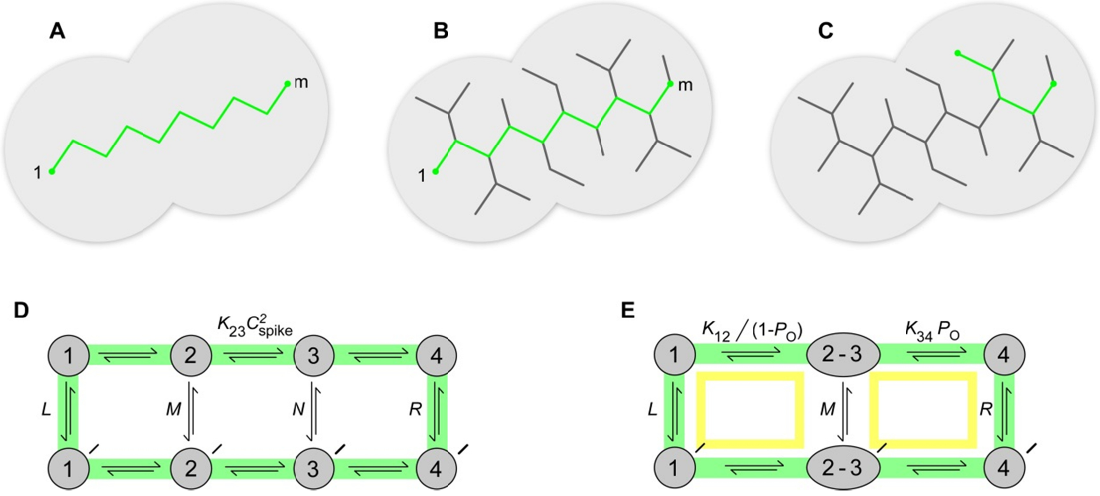

**Figure 6.5. Derivation of general iTL theory.**

(A) In general, a calmodulin regulatory system may be represented by a branched network without cycles, where nodes denote states and branches diagram transitions between states. The green pathway in panel A, consisting of a single ‘forward path,’ illustrates the simplest type of network. iTL analysis posits that the equilibrium occupancy of state *m* depends on $K_{\mathrm{i\ i+1}}$ via a Langmuir relationship.

(B) Adding branches to the forward pathway spares the ability to represent state *m* equilibrium occupancy as a Langmuir relation incorporating $K_{\mathrm{i\ i+1}}$.

(C) For alterations to a transition outside the ‘forward path,’ we may redefine the ‘forward path’ to include this transition.

(D) ‘Slow CaM approximation’ for C-lobe CDI satisfies thermodynamic cycle constraints, enabling iTL analysis. *L*, equilibrium constant from states 1 to 1’. *M*, *N*, and *R* defined similarly for transitions from upper to lower rows.

(E) ‘Rapid-CaM approximation’ for N-lobe CDI also satisfies thermodynamic cycle mandates.

## ◆ CHAPTER 7 ◆

# Structural underpinnings of $Ca^{2+}$ channel calmodulation

---

The structural basis of CaM regulation of $Ca^{2+}$ channels has remained elusive for over a decade. iTL analysis, as described in Chapter 6, furnishes a convenient framework to evaluate the critical structural determinants for $Ca^{2+}$ regulation. Accordingly, we undertook alanine-scanning mutagenesis of $Ca_V1.3$ channel domains, and screened electrophysiologically for altered CaM regulatory hotspots. In parallel, we introduced hotspot mutations into peptides overlapping scanned regions, and estimated $K_{a,EFF}$ of potential CaM binding. For this purpose, we utilized live-cell FRET two-hybrid assays (Erickson et al., 2001; Erickson et al., 2003; Chen et al., 2006), which have the resolution and throughput for the task. If such binding truly reflects holochannel function, then *CDI* should vary with $K_{a,EFF}$ as a Langmuir function (Equation 6.1, Figure 6.2B). By contrast, if $K_{a,EFF}$ changes in a manner unrelated to holochannel CDI, data would diverge from the

Langmuir relation (Figure 6.2C–E, or otherwise). CaM effector interfaces could thus be systematically resolved.

A prevailing model of $Ca^{2+}$ channel regulation has been the 'IQ-centric' theory as reviewed in Chapter 1. In this model, the IQ domain on the carboxy-termini of $Ca^{2+}$ channels serves as a primary preassociation surface for apoCaM (Pitt et al., 2001; Erickson et al., 2003; Liu et al., 2010). More importantly, this element is also believed to comprise the effector site, where $Ca^{2+}$/CaM rebinds in an alternative configuration to induce $Ca^{2+}$ regulation (Peterson et al., 1999; Zuhlke et al., 1999; Zuhlke et al., 2000; DeMaria et al., 2001; Pitt et al., 2001; Kim et al., 2004c; Halling et al., 2006). Recent studies utilizing iTL analysis, however, cast doubt on this paradigm (Figure 7.1) (Bazzazi et al., 2013; Ben-Johny et al., 2013a). Single alanines were substituted at each position of the entire IQ domain of $Ca_V1.3$ channels, while naturally occurring alanines were changed to threonine. CDI of these mutants was then characterized for the isolated N- and C-lobe CDI subsystems, so as to minimize potential complications relating to diminished preassociation with apoCaM (Figure 6.1A, configuration *E*), and masking of CDI effects by cooperative $\lambda$ steps (Figure 6.1A). In general, these IQ mutations resulted in minimal loss of N-lobe CDI, while C-lobe CDI was strongly attenuated by substitutions near the central isoleucine (Ben-Johny et al., 2013a). To test for correspondence between the reductions in C-lobe CDI and altered $Ca^{2+}$/CaM binding, FRET 2-hybrid assays of $Ca^{2+}$/CaM binding to alanine-substituted IQ peptides were performed (Figure 7.1B. By iTL postulate (Equation 6.1), if the IQ domain were the effector site for the N-lobe of $Ca^{2+}$/CaM, the strength of N-lobe CDI over various alanine substitutions should correlate with the measured association constants by a Langmuir relation. However, no such correlation was observed (Figure 7.1C). Likewise, plots of C-lobe CDI versus $K_{a,EFF}$ also deviated from a Langmuir (Figure 7.1D). In particular, some mutations, notably Y[3]D (Figure 7.1D, blue point), sharply attenuated $Ca^{2+}$/CaM binding without altering the strength of C-lobe CDI. Other mutations such as I[0]A blunted C-lobe CDI (Figure 7.1D, red point) without a corresponding change in the association coefficient for $Ca^{2+}$/CaM binding. These outcomes strongly argue against the IQ domain as an effector site for either lobe of $Ca^{2+}$/CaM.

In this chapter, we undertake systematic alanine scanning mutagenesis of various intracellular segments of $Ca^{2+}$ channels and utilize iTL analysis to evaluate the functional relevance of these interfaces for $Ca^{2+}$ regulation. Accordingly, we first consider the NSCaTE element as an effector site for N-lobe of $Ca^{2+}$/CaM. Much of the functional data and FRET 2-hybrid analysis for NSCaTE element were obtained from a past work by Ivy Dick (Dick et al., 2008; Tadross et al., 2008), however, key results been reconfirmed here. The extensive alanine scanning mutagenesis of the proximal CI region in the $Ca_V1.3$ carboxy-terminus was conducted in collaboration with Philemon Yang. Alanine Scanning Data from the IQ domain was obtained from Hojjat Bazzazi.

## RESULTS

***NSCaTE element upheld as effector site for N-lobe of $Ca^{2+}$/CaM*** – Absent a positive outcome for iTL analysis of the IQ domain (Figure 7.1), we next turned to the amino-terminal NSCaTE module (Figure 7.2A, oval), previously proposed as an effector site for N-lobe CDI (Dick et al., 2008; Tadross et al., 2008). For reference, Figure 7.2B displays the wild-type $Ca_V1.3$ profile for N-lobe CDI, apparent from the faster decay of $Ca^{2+}$ (black trace) compared to $Ba^{2+}$ current (gray trace). Single alanines were substituted across the NSCaTE module (Figure 7.2D, top), at residues that were not originally alanine (Dick et al., 2008; Tadross et al., 2008). The bar-graph summary below (Figure 7.2D) indicates strongly diminished N-lobe CDI upon alanine substitution at three residues, previously identified as critical (Dick et al., 2008; Tadross et al., 2008) (W[44]A, I[48]A, and R[52]A). For comparison, the wild-type level of CDI is represented by the green dashed line and affiliated error bars. W[44]A featured the strongest CDI decrement, as shown by the $Ca^{2+}$ current (Figure 7.2B, red trace) and population data (Figure 7.2D, red bar). To pursue iTL analysis, we characterized corresponding binding curves between NSCaTE and $Ca^{2+}/CaM_{34}$ FRET pairs (Figure 7.2C, left). The wild-type pairing exhibited a well-resolved binding curve with $K_{a,EFF}$ = $4\times10^{-4}$ $D_{free}^{-1}$ units (Figure 7.2C, right, black), whereas the W[44]A variant yielded a far lower affinity with $K_{a,EFF}$ ~0 (red). A summary of binding affinities is shown for this and additional mutations within NSCaTE in Figure 7.2E, where the dashed-green line signifies the wild-type profile. The crucial test arises by plotting N-lobe CDI strength as a function of $K_{a,EFF}$, which resolves the Langmuir relation in Figure 7.2F. For reference, wild type is shown in green, and W[44]A in red. The particular formulation of Langmuir relation for NSCaTE analysis was derived as Equation 6.2. Hence, iTL analysis upholds NSCaTE as a predominant effector site for N-lobe CDI, as argued before by other means (Dick et al., 2008; Tadross et al., 2008). By contrast, analysis of C-lobe CDI (Figure 7.3A-F) reveals deviation from a Langmuir relation (Figure 7.3F), much as in Figure 6.2C. This outcome suggests that NSCaTE mutations have little bearing on C-lobe CDI within the holochannel, though such mutations do affect binding of $Ca^{2+}/CaM_{12}$ to an isolated NSCaTE peptide.

***Identification of the C-lobe $Ca^{2+}$/CaM effector interface*** – Satisfied by proof-of-principle tests of the iTL approach, we turned to identification of the as-yet-unknown effector site for the C-lobe form of CDI. Our screen focused upon the entire carboxy tail of $Ca_V1.3$ channels upstream of the IQ domain (Figure 7.4A, PCI domain), because switching these carboxy-terminal segments in chimeric channels sharply influences this type of CDI (de Leon et al., 1995; Mori et al., 2008). For completeness, we initially characterized isolated N-lobe CDI for mutations throughout the PCI, and found no appreciable decrement from wild-type levels (Figure 7.4B, E; Figure 7.5C). Gaps indicate nonexpressing mutant channels. This outcome fits with the predominance of NSCaTE as the effector locus for the N-lobe of $Ca^{2+}$/CaM (Figure 7.2F). For reference, the dashed green line denotes the wild-type CDI level. By contrast, for isolated C-lobe CDI, the sharp diminution of CDI upon LGF→AAA substitution (Figure 7.4C, F, red) exemplifies just one of many newly discovered ‘hotspot’ loci residing in the PCI midsection (Figure 7.4F, rose and red; Figure 7.5B). As a prelude to iTL analysis, we determined the binding of $Ca^{2+}$/CaM to the PCI element (Figure 7.4G, left cartoon), and indeed the LGF substitution weakens the affinity of interaction (Figure. 7.4D). Additionally, for loci demonstrating the strongest reduction in C-lobe CDI (Figure 7.4F, rose and red), corresponding $Ca^{2+}$/CaM affinities were measured and determined to also attenuate $K_{a,EFF}$ (Figure 7.4G; Figure 7.5A). Importantly, graphing C-lobe CDI as a function of binding affinity strikingly resolved a Langmuir relation (Figure 7.4I), furnishing compelling evidence that the PCI midsection comprises an effector interface for the $Ca^{2+}$-bound C-lobe of CaM. For orientation, the green symbol corresponds to wild type, whereas the red datum derives from the LGF mutant. The specific formulation of the Langmuir equation, as it applies here (Figure 7.4I) was derived as Equation 6.3.

Alternatively, a plot of N-lobe CDI as a function of binding affinity deviated from a Langmuir form (Figure 7.4H), much as theorized in Figure 6.2C, E. This result explicitly disfavors the PCI as an N-lobe effector site, as expected from the results with NSCaTE (Figure 7.2). Overall, the impressive mirror-like inversion of results for NSCaTE (Figure 7.2F, Figure 7.3F) and PCI (Figure 7.4H, Figure 7.4I) underscores the considerable ability of iTL analysis to distinguish between effector sites of respective N- and C-lobe CDI.

Two further points warrant mention. First, the enhanced N-lobe CDI for certain mutations (Figure 7.4E) will be explored in the Discussion. Second, the decreased CDI for the YLT cluster (Figure 7.4E, F) likely reflects reduced $Ca^{2+}$ entry from a 30-mV depolarizing shift in activation, not actual attenuation of CDI *per se*. Shifts for all other loci were at most ±10 mV (not shown).

***C-lobe CDI also requires IQ domain interaction with PCI element –*** Though we argue against the IQ domain as an effector site for $Ca^{2+}$/CaM (Figure 7.1), alanine substitutions in the IQ domain nonetheless attenuate C-lobe CDI (Zuhlke et al., 1999;

Zuhlke et al., 2000; DeMaria et al., 2001; Yang et al., 2006; Mori et al., 2008), a result reproduced for reference in Figure 7.6A, B. Might the departure of $Ca^{2+}$/CaM to NSCaTE (Figure 7.2) and PCI (Figure 7.4) elements then allow the IQ domain to rebind elsewhere, in a manner also required for inducing C-lobe CDI? Thus viewed, mutations in the IQ domain could diminish C-lobe CDI by weakening such rebinding, but in a fashion that corresponds poorly to IQ-peptide affinity for $Ca^{2+}$/CaM. A clue arose by recalling that the C-lobe form of CDI can be conferred to certain $Ca_V2$ channels that normally lack such regulation, solely by substituting PCI and IQ elements from $Ca_V1$ channels exhibiting such regulation(de Leon et al., 1995; Mori et al., 2008). We thereby wondered whether the requisite rebinding might take the form of IQ-domain association with the PCI element.

Our initial attempts to detect measurable binding between IQ and PCI modules (Figure 7.6C, left cartoon) yielded low affinity binding (Figure 7.6D, gray). Notably, this initial set of data was acquired in baseline HEK293 cells featuring resting levels (Erickson et al., 2001) of intracellular [$Ca^{2+}$]. In stark contrast, upon elevating cytoplasmic $Ca^{2+}$ by ionomycin, we observed robust interaction between the same IQ/PCI FRET pair, with $K_{\text{a-PCI–IQ}} = 4.35 \times 10^{-5}\ D_{\text{free}}$ units$^{-1}$ (Fig. 6d, black). This $Ca^{2+}$-dependent interaction accords well with a role in triggering CDI, and likely arises from a requirement for $Ca^{2+}$/CaM to bind the PCI domain before appreciable IQ association occurs (Figure 7.7E). Beyond mere binding, however, functionally relevant interaction would also be decreased by the same IQ-domain mutations that reduced C-lobe CDI. In this regard, FRET interactions utilizing IQ elements bearing I[0]A or Q[1]A substitutions indeed demonstrated strong and graded reductions in affinity (Figure 7.6E, respective red and blue symbols), coarsely matching observed deficits in C-lobe CDI (Figure 7.6B). Figure 7.6C summarizes the results of these and other FRET binding assays (Figure 7.7A-D), performed for loci with the strongest effects on C-lobe CDI (Figure 7.6B, colored bars under dashed-gray threshold). Finally, the most rigorous test of functionally relevant IQ/PCI interaction comes from iTL analysis, which predicts a Langmuir relation between the strength of C-lobe CDI and corresponding binding affinities, formulated as a Langmuir equation on $\gamma_2$, corresponding to the IQ/PCI binding step. This procedure yields,

$$CDI / CDI_{\max} = \frac{K_{\mathrm{a,EFF}}}{K_{\mathrm{a,EFF}} + \underbrace{\frac{1 + (1/\varepsilon) + (1/\varepsilon)\cdot(P_{\mathrm{O}}\cdot C_{spike}^{2}\cdot k_{\mathrm{on}}/k_{\mathrm{off}}) + (1/\varepsilon)\cdot(P_{\mathrm{O}}\cdot C_{spike}^{2}\cdot k_{\mathrm{on}}/k_{\mathrm{off}})\cdot\gamma_1}{s\cdot(1/\varepsilon)\cdot(P_{\mathrm{O}}\cdot C_{spike}^{2}\cdot k_{\mathrm{on}}/k_{\mathrm{off}})\cdot\gamma_1}}_{\Lambda}} \tag{7.1}$$

where $P_{\mathrm{O}}$ is the channel open probability, $CDI_{\max}$ is the CDI strength that would be observed if $K_{\mathrm{a,EFF}}$ were to become infinite, $C_{\mathrm{spike}}$ is the free nanodomain $\mathrm{Ca}^{2+}$ concentration at the indwelling CaM during a channel opening (~always constant and the same during openings), and $\gamma_2 = \mathrm{s} \cdot K_{\mathrm{a,EFF}}$, and $s$ is a constant of proportionality).

Remarkably, graphing data from Figure 7.6B, C in this way indeed reveals a Langmuir relation (Figure 7.6F). In all, we argue that C-lobe CDI requires a tripartite complex—comprised of IQ, PCI, and $\mathrm{Ca}^{2+}$/CaM components (Figure 7.6A).

***Likelihood of IQ-PCI-Ca$^{2+}$/CaM tripartite complex*** – Prior studies have argued that $\mathrm{Ca}^{2+}$/CaM binds to the IQ peptide with a very high binding affinity (Pitt et al., 2001; Erickson et al., 2003; Black et al., 2005; Van Petegem et al., 2005; Asmara et al., 2010) (e.g., $K_{\mathrm{a/CaM\text{–}IQ}} = 5.88 \times 10^{-4}\ D_{\mathrm{free}}^{-1}$ units). If so, how could CaM already preassociated with the IQ domain, ever leave upon $\mathrm{Ca}^{2+}$ binding to form the IQ-PCI-$\mathrm{Ca}^{2+}$/CaM tripartite complex?

To address this concern, we reconsider the state transition diagram from Figure 6.3B, but with the PCI/IQ interaction explicitly represented in state 5, and with a state 6 where $\mathrm{Ca}^{2+}$/CaM could potentially rebind to the IQ domain (Figure 7.8). The propensity of $\text{Ca}^{2+}$/CaM to reside in the tripartite complex (state 5, IQ–PCI–$\text{Ca}^{2+}$/CaM) versus the IQ–$\text{Ca}^{2+}$/CaM configuration (state 6) can be estimated as:

$$\frac{\Pr\{state5\}}{\Pr\{state6\}} = \frac{\gamma_1 \cdot \gamma_2 \cdot \Pr\{state3\}}{K_{\text{IQ}} \cdot \Pr\{state3\}} = \frac{\gamma_1 \cdot \gamma_2}{K_{\text{IQ}}} \tag{7.2}$$

It turns out that the *product* of equilibrium constants in the numerator of this expression renders this ratio far greater than unity (Jencks, 1981), as follows. Given that $\text{Ca}^{2+}$/CaM resides within the alcove of the channel, the equilibrium constants $\gamma_1$ and $K_{\text{IQ}}$ includes the local concentration of $\text{Ca}^{2+}$/CaM, as given by:

$$\begin{aligned} \gamma_1 &= \hat{\gamma}_1 \cdot [\text{Ca}^{2+}/\text{CaM}]_{\text{local}} \\ K_{\text{IQ}} &= \hat{K}_{\text{IQ}} \cdot [\text{Ca}^{2+}/\text{CaM}]_{\text{local}} \end{aligned} \tag{7.3}$$

The redefined constants $\hat{\gamma}_1$ and $\hat{K}_{\text{IQ}}$ are proportional to the relative association constants estimated in our FRET 2-hybrid assays (Figure 7.4D and Figure 7.6D). Substituting these relations into Equation 7.2,

$$\frac{\Pr\{state5\}}{\Pr\{state6\}} = \frac{\hat{\gamma}_1 \cdot [\text{Ca}^{2+}/\text{CaM}]_{\text{local}} \cdot \gamma_2}{\hat{K}_{\text{IQ}} \cdot [\text{Ca}^{2+}/\text{CaM}]_{\text{local}}} = \frac{\hat{\gamma}_1 \cdot \gamma_2}{\hat{K}_{\text{IQ}}} \tag{7.4}$$

Given that a single calmodulin resides in the alcove of the channel, and the intramolecular proximity of the IQ and PCI domains, the local concentration of CaM near these domains would be approximately equal. This simplification allows us to cancel out local concentration terms in numerator and denominator, yielding the rightmost expression in Equation 7.4.

Lastly, the transition between states 4 and 5 is an intramolecular reaction. As such, estimating the equilibrium constant $\gamma_2$ requires deduction of the entropic factors associated with this transition. One approach is to represent $\gamma_2$ as:

$$\gamma_2 = \hat{\gamma}_2 \cdot [\text{IQ}]_{\text{local}} \tag{7.5}$$

Here, $\hat{\gamma}_2$ is proportional to the association constant estimated from our FRET 2-hybrid assay from Figure 7.6D, and $[\text{IQ}]_{\text{local}}$ is the local concentration of the IQ domain near the PCI segment.

$$\frac{\Pr\{state\,5\}}{\Pr\{state\,6\}} = \frac{\hat{\gamma}_1 \cdot \hat{\gamma}_2 \cdot [\mathrm{IQ}]_{\mathrm{local}}}{\hat{K}_{\mathrm{IQ}}} \tag{7.6}$$

A first-order approximation for the concentration $[\mathrm{IQ}]_{\mathrm{local}}$ is given by:

$$[\mathrm{IQ}]_{\mathrm{local}} = \frac{1}{N_{\mathrm{Avogadro}} \cdot V_{\mathrm{local,\,IQ}}} \tag{7.7}$$

From the molecular model of the carboxy-terminus (Figure 2.1), we estimate a maximal distance of 45 Å between the IQ and PCI domains, resulting in $[\mathrm{IQ}]_{\mathrm{local}}$ ~ 4.4 mM ($1.36\times10^{8}$ $D_{\mathrm{free}}$ units). Thus, we can compute the value of Equation 7.6 numerically as:

$$\frac{\Pr\{state\,5\}}{\Pr\{state\,6\}} = \frac{\hat{\gamma}_1 \cdot \hat{\gamma}_2 \cdot [\mathrm{IQ}]_{\mathrm{local}}}{\hat{K}_{\mathrm{IQ}}} = \frac{\left(3.45\times10^{-5} D_{\mathrm{free}}^{-1}\right)\left(4.35\times10^{-5} D_{\mathrm{free}}^{-1}\right)\left(1.36\times10^{8} D_{\mathrm{free}}\right)}{5.9\times10^{-4} D_{\mathrm{free}}^{-1}} \approx 350 \tag{7.8}$$

Thus by thermodynamic reasoning, the formation of the C-lobe CDI effector complex (state 5) is far more likely than simple binding of the IQ domain to $\mathrm{Ca}^{2+}$/CaM, despite the high affinity of the latter. This outcome underscores the plausibility of switching CaM interactions as the mechanistic basis for CDI.

Importantly, nature and drug design exploit such enhancement of binding affinity through multivalent ligand mechanisms (Jencks, 1981; Krishnamurthy et al., 2006). Empirically speaking, the improvement in binding may involve far larger local concentrations ($10^{2}$-$10^{5}$ M versus our 4.4 mM estimate) such as seen in peptide-elastase interactions (Thompson, 1974) and succinic anhydride formation (Page and Jencks, 1971). Thus, our coarse estimate of a 4.4 mM local concentration (Equation 7.7) could well understate the actual propensity for tripartite complex formation. Of note, in ITC calorimetry studies of single lobes of $\mathrm{Ca}^{2+}$/CaM binding to the $\mathrm{Ca_V}1.2$ IQ domain, even higher affinities of 2 nM have been reported for the C-lobe (Van Petegem et al., 2005). Even so, formation of the tripartite complex formation would still be favored by a factor of ~15. More relevant may be the conditions under which the ITC calorimetry experiments were conducted. To aid solubility of the IQ domain, low salt concentrations

(5 mM KCl) were employed. However, it has been found that low-ionic-strength conditions artificially increase $Ca^{2+}$/CaM binding to P-57 protein (Alexander et al., 1987). Even greater low-salt enhancement has been found for the interaction of single lobes of $Ca^{2+}$/CaM to IQ domains of myosin V (Martin and Bayley, 2002). Under physiological salt concentrations, then, one might still expect that a boost factor ~350 would hold true (Equation 7.8).

***ApoCaM preassociation within the PCI domain*** – Having explored interactions related to $Ca^{2+}$/CaM, we turned to the origins of apoCaM. Elsewhere (Bazzazi et al., 2013), we have shown that apoCaM starts off preassociated with a surface that at least includes (Pitt et al., 2001; Erickson et al., 2003; Halling et al., 2006; Liu et al., 2010) the IQ element. Moreover, homology modeling of a related apoCaM/IQ structure for $Na_V$ channels (Chagot and Chazin, 2011; Feldkamp et al., 2011) suggests that the $Ca_V1.3$ IQ module mainly interacts with the C-lobe of apoCaM. That said, might the PCI domain bind the N-lobe of apoCaM (Figure 7.9A)? If so, then the earlier PCI mutations could have weakened N-lobe interactions, thereby boosting the fraction of channels without indwelling apoCaM (Figure 6.1A, configuration *E*). This effect would diminish CDI, simply because such channels are incapable of such inactivation. This scenario would be apparent if CDI were measured with only endogenous levels of wild-type CaM present, rather than with the strong overexpression of CaM used in experiments in previous sections. The former approach would allow for characterization of CDI arising from the entire CaM regulatory system (Figure 6.1 including configuration *E*), as schematized on the left in Figure 7.9E. Indeed, CDI measured under this regime ($CDI_{\mathrm{CaMendo}}$, Figure 7.9) reveals many loci where alanine substitutions strongly attenuated $CDI_{\mathrm{CaMendo}}$ (rose and red bars).

The simplest test for decreased preassociation would be to check whether CDI resurged upon strongly overexpressing wild-type CaM ($CaM_{WT}$), a maneuver that should act through mass action to eliminate CaM-less channels (Liu et al., 2010), and restrict channels to the subsystem on the left in Figure 7.9F. We undertook this procedure for all loci demonstrating appreciable reduction of $CDI_{\text{CaMendo}}$ (Figure 7.9E, rose and red); CDI measured under strongly overexpressed $\text{CaM}_{\text{WT}}$ ($CDI_{\text{CaMhi}}$) is summarized below in Figure 7.9F. As baseline, we confirmed that elevating $\text{CaM}_{\text{WT}}$ hardly affected CDI of wild-type channels (compare dashed-green lines (Fig. 7e, f), denoting wild-type profiles). This outcome occurs because the high apoCaM affinity of wild-type channels renders configuration *E* channels rare, even at endogenous levels of apoCaM (Liu et al., 2010). By contrast, the TVM mutant exhibits an impressive return of CDI upon elevating $\text{CaM}_{\text{WT}}$ (Figure 7.9B, C), as do many other mutants (Figure 7.9E and Figure 7.9F). Importantly, scrutiny of the system configurations involved (Figures 7.8E and 7.8F, left schematics) argues that $CDI_{\text{CaMendo}} = CDI_{\text{CaMhi}} \cdot F_{\text{b}}$, where $F_{\text{b}}$ is the fraction of channels preassociated with apoCaM when only endogenous CaM is present. This simple relation arises even if there is a residual $CDI_{\text{CaMhi}}$ shortfall compared to wild type (e.g., Figure 7.9F, LGF). This is so because the $CDI_{\text{CaMhi}}$ deficit reflects changes in the diamond subsystem of Figure 7.9F (left), which is identically present in $CDI_{\text{CaMendo}}$ measurements (Figure 7.9E).

Thus aware, we tested directly for changes in apoCaM binding that might mirror the resurgent CDI. Wild-type apoCaM and the whole CI domain (incorporating both IQ and PCI) constituted the FRET pairs (Figure 7.9G, left cartoon). The wild-type pairing showed robust interaction with $K_{\text{a,EFF}} = 2.5 \times 10^{-4}\ D_{\text{free}}\ \text{units}^{-1}$ (Figure 7.9D, black; Figure 7.9G, green dashed line). By contrast, the TVM pairing, corresponding to a mutant channel showing marked resurgent CDI (Figure 7.9B, C), exhibited far diminished affinity (Figure 7.9D, G, red; $K_{\text{a,EFF}} = 0.13 \times 10^{-4}\ D_{\text{free}}\ \text{units}^{-1}$). Figure 7.9G displays the $K_{\text{a,EFF}}$ for these and other pairings, indicating graded weakening of apoCaM interaction by these various PCI mutations.

The most rigorous test comes from iTL analysis. If PCI contacts indeed mediate apoCaM preassociation, then plotting $CDI_{\mathrm{CaMendo}}$ / $CDI_{\mathrm{CaMhi}}$ (= $F_{\mathrm{b}}$) versus the various association constants for apoCaM/CI interaction (Figure 7.9G) should decorate a Langmuir. Indeed, just such a relation (Figure 7.9H) is resolved experimentally (Figure 7.9E-G), arguing that the N-lobe interfaces with corresponding PCI loci. Notably, this relation is identical to that defined by IQ mutations on the same CI module, as reported for the C-lobe of apoCaM (Bazzazi et al., 2013). Figure 7.9I emphasizes this equivalence by overlaying PCI results onto IQ data (in blue). This striking resolution of a single Langmuir accords with one and the same apoCaM interacting with PCI and IQ domains.

## DISCUSSION

These experiments fundamentally transform the prevailing molecular view of CaM regulation of $Ca^{2+}$ channels. The field has long been dominated by an IQ-centric scheme (Peterson et al., 1999; Zuhlke et al., 1999; Zuhlke et al., 2000; DeMaria et al., 2001; Pitt et al., 2001; Kim et al., 2004c; Halling et al., 2006), wherein indwelling apoCaM begins preassociated with a carboxy-terminal IQ domain (Figure 7.1A, right), and remains bound to this element in a different conformation upon CaM interaction with $Ca^{2+}$. Motivated by this view, numerous atomic structures of $Ca^{2+}$/CaM complexed with IQ peptides have been obtained (Fallon et al., 2005; Van Petegem et al., 2005; Kim et al., 2008; Mori et al., 2008). Here, we furnish a new proposal for large-scale exchange of CaM interaction to alternative effector loci (Figure 7.10A). ApoCaM begins preassociated with an interface that includes, but is not limited to the IQ domain (configuration *A*): the C-lobe of apoCaM interacts with the IQ (cyan circle), and the N-lobe with the central midsection of the PCI (green box) (Figure 7.9). Upon $Ca^{2+}$ binding to the N-lobe of CaM, the system adopts configuration $I_{\mathrm{N}}$, wherein this lobe interacts with the NSCaTE module on the channel amino terminus (pink oval) to trigger N-lobe CDI (Figure 7.2). Upon ensuing $Ca^{2+}$ binding to the C-lobe, the system assumes configuration $I_{\mathrm{CN}}$, distinguished by C-lobe interaction with the proximal midsection of the PCI (green square) (Figure 7.4), along with IQ engagement of this complex (Kim et al., 2004c) (Figure 7.6). If $Ca^{2+}$ only binds to the C-lobe, the system adopts configuration $I_C$, corresponding to C-lobe CDI. Only a single CaM is shown, given the evidence for a single regulatory CaM per channel (Mori et al., 2004; Yang et al., 2007).

The structural details of most of these configurations are presently unknown, but *ab initio* and homology modeling confirms the plausibility of these configurations, as follows. Concerning the apoCaM/channel complex, Figure 7.10B displays a homology model of the C-lobe of apoCaM complexed with the IQ domain (Bazzazi et al., 2013), based on an analogous atomic structure from $Na_V$ channels (Chagot and Chazin, 2011; Feldkamp et al., 2011). Many of the important IQ-domain hotspots for apoCaM preassociation, as determined from iTL analysis, are rationalized by this model (Bazzazi et al., 2013). To portray the disposition of the N-lobe of apoCaM shown in Figure 7.10B, we utilized *ab initio* structural prediction of the CI domain with the *Rosetta* package (Kim et al., 2004c), yielding a PCI domain containing two EF-hand-like motifs, and a long protruding helix ('preIQ' subelement). The EF-hand-containing module resembles an atomic structure of the homologous segment of $Na_V$ channels (Chagot et al., 2009; Wang et al., 2012), and a long helical segment has been resolved in atomic structures of closely homologous $Ca_V1.2$ segments (Fallon et al., 2009; Kim et al., 2010). It is reassuring that N-lobe apoCaM hotspots adorn the surface of this PCI model (red coloration), within the more C-terminal of two EF hands. Accordingly, we apposed the atomic structure of the N-lobe of apoCaM (1CFD) to this segment of the PCI model, initially using a shape-complementarity docking algorithm (Schneidman-Duhovny et al., 2005) (*PatchDock*), followed by refinement with docking protocols of *Rosetta*. Of note, the configuration of the N-lobe of apoCaM portrayed in Figure 7.10B fits nicely with the outright enhancement of N-lobe CDI by PCI mutations in the region of putative N-lobe contact (compare Figure 7.4E and Figure 7.10E, GKL through TLF). With reference to Figure 6.2A, weakening of channel binding to the N-lobe of apoCaM (state 1) would, through connection to other states, increase occupancy of the inactivated state (state 5), thereby accentuating N-lobe CDI. Reassuringly, for IQ-domain residues implicated in apoCaM preassociation, those including the central isoleucine (I[0]) and downstream did not enhance N-lobe CDI (Bazzazi et al., 2013), consistent with their binding the C-lobe of apoCaM.

Figure 7.10C displays structural modeling of the arrangement of $Ca^{2+}$/CaM complexed with the channel. The arrangement of the N-lobe of $Ca^{2+}$/CaM complexed with NSCaTE comes from a recent NMR structure (Liu and Vogel, 2012). Notably, the key hotspot residues of NSCaTE interaction with the N-lobe of $Ca^{2+}$/CaM, as deduced by iTL analysis, indeed correspond to intimate contact points in this atomic structure (deep red). As for C-lobe CDI, the functional hotspots also adorn the surface of the upstream EF-hand-like region of an *ab initio* model of the PCI domain (Figure 7.10C, red coloration). Accordingly, the IQ domain and an atomic structure of the C-lobe of $Ca^{2+}$/CaM (3BXL) were docked using *PatchDock* and *PyRosetta* algorithms. Overall, this framework sets the table for future structural biological work, identifying critical domains and offering a functional guide for new structures.

More broadly, our CaM regulatory mechanism ushers in new horizons. Figure 7.10 portrays an unprecedented mechanism of CaM exchange, far exceeding the textbook engram of CaM kinase II regulation involving single-CaM-binding-site removal of an inhibitory domain. Our scheme offers new molecular interfaces that may be targeted by native modulators and small-molecule drug discovery. Of note, because L-type channel CDI strongly controls cardiac excitability and arrhythmogenic potential (Alseikhan et al., 2002; Mahajan et al., 2008), as well as $Ca^{2+}$ load in substantia nigral neurons prone to degeneration in Parkinsons disease (Chan et al., 2007), one could now envisage a screen for selective modulators of N- versus C-lobe CDI (Anderson and Mohler, 2009). Furthermore, a promising avenue for exploring the physiological roles of CDI involves targeted knock-in of mutant L-type channels within transgenic mice. Unfortunately, the

I[0]E mutant $Ca_V1.2$ channels employed thus far (Poomvanicha et al., 2011) exhibits a spectrum of CaM-regulatory alterations (decreased C-lobe CDI and apoCaM preassociation), whereas our alanine scan offers variant channels with surgical manipulation of CDI. As another perspective, our mechanism represents a prototype for higher-order $Ca^{2+}$ signal detection; the multi-state character of the scheme may fundamentally permit an expanded signaling repertoire(Dick et al., 2008; Tadross et al., 2008) (Figure 6.3A). $Na_V$ channels also feature a homologous CI region with similar fold (Chagot et al., 2009; Wang et al., 2012), apoCaM preassociation with an IQ element (Chagot et al., 2009; Feldkamp et al., 2011; Wang et al., 2012), and CaM regulatory phenomena purported to involve some CaM movement among segments (Chagot et al., 2009; Sarhan et al., 2009). Finally, the extensive characterization and mechanistic framework of channel domains (Figure 7.2, Figure 7.4 Figure 7.6, Figure 7.9) offers a high-resolution roadmap for understanding a growing list of $Ca_V1$-2 splice and editing variants, as well as channelopathies (Adams and Snutch, 2007). In these and related realms, the iTL approach may prove to be a valuable strategy for advance.

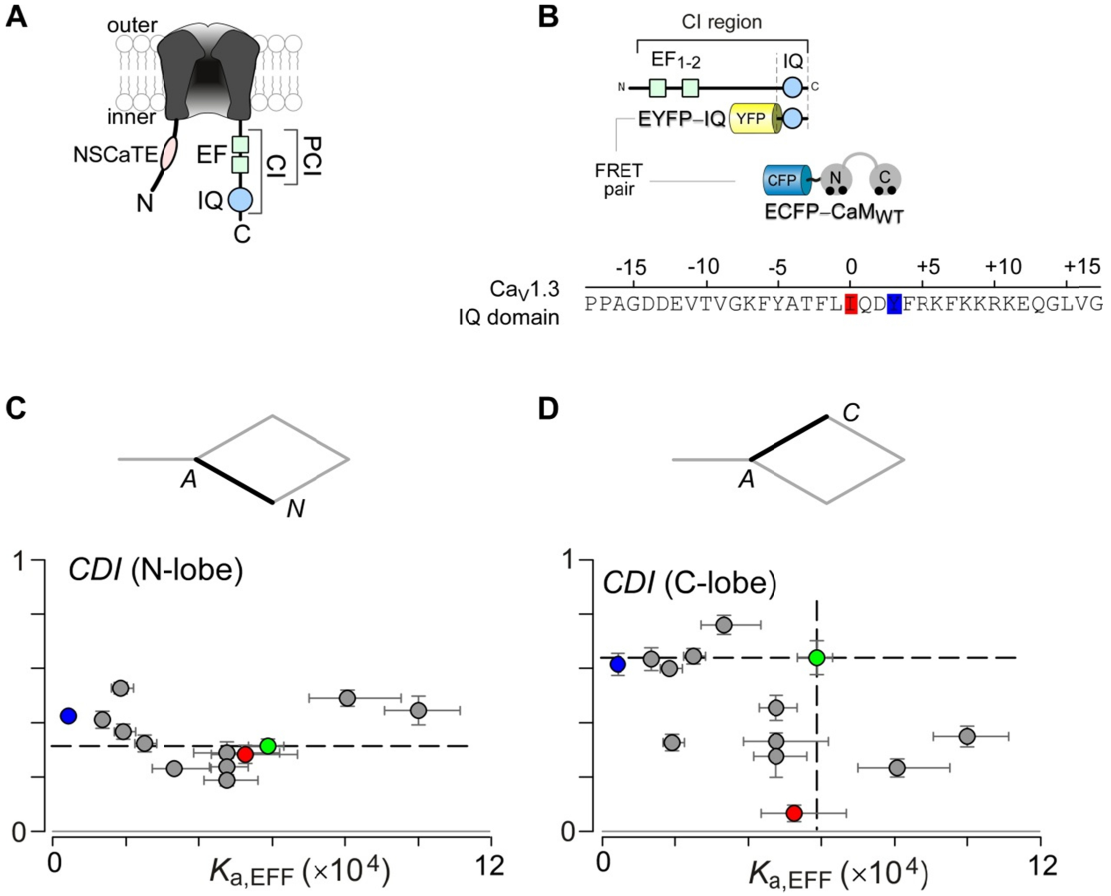
A
outer
inner
NSCaTE
N
EF
IQ
C
CI
PCI
B
CI region
EF1-2
IQ
N
C
EYFP–IQ
YFP
FRET pair
CFP
N
C
ECFP–CaMWT
-15
-10
-5
0
+5
+10
+15
CaV1.3 IQ domain
PPAGDDEVTVGKFYATFLIQDYFRKFKKRKEQGLVG
C
A
N
CDI (N-lobe)
1
0
0
12
Ka,EFF (×10^4)
D
A
C
CDI (C-lobe)
1
0
0
12
Ka,EFF (×10^4)

**Figure 7.1. Inconsistencies with IQ domain role as $Ca^{2+}$/CaM effector site.**

(A) Cartoon of $Ca_V1.3$ channel landmarks involved in CaM regulation. $\underline{C}a^{2+}$-$\underline{i}$nactivation (CI) region constitutes the proximal channel carboxy terminus (~160 aa). IQ domain (IQ), comprising the C-terminal ~30 aa of the CI segment, long proposed as preeminent for CaM/channel binding. Dual vestigial EF-hand (EF) motifs span the proximal ~100 aa of the CI module. $\underline{P}$roximal $\underline{C}a^{2+}$-$\underline{i}$nactivating (PCI) region constitutes the CI element exclusive of the IQ domain. NSCaTE on channel amino terminus of $Ca_V1.2$-1.3 channels may be the N-lobe $Ca^{2+}$/CaM effector site.

(B) Cartoon illustrates FRET 2-hybrid assay used to deduce relative $Ca^{2+}$/CaM binding affinity for wild-type and mutant IQ domain. Briefly, IQ domain peptide is tagged with an eYFP on the amino-terminus. CaM is tagged with an eCFP on its amino terminus. To probe relative binding affinities, $3^3$-FRET is characterized from single cells expressing both IQ domain peptides and CaM. The peptide sequence for the wild-type $Ca_V1.3$ IQ domain is shown in bottom subpanel. I[0] and Y[3] correspond to two important residues whose function is probed in panel C and D.

(C) Schematic illustrates N-lobe CDI subsystem isolated by $CaM_{34}$. Plotting N-lobe *CDI* versus $K_{a,EFF}$ demonstrates deviation from Equation 6.1, much as in Figure 6.2C. Green, wild type; red, I[0]A; blue, Y[3]D. N-lobe CDI is mostly unperturbed or modestly increased, arguing against the IQ domain as an N- lobe $Ca^{2+}$/CaM effector module.

(D) Plots of C-lobe *CDI* versus $K_{a,EFF}$ also diverge from Langmuir form, much as in Figure 6.1E. This result further argues against the IQ element *per se* acting as an effector site for the C-lobe of $Ca^{2+}$/CaM. Symbols as in panel C. I[0]A does not alter $Ca^{2+}$/CaM binding yet abolishes C-lobe CDI. Y[3]D mutation abolishes $Ca^{2+}$/CaM binding yet sustain full C-lobe CDI. These results are inconsistent with IQ domain serving as a C-lobe $Ca^{2+}$/CaM effector site.

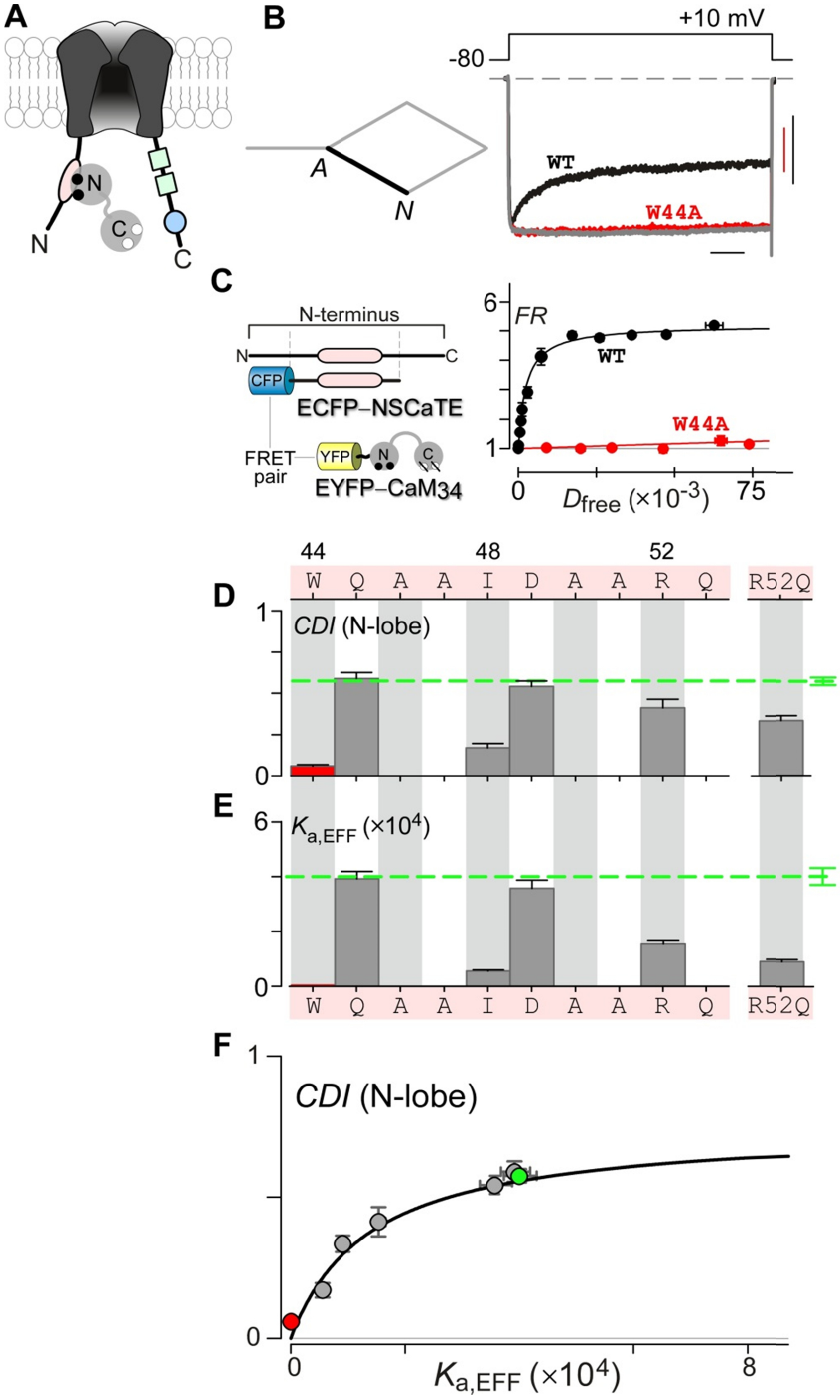
A
N
C
N
C
B
+10 mV
-80
A
N
WT
W44A
C
N-terminus
N
C
CFP
ECFP–NSCaTE
FRET
pair
YFP
N
C
EYFP–CaM34
6
FR
WT
W44A
1
0
$D_{\mathrm{free}}$ (×10$^{-3}$)
75
44
48
52
W Q A A I D A A R Q
R52Q
D
1
CDI (N-lobe)
0
E
6
$K_{\mathrm{a,EFF}}$ (×10$^4$)
0
W Q A A I D A A R Q
R52Q
F
1
CDI (N-lobe)
0
0
$K_{\mathrm{a,EFF}}$ (×10$^4$)
8

**Figure 7.2. iTL analysis of NSCaTE module of as N-lobe $Ca^{2+}$/CaM effector site**

(A) Cartoon depicting NSCaTE as putative effector interface for N-lobe of $Ca^{2+}$/CaM.

(B) Exemplar $Ca_V1.3$ whole-cell currents exhibiting robust isolated N-lobe CDI, as seen from the rapid decay of $Ca^{2+}$ current (black trace). Corresponding stick-figure subsystem appears on the left. W[44]A mutation abolishes N-lobe CDI, as seen from the lack of appreciable $Ca^{2+}$ current decay (red trace). Gray trace, averaged $Ba^{2+}$ trace for wild-type (WT) and W[44]A constructs.

(C) FRET 2-hybrid binding curves for $Ca^{2+}/CaM_{34}$ and NSCaTE segment, with FRET partners schematized on the left. Wild-type pairing (WT) in black; W[44]A mutant pairing in red. Each symbol, mean ± SEM of ~5 cells.

(D) Bar-graph summary of N-lobe *CDI* for NSCaTE mutations measured after 800-ms depolarization, with NSCaTE sequence at the top, as numbered by position within $Ca_V1.3$.. Data for W[44]A in red; dashed green line, wild type.

(E) Association constants ($K_{a,EFF} = 1 / K_{d,EFF}$) for $Ca^{2+}/CaM_{34}$ binding to NSCaTE module evaluated for constructs exhibiting significant effects in panel D. Error bars, nonlinear standard deviation estimates. Data for W[44]A in red; dashed green line, wild type.

(F) Plotting N-lobe *CDI* versus $K_{a,EFF}$ uncovers a Langmuir relationship, identifying NSCaTE as a functionally relevant effector interface. W[44]A in red; wild type in green.

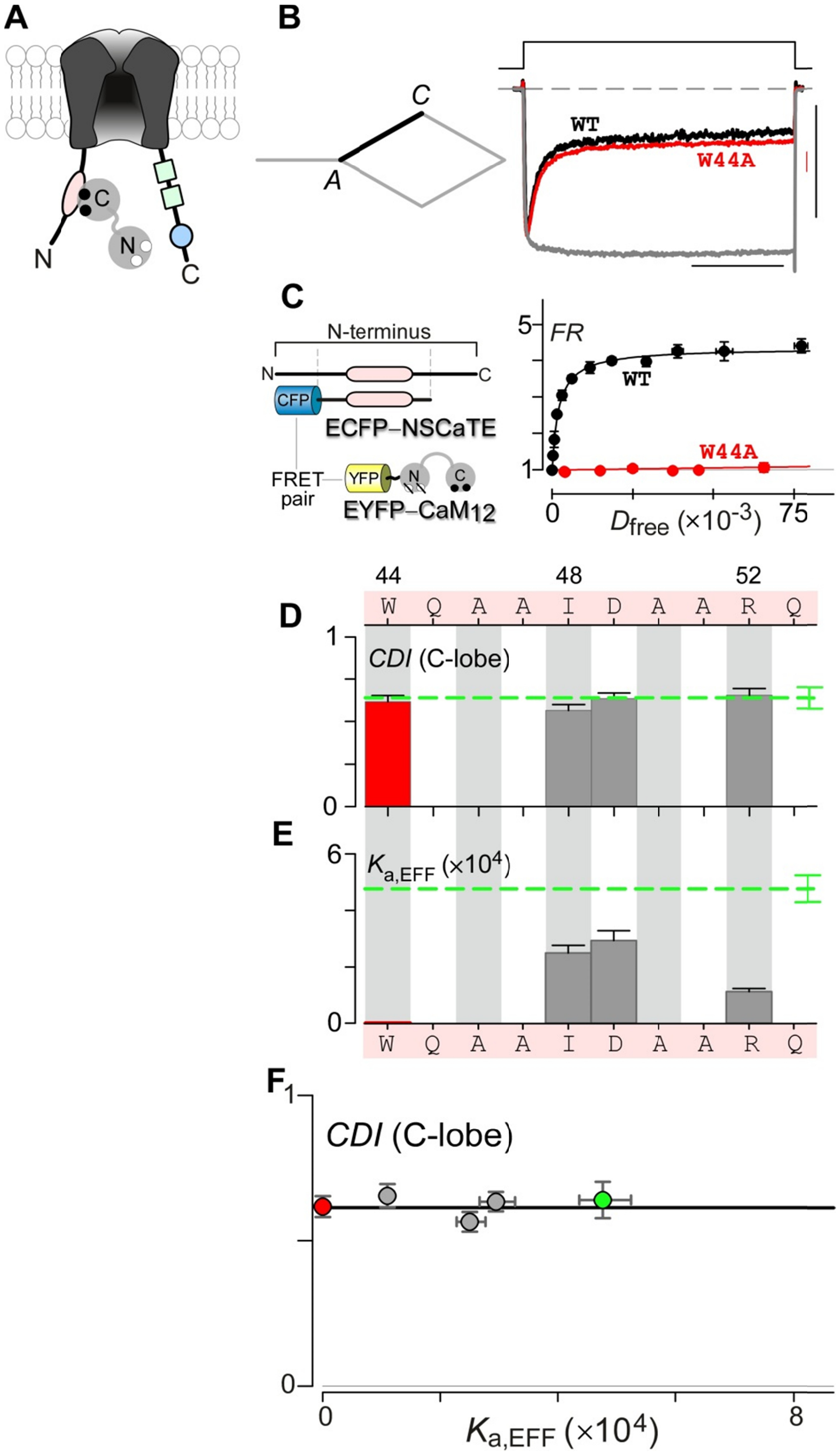
A
C
N
N
C
B
C
A
WT
W44A
C
N-terminus
N
C
CFP
ECFP–NSCaTE
FRET pair
YFP
N
C
EYFP–CaM12
5
FR
WT
W44A
1
0
Dfree (×10-3)
75
44
48
52
W Q A A I D A A R Q
D
1
CDI (C-lobe)
0
E
6
Ka,EFF (×10^4)
0
W Q A A I D A A R Q
F
1
CDI (C-lobe)
0
0
Ka,EFF (×10^4)
8

**Figure 7.3. iTL analysis shows NSCaTE module is not C-lobe Ca$^{2+}$/CaM effector site**

iTL fails to uphold NSCaTE as an effector site for the C-lobe of Ca$^{2+}$/CaM. Format is the same as Figure 7.2.

(B, D) C-lobe CDI, measured at 300 ms, remains unchanged by NSCaTE mutations.

(C, E) Changes in $K_{\mathrm{a,EFF}}$ of NSCaTE module for Ca$^{2+}$/CaM$_{12}$ characterized by 3$^3$-FRET. Each symbol, mean ± SEM of ~5 cells.

(F) Plotting C-lobe *CDI* versus $K_{\mathrm{a,EFF}}$ deviates from a Langmuir relation, much as in Figure 6.2C.

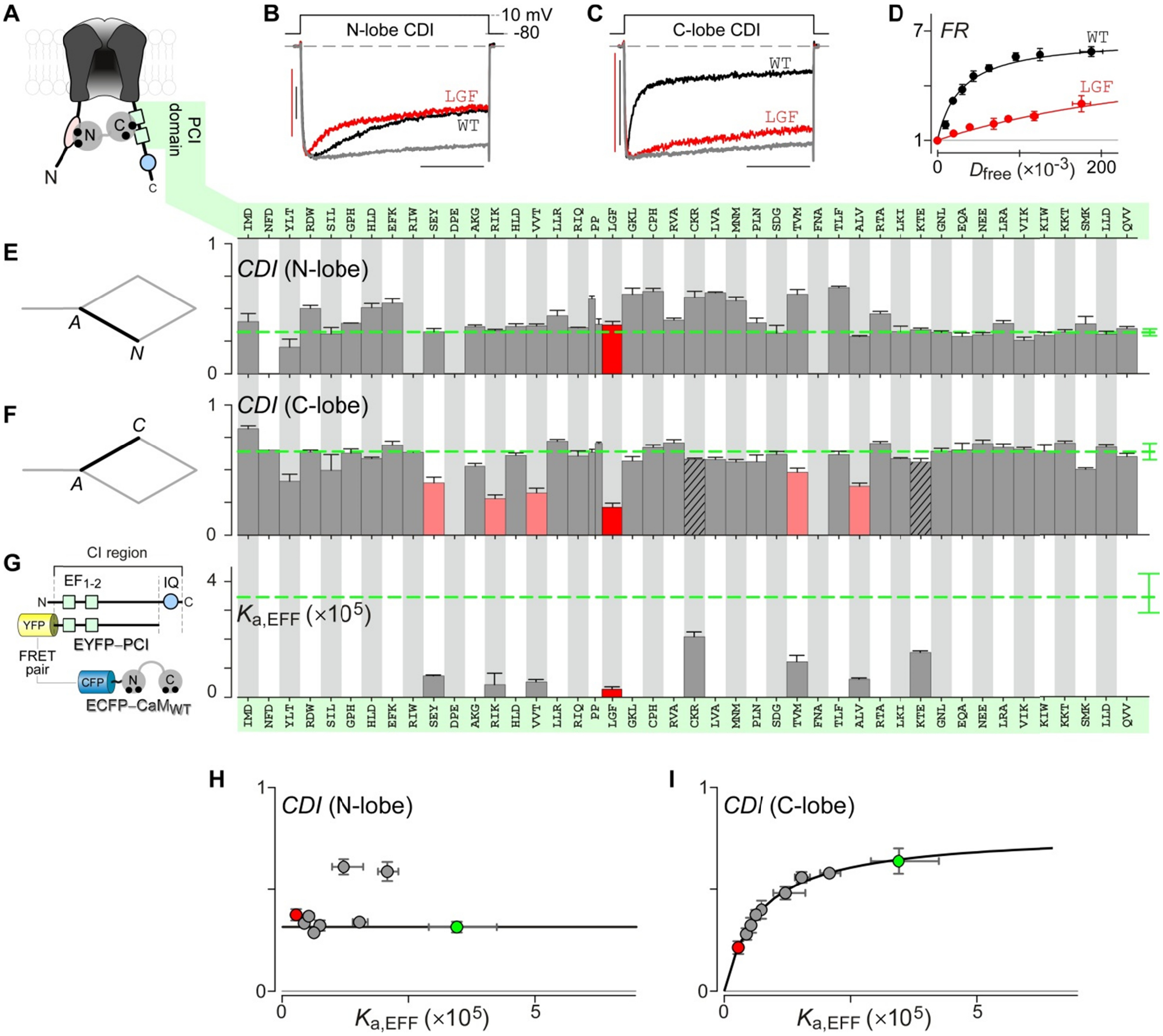
A
N
C
N
C
PCI domain
B
10 mV
-80
N-lobe CDI
LGF
WT
C
C-lobe CDI
WT
LGF
D
7
FR
WT
LGF
1
0
200
$D_{\mathrm{free}}$ (×$10^{-3}$)
IMD NFD YLT RDW SIL GPH HLD EFK RIW SEY DPE AKG RIK HLD VVT LLR RIQ PP LGF GKL CPH RVA CKR LVA MNM PLN SDG TVM FNA TLF ALV RTA LKI KTE GNL EQA NEE LRA VIK KIW KKT SMK LLD QVV
E
A
N
1
CDI (N-lobe)
0
F
C
A
1
CDI (C-lobe)
0
G
CI region
EF1-2
IQ
N
C
YFP
EYFP–PCI
FRET pair
CFP
N
C
ECFP–CaMWT
4
$K_{a,\mathrm{EFF}}$ (×$10^5$)
0
H
1
CDI (N-lobe)
0
0
5
$K_{a,\mathrm{EFF}}$ (×$10^5$)
I
1
CDI (C-lobe)
0
0
5
$K_{a,\mathrm{EFF}}$ (×$10^5$)

**Figure 7.4. iTL analysis of PCI segment as C-lobe $Ca^{2+}$/CaM effector interface.**

(A) Cartoon depicts PCI segment as putative effector site for C-lobe of $Ca^{2+}$/CaM.

(B) Isolated N-lobe CDI for wild type (WT) and LGF→AAA (LGF) mutant channels. $Ca^{2+}$ current for WT in red, and for LGF in red. Gray, averaged $Ba^{2+}$ trace.

(C) Isolated C-lobe CDI for WT and LGF mutant channels, indicating strong CDI attenuation by LGF mutation. Format as in panel B.

(D) FRET 2-hybrid binding curves for $Ca^{2+}$/CaM pitted against PCI segments, for WT (black) and LGF (red). Each symbol, mean ± SEM from ~ 9 cells.

(E) Bar-graph summary confirming no appreciable reduction of isolated N-lobe CDI, over all alanine scanning mutants across the PCI region (sequence at the top). Schematic of corresponding system under investigation at the left. Green dashed line, wild type; red, LGF mutant; gaps, nonexpressing configurations.

(F) Bar-graph summary, isolated C-lobe *CDI* for alanine scan of PCI. Red bar, LGF→AAA mutant showing strong CDI reduction. Rose bar, other loci showing substantial CDI reduction. Hashed, randomly chosen loci for subsequent FRET analysis.

(G) Association constants for $Ca^{2+}$/CaM binding to PCI region, with FRET partners as diagrammed on the left. Green dashed line shows wild-type profile. PCI mutations with appreciable deficits in C-lobe *CDI* were chosen for FRET analysis (red and rose in panel F), as well as those chosen at random (hashed in panel F). Error bars, nonlinear estimates of standard deviation.

(H) Plotting N-lobe CDI versus $K_{a,EFF}$ for $Ca^{2+}$/CaM binding to PCI exhibited marked deviation from Langmuir relationship. Red, LGF; green, WT.

(I) Alternatively, plotting C-lobe CDI revealed a well-resolved Langmuir relation, supporting the PCI region as a C-lobe $Ca^{2+}$/CaM effector site. Symbols as in panel H.

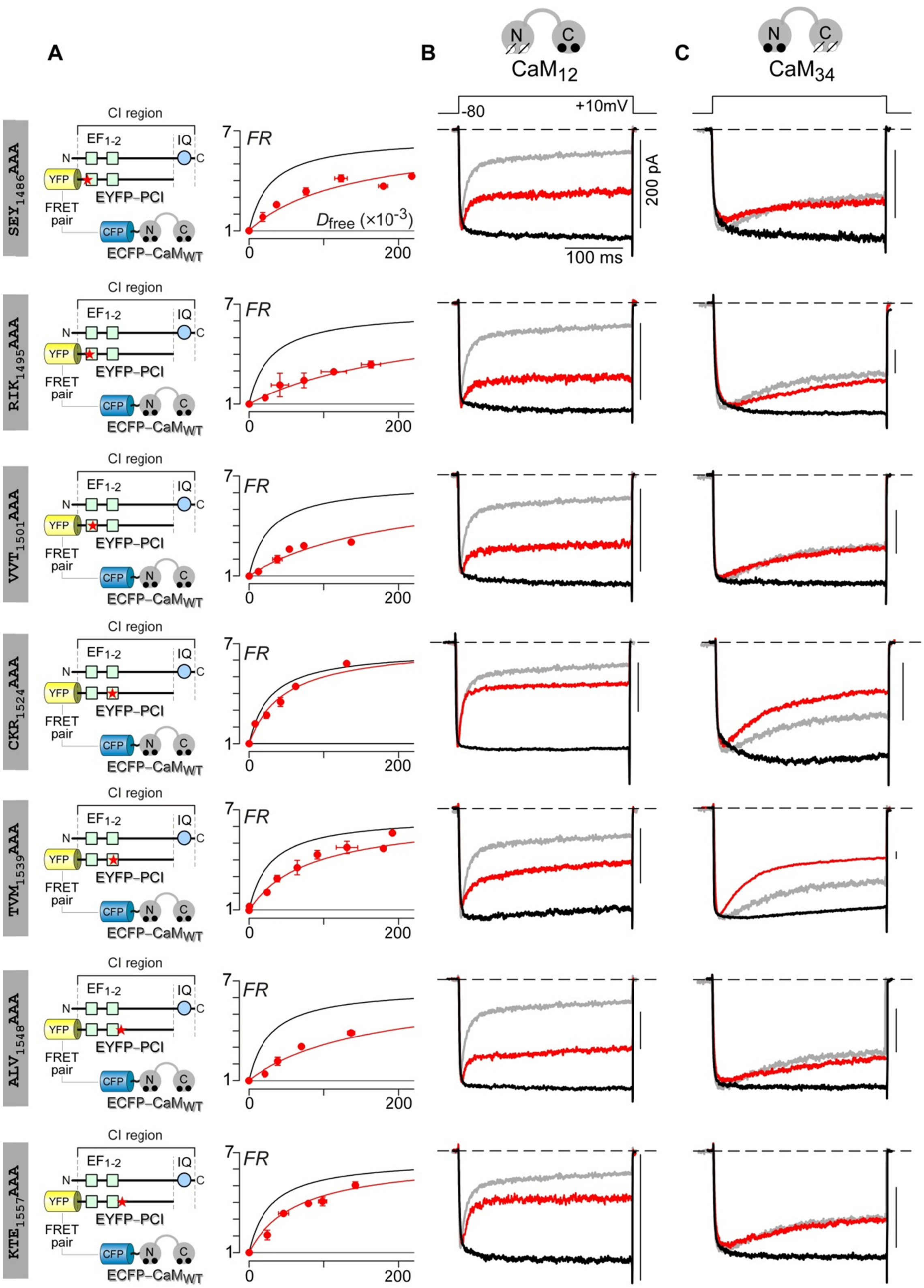
A
B
C
CaM$_{12}$
CaM$_{34}$
N
C
-80
+10mV
200 pA
100 ms
SEY$_{1486}$AAA
RIK$_{1495}$AAA
VVT$_{1501}$AAA
CKR$_{1524}$AAA
TVM$_{1539}$AAA
ALV$_{1548}$AAA
KTE$_{1557}$AAA
CI region
EF$_{1-2}$
IQ
YFP
EYFP–PCI
FRET pair
CFP
ECFP–CaM$_{WT}$
FR
7
1
0
200
$D_{free}$ (×10$^{-3}$)

**Figure 7.5. Extended analysis of PCI region as C-lobe $Ca^{2+}$/CaM effector site.**

(A) FRET 2-hybrid assay used to systematically characterize changes in $K_{a,EFF}$ of $Ca^{2+}$/CaM binding to mutant PCI region (red star). For reference, fits for wild-type YFP-PCI peptide binding to $Ca^{2+}$/CaM is reproduced in black from Figure 7.4. For each construct, $3^3$-FRET ratios measured from single cells were binned into symbols averaging ~5 cells (red circles).

(B) For each mutation, C-lobe CDI was characterized by co-expressing $CaM_{12}$ with mutant $Ca_V1.3$ channels. Whole-cell $Ca^{2+}$ currents in red, $Ba^{2+}$ currents in black. Compared to wild-type (Figure 7.4C), mutations in PCI region disrupt C-lobe CDI. Corresponding wild-type $Ca^{2+}$ current traces are shown as gray.

(C) Whole-cell currents from mutant channels coexpressed with $CaM_{34}$ showed no appreciable deficit in N-lobe CDI; format as in panel B. Corresponding wild-type $Ca^{2+}$ current traces are shown as gray.

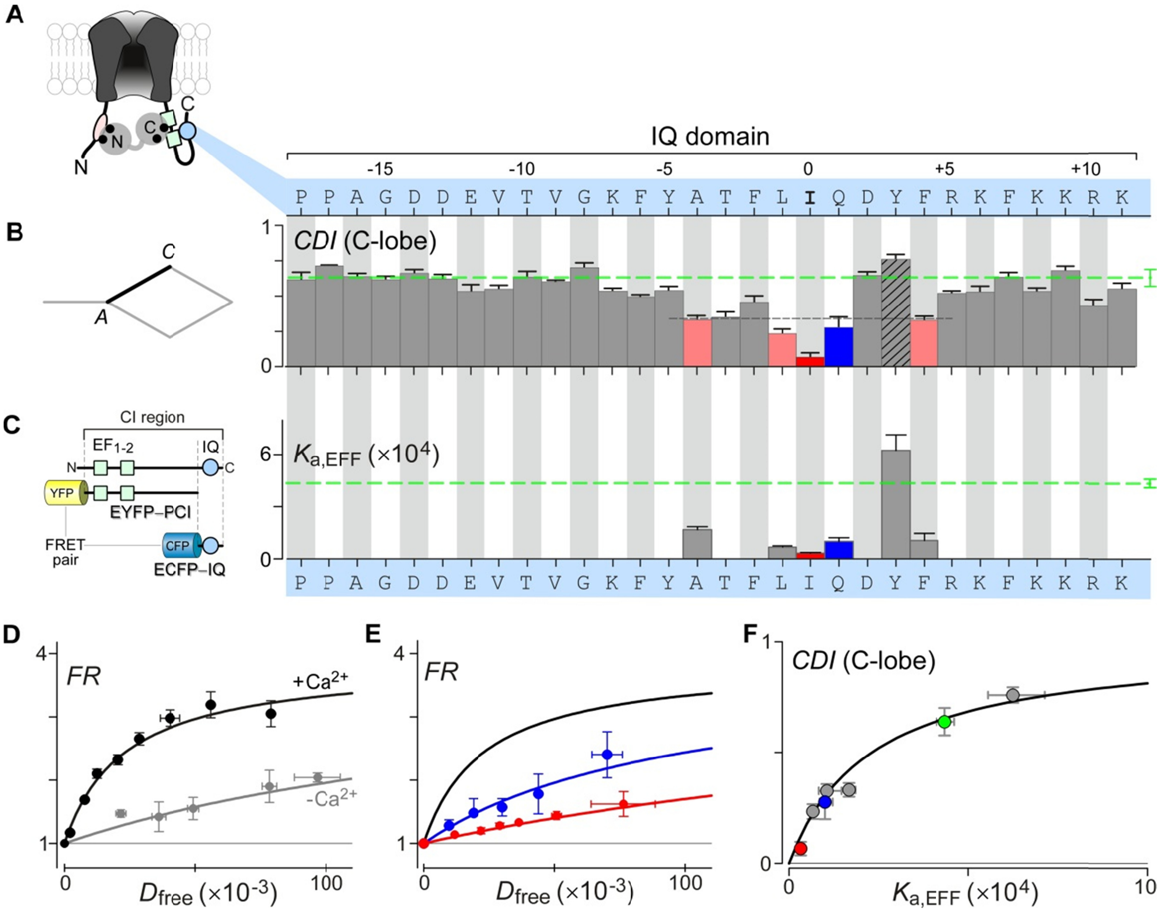
A
N
N
C
C
IQ domain
-15
-10
-5
0
+5
+10
P P A G D D E V T V G K F Y A T F L I Q D Y F R K F K K R K
B
C
A
1
0
CDI (C-lobe)
C
CI region
EF1-2
IQ
N
C
YFP
EYFP–PCI
FRET pair
CFP
ECFP–IQ
6
0
Ka,EFF (×10⁴)
P P A G D D E V T V G K F Y A T F L I Q D Y F R K F K K R K
D
4
1
FR
+Ca2+
-Ca2+
0
100
Dfree (×10-3)
E
4
1
FR
0
100
Dfree (×10-3)
F
1
0
CDI (C-lobe)
0
10
Ka,EFF (×10⁴)

**Figure 7.6. Role of IQ domain in C-lobe CDI.**

(A) Cartoon depicting putative binding interaction between IQ domain and PCI segment, which is also required for C-lobe CDI.

(B) Bar-graph summary of C-lobe CDI measured for alanine scan of IQ domain (Ben-Johny et al., 2013a). Strongest CDI reduction for I[0]A mutant (red), followed closely by loci affiliated with rose and blue bars underneath dashed-line.

(C) Association constants $K_{\mathrm{a,EFF}}$ determined for $3^3$-FRET binding between IQ domain and PCI region (partners diagrammed at left), under elevated levels of $Ca^{2+}$. Wild-type profile, green dashed line. Bars, $K_{\mathrm{a,EFF}}$ for mutants with strongest effects (colored bars in panel B) or chosen at random (hashed bars in panel B). Error bars, nonlinear standard deviation estimates.

(D) Exemplar $3^3$-FRET binding curves for IQ/PCI interaction. Each symbol, mean ± SEM of ~8 cells. Absent $Ca^{2+}$, the IQ domain associates only weakly with the PCI region (gray). However, elevated $Ca^{2+}$ greatly enhances binding (black).

(E) $3^3$-FRET binding curves for I[0]A (red) and Q[1]A (blue) mutations under elevated $Ca^{2+}$. Each symbol, mean ± SEM of ~5 cells. Fit for wild type IQ/PCI interaction reproduced from panel D in black.

(F) Plotting C-lobe CDI versus $K_{\mathrm{a,EFF}}$ under elevated $Ca^{2+}$ unveils a well-resolved Langmuir relation. WT (green), I[0]A (red), and Q[1]A (blue).

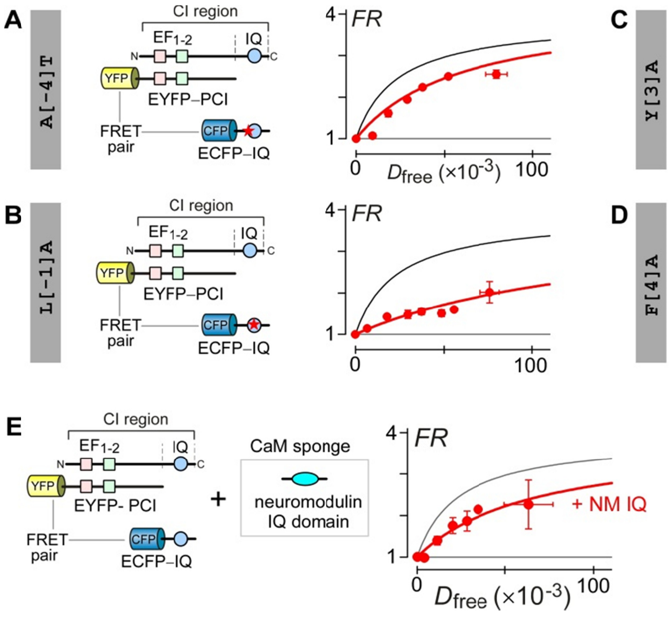

**Figure 7.7. Extended data characterizing PCI/IQ interaction.**

(A – D) FRET 2-hybrid assays probe interaction between IQ domain and PCI segment under elevated $Ca^{2+}$ conditions for various IQ domain mutants. Symbols average FRET measurements from ~4 cells each. In comparison to the wild-type IQ domain (black fit), mutations like A[-4]T (A), L[-1]A (B), and F[**4**]A (D) weakened IQ/PCI interaction in accord with diminished C-lobe CDI in these mutants (main text Fig. 6b). In contrast, the mutation Y[3]A resulted in a slight increase in the binding affinity (C), rationalizing in this case the slight increase in C-lobe CDI (Figure 7.6B). FRET data were fit (red curves) with the same maximal FRET efficiencies ($FR_{\text{max}} = 3.9$).

(E) Left, FRET 2-hybrid assay probing $Ca^{2+}$-dependent interaction between IQ domain and PCI segment. Right, For reference, the black fit shows binding curve for IQ/PCI binding in presence of $Ca^{2+}$, as reproduced from Figure 7.6D. Coexpression of a $Ca^{2+}$/CaM chelator, the IQ domain of neuromodulin, significantly weakened this interaction (red symbols and fit). This weakening is fully consistent with $Ca^{2+}$/CaM facilitating the $Ca^{2+}$-dependence of IQ/PCI interaction. $3^3$-FRET measured from single cells were binned into symbols averaging ~6 cells each.

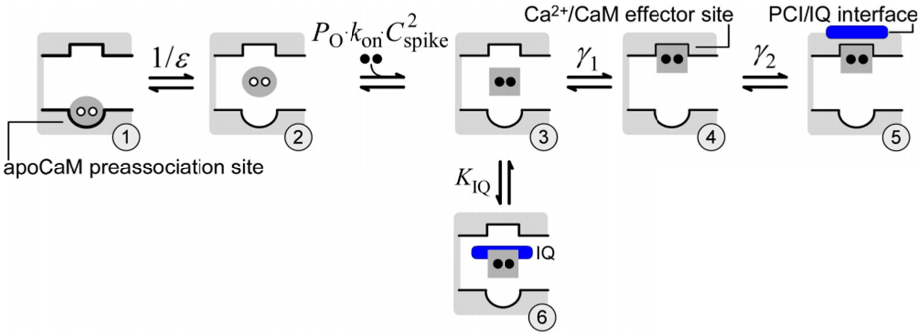
Ca2+/CaM effector site
PCI/IQ interface
$1/\varepsilon$
$P_O \cdot k_{on} \cdot C^2_{spike}$
$\gamma_1$
$\gamma_2$
$K_{IQ}$
IQ
①
②
③
④
⑤
⑥
apoCaM preassociation site

**Figure 7.8. Estimating the propensity of $Ca^{2+}$/CaM to leave the IQ domain.**

We add an additional state (state 6) to the reaction diagram of Figure 6.3B, where the IQ domain can potentially rebind $Ca^{2+}$/CaM. $K_{IQ}$, association constant for IQ domain binding to $Ca^{2+}$/CaM. To study the possibility of $Ca^{2+}$/CaM departing from the IQ domain, we consider the probability of occupying state 5 versus state 6.

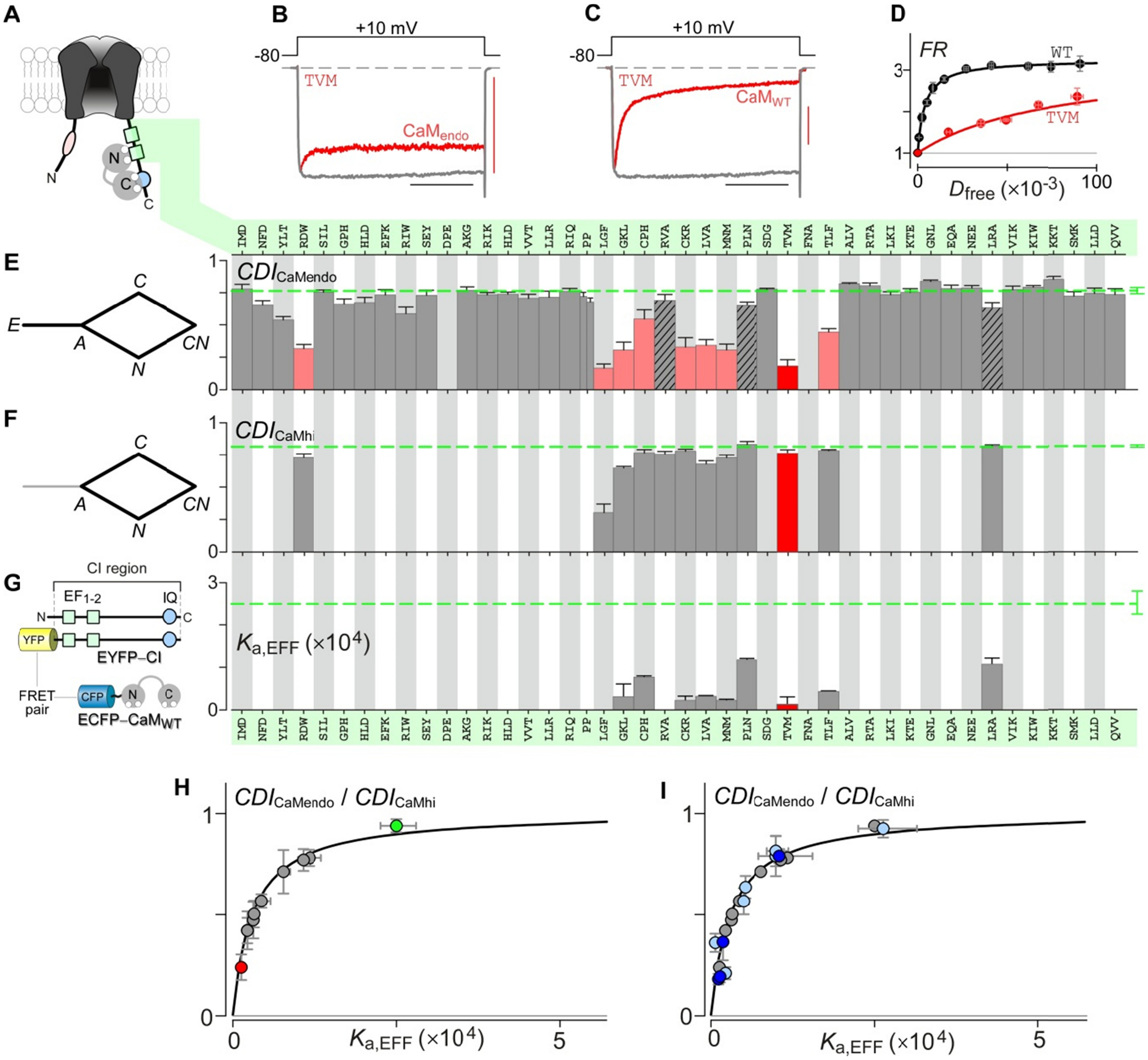
A
N
C
N
C
B
+10 mV
-80
TVM
CaM$_{endo}$
C
+10 mV
-80
TVM
CaM$_{WT}$
D
FR
WT
TVM
3
1
0
100
$D_{free}$ (×10$^{-3}$)
IMD NFD YLT RDW SIL GPH HLD EFK RIW SEY DPE AKG RIK HLD VVT LLR RIQ PP LGF GKL CPH RVA CKR LVA MNM PLN SDG TVM FNA TLF ALV RTA LKI KTE GNL EQA NEE LRA VIK KIW KKT SMK LLD QVV
E
E
A
C
N
CN
1
0
$CDI_{CaMendo}$
F
A
C
N
CN
1
0
$CDI_{CaMhi}$
G
CI region
EF$_{1-2}$
IQ
N
C
YFP
EYFP–CI
FRET pair
CFP
N
C
ECFP–CaM$_{WT}$
3
0
$K_{a,EFF}$ (×10$^4$)
H
$CDI_{CaMendo}$ / $CDI_{CaMhi}$
1
0
0
5
$K_{a,EFF}$ (×10$^4$)
I
$CDI_{CaMendo}$ / $CDI_{CaMhi}$
1
0
0
5
$K_{a,EFF}$ (×10$^4$)

**Figure 7.9. Footprint of apoCaM preassociation with the PCI segment.**

(A) Channel cartoon depicting apoCaM preassociated with the CI region, with C-lobe engaging IQ domain, and N-lobe associated with PCI region.

(B) Whole-cell currents for TVM→AAA mutant in the PCI segment ($Ca^{2+}$ in red; $Ba^{2+}$ in gray), with only endogenous CaM present.

(C) Overexpressing $CaM_{WT}$ rescues CDI for TVM→AAA mutation, suggesting that PCI region harbors an apoCaM preassociation locus.

(D) $3^3$-FRET binding curves show strong apoCaM binding to CI region. Wild type (WT) in black; TVM→AAA in red. Each symbol, mean ± SEM of ~7 cells.

(E) Bar-graph summary of CDI with only endogenous CaM present ($CDI_{\mathrm{CaMendo}}$), across alanine scan of PCI region. TVM→AAA (red) shows strongest effect, with rose colored bars also showing appreciable CDI reduction. Left, schematic of relevant CaM subsystem.

(F) Bar-graph summary of CDI rescue upon overexpressing $CaM_{WT}$ ($CDI_{\mathrm{CaMhi}}$), for mutations showing significant loss of CDI (colored bars in panel E), or chosen at random (hashed bars in panel E). Corresponding subsystem of regulation on the left.

(G) Bar-graph summary of $K_{\mathrm{a,EFF}}$ for apoCaM binding to CI region, with partners as sketched on the left. Data obtained for nearly all mutants with significant CDI reduction (colored in panel E), and for some mutants chosen at random (hashed in panel E). Error bars, nonlinear estimates of standard deviation.

(H) iTL analysis confirms role of PCI as a functionally relevant apoCaM site. Plotting $CDI_{\mathrm{CaMendo}}$ / $CDI_{\mathrm{CaMhi}}$ (panel E and F) versus $K_{\mathrm{a,EFF}}$ for apoCaM/CI binding uncovers a well-resolved Langmuir relation. TVM→AAA, red; WT, green.

(I) Overlaying like data for IQ-domain analysis presented elsewhere (Bazzazi et al., 2013) (blue symbols here) displays remarkable agreement, consistent with the same apoCaM binding both PCI and IQ domains. Deep blue symbols, A[-4], I[0], F[+4] hotspots for apoCaM interaction with IQ element.

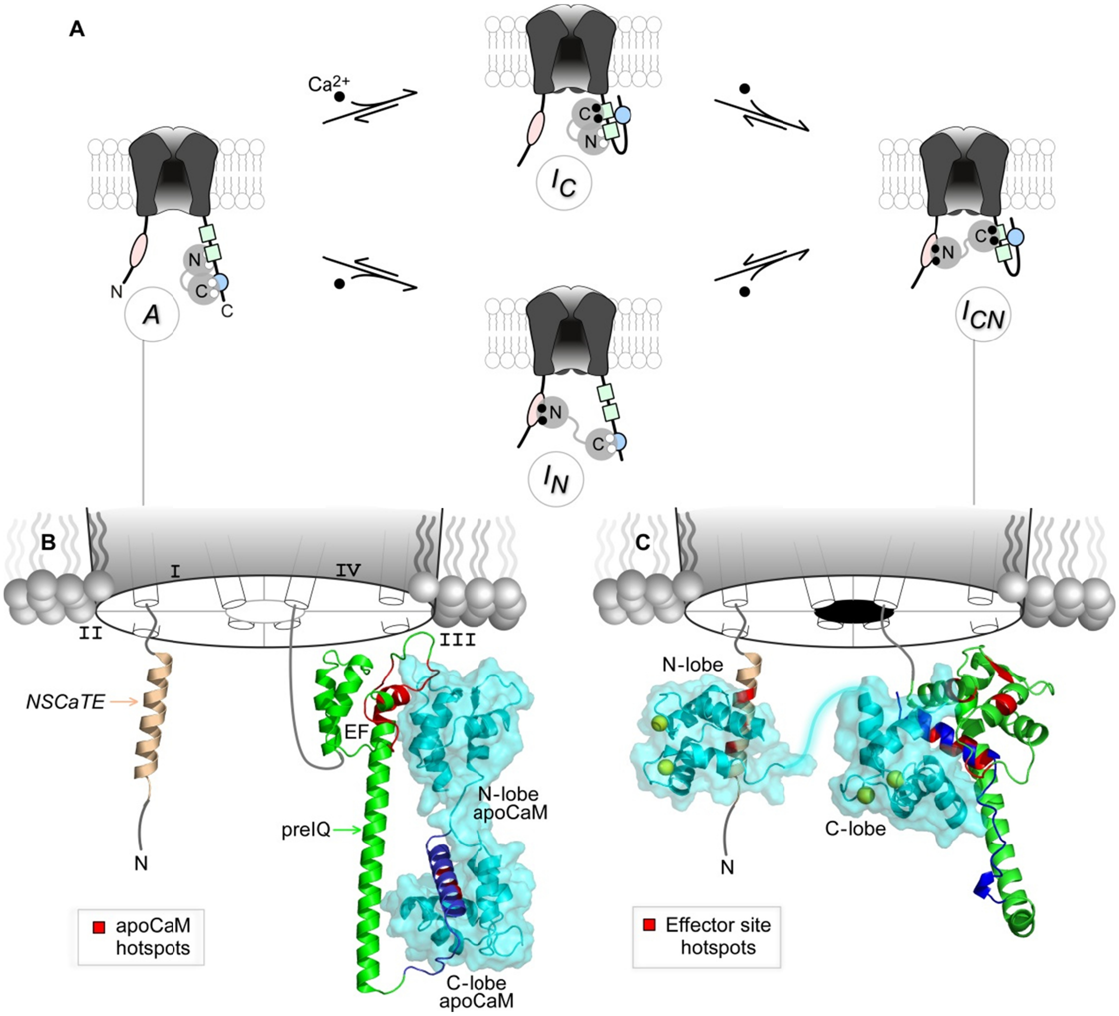
A
Ca2+
A
N
N
C
C
$I_C$
C
N
$I_N$
N
C
$I_{CN}$
N
C
B
I
IV
II
III
NSCaTE
EF
preIQ
N-lobe
apoCaM
C-lobe
apoCaM
N
🟥 apoCaM hotspots
C
N-lobe
C-lobe
N
🟥 Effector site hotspots

**Figure 7.10. Next generation view of CaM regulatory configurations of Ca$_V$1.3.**

(A) Molecular layout of configurations *A*, $I_C$, $I_N$, and $I_{CN}$ from general conceptual scheme Fig. 1a. ApoCaM begins preassociated to the CI region, with the C-lobe articulating the IQ domain, and the N-lobe engaging the PCI segment. Once $Ca^{2+}$ binds CaM, the N-lobe of $Ca^{2+}$/CaM departs to NSCaTE on the channel amino terminus, eliciting N-lobe CDI ($I_N$). Alternatively, the C-lobe of $Ca^{2+}$/CaM migrates to PCI segment, recruiting IQ domain to tri-partite complex ($I_C$). Finally, $I_{CN}$ corresponds to channel that has undergone both N- and C-lobe CDI.

(B) *De novo* structural modeling of Ca$_V$1.3 CI region with apoCaM docked (PCI region: green; IQ domain: blue). ApoCaM hotspots identified in Figure 7.9E-G highlighted in red. C-lobe of apoCaM intimately contacts IQ domain, while N-lobe preassociates with EF-hand region.

(C) Left, atomic structure of the NSCaTE bound to N-lobe of $Ca^{2+}$/CaM (2LQC (Liu and Vogel, 2012)). NSCaTE peptide shaded in pink, and N-lobe $Ca^{2+}$/CaM in cyan. N-lobe CDI hotspots on NSCaTE highlighted in red. Right, *de novo* molecular model of tripartite IQ-PCI-$Ca^{2+}$/CaM complex (PCI region, green; and IQ domain, blue). Highlighted in red are C-lobe CDI hotspots on both PCI and IQ domains.

## CHAPTER 8

# Conclusions – An ancient $Ca^{2+}$ regulatory module

It was nearly four decades ago that Paul Brehm and Roger Eckert described the curious phenomenon of $Ca^{2+}$ channels in *Paramecium* – the $Ca^{2+}$ ions that flux through the channel also inactivated the channel, a behavior notably distinct from the classic Hodgkin-Huxley model of Na channel inactivation (Hodgkin and Huxley, 1952). As it turns out, this phenomenon is not merely a curiosity, rather somewhat a rule in the modulation of four-domain voltage gated ion channels with important physiological implications. Both the function and mechanism of $Ca^{2+}$ regulation appear to be highly similar across $Ca^{2+}$ and Na channel superfamilies, featuring CaM as a modulatory partner. But how similar is similar? We find that this parallelism in channel regulation likely corresponds to underlying molecular structures, and thereby establishes CaM regulation as kindred modulation conferred by a conserved protein module.

***Towards a shared structural framework of $Ca^{2+}$ and Na channels -*** For $Ca^{2+}$ channels, obtaining atomic structures of the large segments of the channel carboxy terminus has been a formidable challenge resulting in the resolution of only short channel segments such as the IQ domain and preIQ segment (Figure 7.1) in complex with $Ca^{2+}$/CaM (Fallon et al., 2005; Van Petegem et al., 2005; Kim et al., 2008; Mori et al., 2008; Kim et al., 2010). In addition, no structures of apoCaM bound $Ca^{2+}$ channel carboxy-terminal segments are currently available. By contrast, structural studies of the Na channels have been comparatively more profitable with the unveiling of multiple atomic-resolution structures of various segments of the channel carboxy-terminus (Chagot et al., 2009; Miloushev et al., 2009; Chagot and Chazin, 2011; Feldkamp et al., 2011) and more recently, the entire CI region of these channels (Wang et al., 2012; Gabelli et al., 2014; Wang et al., 2014). In particular, the structure of the $Na_V1.5$ channel CI region in complex with apoCaM has been solved (Figure 8.1) (Gabelli et al., 2014). Stunningly, in this structure, apoCaM is found to interact with the $Na_V1.5$ CI region in a 'lock-washer' configuration (Figure 8.1). The C-lobe of CaM adopts a semi-open configuration with the partially exposed hydrophobic core interacting with the IQ domain, while the N-lobe adopts a closed configuration and interacts with the channel dual vestigial EF hand residues through exposed sidechains. The central 'isoleucine' residue of the channel IQ domain is shown as a red stick buried in the C-lobe of apoCaM. This configuration is remarkably similar to the model of apoCaM preassociation presented in Chapter 7 for $Ca^{2+}$ channels where again a bipartite model for apoCaM preassociation was postulated (Figure 7.10). Figure 8.1B shows a homology model of the $Ca_V1.3$ channel carboxy-terminus based on the corresponding $Na_V1.5$ structure presented in Figure 8.1A. Residues determined to be critical for apoCaM preassociation based on extensive alanine scanning mutagenesis and iTL analysis are shaded pink (for N-lobe contacts) and red (for C-lobe contacts). These functionally-identified hotspot residues for $Ca_V1.3$ channels are seen to interact intimately with apoCaM with the predicted lobe-preference. It is worth mentioning that an alternate structure of $Na_V1.5$ CI region in complex with apoCaM has also been solved (Wang et al., 2012). However, this structure also contains another Na channel interacting protein, fibroblast growth factor homologous factors (FHF). Importantly, the FHF molecule was found to interact with the channel dual vestigial EF hand segments allosterically by dislodging the N-lobe of apoCaM from the channel interface. This switch in CaM binding configuration suggests that FHFs may alter $Ca^{2+}$ regulation, an effect yet to be confirmed experimentally. Overall, the striking convergence of functional data for $Ca^{2+}$ channels with structural data from Na channels argues for a shared structural blueprint of apoCaM binding to the two channels. Thus, it seems plausible that the CI region of the two channels bears structural likeness after all, raising the possibility that this channel segment may comprise a modular element – a possibility we will explicitly demonstrate in this chapter.

***ApoCaM itself modulates channel baseline $P_O$*** – Traditionally, apoCaM has often appeared to be biologically inert and modulation of target molecules is thought to occur only upon conversion to $Ca^{2+}$/CaM. Fitting with this model, prior studies of Na and $Ca^{2+}$ channels have often considered apoCaM to be a resident $Ca^{2+}$ sensor that simply awaits $Ca^{2+}$ signals to elicit its modulatory effect. However, a recent study has revised this perspective by demonstrating that apoCaM binding to the $Ca^{2+}$ channel itself markedly upregulates their baseline channel $P_O$ (Figure 8.2). Exemplar single-channel records of wild-type $Ca_V1.3$ channels ($Ca_V1.3_{IQ}$) show normal openings (Figure 8.2A). Plotting the single-channel $P_O$ versus voltage illustrates the high open probability of these channels (Figure 8.2B). Importantly, these channels possess high apoCaM binding affinity, and therefore are charged with an apoCaM at endogenous CaM levels in a cell. By contrast, substituting methionines for the central isoleucine residue within the IQ domain results in mutant channels ($Ca_V1.3_{MQ}$) with a sharply diminished apoCaM binding affinity (Bazzazi et al., 2013). Curiously, the single-channel recordings of $Ca_V1.3_{MQ}$ channels showed a marked reduction in their baseline $P_O$ at endogenous CaM levels (Figure 8.2C-D). Remarkably, this effect is readily reversed upon overexpression of wild-type CaM (Figure 8.2E-F), suggesting that apoCaM binding is essential for normal opening of $Ca_V1.3$ channels. In fact, RNA-editing and alternative splicing of $Ca_V1.3$ result in an assortment of native $Ca^{2+}$ channels whose $P_O$ is readily tuned by changes in the ambient CaM concentration in cells (Adams et al., 2014).

Given the extensive structural similarity in apoCaM binding to both $Ca^{2+}$ and Na channel CI regions, and the like resemblance in functional manifestation of $Ca^{2+}$/CaM regulation, we wondered whether apoCaM itself might tune the baseline $P_O$ of Na channels. Fitting with this possibility, prior studies of $Na_V1.4$ channels have shown that alanine substitutions in the IQ domain both reduce CaM binding and decrease current density (Herzog et al., 2003). To explicitly test for apoCaM modulatory effects, we compared the single-channel activity of wild-type $Na_V1.4$ (which avidly binds apoCaM at baseline) with that of a mutant $Na_V1.4_{IQ/AA}$ exhibiting weakened apoCaM affinity via IQ to AA substitution within the IQ domain (Herzog et al., 2003; Biswas et al., 2008; Adams et al., 2014). Wild-type recombinant $Na_V1.4$ channels exhibited frequent stochastic openings of millisecond duration (Figure 8.3A). Normalizing the ensemble average of many such records (by unitary current $i$ and number of channels $N$) yields a robust $P_O$ waveform that peaks at 0.5 (Figure 8.3B). This outcome is confirmed by plots of peak $P_O$ versus step potential (Figure 8.3C), averaged from multiple patches. By contrast, $Na_V1.4_{IQ/AA}$ channels might often lack apoCaM at baseline. Fitting with a mechanism where such channels would be reluctant to open, corresponding single-molecule records display a sparser pattern of activity with briefer openings (Figure 8.3D). The ensemble average explicitly confirms this impression, yielding a diminutive $P_O$ waveform (Figure 8.3E) and $P_O$–$V$ relation (Figure 8.3F). Still, this reduced opening could be an intrinsic effect of mutation, rather than that of lacking apoCaM. To exclude the former possibility, we strongly coexpressed CaM with $Na_V1.4_{IQ/AA}$ channels, a maneuver that should restore apoCaM binding via mass action. Reassuringly, corresponding single-molecule records again exhibit robust activity (Figure 8.3G), and peak $P_O$ is rescued to near wild-type levels (Figures 8.3H and 8.3I), confirming a primary ability of apoCaM to elevate $P_O$.

These data therefore support conservation of apoCaM modulation of $P_O$ in both $Ca_V$ and $Na_V$ channel superfamilies. Biologically important, the CI region of many Na channels including $Na_V1.5$ harbor myriad disease-associated mutations (Lossin, 2009; Kapplinger et al., 2010). Our results suggest that diminished Na channel peak $P_O$ resulting from altered apoCaM preassociation could be an important new dimension in the pathophysiology of Na channelopathies.

***CI region as a modular element*** – From the perspective of conservation, it is intriguing that nearly all high-voltage gated $Ca^{2+}$ channels that possess highly similar CI regions and functionally depict robust and recognizably similar forms of CaM regulation (Figure 8.4A). The low voltage-activated (T-type) $Ca^{2+}$ channels lack the CI region (Perez-Reyes et al., 1998; Perez-Reyes, 2006) and are also insensitive to direct regulation by $Ca^{2+}$/CaM (Figure 8.4A) (Perez-Reyes, 2003). By contrast, all members of the mammalian voltage-gated Na channel family possess the CI region (Van Petegem et al., 2012). So far, the $Na_V1.4$ channel has been shown to be modulated by $Ca^{2+}$/CaM in a manner highly similar to $Ca^{2+}$ channel calmodulation. $Na_V1.5$ channels also possess latent $Ca^{2+}$/CaM unveiled by mutagenesis (Chapter 5). Functional $Ca^{2+}$ regulation of other members of the Na channel superfamily (Figure 8.4A, $Na_V1.1$–$Na_V1.9$, except $Na_V1.5$) remains an open question. To this end, our methods of rapid $Ca^{2+}$-delivery furnishes a convenient approach to undertake systematic characterization of these channels.

That notwithstanding, the extensive parallels between calmodulation in Na and $Ca^{2+}$ channels, suggests the persistence of a common CaM-CI regulatory element amongst $Ca^{2+}$ and Na channels. We therefore attempted a final, patently simple test for this possibility – the transplantation of the CI module from one channel superfamily to another. Upon adjoining the core of a $Ca_V1.3$ channel to the carboxy tail of a $Na_V1.4$ channel, not only were sizeable currents expressed, the faster decay of $Ca^{2+}$ versus $Ba^{2+}$ currents (top), according to a classic voltage-dependent profile ($r_{300}$ plot below), indicates the presence of $Ca^{2+}$ regulation (CDI) in this chimera (Figure 8.4B). Importantly, this

$Ca^{2+}$ regulation is abolished by coexpression of mutant $CaM_{1234}$ (Figure 8.4C) just as with $Na_V1.4$ channels (Figure 5.2). Recapitulating $Ca^{2+}$ regulation in these chimeric channels then argues strongly that the regulatory design of one superfamily persists with sufficient congruity to functionally interface with the core of another. This modularity may rival that of voltage-paddle elements transferable from $Na_V$ to $K_V$ channels (Bosmans et al., 2008). Thus established, the commonality of the CaM-CI module promises valuable insights from synergistic co-investigation of Na and $Ca^{2+}$ channels.

***Antiquity of CaM-CI module*** – More general implications concern the antiquity of the CaM-CI $Ca^{2+}$ regulatory module. Figure 8.5 depicts the phylogenetic tree of Na and $Ca^{2+}$ channel superfamilies based on multiple sequence alignment of carboxy tails. The CI region is conserved across the top branches of this tree, conferring $Ca^{2+}$ regulation to certain Na and high-voltage activated $Ca^{2+}$ channels ($Ca_V1$ and $Ca_V2$ branches). To explore the historical basis for the $Ca^{2+}$ and Na channel CI region, Figure 8.5 undertakes sequence alignment and phylogenetic analysis of $Ca^{2+}$ and Na channels from major eukaryotic phyla, starting with the single-celled protozoa *Paramecia*. This organism lacks voltage-gated Na channels, but possesses a $Ca^{2+}$ channel for which robust $Ca^{2+}$ regulation has been long-established (Brehm and Eckert, 1978). From this start, the $Ca^{2+}$ channel clade for more advanced organisms branches towards the top, and the Na channel clade towards the bottom. Remarkably, sequence similarity in the dual vestigial EF hand motifs and the canonical IQ domains of the CI region is conserved throughout. Thus, given the common heritage of these channels dating to the early days of eukaryotes (~1 billion years ago), our results substantiate the preservation of a primordial $Ca^{2+}$ regulatory design across channel superfamilies, featuring calmodulin as a modulatory partner throughout much of living history.

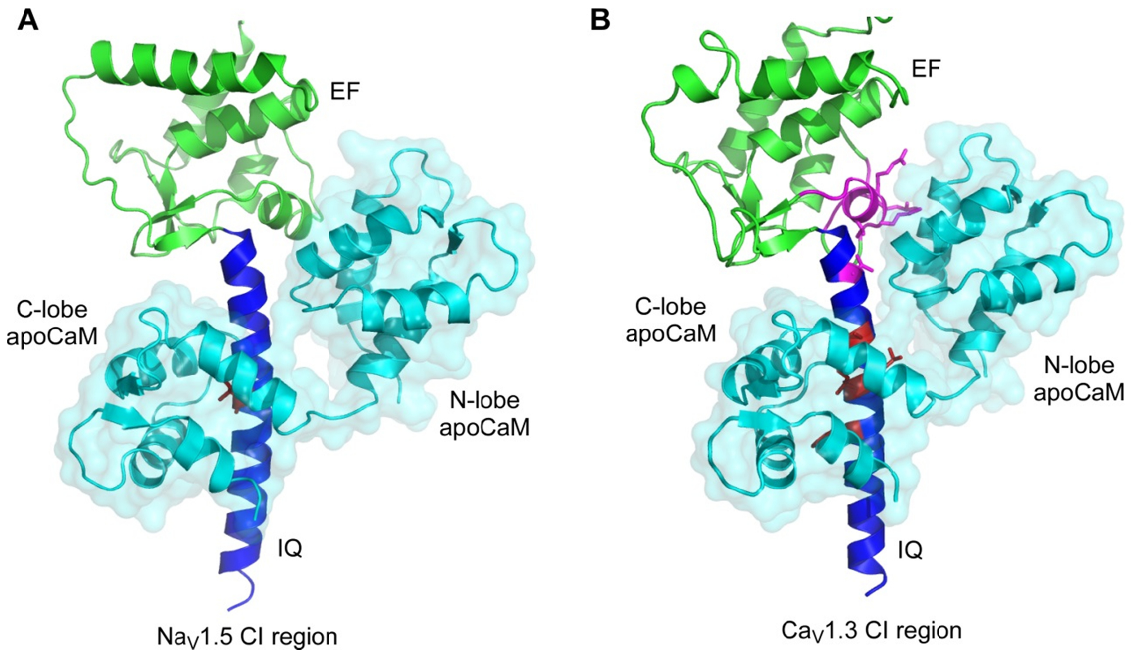
A
EF
C-lobe apoCaM
N-lobe apoCaM
IQ
$Na_V$1.5 CI region
B
EF
C-lobe apoCaM
N-lobe apoCaM
IQ
$Ca_V$1.3 CI region

**Figure 8.1. ApoCaM binding to the CI region of $Na_V$1.5 and $Ca_V$1.3 channels.**

(A) Crystal structure of $Na_V$1.5 CI region in complex with apoCaM alone (Gabelli et al., 2014). The EF hand segment is shaded green, IQ domain is colored blue, and apoCaM is shaded cyan. CaM adopts a ‘lock-washer’ configuration around the CI region. The C-lobe of apoCaM preassociates with the IQ domain while the N-lobe of apoCaM binds to the vestigial EF hand segment (EF2).

(B) Homology model of apoCaM bound to the $Ca_V$1.3 CI region based on the $Na_V$1.5 structure in panel A. As with the model presented in Figure 7.10B, the C-lobe of apoCaM is bound to the IQ domain and the N-lobe of apoCaM is preassociated to the vestigial EF hand (EF2). The hotspots for apoCaM binding identified in our functional studies are shaded red (C-lobe contacts) and pink (N-lobe contacts).

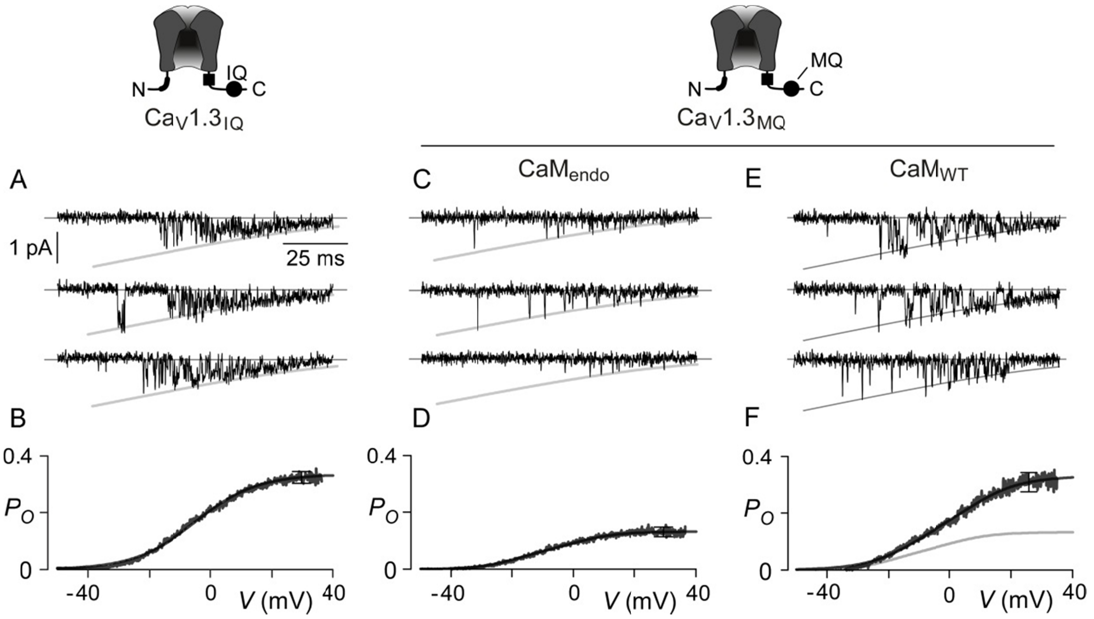

**Figure 8.2. ApoCaM modulates baseline $P_O$ of Ca$_V$1.3 channels.**

(A) Wild-type Ca$_V$1.3 channels possess a high affinity for apoCaM. Exemplar single-channel records of wild-type Ca$_V$1.3 in response to a voltage-ramp protocol.

(B) Ensemble average of single-channel records from panel A, normalized for the unitary current yields the average single-channel $P_O$ versus voltage. The wild-type Ca$_V$1.3 channel opens with a high $P_O$.

(C) ApoCaM preassociation to Ca$_V$1.3 is weakened by methionine substitution of the central isoleucine (Ca$_V$1.3$_{S/MQ}$). Exemplar single-channel records show sparse opening of these mutant channels at endogenous levels of CaM.

(D) Ensemble average depicts low $P_O$ of mutant Ca$_V$1.3$_{S/MQ}$ channel.

(E-F) Overexpression of wildtype CaM enhances baseline $P_O$ of Ca$_V$1.3$_{S/MQ}$ channel.

* Data reproduced with permission (Adams et al., 2014).

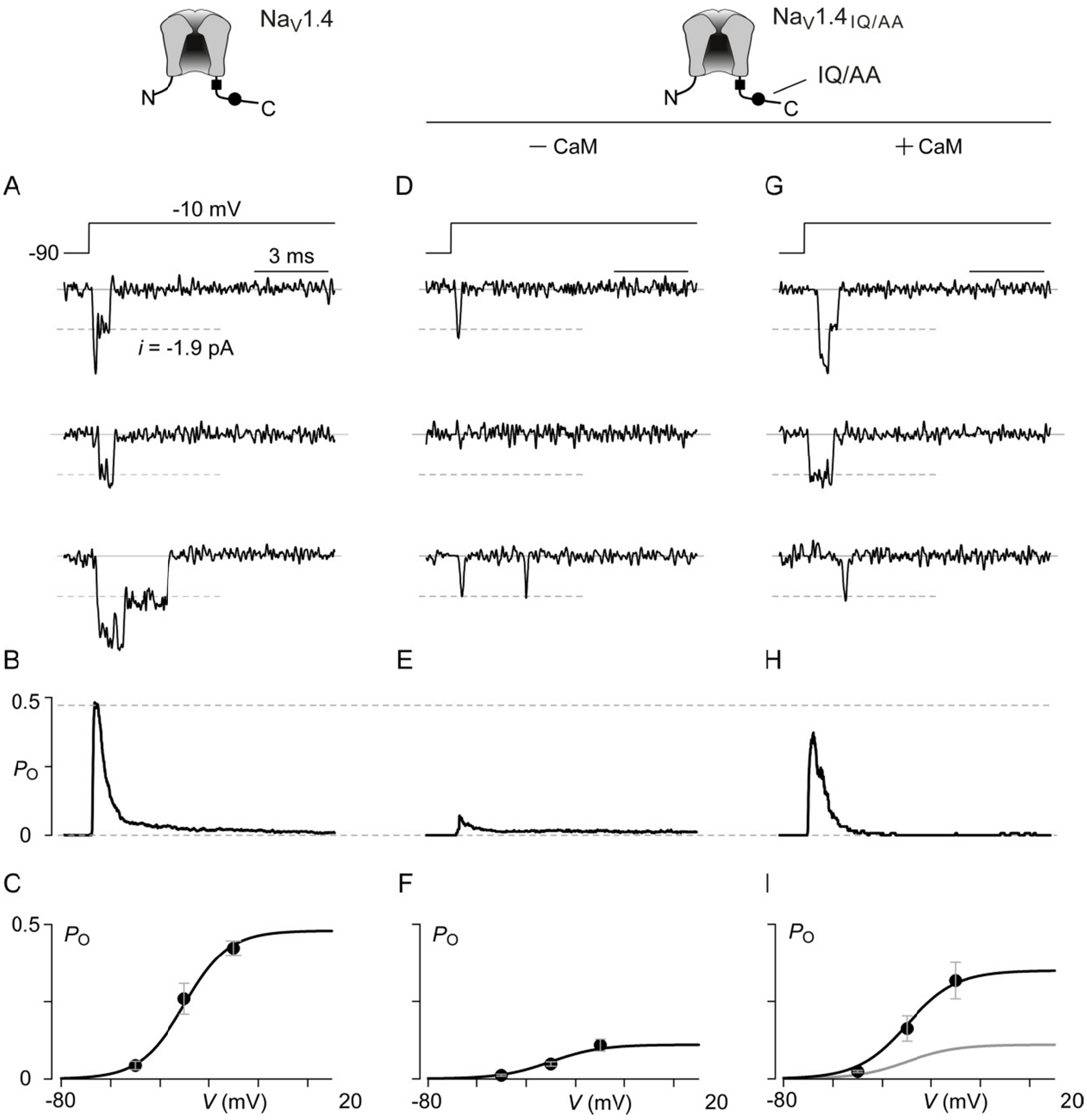

$Na_V1.4$
N
C
$Na_V1.4_{IQ/AA}$
IQ/AA
N
C
− CaM
+ CaM
A
-10 mV
-90
3 ms
i = -1.9 pA
D
G
B
0.5
$P_O$
0
E
H
C
0.5
$P_O$
0
-80
V (mV)
20
F
$P_O$
-80
V (mV)
20
I
$P_O$
-80
V (mV)
20

**Figure 8.3. ApoCaM modulates baseline $P_O$ of Na$_V$1.4 channels.**

(A) Single-molecule records of wild-type Na$_V$1.4 channels transiently expressed in HEK cells, with only endogenous CaM.

(B) $P_O$ waveform obtained by normalizing ensemble average of >100 records by unitary current $i$ and number of channels $N$.

(C) Plot of peak $P_O$ versus step potential (from -90 mV holding potential), averaged over multiple patches.

(D – F) Single-channel records for Na$_V$1.4 channels containing IQ to AA substitution (Na$_V$1.4$_{IQ/AA}$) at low CaM levels (D). Corresponding $P_O$ waveform (E) and $P_O$–$V$ relation (F). Channels are coexpressed with the CaM chelator, BSCaM$_{IQ}$, to minimize free CaM levels .

(G – H) Single-channel traces for Na$_V$1.4$_{IQ/AA}$ paired with overexpressed CaM (G). Corresponding $P_O$ waveform (H) and $P_O$–$V$ relation (I) both restored to near wild-type levels. $P_O$–$V$ relations averaged from $n$ = 5-8 patches each. Error bars, SEM.

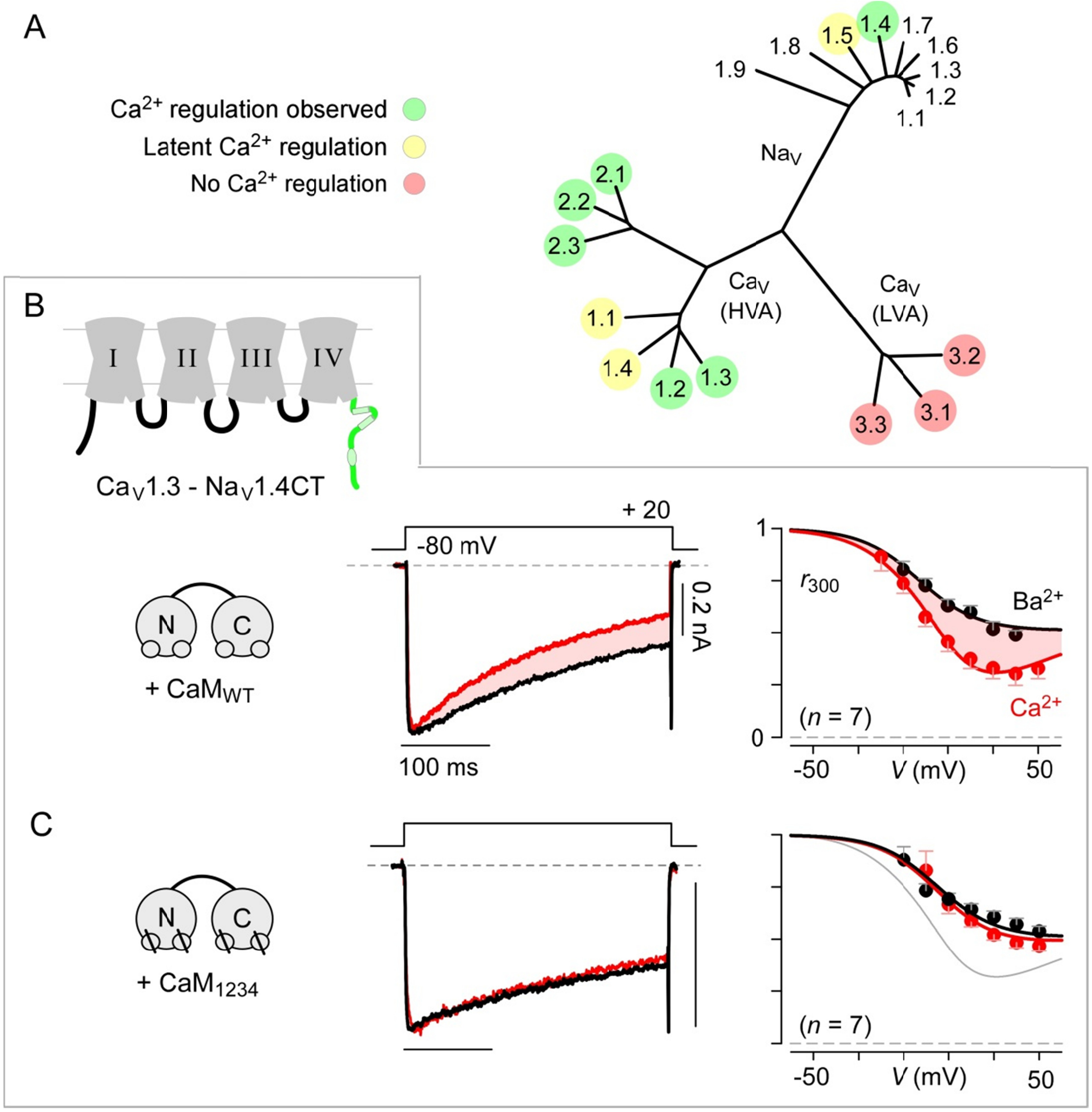

A
Ca$^{2+}$ regulation observed
Latent Ca$^{2+}$ regulation
No Ca$^{2+}$ regulation
Na$_V$
1.9
1.8
1.5
1.4
1.7
1.6
1.3
1.2
1.1
2.1
2.2
2.3
Ca$_V$ (HVA)
1.1
1.4
1.2
1.3
Ca$_V$ (LVA)
3.2
3.1
3.3
B
I
II
III
IV
Ca$_V$1.3 - Na$_V$1.4CT
N
C
+ CaM$_{WT}$
+ 20
-80 mV
0.2 nA
100 ms
1
$r_{300}$
Ba$^{2+}$
Ca$^{2+}$
($n$ = 7)
0
-50
$V$ (mV)
50
C
N
C
+ CaM$_{1234}$
($n$ = 7)
-50
$V$ (mV)
50

**Figure 8.4. CI region as a shared module across $Ca^{2+}$ and Na channels.**

(B) Phylogenetic tree of the $Na_V/Ca_V$ ion-channel superfamilies. CI region is present in $Ca_V1/2$ channels and $Na_V$ channels. $Ca^{2+}$ regulation is observed for nearly all $Ca_V1/2$ channels and $Na_V1.4$ channels.

(C) Transplanting the $Na_V1.4$ channel carboxy terminus onto $Ca_V1.3$ backbone, yielding $Ca_V1.3$-$Na_V1.4$CT chimeric channels, retains a form of $Ca^{2+}$ regulation. $Ca^{2+}$ currents shown in red and $Ba^{2+}$ currents shown in black. Each symbol, mean ± SEM from 7 cells. Here, CDI was measured under low $Ca^{2+}$ buffering.

(D) Coexpression of $CaM_{1234}$ abolishes CDI of the $Ca_V1.3$-$Na_V1.4$CT chimeric channels. Format as in panel C. Each symbol, mean ± SEM from 7 cells. CDI was again measured under low $Ca^{2+}$ buffering conditions as in panel C.

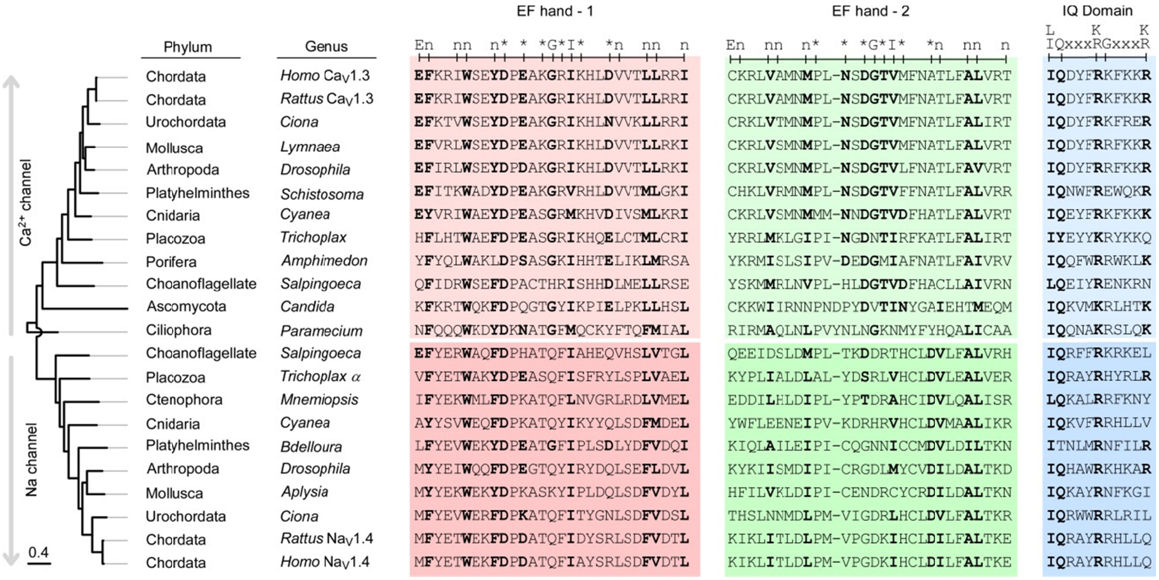
EF hand - 1
EF hand - 2
IQ Domain
Phylum
Genus
En nn n* * *G*I* *n nn n
En nn n* * *G*I* *n nn n
L K K
IQxxxRGxxxR
Ca$^{2+}$ channel
Na channel
0.4
Chordata Homo Ca$_V$1.3 EFKRIWSEYDPEAKGRIKHLDVVTLLRRI CKRLVAMNMPL-NSDGTVMFNATLFALVRT IQDYFRKFKKR
Chordata Rattus Ca$_V$1.3 EFKRIWSEYDPEAKGRIKHLDVVTLLRRI CKRLVAMNMPL-NSDGTVMFNATLFALVRT IQDYFRKFKKR
Urochordata Ciona EFKTVWSEYDPEAKGRIKHLNVVKLLRRI CRKLVTMNMPL-NSDGTVMFNATLFALIRT IQDYFRKFRER
Mollusca Lymnaea EFVRLWSEYDPEAKGRIKHLDVVTLLRKI CKRLVSMNMPL-NSDGTVMFNATLFALVRT IQDYFRRFKKR
Arthropoda Drosophila EFIRLWSEYDPDAKGRIKHLDVVTLLRKI CKRLVSMNMPL-NSDGTVLFNATLFAVVRT IQDYFRRFKKR
Platyhelminthes Schistosoma EFITKWADYDPEAKGRVRHLDVVTMLGKI CHKLVRMNMPL-NSDGTVFFNATLFALVRR IQNWFREWQKR
Cnidaria Cyanea EYVRIWAEYDPEASGRMKHVDIVSMLKRI CKRLVSMNMMM-NNDGTVDFHATLFALVRT IQEYFRKFKKK
Placozoa Trichoplax HFLHTWAEFDPEASGRIKHQELCTMLCRI YRRLMKLGIPI-NGDNTIRFKATLFALIRT IYEYYKRYKKQ
Porifera Amphimedon YFYQLWAKLDPSASGKIHHTELIKLMRSA YKRMISLSIPV-DEDGMIAFNATLFAIVRV IQQFWRRWKLK
Choanoflagellate Salpingoeca QFIDRWSEFDPACTHRISHHDLMELLRSE YSKMMRLNVPL-HLDGTVDFHACLLAIVRN LQEIYRENKRN
Ascomycota Candida KFKRTWQKFDPQGTGYIKPIELPKLLHSL CKKWIIRNNPNDPYDVTINYGAIEHTMEQM IQKVMKRLHTK
Ciliophora Paramecium NFQQQWKDYDKNATGFMQCKYFTQFMIAL RIRMAQLNLPVYNLNGKNMYFYHQALICAA IQQNAKRSLQK
Choanoflagellate Salpingoeca EFYERWAQFDPHATQFIAHEQVHSLVTGL QEEIDSLDMPL-TKDDRTHCLDVLFALVRH IQRFFRKRKEL
Placozoa Trichoplax α VFYETWAKYDPEASQFISFRYLSPLVAEL KYPLIALDLAL-YDSRLVHCLDVLEALVER IQRAYRHYRLR
Ctenophora Mnemiopsis IFYEKWMLFDPKATQFLNVGRLRDLVMEL EDDILHLDIPL-YPTDRAHCIDVLQALISR LQKALRRFKNY
Cnidaria Cyanea AYYSVWEQFDPKATQYIKYYQLSDFMDEL YWFLEENEIPV-KDRHRVHCLDVMAALIKR IQKVFRRHLLV
Platyhelminthes Bdelloura LFYEVWEKYDPEATGFIPLSDLYDFVDQI KIQLAILEIPI-CQGNNICCMDVLDILTKN ITNLMRNFILR
Arthropoda Drosophila MYYEIWQQFDPEGTQYIRYDQLSEFLDVL KYKIISMDIPI-CRGDLMYCVDILDALTKD IQHAWRKHKAR
Mollusca Aplysia MYYEKWEKYDPKASKYIPLDQLSDFVDYL HFILVKLDIPI-CENDRCYCRDILDALTKN IQKAYRNFKGI
Urochordata Ciona MFYEVWERFDPKATQFITYGNLSDFVDSL THSLNNMDLPM-VIGDRLHCLDVLFALTKR IQRWWRRLRIL
Chordata Rattus Na$_V$1.4 MFYETWEKFDPDATQFIDYSRLSDFVDTL KIKLITLDLPM-VPGDKIHCLDILFALTKE IQRAYRRHLLQ
Chordata Homo Na$_V$1.4 MFYETWEKFDPDATQFIAYSRLSDFVDTL KIKLITLDLPM-VPGDKIHCLDILFALTKE IQRAYRRHLLQ

**Figure 8.5. CI region – a primordial Ca$^{2+}$-regulatory module**

Maximum likelihood phylogenetic tree shows the extensive conservation of both Ca$^{2+}$ and Na channel CI regions, across the major eukaryotic phyla. Consensus sequence patterns for motifs on top. The sequence alignment is organized starting at the center with the Ca$^{2+}$ channel from the single-cell protozoan *Paramecium*. Ca$^{2+}$ channels from more advanced organisms are shown branching to the top (pale colors). The Na channel clade is shown branching to the bottom (darker colors).

# REFERENCES

Adams, P.J., M. Ben-Johny, I.E. Dick, T. Inoue, and D.T. Yue. 2014. Apocalmodulin itself promotes ion channel opening and Ca(2+) regulation. *Cell*. 159:608-622.

Adams, P.J., R.L. Rungta, E. Garcia, A.M. van den Maagdenberg, B.A. MacVicar, and T.P. Snutch. 2010. Contribution of calcium-dependent facilitation to synaptic plasticity revealed by migraine mutations in the P/Q-type calcium channel. *Proc Natl Acad Sci U S A*. 107:18694-18699.

Adams, P.J., and T.P. Snutch. 2007. Calcium channelopathies: voltage-gated calcium channels. *Sub-cellular biochemistry*. 45:215-251.

Adelman, J.P., J. Maylie, and P. Sah. 2012. Small-conductance Ca2+-activated K+ channels: form and function. *Annu Rev Physiol*. 74:245-269.

Aiba, T., G.G. Hesketh, T. Liu, R. Carlisle, M.C. Villa-Abrille, B. O'Rourke, F.G. Akar, and G.F. Tomaselli. 2009. Na+ channel regulation by Ca2+/calmodulin and Ca2+/calmodulin-dependent protein kinase II in guinea-pig ventricular myocytes. *Cardiovascular research*. 85:454-463.

Albuquerque, E.X., and S. Thesleff. 1967. Influence of phospholipase C on some electrical properties of the skeletal muscle membrane. *J Physiol*. 190:123-137.

Alexander, K.A., B.M. Cimler, K.E. Meier, and D.R. Storm. 1987. Regulation of calmodulin binding to P-57. A neurospecific calmodulin binding protein. *J Biol Chem*. 262:6108-6113.

Alseikhan, B.A., C.D. DeMaria, H.M. Colecraft, and D.T. Yue. 2002. Engineered calmodulins reveal the unexpected eminence of $Ca^{2+}$ channel inactivation in controlling heart excitation. *Proc Natl Acad Sci U S A*. 99:17185-17190.

Anderson, M.E., and P.J. Mohler. 2009. Rescuing a failing heart: think globally, treat locally. *Nature medicine*. 15:25-26.

Armstrong, C.M., and G. Cota. 1991. Calcium ion as a cofactor in Na channel gating. *Proc Natl Acad Sci U S A*. 88:6528-6531.

Armstrong, D., C. Erxleben, D. Kalman, Y. Lai, a. Nairn, and P. Greengard. 1988. Intracellular Calcium Controls the Activity of Dihydropyridine-sensitive Calcium Channels through Protein Phosphorylation and Its Removal. *Journal of General Physiology*. 92:10a.

Arnaiz, O., and L. Sperling. 2011. ParameciumDB in 2011: new tools and new data for functional and comparative genomics of the model ciliate Paramecium tetraurelia. *Nucleic acids research*. 39:D632-636.

Ashcroft, F.M., and P.R. Stanfield. 1981. Calcium dependence of the inactivation of calcium currents in skeletal muscle fibers of an insect. *Science*. 213:224-226.

Ashpole, N.M., A.W. Herren, K.S. Ginsburg, J.D. Brogan, D.E. Johnson, T.R. Cummins, D.M. Bers, and A. Hudmon. 2012. Ca2+/calmodulin-dependent protein kinase II (CaMKII) regulates cardiac sodium channel NaV1.5 gating by multiple phosphorylation sites. *J Biol Chem*. 287:19856-19869.

Asmara, H., E. Minobe, Z.A. Saud, and M. Kameyama. 2010. Interactions of calmodulin with the multiple binding sites of Cav1.2 Ca2+ channels. *Journal of pharmacological sciences*. 112:397-404.

Babitch, J. 1990. Channel hands. *Nature*. 346:321-322.

Babu, Y.S., J.S. Sack, T.J. Greenhough, C.E. Bugg, A.R. Means, and W.J. Cook. 1985. Three-dimensional structure of calmodulin. *Nature*. 315:37-40.

Barbato, G., M. Ikura, L.E. Kay, R.W. Pastor, and A. Bax. 1992. Backbone dynamics of calmodulin studied by 15N relaxation using inverse detected two-dimensional NMR spectroscopy: the central helix is flexible. *Biochemistry*. 31:5269-5278.

Baylor, S.M., and S. Hollingworth. 2012. Intracellular calcium movements during excitation-contraction coupling in mammalian slow-twitch and fast-twitch muscle fibers. *J Gen Physiol*. 139:261-272.

Bazzazi, H., M. Ben Johny, P.J. Adams, T.W. Soong, and D.T. Yue. 2013. Continuously tunable Ca(2+) regulation of RNA-edited CaV1.3 channels. *Cell reports*. 5:367-377.

Bean, B.P. 2007. Neurophysiology: stressful pacemaking. *Nature*. 447:1059-1060.

Ben-Johny, M., P.S. Yang, H. Bazzazi, and D.T. Yue. 2013a. Dynamic switching of calmodulin interactions underlies Ca2+ regulation of CaV1.3 channels. *Nature communications*. 4:1717.

Ben-Johny, M., P.S. Yang, H.X. Bazzazi, and D.T. Yue. 2013b. Dynamic switching of calmodulin interactions underlies $Ca^{2+}$ regulation of $Ca_V1.3$ channels. *Nature communications*. 4:1717.

Ben-Johny, M., P.S. Yang, J. Niu, W. Yang, R. Joshi-Mukherjee, and D.T. Yue. 2014. Conservation of Ca2+/calmodulin regulation across Na and Ca2+ channels. *Cell*. 157:1657-1670.

Ben-Johny, M., and D.T. Yue. 2014. Calmodulin regulation (calmodulation) of voltage-gated calcium channels. *J Gen Physiol*. 143:679-692.

Benson, D.A., I. Karsch-Mizrachi, D.J. Lipman, J. Ostell, and D.L. Wheeler. 2005. GenBank. *Nucleic acids research*. 33:D34-38.

Berridge, M.J., P. Lipp, and M.D. Bootman. 2000. The versatility and universality of calcium signalling. *Nat Rev Mol Cell Biol*. 1:11-21.

Bers, D.M. 2002. Cardiac excitation-contraction coupling. *Nature*. 415:198-205.

Bers, D.M., C.W. Patton, and R. Nuccitelli. 2010. A practical guide to the preparation of Ca(2+) buffers. *Methods in cell biology*. 99:1-26.

Bezprovanny, I. 2009. Calcium signaling and neurodegenerative diseases. *Trends in Molecular Medicine*. 15:89-100.

Bezzina, C., M.W. Veldkamp, M.P. van Den Berg, A.V. Postma, M.B. Rook, J.W. Viersma, I.M. van Langen, G. Tan-Sindhunata, M.T. Bink-Boelkens, A.H. van Der Hout, M.M. Mannens, and A.A. Wilde. 1999. A single Na(+) channel mutation causing both long-QT and Brugada syndromes. *Circ Res*. 85:1206-1213.

Biswas, S., I. Deschenes, D. Disilvestre, Y. Tian, V.L. Halperin, and G.F. Tomaselli. 2008. Calmodulin regulation of Nav1.4 current: role of binding to the carboxyl terminus. *J Gen Physiol*. 131:197-209.

Biswas, S., D. DiSilvestre, Y. Tian, V.L. Halperin, and G.F. Tomaselli. 2009. Calcium-mediated dual-mode regulation of cardiac sodium channel gating. *Circ Res*. 104:870-878.

Black, D.J., D.B. Halling, D.V. Mandich, S.E. Pedersen, R.A. Altschuld, and S.L. Hamilton. 2005. Calmodulin interactions with IQ peptides from voltage-dependent calcium channels. *Am J Physiol Cell Physiol*. 288:C669-676.

Bock, G., M. Gebhart, A. Scharinger, W. Jangsangthong, P. Busquet, C. Poggiani, S. Sartori, M.E. Mangoni, M.J. Sinnegger-Brauns, S. Herzig, J. Striessnig, and A. Koschak. 2011. Functional properties of a newly identified C-terminal splice variant of Cav1.3 L-type Ca2+ channels. *J Biol Chem*. 286:42736-42748.

Boczek, N.J., J.M. Best, D.J. Tester, J.R. Giudicessi, S. Middha, J.M. Evans, T.J. Kamp, and M.J. Ackerman. 2013. Exome sequencing and systems biology converge to identify novel mutations in the L-type calcium channel, CACNA1C, linked to autosomal dominant long QT syndrome. *Circulation. Cardiovascular genetics*. 6:279-289.

Bosmans, F., M.F. Martin-Eauclaire, and K.J. Swartz. 2008. Deconstructing voltage sensor function and pharmacology in sodium channels. *Nature*. 456:202-208.

Bradley, J., W. Bonigk, K.W. Yau, and S. Frings. 2004. Calmodulin permanently associates with rat olfactory CNG channels under native conditions. *Nat Neurosci*. 7:705-710.

Bradley, J., J. Reisert, and S. Frings. 2005. Regulation of cyclic nucleotide-gated channels. *Curr Opin Neurobiol*. 15:343-349.

Branchaw, J.L., M.I. Banks, and M.B. Jackson. 1997. Ca2+- and voltage-dependent inactivation of Ca2+ channels in nerve terminals of the neurohypophysis. *J Neurosci*. 17:5772-5781.

Brehm, P., and R. Eckert. 1978. Calcium entry leads to inactivation of calcium channel in *Paramecium*. *Science*. 202:1203-1206.

Budde, T., S. Meuth, and H.C. Pape. 2002. Calcium-dependent inactivation of neuronal calcium channels. *Nat. Rev. Neurosci.* 3:873-883.

Cannon, S.C. 1997. From mutation to myotonia in sodium channel disorders. *Neuromuscular disorders : NMD*. 7:241-249.

Casini, S., A.O. Verkerk, M.M. van Borren, A.C. van Ginneken, M.W. Veldkamp, J.M. de Bakker, and H.L. Tan. 2009. Intracellular calcium modulation of voltage-gated sodium channels in ventricular myocytes. *Cardiovascular research*. 81:72-81.

Catterall, W.A., F. Kalume, and J.C. Oakley. 2010. NaV1.1 channels and epilepsy. *J Physiol*. 588:1849-1859.

Chad, J.E., and R. Eckert. 1986. An enzymatic mechanism for calcium current inactivation in dialysed Helix neurones. *J Physiol*. 378:31-51.

Chagot, B., and W.J. Chazin. 2011. Solution NMR structure of Apo-calmodulin in complex with the IQ motif of human cardiac sodium channel NaV1.5. *J Mol Biol*. 406:106-119.

Chagot, B., F. Potet, J.R. Balser, and W.J. Chazin. 2009. Solution NMR structure of the C-terminal EF-hand domain of human cardiac sodium channel NaV1.5. *J Biol Chem*. 284:6436-6445.

Chan, C.S., J.N. Guzman, E. Ilijic, J.N. Mercer, C. Rick, T. Tkatch, G.E. Meredith, and D.J. Surmeier. 2007. 'Rejuvenation' protects neurons in mouse models of Parkinson's disease. *Nature*. 447:1081-1086.

Chao, S.H., Y. Suzuki, J.R. Zysk, and W.Y. Cheung. 1984. Activation of calmodulin by various metal cations as a function of ionic radius. *Mol. Pharmacol.* 26:75-82.

Chaudhuri, D., B.A. Alseikhan, S.Y. Chang, T.W. Soong, and D.T. Yue. 2005. Developmental activation of calmodulin-dependent facilitation of cerebellar P-type Ca2+ current. *J. Neurosci.* 25:8282-8294.

Chaudhuri, D., S.Y. Chang, C.D. DeMaria, R.S. Alvania, T.W. Soong, and D.T. Yue. 2004. Alternative splicing as a molecular switch for Ca2+/calmodulin-dependent facilitation of P/Q-type Ca2+ channels. *J Neurosci*. 24:6334-6342.

Chaudhuri, D., J.B. Issa, and D.T. Yue. 2007. Elementary Mechanisms Producing Facilitation of Cav2.1 (P/Q-type) Channels. *J Gen Physiol*. 129:385-401.

Chaudhury, S., S. Lyskov, and J.J. Gray. 2010. PyRosetta: a script-based interface for implementing molecular modeling algorithms using Rosetta. *Bioinformatics*. 26:689-691.

Chen, H., H.L. Puhl, 3rd, S.V. Koushik, S.S. Vogel, and S.R. Ikeda. 2006. Measurement of FRET efficiency and ratio of donor to acceptor concentration in living cells. *Biophys J*. 91:L39-41.

Chen, T.W., T.J. Wardill, Y. Sun, S.R. Pulver, S.L. Renninger, A. Baohan, E.R. Schreiter, R.A. Kerr, M.B. Orger, V. Jayaraman, L.L. Looger, K. Svoboda, and D.S. Kim. 2013. Ultrasensitive fluorescent proteins for imaging neuronal activity. *Nature*. 499:295-300.

Chen, T.Y., and K.W. Yau. 1994. Direct modulation by Ca(2+)-calmodulin of cyclic nucleotide-activated channel of rat olfactory receptor neurons. *Nature*. 368:545-548.

Cheney, R.E., and M.S. Mooseker. 1992. Unconventional myosins. *Curr Opin Cell Biol*. 4:27-35.

Cheung, W.Y. 1969. Cyclic 3',5'-nucleotide phosphodiesterase. Preparation of a partially inactive enzyme and its subsequent stimulation by snake venom. *Biochim Biophys Acta*. 191:303-315.

Cheung, W.Y. 1970. Cyclic 3',5'-nucleotide phosphodiesterase. Demonstration of an activator. *Biochem Biophys Res Commun*. 38:533-538.

Cheung, W.Y. 1971. Cyclic 3',5'-nucleotide phosphodiesterase. Evidence for and properties of a protein activator. *J Biol Chem*. 246:2859-2869.

Cheung, W.Y. 1980. Calmodulin plays a pivotal role in cellular regulation. *Science*. 207:19-27.

Chin, D., and A.R. Means. 2000. Calmodulin: a prototypical calcium sensor. *Trends Cell Biol*. 10:322-328.

Consortium, T.U. 2013. Update on activities at the Universal Protein Resource (UniProt) in 2013. *Nucleic acids research*. 41:D43-D47.

Cross-Disorder Group of the Psychiatric Genomics, C. 2013. Identification of risk loci with shared effects on five major psychiatric disorders: a genome-wide analysis. *Lancet*.

Crotti, L., C.N. Johnson, E. Graf, G.M. De Ferrari, B.F. Cuneo, M. Ovadia, J. Papagiannis, M.D. Feldkamp, S.G. Rathi, J.D. Kunic, M. Pedrazzini, T. Wieland, P. Lichtner, B.M. Beckmann, T. Clark, C. Shaffer, D.W. Benson, S. Kaab, T. Meitinger, T.M. Strom, W.J. Chazin, P.J. Schwartz, and A.L. George, Jr. 2013. Calmodulin mutations associated with recurrent cardiac arrest in infants. *Circulation*. 127:1009-1017.

Crouch, T.H., and C.B. Klee. 1980. Positive cooperative binding of calcium to bovine brain calmodulin. *Biochemistry*. 19:3692-3698.

Crump, S.M., D.A. Andres, G. Sievert, and J. Satin. 2013. The cardiac L-type calcium channel distal carboxy terminus autoinhibition is regulated by calcium. *American journal of physiology. Heart and circulatory physiology*. 304:H455-464.

Dasgupta, M., T. Honeycutt, and D.K. Blumenthal. 1989. The gamma-subunit of skeletal muscle phosphorylase kinase contains two noncontinguous domains that act in concert to bind calmodulin. *Journal of Biological Chemistry*. 264:17156-17163.

de Leon, M., Y. Wang, L. Jones, E. Perez-Reyes, X. Wei, T.W. Soong, T.P. Snutch, and D.T. Yue. 1995. Essential Ca(2+)-binding motif for Ca(2+)-sensitive inactivation of L-type Ca2+ channels. *Science*. 270:1502-1506.

DeCaen, P.G., M. Delling, T.N. Vien, and D.E. Clapham. 2013. Direct recording and molecular identification of the calcium channel of primary cilia. *Nature*. 504:315-318.

DeMaria, C.D., T.W. Soong, B.A. Alseikhan, R.S. Alvania, and D.T. Yue. 2001. Calmodulin bifurcates the local Ca2+ signal that modulates P/Q-type Ca2+ channels. *Nature*. 411:484-489.

Denk, W., R. Yuste, K. Svoboda, and D.W. Tank. 1996. Imaging calcium dynamics in dendritic spines. *Curr Opin Neurobiol*. 6:372-378.

Deschenes, I., N. Neyroud, D. DiSilvestre, E. Marban, D.T. Yue, and G.F. Tomaselli. 2002. Isoform-specific modulation of voltage-gated Na(+) channels by calmodulin. *Circ Res*. 90:E49-57.

Dick, I.E., R. Joshi-Mukherjee, W. Yang, and D.T. Yue. 2012. Nonlinear threshold behavior in the induction of arryhthmias by channels bearing Timothy Syndrome mutations (abstr.). *Biophysical Journal*. 102:542a.

Dick, I.E., M.R. Tadross, H. Liang, L.H. Tay, W. Yang, and D.T. Yue. 2008. A modular switch for spatial $Ca^{2+}$ selectivity in the calmodulin regulation of $Ca_V$ channels. *Nature*. 451:830-834.

Dobrunz, L.E., P.H. Backx, and D.T. Yue. 1995. Steady-state [Ca2+]i-force relationship in intact twitching cardiac muscle: direct evidence for modulation by isoproterenol and EMD 53998. *Biophys J*. 69:189-201.

Dolz-Gaiton, P., M. Nunez, L. Nunez, A. Barana, I. Amoros, M. Matamoros, M. Perez-Hernandez, M. Gonzalez de la Fuente, M. Alvarez-Lopez, R. Macias-Ruiz, L. Tercedor-Sanchez, J. Jimenez-Jaimez, E. Delpon, R. Caballero, and J. Tamargo. 2013. Functional characterization of a novel frameshift mutation in the C-terminus of the Nav1.5 channel underlying a Brugada syndrome with variable expression in a Spanish family. *PloS one*. 8:e81493.

Dunlap, K. 2007. Calcium channels are models of self-control. *J. Gen. Physiol.* 129:379-383.

Eckert, R., and J. Chad. 1984a. Inactivation of Ca Channels. *Prog.Biophys.Molec.Biol.(Lond.)*. 44:215-267.

Eckert, R., and J.E. Chad. 1984b. Inactivation of Ca channels. *Progress in biophysics and molecular biology*. 44:215-267.

Eckert, R., and D. Tillotson. 1981. Calcium-Mediated Inactivation of the Calcium Conductance in Caesium-Loaded Giant Neurones of Aplysia Californica. *Journal of Physiology*. 314:265-280.

Edgar, R.C. 2004. MUSCLE: multiple sequence alignment with high accuracy and high throughput. *Nucleic acids research*. 32:1792-1797.

Ehlers, M.D., S. Zhang, J.P. Bernhadt, and R.L. Huganir. 1996. Inactivation of NMDA receptors by direct interaction of calmodulin with the NR1 subunit. *Cell*. 84:745-755.

Erickson, M.G., B.A. Alseikhan, B.Z. Peterson, and D.T. Yue. 2001. Preassociation of calmodulin with voltage-gated Ca(2+) channels revealed by FRET in single living cells. *Neuron*. 31:973-985.

Erickson, M.G., H. Liang, M.X. Mori, and D.T. Yue. 2003. FRET two-hybrid mapping reveals function and location of L-type $Ca^{2+}$ channel CaM preassociation. *Neuron*. 39:97-107.

Fallon, J.L., M.R. Baker, L. Xiong, R.E. Loy, G. Yang, R.T. Dirksen, S.L. Hamilton, and F.A. Quiocho. 2009. Crystal structure of dimeric cardiac L-type calcium channel regulatory domains bridged by Ca2+ calmodulins. *Proc Natl Acad Sci U S A*. 106:5135-5140.

Fallon, J.L., D.B. Halling, S.L. Hamilton, and F.A. Quiocho. 2005. Structure of calmodulin bound to the hydrophobic IQ domain of the cardiac Ca(v)1.2 calcium channel. *Structure*. 13:1881-1886.

Feldkamp, M.D., L. Yu, and M.A. Shea. 2011. Structural and energetic determinants of apo calmodulin binding to the IQ motif of the Na(V)1.2 voltage-dependent sodium channel. *Structure*. 19:733-747.

Findeisen, F., A. Tolia, R. Arant, E.Y. Kim, E. Isacoff, and D.L. Minor, Jr. 2011. Calmodulin overexpression does not alter Cav1.2 function or oligomerization state. *Channels*. 5:320-324.

Gabelli, S.B., A. Boto, V.H. Kuhns, M.A. Bianchet, F. Farinelli, S. Aripirala, J. Yoder, J. Jakoncic, G.F. Tomaselli, and L.M. Amzel. 2014. Regulation of the NaV1.5 cytoplasmic domain by calmodulin. *Nature communications*. 5:5126.

Gamper, N., Y. Li, and M.S. Shapiro. 2005. Structural requirements for differential sensitivity of KCNQ K+ channels to modulation by Ca2+/calmodulin. *Molecular biology of the cell*. 16:3538-3551.

Gamper, N., and M.S. Shapiro. 2003. Calmodulin mediates Ca2+-dependent modulation of M-type K+ channels. *J Gen Physiol*. 122:17-31.

Gaudioso, C., E. Carlier, F. Youssouf, J.J. Clare, D. Debanne, and G. Alcaraz. 2011. Calmodulin and calcium differentially regulate the neuronal Nav1.1 voltage-dependent sodium channel. *Biochem Biophys Res Commun*. 411:329-334.

Ghosh, S., D.A. Nunziato, and G.S. Pitt. 2006. KCNQ1 assembly and function is blocked by long-QT syndrome mutations that disrupt interaction with calmodulin. *Circ Res*. 98:1048-1054.

Gilli, R., D. Lafitte, C. Lopez, M. Kilhoffer, A. Makarov, C. Briand, and J. Haiech. 1998. Thermodynamic analysis of calcium and magnesium binding to calmodulin. *Biochemistry*. 37:5450-5456.

Glaaser, I.W., J.R. Bankston, H. Liu, M. Tateyama, and R.S. Kass. 2006. A carboxyl-terminal hydrophobic interface is critical to sodium channel function. Relevance to inherited disorders. *J Biol Chem*. 281:24015-24023.

Gordon-Shaag, A., W.N. Zagotta, and S.E. Gordon. 2008. Mechanism of Ca(2+)-dependent desensitization in TRP channels. *Channels*. 2:125-129.

Grigoriev, I.V., H. Nordberg, I. Shabalov, A. Aerts, M. Cantor, D. Goodstein, A. Kuo, S. Minovitsky, R. Nikitin, R.A. Ohm, R. Otillar, A. Poliakov, I. Ratnere, R. Riley, T.

Smirnova, D. Rokhsar, and I. Dubchak. 2012. The genome portal of the Department of Energy Joint Genome Institute. *Nucleic acids research*. 40:D26-32.

Guzman, J.N., J. Sanchez-Padilla, C.S. Chan, and D.J. Surmeier. 2009. Robust pacemaking in substantia nigra dopaminergic neurons. *J Neurosci*. 29:11011-11019.

Halling, D.B., P. Aracena-Parks, and S.L. Hamilton. 2006. Regulation of voltage-gated Ca2+ channels by calmodulin. *Sci STKE*. 2006:er1.

Hayward, L.J., R.H. Brown, Jr., and S.C. Cannon. 1997. Slow inactivation differs among mutant Na channels associated with myotonia and periodic paralysis. *Biophys J*. 72:1204-1219.

Helmchen, F., J.G. Borst, and B. Sakmann. 1997. Calcium dynamics associated with a single action potential in a CNS presynaptic terminal. *Biophys J*. 72:1458-1471.

Helmchen, F., K. Imoto, and B. Sakmann. 1996. Ca2+ buffering and action potential-evoked Ca2+ signaling in dendrites of pyramidal neurons. *Biophys J*. 70:1069-1081.

Herzberg, O., and M.N. James. 1985. Structure of the calcium regulatory muscle protein troponin-C at 2.8 A resolution. *Nature*. 313:653-659.

Herzog, R.I., C. Liu, S.G. Waxman, and T.R. Cummins. 2003. Calmodulin binds to the C terminus of sodium channels Nav1.4 and Nav1.6 and differentially modulates their functional properties. *J Neurosci*. 23:8261-8270.

Hill, T.L. 1977. Free energy transduction in biology: the steady-state kinetic and thermodynamic formalism. Academic Press, New York. 229 pp.

Hille, B. 1984. Ionic channels of excitable membranes. Sinauer Associates, Sunderland, MA. 226-248 pp.

Hille, B. 2001. Ionic channels of excitable membranes. 3rd.ed. Sinauer Associates, Sunderland, MA. 814 pp.

Hodgkin, A.L., and A.F. Huxley. 1952. A quantitative description of membrane current and its application to conduction and excitation in nerve. *J Physiol*. 117:500-544.

Hollingworth, S., M.M. Kim, and S.M. Baylor. 2012. Measurement and simulation of myoplasmic calcium transients in mouse slow-twitch muscle fibres. *J Physiol*. 590:575-594.

Huang, H., B.Z. Tan, Y. Shen, J. Tao, F. Jiang, Y.Y. Sung, C.K. Ng, M. Raidar, G. Kohr, M. Higuchi, H. Fatemi-Shariatpanahr, B. Harden, D.T. Yue, and T.W. Soong. 2012. RNA editing of the IQ domain of $Ca_V1.3$ channels modulates their $Ca^{2+}$-dependent inactivation. *Neuron*. 73:304-316.

Hui, A., P.T. Ellinor, O. Krizanova, J.J. Wang, R.J. Diebold, and A. Schwartz. 1991. Molecular cloning of multiple subtypes of a novel rat brain isoform of the alpha 1 subunit of the voltage-dependent calcium channel. *Neuron*. 7:35-44.

Hwang, H.S., F.R. Nitu, Y. Yang, K. Walweel, L. Pereira, C.N. Johnson, M. Faggioni, W.J. Chazin, D. Laver, A.L. George, Jr., R.L. Cornea, D.M. Bers, and B.C. Knollmann. 2014. Divergent regulation of ryanodine receptor 2 calcium release channels by arrhythmogenic human calmodulin missense mutants. *Circ Res*. 114:1114-1124.

Ikura, M., G.M. Clore, A.M. Gronenborn, G. Zhu, C.B. Klee, and A. Bax. 1992. Solution structure of a calmodulin-target peptide complex by multidimensional NMR. *Science*. 256:632-638.

Imredy, J.P., and D.T. Yue. 1992. Submicroscopic Ca2+ diffusion mediates inhibitory coupling between individual Ca2+ channels. *Neuron*. 9:197-207.

Imredy, J.P., and D.T. Yue. 1994. Mechanism of $Ca^{2+}$-sensitive inactivation of L-type $Ca^{2+}$ channels. *Neuron*. 12:1301-1318.

Issa, J.B., B.D. Haeffele, A. Agarwal, D.E. Bergles, E.D. Young, and D.T. Yue. 2014. Multiscale optical ca(2+) imaging of tonal organization in mouse auditory cortex. *Neuron*. 83:944-959.

Ivanina, T., Y. Blumenstein, E. Shistik, R. Barzilai, and N. Dascal. 2000. Modulation of L-type $Ca^{2+}$ channels by $G_{\beta\gamma}$ and calmodulin via interactions with N and C termini of $\alpha_{1C}$. *J. Biol. Chem.* 275:39846-39854.

James, P., T. Vorherr, and E. Carafoli. 1995. Calmodulin-binding domains: just two faced or multi-faceted? *Trends in Biochemical Sciences*. 20.

Jan, L.Y., and Y.N. Jan. 1989. Voltage-sensitive ion channels. *Cell*. 56:13-25.

Jarrett, H.W., and R. Madhavan. 1991. Calmodulin-binding proteins also have a calmodulin-like binding site within their structure. The flip-flop model. *J.Biol.Chem.* 266:362-371.

Jencks, W.P. 1981. On the attribution and additivity of binding energies. *Proc Natl Acad Sci U S A*. 78:4046-4050.

Jurado, L.A., P.S. Chockalingam, and H.W. Jarrett. 1999. Apocalmodulin. *Physiol Rev*. 79:661-682.

Kakiuchi, S., R. Yamazaki, Y. Teshima, and K. Uenishi. 1973. Regulation of nucleoside cyclic 3':5'-monophosphate phosphodiesterase activity from rat brain by a modulator and Ca2+. *Proc Natl Acad Sci U S A*. 70:3526-3530.

Kang, S., G. Cooper, S.F. Dunne, B. Dusel, C.H. Luan, D.J. Surmeier, and R.B. Silverman. 2012. CaV1.3-selective L-type calcium channel antagonists as potential new therapeutics for Parkinson's disease. *Nature communications*. 3:1146.

Kapplinger, J.D., D.J. Tester, M. Alders, B. Benito, M. Berthet, J. Brugada, P. Brugada, V. Fressart, A. Guerchicoff, C. Harris-Kerr, S. Kamakura, F. Kyndt, T.T. Koopmann, Y. Miyamoto, R. Pfeiffer, G.D. Pollevick, V. Probst, S. Zumhagen, M. Vatta, J.A. Towbin, W. Shimizu, E. Schulze-Bahr, C. Antzelevitch, B.A. Salisbury, P. Guicheney, A.A. Wilde, R. Brugada, J.J. Schott, and M.J. Ackerman. 2010. An international compendium of mutations in the SCN5A-encoded cardiac sodium channel in patients referred for Brugada syndrome genetic testing. *Heart Rhythm*. 7:33-46.

Kass, R.S., and M. Sanguinetti. 1984. Inactivation of calcium channel current in the calf cardiac Purkinje fiber. Evidence for voltage- and calcium-mediated mechanisms. *Journal of General Physiology*. 84:705-726.

Kemp, B.E., R.B. Pearson, V. Guerriero, Jr., I.C. Bagchi, and A.R. Means. 1987. The calmodulin binding domain of chicken smooth muscle myosin light chain kinase contains a pseudosubstrate sequence. *J Biol Chem*. 262:2542-2548.

Kim, D.E., D. Chivian, and D. Baker. 2004a. Protein structure prediction and analysis using the Robetta server. *Nucleic acids research*. 32:W526-531.

Kim, E.Y., C.H. Rumpf, Y. Fujiwara, E.S. Cooley, F. Van Petegem, and D.L. Minor, Jr. 2008. Structures of CaV2 Ca2+/CaM-IQ domain complexes reveal binding modes that underlie calcium-dependent inactivation and facilitation. *Structure*. 16:1455-1467.

Kim, E.Y., C.H. Rumpf, F. Van Petegem, R.J. Arant, F. Findeisen, E.S. Cooley, E.Y. Isacoff, and D.L. Minor, Jr. 2010. Multiple C-terminal tail Ca(2+)/CaMs regulate Ca(V)1.2 function but do not mediate channel dimerization. *The EMBO journal*. 29:3924-3938.

Kim, J., S. Ghosh, H. Liu, M. Tateyama, R.S. Kass, and G.S. Pitt. 2004b. Calmodulin mediates Ca2+ sensitivity of sodium channels. *J Biol Chem*. 279:45004-45012.

Kim, J., S. Ghosh, D.A. Nunziato, and G.S. Pitt. 2004c. Identification of the components controlling inactivation of voltage-gated $Ca^{2+}$ channels. *Neuron*. 41:745-754.

Kink, J.A., M.E. Maley, R.R. Preston, K.Y. Ling, M.A. Wallen-Friedman, Y. Saimi, and C. Kung. 1990. Mutations in paramecium calmodulin indicate functional differences between the C-terminal and N-terminal lobes in vivo. *Cell*. 62:165-174.

Klee, C.B., T.H. Crouch, and P.G. Richman. 1980. Calmodulin. *Annu Rev Biochem*. 49:489-515.

Kretsinger, R.H. 1975. Hypothesis: calcium modulated proteins contain EF-hands. *In* Calcium Transport in Contraction and Secretion. E. Carfoli, editor. Elsevier, Bressanone, Italy. 469-478.

Kretsinger, R.H., S.E. Rudnick, and L.J. Weissman. 1986. Crystal structure of calmodulin. *Journal of inorganic biochemistry*. 28:289-302.

Krishnamurthy, V.M., L.A. Estroff, and G.M. Whitesides. 2006. Multivalency in ligand design. *In* Fragment-based approaches in drug discovery. W. Jahnke and D.A. Erlanson, editors. Wiley-VCH, Weinheim. 11-53.

Kuboniwa, H., N. Tjandra, S. Grzesiek, H. Ren, C.B. Klee, and A. Bax. 1995. Solution structure of calcium-free calmodulin. *Nature structural biology*. 2:768-776.

Kubota, T., M. Kinoshita, R. Sasaki, F. Aoike, M.P. Takahashi, S. Sakoda, and K. Hirose. 2009. New mutation of the Na channel in the severe form of potassium-aggravated myotonia. *Muscle Nerve*. 39:666-673.

Lau, S.Y., E. Procko, and R. Gaudet. 2012. Distinct properties of Ca2+-calmodulin binding to N- and C-terminal regulatory regions of the TRPV1 channel. *J Gen Physiol*. 140:541-555.

Lee, A., S.T. Wong, D. Gallagher, B. Li, D.R. Storm, T. Scheuer, and W.A. Catterall. 1999. Ca2+/calmodulin binds to and modulates P/Q-type calcium channels. *Nature*. 399:155-159.

Lee, A., H. Zhou, T. Scheuer, and W.A. Catterall. 2003. Molecular determinants of Ca(2+)/calmodulin-dependent regulation of Ca(v)2.1 channels. *Proc Natl Acad Sci U S A*. 100:16059-16064.

Lee, K., E. Marban, and R.W. Tsien. 1985. Inactivation of calcium channels in mammalian heart cells: Joint dependence on membrane potential and intracellular calcium. *Journal of Physiology*. 364:395-411.

Liang, H., C.D. DeMaria, M.G. Erickson, M.X. Mori, B.A. Alseikhan, and D.T. Yue. 2003. Unified mechanisms of $Ca^{2+}$ regulation across the $Ca^{2+}$ channel family. *Neuron*. 39:951-960.

Limpitikul, W.B., I.E. Dick, R. Joshi-Mukherjee, M.T. Overgaard, A.L. George, Jr., and D.T. Yue. 2014. Calmodulin mutations associated with long QT syndrome prevent inactivation of cardiac L-type Ca(2+) currents and promote proarrhythmic behavior in ventricular myocytes. *J Mol Cell Cardiol*. 74:115-124.

Linse, S., and S. Forsen. 1995. Determinants that govern high-affinity calcium binding. *Advances in Second Messenger Phosphoprotein Research*. 30:89-151.

Linse, S., A. Helmersson, and S. Forsen. 1991. Calcium binding to calmodulin and its globular domains. *J Biol Chem*. 266:8050-8054.

Liu, X., P.S. Yang, W. Yang, and D.T. Yue. 2010. Enzyme-inhibitor-like tuning of Ca(2+) channel connectivity with calmodulin. *Nature*. 463:968-972.

Liu, Z., and H.J. Vogel. 2012. Structural basis for the regulation of L-type voltage-gated calcium channels: interactions between the N-terminal cytoplasmic domain and Ca(2+)-calmodulin. *Frontiers in molecular neuroscience*. 5:38.

Lossin, C. 2009. A catalog of SCN1A variants. *Brain & development*. 31:114-130.

Lyskov, S., and J.J. Gray. 2008. The RosettaDock server for local protein-protein docking. *Nucleic acids research*. 36:W233-238.

Mahajan, A., D. Sato, Y. Shiferaw, A. Baher, L.H. Xie, R. Peralta, R. Olcese, A. Garfinkel, Z. Qu, and J.N. Weiss. 2008. Modifying L-type calcium current kinetics: consequences for cardiac excitation and arrhythmia dynamics. *Biophys J*. 94:411-423.

Makita, N., N. Yagihara, L. Crotti, C.N. Johnson, B.M. Beckmann, M.S. Roh, D. Shigemizu, P. Lichtner, T. Ishikawa, T. Aiba, T. Homfray, E.R. Behr, D. Klug, I. Denjoy, E. Mastantuono, D. Theisen, T. Tsunoda, W. Satake, T. Toda, H. Nakagawa, Y. Tsuji, T. Tsuchiya, H. Yamamoto, Y. Miyamoto, N. Endo, A. Kimura, K. Ozaki, H. Motomura, K. Suda, T. Tanaka, P.J. Schwartz, T. Meitinger, S. Kaab, P. Guicheney, W. Shimizu, Z.A. Bhuiyan, H. Watanabe, W.J. Chazin, and A.L. George, Jr. 2014. Novel calmodulin mutations associated with congenital arrhythmia susceptibility. *Circulation. Cardiovascular genetics*. 7:466-474.

Mantegazza, M., F.H. Yu, W.A. Catterall, and T. Scheuer. 2001. Role of the C-terminal domain in inactivation of brain and cardiac sodium channels. *Proc Natl Acad Sci U S A*. 98:15348-15353.

Marshall, M.R., J.P. Clark, 3rd, R. Westenbroek, F.H. Yu, T. Scheuer, and W.A. Catterall. 2011. Functional roles of a C-terminal signaling complex of CaV1 channels and A-kinase anchoring protein 15 in brain neurons. *J Biol Chem*. 286:12627-12639.

Marsman, R.F., J. Barc, L. Beekman, M. Alders, D. Dooijes, A. van den Wijngaard, I. Ratbi, A. Sefiani, Z.A. Bhuiyan, A.A. Wilde, and C.R. Bezzina. 2014. A mutation in CALM1 encoding calmodulin in familial idiopathic ventricular fibrillation in childhood and adolescence. *J Am Coll Cardiol*. 63:259-266.

Martin, S.R., A. Andersson Teleman, P.M. Bayley, T. Drakenberg, and S. Forsen. 1985. Kinetics of calcium dissociation from calmodulin and its tryptic fragments. A stopped-flow fluorescence study using Quin 2 reveals a two-domain structure. *Eur J Biochem*. 151:543-550.

Martin, S.R., and P.M. Bayley. 2002. Regulatory implications of a novel mode of interaction of calmodulin with a double IQ-motif target sequence from murine dilute myosin V. *Protein science : a publication of the Protein Society*. 11:2909-2923.

Martin, S.R., L. Masino, and P.M. Bayley. 2000. Enhancement by Mg2+ of domain specificity in Ca2+-dependent interactions of calmodulin with target sequences. *Protein science : a publication of the Protein Society*. 9:2477-2488.

Mashiach, E., D. Schneidman-Duhovny, N. Andrusier, R. Nussinov, and H.J. Wolfson. 2008. FireDock: a web server for fast interaction refinement in molecular docking. *Nucleic acids research*. 36:W229-232.

McAllister, R.E., D. Noble, and R.W. Tsien. 1975. Reconstruction of the electrical activity of cardiac Purkinje fibres. *J Physiol*. 251:1-59.

Meador, W.E., A.R. Means, and F.A. Quiocho. 1992. Target enzyme recognition by calmodulin: 2.4 A structure of a calmodulin-peptide complex. *Science*. 257:1251-1255.

Meador, W.E., A.R. Means, and F.A. Quiocho. 1993. Modulation of calmodulin plasticity in molecular recognition on the basis of x-ray structures. *Science*. 262:1718-1721.

Mentrard, D., G. Vassort, and R. Fischmeister. 1984. Calcium-mediated Inactivation of the Calcium Conductance in Cesium-loaded Frog Heart Cells. *Journal of General Physiology*. 83:105-131.

Mercado, J., A. Gordon-Shaag, W.N. Zagotta, and S.E. Gordon. 2010. Ca2+-dependent desensitization of TRPV2 channels is mediated by hydrolysis of phosphatidylinositol 4,5-bisphosphate. *J Neurosci*. 30:13338-13347.

Miloushev, V.Z., J.A. Levine, M.A. Arbing, J.F. Hunt, G.S. Pitt, and A.G. Palmer, 3rd. 2009. Solution structure of the NaV1.2 C-terminal EF-hand domain. *J Biol Chem*. 284:6446-6454.

Minor, D.L., Jr., and F. Findeisen. 2010. Progress in the structural understanding of voltage-gated calcium channel (CaV) function and modulation. *Channels*. 4:459-474.

Miriyala, J., T. Nguyen, D.T. Yue, and H.M. Colecraft. 2008. Role of CaVbeta subunits, and lack of functional reserve, in protein kinase A modulation of cardiac CaV1.2 channels. *Circ Res*. 102:e54-64.

Moews, P.C., and R.H. Kretsinger. 1975a. Refinement of the structure of carp muscle calcium-binding parvalbumin by model building and difference Fourier analysis. *J Mol Biol*. 91:201-225.

Moews, P.C., and R.H. Kretsinger. 1975b. Terbium replacement of calcium in carp muscle calcium-binding parvalbumin: an x-ray crystallographic study. *J Mol Biol*. 91:229-232.

Mori, M., T. Konno, T. Ozawa, M. Murata, K. Imoto, and K. Nagayama. 2000. Novel interaction of the voltage-dependent sodium channel (VDSC) with calmodulin: does VDSC acquire calmodulin-mediated Ca2+-sensitivity? *Biochemistry*. 39:1316-1323.

Mori, M.X., M.G. Erickson, and D.T. Yue. 2004. Functional stoichiometry and local enrichment of calmodulin interacting with Ca2+ channels. *Science*. 304:432-435.

Mori, M.X., C.W. Vander Kooi, D.J. Leahy, and D.T. Yue. 2008. Crystal structure of the CaV2 IQ domain in complex with Ca2+/calmodulin: high-resolution mechanistic implications for channel regulation by Ca2+. *Structure*. 16:607-620.

Mullins, F.M., C.Y. Park, R.E. Dolmetsch, and R.S. Lewis. 2009. STIM1 and calmodulin interact with Orai1 to induce Ca2+-dependent inactivation of CRAC channels. *Proc Natl Acad Sci U S A*. 106:15495-15500.

Munjaal, R.P., J.R. Dedman, and A.R. Means. 1980. Isolation of the structural gene for calmodulin. *Ann N Y Acad Sci*. 356:110-118.

Neher, E. 1986. Concentration profiles of intracellular calcium in the presence of a diffusible chelator. *Exp. brain research*. 14:80-96.

Nguyen, H., and H. Higuchi. 2005. Motility of myosin V regulated by the dissociation of single calmodulin. *Nat Struct Mol Biol*. 12:127-132.

Numazaki, M., T. Tominaga, K. Takeuchi, N. Murayama, H. Toyooka, and M. Tominaga. 2003. Structural determinant of TRPV1 desensitization interacts with calmodulin. *Proc Natl Acad Sci U S A*. 100:8002-8006.

Nyegaard, M., M.T. Overgaard, M.T. Sondergaard, M. Vranas, E.R. Behr, L.L. Hildebrandt, J. Lund, P.L. Hedley, A.J. Camm, G. Wettrell, I. Fosdal, M. Christiansen, and A.D. Borglum. 2012. Mutations in calmodulin cause ventricular tachycardia and sudden cardiac death. *Am J Hum Genet*. 91:703-712.

Ohki, S., M. Ikura, and M. Zhang. 1997. Identification of Mg2+-binding sites and the role of Mg2+ on target recognition by calmodulin. *Biochemistry*. 36:4309-4316.

Oliveria, S.F., M.L. Dell'Acqua, and W.A. Sather. 2007. AKAP79/150 anchoring of calcineurin controls neuronal L-type Ca2+ channel activity and nuclear signaling. *Neuron*. 55:261-275.

Oliveria, S.F., P.J. Dittmer, D.H. Youn, M.L. Dell'Acqua, and W.A. Sather. 2012. Localized calcineurin confers Ca2+-dependent inactivation on neuronal L-type Ca2+ channels. *J Neurosci*. 32:15328-15337.

Page, M.I., and W.P. Jencks. 1971. Entropic contributions to rate accelerations in enzymic and intramolecular reactions and the chelate effect. *Proc Natl Acad Sci U S A*. 68:1678-1683.

Pate, P., J. Mochca-Morales, Y. Wu, J.Z. Zhang, G.G. Rodney, Serysheva, II, B.Y. Williams, M.E. Anderson, and S.L. Hamilton. 2000. Determinants for calmodulin binding on voltage-dependent $Ca^{2+}$ channels. *J. Biol. Chem.* 275:39786-39792.

Pearson, R.B., R.E. Wettenhall, A.R. Means, D.J. Hartshorne, and B.E. Kemp. 1988. Autoregulation of enzymes by pseudosubstrate prototopes: myosin light chain kinase. *Science*. 241:970-973.

Perez-Reyes, E. 2003. Molecular physiology of low-voltage-activated t-type calcium channels. *Physiol Rev*. 83:117-161.

Perez-Reyes, E. 2006. Molecular characterization of T-type calcium channels. *Cell Calcium*. 40:89-96.

Perez-Reyes, E., L.L. Cribbs, A. Daud, A.E. Lacerda, J. Barclay, M.P. Williamson, M. Fox, M. Rees, and J.H. Lee. 1998. Molecular characterization of a neuronal low-voltage-activated T-type calcium channel. *Nature*. 391:896-900.

Persechini, A., and R.H. Kretsinger. 1988. The central helix of calmodulin functions as a flexible tether. *J Biol Chem*. 263:12175-12178.

Persechini, A., N.D. Moncrief, and R.H. Kretsinger. 1989. The EF-hand family of calcium-modulated proteins. *Trends Neurosci*. 12:462-467.

Peterson, B.Z., C.D. DeMaria, J.P. Adelman, and D.T. Yue. 1999. Calmodulin is the $Ca^{2+}$ sensor for Ca2+ -dependent inactivation of L- type calcium channels. *Neuron*. 22:549-558.

Peterson, B.Z., J.S. Lee, J.G. Mulle, Y. Wang, M. DeLeon, and D.T. Yue. 2000. Critical determinants of $Ca^{2+}$-dependent inactivation within an EF-hand motif of L-type $Ca^{2+}$ channels. *Biophysical Journal*. 78:1906-1920.

Pitt, G.S., R.D. Zuhlke, A. Hudmon, H. Schulman, H. Reuter, and R.W. Tsien. 2001. Molecular basis of calmodulin tethering and Ca2+-dependent inactivation of L-type Ca2+ channels. *J. Biol. Chem.* 276:30794-30802.

Plant, T., N. Standen, and T. Ward. 1983. The Effects of Injection of Calcium Ions and Calcium Chelators on Calcium Channel Inactivation in Helix Neurones. *Journal of Physiology*. 334:189-212.

Poomvanicha, M., J.W. Wegener, A. Blaich, S. Fischer, K. Domes, S. Moosmang, and F. Hofmann. 2011. Facilitation and Ca2+-dependent inactivation are modified by mutation of the Ca(v)1.2 channel IQ motif. *J Biol Chem*. 286:26702-26707.

Potet, F., B. Chagot, M. Anghelescu, P.C. Viswanathan, S.Z. Stepanovic, S. Kupershmidt, W.J. Chazin, and J.R. Balser. 2009. Functional Interactions between Distinct Sodium Channel Cytoplasmic Domains through the Action of Calmodulin. *J Biol Chem*. 284:8846-8854.

Powell, J.A., M.A. Carrasco, D.S. Adams, B. Drouet, J. Rios, M. Muller, M. Estrada, and E. Jaimovich. 2001. IP(3) receptor function and localization in myotubes: an unexplored Ca(2+) signaling pathway in skeletal muscle. *J Cell Sci*. 114:3673-3683.

Powell, J.A., L. Petherbridge, and B.E. Flucher. 1996. Formation of triads without the dihydropyridine receptor alpha subunits in cell lines from dysgenic skeletal muscle. *J Cell Biol*. 134:375-387.

Preston, R.R., J.A. Kink, R.D. Hinrichsen, Y. Saimi, and C. Kung. 1991. Calmodulin mutants and $Ca^{2+}$-dependent channels in Paramecium. *Annu Rev Physiol*. 53:309-319.

Prod'hom, B., D. Pietrobon, and P. Hess. 1987. Direct measurement of proton transfer rates to a group controlling the dihydropyridine-sensitive Ca2+ channel. *Nature*. 329:243-246.

Puopolo, M., E. Raviola, and B.P. Bean. 2007. Roles of subthreshold calcium current and sodium current in spontaneous firing of mouse midbrain dopamine neurons. *J Neurosci*. 27:645-656.

Putkey, J.A., Q. Kleerekoper, T.R. Gaertner, and M.N. Waxham. 2003. A new role for IQ motif proteins in regulating calmodulin function. *J Biol Chem*. 278:49667-49670.

Putkey, J.A., K.F. Ts'ui, T. Tanaka, L. Lagace, J.P. Stein, E.C. Lai, and A.R. Means. 1983. Chicken calmodulin genes. A species comparison of cDNA sequences and isolation of a genomic clone. *J Biol Chem*. 258:11864-11870.

Qin, N., R. Olcese, M. Bransby, T. Lin, and L. Birnbaumer. 1999. Ca2+-induced inhibition of the cardiac Ca2+ channel depends on calmodulin. *Proc Natl Acad Sci U S A*. 96:2435-2438.

Reed, G.J., N.J. Boczek, S.P. Etheridge, and M.J. Ackerman. 2014. CALM3 mutation associated with long QT syndrome. *Heart Rhythm*.

Rhoads, A.R., and F. Friedberg. 1997. Sequence motifs for calmodulin recognition. *FASEB J.* 11:331-340.

Ringer, S. 1882a. Concerning the Influence exerted by each of the Constituents of the Blood on the Contraction of the Ventricle. *J Physiol*. 3:380-393.

Ringer, S. 1882b. Regarding the Action of Hydrate of Soda, Hydrate of Ammonia, and Hydrate of Potash on the Ventricle of the Frog's Heart. *J Physiol*. 3:195-202 196.

Ringer, S. 1883. A further Contribution regarding the influence of the different Constituents of the Blood on the Contraction of the Heart. *J Physiol*. 4:29-42 23.

Ringer, S. 1885. Regarding the Effect of the Saline Ingredients of the Blood on the Contraction of the Heart. *British medical journal*. 1:731-734.

Ringer, S., and H. Sainsbury. 1882. Concerning the action of Salts of Potash, Soda, and Ammonia on the Frog's Heart. *Medico-chirurgical transactions*. 65:191-224 195.

Rosenbaum, T., A. Gordon-Shaag, M. Munari, and S.E. Gordon. 2004. Ca2+/calmodulin modulates TRPV1 activation by capsaicin. *J Gen Physiol*. 123:53-62.

Rosenberg, O.S., S. Deindl, R.J. Sung, A.C. Nairn, and J. Kuriyan. 2005. Structure of the autoinhibited kinase domain of CaMKII and SAXS analysis of the holoenzyme. *Cell*. 123:849-860.

Rusnak, F., and P. Mertz. 2000. Calcineurin: form and function. *Physiol Rev*. 80:1483-1521.

Saimi, Y., and C. Kung. 2002. Calmodulin as an ion channel subunit. *Annu Rev Physiol*. 64:289-311.

Sali, A., and T.L. Blundell. 1993. Comparative protein modelling by satisfaction of spatial restraints. *J Mol Biol*. 234:779-815.

Sarhan, M.F., C.C. Tung, F. Van Petegem, and C.A. Ahern. 2012. Crystallographic basis for calcium regulation of sodium channels. *Proc Natl Acad Sci U S A*. 109:3558-3563.

Sarhan, M.F., F. Van Petegem, and C.A. Ahern. 2009. A double tyrosine motif in the cardiac sodium channel domain III-IV linker couples calcium-dependent calmodulin binding to inactivation gating. *J Biol Chem*. 284:33265-33274.

Schneggenburger, R., and E. Neher. 2005. Presynaptic calcium and control of vesicle fusion. *Curr Opin Neurobiol*. 15:266-274.

Schneidman-Duhovny, D., Y. Inbar, R. Nussinov, and H.J. Wolfson. 2005. PatchDock and SymmDock: servers for rigid and symmetric docking. *Nucleic acids research*. 33:W363-367.

Schumacher, M.A., M. Crum, and M.C. Miller. 2004. Crystal structures of apocalmodulin and an apocalmodulin/SK potassium channel gating domain complex. *Structure*. 12:849-860.

Senguen, F.T., and Z. Grabarek. 2012. X-ray Structures of Magnesium and Manganese Complexes with the N-Terminal Domain of Calmodulin: Insights into the Mechanism and Specificity of Metal Ion Binding to an EF-Hand. *Biochemistry*. 51:6182-6194.

Shah, V.N., T.L. Wingo, K.L. Weiss, C.K. Williams, J.R. Balser, and W.J. Chazin. 2006. Calcium-dependent regulation of the voltage-gated sodium channel hH1: intrinsic and extrinsic sensors use a common molecular switch. *Proc Natl Acad Sci U S A*. 103:3592-3597.

Shamgar, L., L. Ma, N. Schmitt, Y. Haitin, A. Peretz, R. Wiener, J. Hirsch, O. Pongs, and B. Attali. 2006. Calmodulin is essential for cardiac IKS channel gating and assembly: impaired function in long-QT mutations. *Circ Res*. 98:1055-1063.

Shen, Y., D. Yu, H. Hiel, P. Liao, D.T. Yue, P.A. Fuchs, and T.W. Soong. 2006. Alternative splicing of the Ca(v)1.3 channel IQ domain, a molecular switch for Ca2+-dependent inactivation within auditory hair cells. *J Neurosci*. 26:10690-10699.

Simms, B.A., I.A. Souza, and G.W. Zamponi. 2013. A novel calmodulin site in the Cav1.2 N-terminus regulates calcium-dependent inactivation. *Pflugers Arch*.

Singh, A., D. Hamedinger, J.C. Hoda, M. Gebhart, A. Koschak, C. Romanin, and J. Striessnig. 2006. C-terminal modulator controls $Ca^{2+}$-dependent gating of $Ca_V1.4$ L-type $Ca^{2+}$ channels. *Nat Neurosci*. 9:1108-1116.

Snedden, W.A., and H. Fromm. 1998. Calmodulin, calmodulin-related proteins and plant responses to the environment. *Trends in Plant Sci*. 3:299-304.

Snutch, T.P., and P.B. Reiner. 1992. Ca2+ channels: diversity of form and function. *Curr Opin Neurobiol*. 2:247-253.

Standen, N., and P. Stanfield. 1982. A binding-site model for calcium channel inactivation that depends on calcium entry. *Proc.R.Soc.(Lond.)*. 217:101-110.

Stern, M.D. 1992. Buffering of calcium in the vicinity of a channel pore. *Cell Calcium*. 13:183-192.

Stocker, M. 2004. Ca(2+)-activated K+ channels: molecular determinants and function of the SK family. *Nature reviews. Neuroscience*. 5:758-770.

Stroffekova, K. 2008. Ca2+/CaM-dependent inactivation of the skeletal muscle L-type Ca2+ channel (Cav1.1). *Pflugers Arch*. 455:873-884.

Stroffekova, K. 2011. The IQ motif is crucial for Cav1.1 function. *Journal of biomedicine & biotechnology*. 2011:504649.

Stuhmer, W., F. Conti, H. Suzuki, X.D. Wang, M. Noda, N. Yahagi, H. Kubo, and S. Numa. 1989. Structural parts involved in activation and inactivation of the sodium channel. *Nature*. 339:597-603.

Surmeier, D.J., and D. Sulzer. 2013. The pathology roadmap in Parkinson disease. *Prion*. 7.

Szebenyi, D.M., S.K. Obendorf, and K. Moffat. 1981. Structure of vitamin D-dependent calcium-binding protein from bovine intestine. *Nature*. 294:327-332.

Tadross, M.R., M. Ben Johny, and D.T. Yue. 2010. Molecular endpoints of Ca2+/calmodulin- and voltage-dependent inactivation of Ca(v)1.3 channels. *J Gen Physiol*. 135:197-215.

Tadross, M.R., I.E. Dick, and D.T. Yue. 2008. Mechanism of local and global Ca2+ sensing by calmodulin in complex with a Ca2+ channel. *Cell*. 133:1228-1240.

Tadross, M.R., R.W. Tsien, and D.T. Yue. 2013. Ca2+ channel nanodomains boost local Ca2+ amplitude. *Proc Natl Acad Sci U S A*. 110:15794-15799.

Tadross, M.R., and D.T. Yue. 2010. Systematic mapping of the state dependence of voltage- and Ca2+-dependent inactivation using simple open-channel measurements. *J Gen Physiol*. 135:217-227.

Taiakina, V., A.N. Boone, J. Fux, A. Senatore, D. Weber-Adrian, J.G. Guillemette, and J.D. Spafford. 2013. The calmodulin-binding, short linear motif, NSCaTE is conserved in L-type channel ancestors of vertebrate Cav1.2 and Cav1.3 channels. *PloS one*. 8:e61765.

Tamura, K., D. Peterson, N. Peterson, G. Stecher, M. Nei, and S. Kumar. 2011. MEGA5: molecular evolutionary genetics analysis using maximum likelihood, evolutionary distance, and maximum parsimony methods. *Molecular biology and evolution*. 28:2731-2739.

Tan, B.Z., F. Jiang, M.Y. Tan, D. Yu, H. Huang, Y. Shen, and T.W. Soong. 2011. Functional characterization of alternative splicing in the C terminus of L-type CaV1.3 channels. *J Biol Chem*. 286:42725-42735.

Tan, H.L., S. Kupershmidt, R. Zhang, S. Stepanovic, D.M. Roden, A.A. Wilde, M.E. Anderson, and J.R. Balser. 2002. A calcium sensor in the sodium channel modulates cardiac excitability. *Nature*. 415:442-447.

Tang, W., D.B. Halling, D.J. Black, P. Pate, J.Z. Zhang, S. Pedersen, R.A. Altschuld, and S.L. Hamilton. 2003. Apocalmodulin and Ca2+ calmodulin-binding sites on the CaV1.2 channel. *Biophys J*. 85:1538-1547.

Tay, L.H., I.E. Dick, W. Yang, M. Mank, O. Griesbeck, and D.T. Yue. 2012. Nanodomain Ca(2)(+) of Ca(2)(+) channels detected by a tethered genetically encoded Ca(2)(+) sensor. *Nature communications*. 3:778.

Teo, T.S., and J.H. Wang. 1973. Mechanism of activation of a cyclic adenosine 3':5'-monophosphate phosphodiesterase from bovine heart by calcium ions. Identification of the protein activator as a Ca2+ binding protein. *J Biol Chem*. 248:5950-5955.

Teo, T.S., T.H. Wang, and J.H. Wang. 1973. Purification and properties of the protein activator of bovine heart cyclic adenosine 3',5'-monophosphate phosphodiesterase. *J Biol Chem*. 248:588-595.

Thompson, R.C. 1974. Binding of peptides to elastase: implications for the mechanism of substrate hydrolysis. *Biochemistry*. 13:5495-5501.

Tillotson, D. 1979. Inactivation of Ca conductance dependent on entry of Ca ions in molluscan neurons. *Proc Natl Acad Sci U S A*. 76:1497-1500.

Trimmer, J.S., S.S. Cooperman, W.S. Agnew, and G. Mandel. 1990. Regulation of muscle sodium channel transcripts during development and in response to denervation. *Developmental biology*. 142:360-367.

Trudeau, M.C., and W.N. Zagotta. 2003. Calcium/calmodulin modulation of olfactory and rod cyclic nucleotide-gated ion channels. *J Biol Chem*. 278:18705-18708.

Trudeau, M.C., and W.N. Zagotta. 2004. Dynamics of Ca2+-calmodulin-dependent inhibition of rod cyclic nucleotide-gated channels measured by patch-clamp fluorometry. *J Gen Physiol*. 124:211-223.

Trybus, K.M., E. Krementsova, and Y. Freyzon. 1999. Kinetic characterization of a monomeric unconventional myosin V construct. *J Biol Chem*. 274:27448-27456.

Tsai, M.D., T. Drakenberg, E. Thulin, and S. Forsen. 1987. Is the binding of magnesium (II) to calmodulin significant? An investigation by magnesium-25 nuclear magnetic resonance. *Biochemistry*. 26:3635-3643.

Tufty, R.M., and R.H. Kretsinger. 1975. Troponin and parvalbumin calcium binding regions predicted in myosin light chain and T4 lysozyme. *Science*. 187:167-169.

Van Petegem, F., F.C. Chatelain, and D.L. Minor, Jr. 2005. Insights into voltage-gated calcium channel regulation from the structure of the CaV1.2 IQ domain-Ca2+/calmodulin complex. *Nat Struct Mol Biol*. 12:1108-1115.

Van Petegem, F., P.A. Lobo, and C.A. Ahern. 2012. Seeing the forest through the trees: towards a unified view on physiological calcium regulation of voltage-gated sodium channels. *Biophys J*. 103:2243-2251.

Victor, R.G., F. Rusnak, R. Sikkink, E. Marban, and B. O'Rourke. 1997. Mechanism of Ca(2+)-dependent inactivation of L-type Ca2+ channels in GH3 cells: direct evidence against dephosphorylation by calcineurin. *J Membr Biol*. 156:53-61.

Wahl-Schott, C., L. Baumann, H. Cuny, C. Eckert, K. Griessmeier, and M. Biel. 2006. Switching off calcium-dependent inactivation in L-type calcium channels by an autoinhibitory domain. *Proc Natl Acad Sci U S A*. 103:15657-15662.

Wang, C., B.C. Chung, H. Yan, S.Y. Lee, and G.S. Pitt. 2012. Crystal structure of the ternary complex of a NaV C-terminal domain, a fibroblast growth factor homologous factor, and calmodulin. *Structure*. 20:1167-1176.

Wang, C., B.C. Chung, H. Yan, H.G. Wang, S.Y. Lee, and G.S. Pitt. 2014. Structural analyses of Ca(2)(+)/CaM interaction with NaV channel C-termini reveal mechanisms of calcium-dependent regulation. *Nature communications*. 5:4896.

Wang, X., Q.K. Kleerekoper, L.W. Xiong, and J.A. Putkey. 2010. Intrinsically disordered PEP-19 confers unique dynamic properties to apo and calcium calmodulin. *Biochemistry*. 49:10287-10297.

Watterson, D.M., F. Sharief, and T.C. Vanaman. 1980. The complete amino acid sequence of the Ca2+-dependent modulator protein (calmodulin) of bovine brain. *J Biol Chem*. 255:962-975.

Wei, F., X.M. Xia, J. Tang, H. Ao, S. Ko, J. Liauw, C.S. Qiu, and M. Zhuo. 2003. Calmodulin regulates synaptic plasticity in the anterior cingulate cortex and behavioral responses: a microelectroporation study in adult rodents. *J Neurosci*. 23:8402-8409.

West, J., D. Patton, T. Scheuer, Y. Wang, A. Goldin, and W. Catterall. 1992a. A cluster of hydrophobic amino acid residues required for fast Na+-channel inactivation. *Proceedings of the National Academy of Science USA*. 89:10910-10914.

West, J.W., D.E. Patton, T. Scheuer, Y. Wang, A.L. Goldin, and W.A. Catterall. 1992b. A cluster of hydrophobic amino acid residues required for fast Na(+)-channel inactivation. *Proc Natl Acad Sci U S A*. 89:10910-10914.

Wingo, T.L., V.N. Shah, M.E. Anderson, T.P. Lybrand, W.J. Chazin, and J.R. Balser. 2004. An EF-hand in the sodium channel couples intracellular calcium to cardiac excitability. *Nat Struct Mol Biol*. 11:219-225.

Wolff, D.J., P.G. Poirier, C.O. Brostrom, and M.A. Brostrom. 1977. Divalent cation binding properties of bovine brain Ca2+-dependent regulator protein. *J Biol Chem*. 252:4108-4117.

Wu, F.F., E. Gordon, E.P. Hoffman, and S.C. Cannon. 2005. A C-terminal skeletal muscle sodium channel mutation associated with myotonia disrupts fast inactivation. *J Physiol*. 565:371-380.

Wu, G.Y., K. Deisseroth, and R.W. Tsien. 2001. Activity-dependent CREB phosphorylation: Convergence of a fast, sensitive calmodulin kinase pathway and a slow, less sensitive mitogen-activated protein kinase pathway. *Proc Natl Acad Sci U S A*. 98:2808-2813.

Xia, X.M., B. Fakler, A. Rivard, G. Wayman, T. Johnson-Pais, J.E. Keen, T. Ishii, B. Hirschberg, C.T. Bond, S. Lutsenko, J. Maylie, and J.P. Adelman. 1998. Mechanism of calcium gating in small-conductance calcium-activated potassium channels. *Nature*. 395:503-507.

Xu, J., and L.G. Wu. 2005. The decrease in the presynaptic calcium current is a major cause of short-term depression at a calyx-type synapse. *Neuron*. 46:633-645.

Xu, W., and D. Lipscombe. 2001. Neuronal Ca(V)1.3alpha(1) L-type channels activate at relatively hyperpolarized membrane potentials and are incompletely inhibited by dihydropyridines. *J Neurosci*. 21:5944-5951.

Yang, P.S., B.A. Alseikhan, H. Hiel, L. Grant, M.X. Mori, W. Yang, P.A. Fuchs, and D.T. Yue. 2006. Switching of $Ca^{2+}$-dependent inactivation of $Ca_V1.3$ channels by calcium binding proteins of auditory hair cells. *J. Neurosci.* 26:10677-10689.

Yang, P.S., M.B. Johny, and D.T. Yue. 2014. Allostery in Ca(2)(+) channel modulation by calcium-binding proteins. *Nature chemical biology*. 10:231-238.

Yang, P.S., M.X. Mori, E.A. Antony, M.R. Tadross, and D.T. Yue. 2007. A single calmodulin imparts distinct N- and C-lobe regulatory processes to individual $Ca_V1.3$ channels (abstr.). *Biophys. J.* 92:354a.

Ye, Y., H.W. Lee, W. Yang, S.J. Shealy, A.L. Wilkins, Z.R. Liu, I. Torshin, R. Harrison, R. Wohlhueter, and J.J. Yang. 2001. Metal binding affinity and structural properties of an isolated EF-loop in a scaffold protein. *Protein engineering*. 14:1001-1013.

Yin, G., F. Hassan, A.R. Haroun, L.L. Murphy, L. Crotti, P.J. Schwartz, A.L. George, and J. Satin. 2014. Arrhythmogenic calmodulin mutations disrupt intracellular cardiomyocyte Ca2+ regulation by distinct mechanisms. *Journal of the American Heart Association*. 3:e000996.

Yue, D.T., P.H. Backx, and J.P. Imredy. 1990. Calcium-sensitive inactivation in the gating of single calcium channels. *Science*. 250:1735-1738.

Zamponi, G.W. 2003. Calmodulin lobotomized: novel insights into calcium regulation of voltage-gated calcium channels. *Neuron*. 39:879-881.

Zeilhofer, H.U., N.M. Blank, W.L. Neuhuber, and D. Swandulla. 2000. Calcium-dependent inactivation of neuronal calcium channel currents is independent of calcineurin. *Neuroscience*. 95:235-241.

Zhang, M., T. Tanaka, and M. Ikura. 1995. Calcium-induced conformational transition revealed by the solution structure of apo calmodulin. *Nature structural biology*. 2:758-767.

Zhang, S., M.D. Ehlers, J.P. Bernhardt, C.T. Su, and R.L. Huganir. 1998. Calmodulin mediates calcium-dependent inactivation of N-methyl-D-aspartate receptors. *Neuron*. 21:443-453.

Zhou, H., K. Yu, K.L. McCoy, and A. Lee. 2005. Molecular mechanism for divergent regulation of Cav1.2 Ca2+ channels by calmodulin and Ca2+-binding protein-1. *J Biol Chem*. 280:29612-29619.

Zhou, J., R. Olcese, N. Qin, F. Noceti, L. Birnbaumer, and E. Stefani. 1997. Feedback inhibition of Ca2+ channels by Ca2+ depends on a short sequence of the C terminus that does not include the Ca2+ - binding function of a motif with similarity to Ca2+ -binding domains. *Proc.Natl.Acad.Sci.U.S.A.* 94:2301-2305.

Zimmer, T., and R. Surber. 2008. SCN5A channelopathies--an update on mutations and mechanisms. *Progress in biophysics and molecular biology*. 98:120-136.

Zuhlke, R.D., G.S. Pitt, K. Deisseroth, R.W. Tsien, and H. Reuter. 1999. Calmodulin supports both inactivation and facilitation of L-type calcium channels. *Nature*. 399:159-162.

Zuhlke, R.D., G.S. Pitt, R.W. Tsien, and H. Reuter. 2000. Ca2+-sensitive inactivation and facilitation of L-type Ca2+ channels both depend on specific amino acid residues in a consensus calmodulin-binding motif in the(alpha)1C subunit. *J Biol Chem*. 275:21121-21129.

Zuhlke, R.D., and H. Reuter. 1998. $Ca^{2+}$-sensitive inactivation of L-type $Ca^{2+}$ channels depends on multiple cytoplasmic amino acid sequences of the $\alpha_{1c}$ subunit. *Proceedings of the National Academy of Science USA*. 95:3287-3294.

# CURRICULUM VITAE

Manu Ben Johny
4 Sugarloaf Ct. Apt. T1 / Baltimore, MD 21205
manu@jhmi.edu

---

## EDUCATION

| | |
|---|---|
| 2007 – 2015 | *Doctor of Philosophy* – Biomedical Engineering<br>Johns Hopkins University. Baltimore, MD |
| 2003 – 2007 | *Honors Bachelor of Science* – Biomedical Engineering and Mathematics<br>*summa cum laude*. Saint Louis University, St. Louis, MO |

## RESEARCH EXPERIENCE

| | |
|---|---|
| 2007 – present | *Dissertation Research* – Biomedical Engineering<br>Johns Hopkins University. Baltimore, MD<br>Advisor: David T. Yue, M.D. Ph.D.<br>- Identified conserved Ca$^{2+}$-regulation (calmodulation) of Na and Ca$^{2+}$ channels.<br>- Developed an assay to determine stoichiometry of binding reactions in live cells.<br>- Elucidated various molecular states underlying calmodulation of Ca$^{2+}$ channels.<br>- Allosteric regulation of calmodulation of Na and Ca$^{2+}$ channels.<br>- Synthetic biology of Ca$^{2+}$ channels – minimal Ca$^{2+}$ channels. |
| 2006 - 2007 | *Undergraduate Senior Thesis* – Biomedical Engineering<br>Saint Louis University. St. Louis, MO<br>Advisor: David Barnett, D.Sc.<br>- Real-time classification of rodent sleep stages using machine learning. |
| 2004 – 2006 | *Undergraduate Research* – Pharmacology and Physiology<br>Saint Louis University. St. Louis, MO<br>Advisor: Michael Ariel, Ph.D.<br>- Modeling of synaptic neurotransmission in accessory optic system of turtle brain. |

## TEACHING EXPERIENCE

| | |
|---|---|
| Spring, 2015 | *Guest Lecturer* – Workshop on FRET imaging<br>Department Pharmazie. Ludwig-Maximilians-Universität München, Munich, Germany |
| Spring, 2011 | *Teaching Assistant / Guest Lecturer* – Ion channels of Excitable Membranes<br>Biomedical Engineering. Johns Hopkins University. Baltimore, MD |
| Fall, 2009 | *Teaching Assistant* – Systems Bioengineering I |

| | |
|---|---|
| | Biomedical Engineering. Johns Hopkins University. Baltimore, MD |
| Fall, 2006 | *Teaching Assistant* – Signals and Systems<br>Electrical Engineering. Saint Louis University. St. Louis, MO |
| Fall, 2004 | *Teaching Assistant* – Basic Algebra<br>Mathematics. St. Louis Community College. St. Louis, MO |

## MENTORING EXPERIENCE

*Students mentored:* Jiangyu Li (2014 – present), Po Wei Kang (2013 - present), Jacqueline Niu (2013), Joey Bose (Spring 2012), Shiva Razavi (Fall 2011), and Daniel Yue (Summer, 2011; Summer, 2012).

## PUBLICATIONS

### Manuscripts.

1. Ben-Johny, M., and Yue, D.T. (2015) Calmodulin regulation of voltage-gated calcium channels and beyond. In Ion channel regulation. M. Trudeau and J. Zheng, editors. (*in press*).
2. Adams, P.J., Ben-Johny, M., Dick, I.E., Inoue, T., and Yue, D.T. (2014). Apocalmodulin itself promotes ion channel opening and $Ca^{2+}$ regulation. Cell **159:**608-622.
3. Ben-Johny, M.,Yang, P.S., Niu, J., Yang, W., Joshi-Mukherjee, R., and Yue, D.T. (2014). Conservation of $Ca^{2+}$/calmodulin regulation across Na and $Ca^{2+}$ channels. Cell **157**:1657-1670.
4. Ben-Johny, M., and Yue, D.T. (2014). Calmodulin regulation (calmodulation) of voltage-gated calcium channels. Journal of General Physiology **143**:679-692.
5. Yang, P. S., Ben-Johny, M., and Yue, D.T. (2014). Allostery in $Ca^{2+}$ channel modulation by calcium-binding proteins. Nature Chemical Biology **10**:231-8.
6. Caraveo, G., Auluck, P.K., Whitesell, L., Chung, C.Y., Baru, V., Mosharov, E.V., Yan, X., Ben-Johny, M., Soste, M., Picotti, P., Kim, H., Caldwell, K.A., Caldwell, G.A., Sulzer, D., Yue, D.T., Lindquist, S. (2014) Calcineurin determines toxic versus beneficial responses to α-synuclein. PNAS **111:**E3544-E3552.
7. Bazzazi, H., Ben-Johny, M., Adams, P.J., Soong, T.W., and Yue, D.T. (2013). Continuously tunable $Ca^{2+}$ regulation of RNA-edited $Ca_V1.3$ channels. Cell Reports **5**: 367-77.
8. Ben-Johny, M., Yang, P. S., Bazzazi, H. and Yue, D. T. (2013). Dynamic switching of calmodulin interactions underlies $Ca^{2+}$ regulation of $Ca_V1.3$ channels. Nature communications **4**, 1717.
9. Tadross, M. R., Ben-Johny, M. and Yue, D. T. (2010). Molecular endpoints of $Ca^{2+}$/calmodulin- and voltage-dependent inactivation of $Ca_V1.3$ channels. Journal of General Physiology **135**, 197-215.
10. Ariel, M. and Ben-Johny, M. (2007) Analysis of quantal size of voltage responses to retinal stimulation in the accessory optic system. Brain research **1157**, 41-55.

11. Haidekker, M. A., Lichlyter, D., Ben-Johny, M. and Grimes, C. A. (2006). Probing polymerization dynamics with fluorescent molecular rotors and magnetoelastic sensors. Sensor Letters **4**, 257-261.

**Manuscripts in preparation**

12. Ben-Johny, M., Yue, D.N., and Yue, D.T. Determining the stoichiometry of macromolecular complexes in live-cells using a novel FRET-based assay.
13. Ben-Johny, M., and Yue, D.T. The I-II loop harbors novel structural determinants of PIP2 modulation of $Ca_V1.3$ channels.
14. Ben-Johny, M., and Yue, D.T. Allostery confers specificity in regulating voltage-gated Na and $Ca^{2+}$ channels.
15. Ben-Johny, M., and Yue, D. Towards a synthetic biology of $Ca^{2+}$ channels.
16. Kang, P-W., Ben-Johny, M., and Yue, D.T. $Na_V1.5$ mutations associated with Brugada Syndrome result in loss of functional apocalmodulin regulation.

## ABSTRACTS

1. Ben-Johny, M., Persistent glimmer of common design across a billion years – conserved regulation of sodium and calcium channels by $Ca^{2+}$/calmodulin. Biomedical Engineering Departmental Seminar. Johns Hopkins University. (2014). (*Talk*)
2. Ben-Johny, M., Yang, P.S., Niu, J., Yang, W., Joshi-Mukhurjee, R., and Yue, D.T. Conservation of calcium/calmodulin regulation across sodium and calcium channels (abstr.). Gordon Research Seminar on Ion channels (2014). (*Talk*)
3. Ben-Johny, M., Yang, P.S., Niu, J., Yang, W., Joshi-Mukhurjee, R., and Yue, D.T. Conservation of calmodulin regulation across voltage-gated sodium and calcium channels (abstr.). *Biophysical Journal* 106 (2014). (*Talk*)
4. Yue, D.T. Ben-Johny, M., and Adams, P.J. Powerful and ancient embrace of four-domain voltage-gated channels with calmodulin (abstr.). *Biophysical Journal* 106 (2014).
5. Yang P.S., Ben-Johny, M., and Yue, D.T. A unified framework for calcium channel modulation by calcium binding proteins (abstr.). *Biophysical Journal* 106 (2014).
6. Adams, P.J., Ben-Johny, M., Dick, I.E., and Yue, D.T. Chemical-biological generators of step increases in calmodulin reveals dual modulation of L-type $Ca^{2+}$ channels (abstr.). *Biophysical Journal* 106 (2014).
7. Ben-Johny, M., Yang, P. S., and Yue, D. T. Towards a synthetic biology of calcium-regulation of $Ca_V$ channels (abstr.). *Biophysical Journal* 104, 462a. (2013).
8. Ben-Johny, M., Yue D.N., and Yue, D. T. A novel FRET-based assay reveals 1:1 stoichiometry of apocalmodulin binding across voltage-gated $Ca^{2+}$ and Na ion channels (abstr.). *Janelia Farm Research Conference* (2013).
9. Ben-Johny, M., Yang P.S., Bazzazi H., and Yue, D. T. Large-scale movements of calmodulin underlying $Ca^{2+}$ regulation of $Ca_V1.3$ channels (abstr.). *Gordon Research Conference on Ion channels* (2013).
10. Yang, P. S., Ben-Johny, M., and Yue, D. T. How CaBPs prevail over CaM in modulating $Ca_V1$ channels (abstr.). *Biophysical Journal* 104, 460a. (2013).

11. Lee, S. R., Ben-Johny, M., and Yue, D. T. Large $Ca^{2+}$-dependent facilitation of $Ca_V2.1$ channels induced by $Ca^{2+}$ photouncaging (abstr.). *Biophysical Journal* 104, 461a (2013).
12. Adams, P.J., Dick, I.E., Ben-Johny, M., Yang, P.S., Bazzazi, H. and Yue, D. T. Novel modulatory action of calmodulin complexation with L-type channels (abstr.). *Biophysical Journal* 104, 461a-461a (2013).
13. Limpitikul, W., Ben-Johny, M., and Yue, D. T. Autism-associated point mutation in $Ca_V1.3$ calcium channels alters their regulation by $Ca^{2+}$ (abstr.). *Biophysical Journal* 104, 459a. (2013).
14. Ben-Johny, M., Yue, D. N., and Yue, D. T. A novel FRET-based assay reveals 1:1 stoichiometry of apocalmodulin binding across voltage-gated Ca and Na ion channels (abstr.). *Biophysical Journal* 102, 125a. (2012).
15. Yang, P. S., Ben-Johny, M., and Yue, D. T. Calcium Binding Proteins (CaBPs) selectively modulate $Ca_V1$ versus $Ca_V2$ channels (abstr.). *Biophysical Journal* 102, 412a. (2012).
16. Sang, L., Bazzazi, H., Ben-Johny, M., and Yue, D. T. Resolving the grip of the distal carboxy tail on the proximal calmodulatory region of $Ca_V$ channels (abstr.). *Biophysical Journal* 102, 126a. (2012).
17. Adams, P.J., Dick, I.E., Ben-Johny, M., Yang, P.S., Bazzazi, H. and Yue, D. T. The distal carboxy tail (DCT) of $Ca_V1.4$ modulates more than $Ca^{2+}$/CaM-dependent inactivation (CDI) (abstr.). *Biophysical Journal* 102, 432a. (2012).
18. Hedjoudje, A., Hayden, R., Dai, C., Ahn, J.H., Rahman, M.A., Ben-Johny, M., Olds, K., Mori, S., Della Santina, C.C., Virtual labyrinth model accurately predicts responses to stimulation using a multichannel vestibular prosthesis in Rhesus monkeys. *Association for Research in Otolaryngology.* 1024 (2012).
19. Yang P.S., Ben-Johny, M., and Yue, D.T. Insights into CaBP4 regulation of L-type calcium channel through systematic identification of novel binding sites. *Society for Neuroscience*. 240.25. (2011).
20. Ben-Johny, M., Yang, P.S., and Yue, D. T. Molecular events beyond apoCaM preassociation in the CaM regulation of $Ca_V1.3$ channels (abstr.). *Biophysical Journal* 100, 529a. (2011). (*Talk*)
21. Joshi-Mukhurjee, R., Dick, I.E., Ben-Johny, M., Liu T., O'Rourke, B., Tung, L., and Yue, D.T. Normalizing action-potential morphology in long-term cultures of adult guinea-pig ventricular cardiomyocytes by $Ca_V$□ expression (abstr.). *Biophysical Journal.* 100, 574a. (2011).
22. Bazzazi, H., Ben-Johny, M., and Yue, D.T. Departure of calmodulin from the IQ domain of $Ca_V1.3$ channels during calcium-dependent inactivation. *Biophysical Journal.* 100, 571a. (2010).
23. Yang P.S., Ben-Johny, M., and Yue, D.T. Calmodulin-like region of $Ca_V1.3$ harbors novel structural determinants underlying CaM-mediated channel regulation. *Biophysical Journal.* 98, 134a. (2010).
24. Bazzazi, H., Ben-Johny, M., and Yue, D.T. Calmodulin release from the IQ domain of $Ca_V1.3$ channels during calcium-dependent inactivation. *Biophysical Journal.* 98, 519a. (2010).

25. Tadross, M.R., Ben-Johny, M., and Yue, D.T. End-stage mechanisms underlying voltage and $Ca^{2+}$/Calmodulin-dependent inactivation (VDI and CDI) of $Ca_V1.3$ channels. *Biophysical Jorunal*. 96, 222a. (2009).
26. Mori, M., der Kooi, V., Leahy, D., Ben-Johny, M., and Yue, D.T. Atomic structure of $Ca_V2$ IQ domain complex with $Ca^{2+}$/Calmodulin: high resolution structure – function implication (abstr.). *Society for Neuroscience*. (2008).
27. Ben-Johny, M., Diamond, S.G., Huppert, T.J., Laxminarayan, S., and Boas, D.A. A physiologically based model for fusion of electroencephalography (EEG) and diffuse optical tomography (DOT) (abstr.). *Biomedical Engineering Society Annual Meeting* Chicago, IL (2006).
28. Ben-Johny, M., Grimes, C.A., and Haidekker, M.A. Comparing fluorescent molecular rotors and magnetoelastic sensors to probe polymerization dynamics. *Institute of Biological Engineering conference on Biologically inspired Engineering*. Tucson, AZ (2006)
29. Laxminarayan, S., Ben-Johny, M., Diamond, S.G., Brooks, D., Tadmore, G., Miller, E., and Boas, D. Controlling dimensionality in a systems approach to dynamic multimodal functional brain imaging. *Research Thrust R2 presentations*. Paper 14. (2006)

## HONORS & AWARDS

| | |
|---|---|
| 2014 | *Nupur Dinesh Thekdi Research Award.*<br>Johns Hopkins University School of Medicine. Baltimore, MD.<br>- High honor for distinguished graduate research |
| 2014 | *Journal of General Physiology Award for Best Poster.*<br>Gordon Research Conference on Ion Channels. |
| 2010 – 2014 | *Ruth L. Kirschstein National Research Service Award for Predoctoral Fellows.*<br>Mechanisms of $Ca^{2+}$- and voltage-dependent inactivation of $Ca_V$ channels. (F31MH088109)<br>National Institute of Mental Health. |
| 2003 – 2007 | Dean's List. Saint Louis University. |
| 2003 – 2007 | Vision Scholarship. Saint Louis University. |
| 2003 – 2004 | Monsanto Scholarship. 2003 – 2004. |